The Effect of Post-Catalyst Exhaust Gas Recirculation on Combustion in Highly Rated SI Engines

Parsons, Dominic

Award date:
2020

Awarding institution:
University of Bath

The Effect of Post-Catalyst Exhaust Gas Recirculation on Combustion in Highly Rated SI Engines

submitted by

Dominic Parsons

for the degree of Doctor of Philosophy

of the

University of Bath

Department of Mechanical Engineering

July 2019

Summary

Despite the growing push by governments towards vehicle electrification, the SI engine will remain integral to automotive powertrain technology for the foreseeable future. With increasingly stringent emissions standards and testing protocols, further improvements in SI engine efficiency are required.

Engine downsizing and downspeeding are effective strategies for reducing CO_2 emissions from GDI engines, but anticipated upcoming restrictions on CO emissions in the Euro 7 emissions standards have intensified the focus on knock control methods which can maintain stoichiometric combustion at high load.

Exhaust gas recirculation (EGR) has been proven to be a valuable technology for controlling knock whilst maintaining lambda one operation [1], and is also capable of providing efficiency gains at low load [2]. Whilst the evidence supporting the benefits of EGR is unanimous, there is no consensus on optimum EGR strategies amongst the wealth of various possible architectures.

Few studies in the literature address the question of EGR composition effects, namely whether the EGR gas is sourced from before or after the catalyst, and this remains an area which is often overlooked during assessments of EGR performance.

This thesis focuses on the combustion effects of EGR catalysis on high load operation using both experimental and modelling methods. An artificial boosting system replaced the turbomachinery for the experimental work, which allowed the combustion effects to be assessed at constant load and engine boundary conditions.

Two experimental campaigns were carried out on two different high load GDI engines, with the experimental techniques evolved for the second iteration to improve the quality of the results. The increased knock inhibiting effects of catalysed EGR were confirmed, with the catalysed EGR increasing knock limits by 0.5-1 CAD over equivalent non-

catalysed conditions. It became apparent that the presence of NO in the EGR is one of the most significant factors in this difference, which supports evidence from the literature on NO effects on autoignition [3].

The modelling study revealed more detail on how the different EGR species affect the combustion process whilst also providing an opportunity to assess the current state of the art in combustion simulation methods. The modelling results further support the evidence of NO being a major autoignition promoter.

The relatively new simulation technique of stochastic reactor modelling was employed to carry out the modelling work. Initial tests vastly underestimated the dilution effect of EGR, with high burn rates causing peak pressures to be over-predicted by up to 10 bar at 9% EGR. Adjustments to the laminar flame speed correlation improved the accuracy of the predicted burn rate but the peak pressure was still up to 5% higher than experimental results with EGR. Further adjustments to the fractal flame propagation model provided more improvement to the model's EGR response within the speed/load condition tested.

With the increasing complexity of vehicle powertrains there is a growing dependence on simulation methods to reduce the time and cost of powertrain design and optimisation processes, and combustion modelling is one of the key obstacles to progress in this field. This work highlights the importance in considering the chemical effects in determining optimal EGR architectures, and identifies where improvements are required for integration of more detailed combustion models into 1-D engine simulations. Ultimately these methods could contribute to improved accuracy in simulation-based engine design validation and optimisation processes.

ACKNOWLEDGEMENTS

There are so many people that I must thank for helping me along the way.

I would like to thank my supervisors, Professor Chris Brace, Professor Sam Akehurst and Doctor Andrew Lewis for their guidance and support throughout my PhD.

Doctor Karl Giles has been enormously supportive as a colleague at the University of Bath, a friend, and as my flatmate for the last six years, and I am very grateful for his willingness to discuss all the various questions I have come to him with when I am sure he would much rather be doing anything else.

I am very grateful to the PVRC technician team (James Burge, Craig Bayliss, Bob Gusthart, James Cansell, Tom Holley and Ben Hampton) for their assistance in setting up and modifying the test rigs and setting me straight when I am over-ambitious with my testing plans.

I would also like to thank my colleagues within the PVRC, both past and present, in particular those involved with both the Ultraboost and Dynamo projects with whom I collected the bulk of my data for this thesis. I have enjoyed sharing an office with all of you!

My coach, Rob Ellchuk, has also played a huge part in my life and I am hugely grateful for his guidance in sport, life, and academia which has helped to shape the person I am today.

Finally I would like to thank my wife, Jackie, for being so supportive and understanding – especially during my long absences whilst finishing this thesis.

CONTENTS

LIST OF FIGURES

LIST OF TABLES

NOTATION

°CA	Crank angle degrees
AHRR	Apparent heat release rate
AI	Autoignition
ASTM	American Society for the Testing of Materials
BEV	Battery electric vehicle
BMEP	Brake mean effective pressure
BSFC	Brake specific fuel consumption
CAHU	Combustion air handling unit
cEGR	Catalysed exhaust gas recirculation
CFD	Computational fluid dynamics
CR	Compression ratio
DI	Direct injection
DISI	Direct injection spark ignition
DNS	Direct numerical simulation
DOHC	Double overhead camshafts
EGR	Exhaust gas recirculation
EIVC	Early inlet valve closing
EVC	Exhaust valve closing
EVO	Exhaust valve opening

FCEV	Fuel cell electric vehicle
FIS	Forced induction simulator
FMEP	Frictional mean effective pressure
FS	(Of) full scale
HC	hydrocarbon
HCCI	Homogeneous charge compression ignition
HP	High pressure
IC	Internal combustion
IEM	Interaction by exchange with the mean
IGR	Internal gas residual
IVC	Inlet valve closing
IVO	Inlet valve opening
KI	Knock intensity
KLSA	Knock limited spark advance
LES	Large eddy simulation
LHV	Lower heating value
LIVC	Late inlet valve closing
LP	Low pressure
MAPO	Maximum amplitude of pressure oscillations
MFB	Mass fraction burned
NEDC	New European driving cycle
nEGR	Un(non)-catalysed exhaust gas recirculation
NO	Nitric oxide
NOx	Oxides of nitrogen
NTC	Negative temperature coefficient
OEMs	Original equipment manufacturers
PaSPFR	Partially stirred plug flow reactor
PDF	Probability density function
PHEV	Plug-in hybrid electric vehicle
PLR	Piecewise linear regression

PMEP	Pumping mean effective pressure
PPCI	Partially premixed compression ignition
PRF	Primary reference fuel
PSD	Power spectral density
RANS	Reynolds averaged Navier Stokes
RDE	Real driving emissions
RGF	Residual gas fraction
sEGR	Synthetic exhaust gas recirculation
SEPO	Signal energy of pressure oscillations
SER	Signal energy ratio
SI	Spark ignition
SOI	Start of combustion
SRM	Stochastic reactor model
TPRF	Toluene primary reference fuel
TRF	Toluene reference fuel
UEGO (sensor)	Universal exhaust gas oxygen (sensor)
ULG	Unleaded gasoline
VCR	Variable compression ratio
VVT	Variable valve train
WOT	Wide open throttle

CHAPTER 1

INTRODUCTION

Tightening legislation on vehicle emissions and fuel economy are putting increasing pressure on the development of low emission powertrain systems.

Whilst electrification of the powertrain can assist in achieving these targets, ICEs will still play a pivotal role in future powertrains.

EGR is one promising technology in helping to achieve cleaner combustion systems, but questions still remain over the optimum EGR architecture and the accuracy of EGR simulation techniques.

This chapter outlines the background for the research in this thesis in the context of current and future powertrains. Aims and objectives of the research are presented, followed by details of the layout of this thesis.

1.1 Background and motivation

The impact of vehicle emissions amongst global environmental concerns is putting huge pressure on the automotive industry. Restrictions and incentives to push the automotive market towards vehicle electrification are becoming common in urban areas, and announcements of intentions for future nationwide restrictions on the sales of ICE powered vehicles have been made in a number of countries.

Despite this the IC engine currently features strongly in new car sales[1], and forecasts predict that this will still be the case beyond 2030 [11]. In most markets worldwide the sales of electric vehicles is inhibited by high costs, shortcomings in infrastructure (such as charging facilities or clean energy generation), and limited range of electric vehicles.

Vehicle fleets are increasingly moving towards electrification of the powertrain to various extents in the form of hybridisation. Whilst hybridisation is a move towards electrification, it still relies upon the IC engine to achieve emissions targets; therefore the development of IC engines must still be a priority in delivering cleaner vehicle drivetrains.

The potential of the IC engine to realise more efficient operation and reduced emissions lies in the development of several advanced technologies. Modern gasoline engines commonly use direct injection, and have seen a vast trend in downsizing and downspeeding to reduce the frictional and pumping losses associated with higher displacement engines.

In order to achieve the power outputs of their larger counterparts these downsized engines often use turbocharging to recover waste heat from the exhaust gases and increase their output. This increases the level of component protection that must be employed in certain regions of their operating strategies – both to control knock and to reduce exhaust temperatures to protect the turbomachinery. A common solution for this is to retard the

[1] In 2016 only 1% of new car sales worldwide were electric [11] and in the UK electric vehicle sales (including BEVs, PHEVs and hydrogen fuel cell vehicles (FCEVs) made up 2.8% of the new car market in 2018 [12].

ignition to avoid knocking conditions, and inject excess fuel to cool the exhaust gases. Needless to say, this is harmful to the engine emissions and fuel economy.

There are a number of alternative strategies for controlling knock without the need for overfuelling and EGR is particularly prominent in this area [1]. The dilution effect of EGR can mitigate the risk of knocking combustion at high loads whilst also providing fuel economy benefits at low load by reducing throttling losses [13].

Anticipated CO restrictions in the Euro 7 emissions regulations, alongside the real driving emissions (RDE) test protocols, have added to the pressure on OEMs to realise lambda one operation across the entire operating range of their engines. Whilst EGR is a promising technology in the field, it sits amongst a number of other promising technologies such as variable compression ratios (VCRs), water injection, and hybridisation.

EGR systems can take a number of different forms of varying complexity. The location of its source and delivery points in relation to the turbocharger define the architecture of an EGR system, the two most common architectures being low pressure (LP) and high pressure (HP). The former sources the EGR gases from after the turbine, and delivers them pre-compressor. The latter sources them from before the turbine and delivers them post-compressor. Mixed pressure architectures are also possible but are less common. The one overruling requirement is a positive pressure differential between the source and delivery locations of the EGR system, and this can be a limiting factor at some operating conditions.

Additional factors in the design of EGR systems include the potential for condensate to damage the compressor in LP architectures, and additional demands that cooled EGR can place on vehicle cooling systems.

Whilst most studies into EGR operation report the impact of the different architectures, its chemical composition introduces a further variable to consider. Until now only a few studies have investigated the impact of the catalyst in EGR operation, and these results

are heavily impacted by the turbocharger performance and its sensitivity to changes in pressure differentials.

EGR does provide obvious benefits, but optimising future powertrains is dependent on the synergy between different advanced technologies that are applied to a given powertrain system.

The challenge to OEMs is to balance the cost of new technologies against the reduction in emissions that they can provide, which is becoming increasingly challenging with the complexity of new powertrains and the interactions between different advanced technologies. Simulation methods have become increasingly popular as a method of assessing the potential performance of powertrain systems within vehicles, but the accuracy in these methods is not yet high enough to allow the concept validation process to become entirely virtual. Improvements in these methods could become integral to optimising the synergy between various technologies in IC engines, and in reducing the cost of the concept validation and development processes by enabling a more virtual design validation and development process.

This thesis focuses on the combustion effects of different EGR mixtures to further the understanding of how the EGR composition can impact combustion, using both experimental and simulation techniques.

The experimental work in this thesis is largely based around engine tests performed with an artificial boost rig replacing the turbomachinery on the engine, therefore allowing comparisons of the EGR effects independently of the impact on the boosting hardware.

The modelling work follows on from the experimental work with a model of the combustion system to compare its performance against experimental data. The assessment follows two avenues: the numerical models, and the chemical models. Both of these aspects must be addressed to improve vehicle simulation accuracy, since reliable simulation methods to assess EGR performance within an entire powertrain system are invaluable

in order to guide the decision-making process for future powertrain design.

1.2 Aims and objectives

This investigation endeavours to further the understanding of EGR composition effects on GDI combustion at high load and to characterise this effect in a combustion model.

The primary objectives are listed below:

1. To conduct a detailed literature review on the current status of EGR application in GDI engines and how EGR composition integrates into this understanding. This will progress into a review of combustion simulation methods with respect to the effects of inlet charge composition.

2. To design and execute an experimental campaign capable of delivering combustion data across a range of dilution concentrations to observe the effects on knocking combustion and engine performance.

3. To build a model of the combustion system and assess its accuracy in predicting dilution effects against experimental data.

4. To gather information on the most pertinent mechanisms that are relevant to comparisons in EGR composition.

5. To review the major findings from the thesis and make recommendations on future work.

1.3 Layout of this thesis

The layout of this thesis has the following structure:

Chapter 2 introduces the concept of EGR and its evolution up to this point. The literature on EGR performance at high load is assessed before focusing on the effects associated with catalysed EGR. A brief overview of the kinetics of hydrocarbon combustion kinetics is given before then reviewing the kinetic effects associated with minor species found in EGR. This is followed by a discussion of the modelling methods that are available for simulation of combustion effects, with a particular focus on the novel method of stochastic modelling.

Chapter 3 describes an experimental process to assess the impact of EGR catalysis on a high load combustion system. The experimental facilities and processes are described before presentation of the results and an assessment of the accuracy of these results.

Chapter 4 applies the lessons from Chapter 3 to the design and implementation of a second experimental campaign to investigate the effects of EGR catalysis. The experimental processes are evolved from the previous chapter which allows a more in depth analysis of the results.

Chapter 5 attempts to model the combustion system from Chapter 4 and assesses the response of this model to EGR dilution. This model is then used to analyse the chemical impacts of the minor species in EGR.

Chapter 6 summarises the process and findings from this thesis. The aims and objectives are compared to the results from each section to draw conclusions from the project and recommendations are made on the direction of further work in this area.

CHAPTER 2

REVIEW OF THE LITERATURE

This chapter starts by reviewing the literature relating to exhaust gas recirculation, then expands upon the area of catalysed exhaust gas recirculation, with particular attention paid to the reported effects of NO.

The second section looks at the current literature on modelling methods for combustion in the context of dilution effects. Starting with a brief summary of the available methods before then focusing on the use of PDF models. The most relevant areas to kinetic modelling are then discussed, being kinetic mechanisms and surrogate fuels.

Aspects of this chapter have been published in the International Journal of Engine Research [14].

2.1 The concept of exhaust gas recirculation

Exhaust gas recirculation (EGR) is often referred to as a 'promising technology' but has been present in the literature for close to century now. Early work by Sir Harry Ricardo [15, 16] promotes the use of "inert exhaust gas" as a knock control method, where he uses it to achieve higher compression ratios in aircraft engines without the risk of pre-ignition at lower altitudes.

This section will summarise the evolution of EGR technologies in gasoline engines up to the present day, in particular in relation to knock control, and will compare it to alternative knock control strategies.

2.1.1 Early EGR studies

Headlines on automotive emissions and the drive to reduce pollutants in the automotive sector are not only a symptom of modern day society, but have been a driver in IC engine development for a number of decades. This is apparent in work from the late sixties and early seventies with Eyzat et al [17] citing the "current effort to reduce air pollution", and a number of studies around this time attempted to tackle NOx emissions by presenting theories on the formation of NO during combustion [17, 18].

Early simulation methods were demonstrated by Newhall [19] in assessing EGR performance and resulting reduction in NOx emissions, but even he refers to his own models as 'oversimplified', highlighting a need for more detailed understanding of the NOx formation mechanisms.

Deisel engines adopted EGR as a NOx suppression technology since the introduction of modern direct injection (DI) deisel engines in the mid 1990s [20], but the use of EGR has been rare in production gasoline engines. The recent move towards downsizing and direct injection for gasoline engines seems to have stimulated renewed interest in EGR, with a multitude of studies investigating its use in recent years.

2.1.2 Mechanisms of EGR

The benefits associated with EGR can be related to both high and low load operation via different mechanisms. At low load, the EGR gases displace a proportion of the inlet charge, thereby de-throttling the engine without the associated losses of mechanical throttling. This can benefit the fuel efficiency at these conditions.

At high load EGR can advance knock limits, thereby allowing stoichiometric combustion closer to maximum brake torque (MBT) spark timing. This can offer both improved efficiency and also reduced NOx emissions due to lower combustion temperatures and pressures.

Knock is a major limiting factor in reaching the efficiency potential of gasoline engines. Knock stems from autoignition in the end gas before the advancing flame front has consumed the unburned mixture. The resulting pressure oscillations can lead to damage to engine components and, if strong enough, can lead to catastrophic failures. Engine control units (ECUs) avoid heavily knocking conditions by retarding the spark angle, which can then introduce the requirement for over-fuelling to control exhaust temperatures. These two actions are both counter-productive to engine efficiency, as they move combustion phasing to sub-optimal regions as well as increasing fuel consumption with little or no benefit to torque output.

Subsequently, a major focus in engine combustion research has been on the mechanisms behind knocking combustion and strategies to control it without penalties to engine performance and efficiency.

The onset of autoignition is primarily influenced by the pressure and temperature histories in the end gas [21]. The end gas undergoes heating and compression as a result of the advancing flame front and the upward movement of the piston. The propensity to autoignite increases with the temperature, but is also dependent on the chemical properties of the unburned mixture and the presence of any hotspots. Konig et al used high speed schlieren photography to record autoignition events originating from one or

multiple local hotspots, which if close enough could combine to increase the intensity of the resulting pressure waves [22]. If these hotspots reach the point of ignition before the flame consumes it knock can be observed.

The addition of EGR has both a thermodynamic and chemical effect on the cylinder pressure and temperature histories. As described by Ricardo as early as 1919 [15], the inert species can "insulate the fuel and oxygen particles" somewhat to slow combustion rates. This is elaborated upon in more recent work to put this into the context of chemical reaction rates [23]. Reaction rates are dependent on the rate constant and concentrations of each of the substrates – resulting in the following relationship, which assumes that the number of molecules reacting is proportional to the number of collisions between them:

$$r = kc_1c_2 \tag{2.1}$$

where k is the rate constant and c_1 and c_2 are volume concentrations of each substrate.

Not every collision between the substrate molecules will be successful. Both the collision energy and orientation of the relevant molecules (larger molecules require collisions between their active centres) will dictate whether the collision produces a successful reaction. So even before thermodynamic effects are considered, the dilution of the reactants can provide a significant reduction to reaction rates by reducing the number of successful collisions.

The burned gases also have a higher mass (and heat capacity) than the air that they displace (for a given output), but this is partially offset by the relative reduction in the proportion of fuel in the cylinder – leading to the cylinder charge actually having a reduced specific heat capacity (C_p) and therefore higher specific heat ratio (γ) leading to a higher isentropic temperature increase [24][1] .

[1] This is according to: $\frac{T_2}{T_1} = \left(\frac{p2}{p1}\right)^{1-\frac{1}{\gamma}}$

2.1.3 Alternative knock control methods

The motivation to increase the knock resistance of engines is almost as old as the IC engine itself. Sir Harry Ricardo relates the knock propensity of an engine to its highest achievable compression ratio [16] and discusses alternative methods to reduce the flame propagation rate or the temperature at which autoignition will occur in an engine. Since autoignition is often triggered by inhomogeneity in the end gas, a great deal of research has focused on turbulence enhancement to promote mixing, along with more effective cooling strategies, in an effort to employ larger compression ratios to benefit the thermal efficiency of an engine.

The following sections describe more novel technologies that have been demonstrated to improve the knock limits of gasoline combustion.

Cam phasing

The motivation to develop technologies to reduce knocking combustion has led to investigations into a number of alternative strategies besides EGR. The most common of these is variable valve timing (VVT), into which a huge amount of research has given a fairly robust foundation upon which some modern production engines have based some significant performance gains.

VVT allows independent control over the breathing of the engine, giving freedom to operate with high residuals (sometimes referred to as internal EGR), reduced effective compression ratios, and reduced pumping losses via various methods of VVT implementation.

A study in the late 90s by Hatamura et al [25] demonstrated the potential of Miller cycle operation, achievable by either early inlet valve closing (EIVC) or late inlet valve closing (LIVC), on a supercharged engine to realise higher BMEP (brake mean effective pressure) by improvement of the combustion phasing at high load by effectively reducing the compression ratio at these conditions.

Li et al [26] also discussed the benefits of using a Miller cycle to allow operation with higher geometric compression ratios without suffering from knock at high loads. Their study found benefits in BSFC (brake specific fuel consumption) of 4.7% at high load, and 7.3% at low load, by increasing the compression ratio from 9.3 to 12 in combination with Miller cycle operation at high load.

A fairly comprehensive review on the subject of both Miller and Atkinson cycles (referred to as "overexpansion" cycles) was written more recently by Zhao et al [27]. They focus on the context of hybrid powertrains, claiming that Miller/Atkinson cycle operation can improve the synergy between the internal combustion and electric components in the powertrain.

This technology is already well established, with a number of production engines employing Miller cycle operation in combination with other technologies to achieve efficiency gains across their operating map [28, 29].

Water injection

Water injection is a technology that has received renewed interest in recent years [30–33], long after Ricardo described it as having several "objections" in the 1920s, including the quantity and purity of the water required [16]. It was, however, used successfully in wartime aircraft engines to control detonation [34] and has long been lauded as a valuable technology for reducing NOx emissions in diesel engines.

Water injection can take the form of either port or direct injection, with direct injection either taking the form of a fuel/water emulsion being injected via the fuel injectors, or incorporating additional water injectors into the cylinder head. The advantages of water injection to cool the inlet charge are well known, and there are even a number of after-market kits available for car enthusiasts to convert their own cars to operate with port or manifold water injection (often water and methanol injection) to allow them to run at higher loads.

The high latent heat of vaporisation of water provides significant evaporative cooling

to the charge air to slow combustion rates and increase knock limits, as well as acting as a diluent during combustion processes. The charge cooling effect is maximised with direct injection of the water, since wall wetting and premature vaporisation outside of the cylinder can reduce the effectiveness of port injected water [35].

Bozza compares water injection against EGR operation via 1-D simulation to confirm that both are viable technologies to improve knock limits [1].

Despite its obvious benefits during experimentation, the challenges of potential oil emulsions forming and of ensuring a water reservoir is capable of supplying an adequate quantity of water without the risk of freezing in cold conditions, still provide obstacles to vehicle integration [36].

BMW performed on-engine trials to overcome these obstacles in 2016 with some success [37]. They came up with a novel solution of sourcing the water from the air-conditioning condensate which is then directly injected into the cylinders. The high pressure water pump is reversed after the engine is stopped to remove all water from the injectors, and the supply line is equipped with a 'damping volume' to avoid damage to components if the water does freeze.

Lean boost

The lean boost system was proposed near the start of the millennium by some researchers at Ricardo [38] to improve efficiency of downsized gasoline engines. They compared its performance to cooled EGR operation, Miller cycle operation, and dual injection strategies, finding a marked reduction in CO_2 emissions with the lean boost concept [39]. They do cite some drawbacks to the approach, such as the difficulty in reaching sufficiently high after treatment conversion efficiencies from production catalysts, and high NOx emissions.

Cairns et al conducted a number of studies into the effectiveness of EGR including comparisons against lean boost and overfuelling [40–42]. Contrary to the researchers at Ricardo, they found EGR to be a more effective knock suppressant than either excess

air or fuel, with large fuel consumption benefits of up to 17% at high load coming from the elimination of the need for over fuelling. Significant CO, CO_2 and HC emissions improvements were also observed, although it should be noted that the CO and HC emissions are very sensitive to variations in relative air-fuel ratio (λ), as highlighted by Alger et al [13].

Grandin et al also make a similar comparison between EGR and lean burn, but seem less decisive on deciding which concept offers more potential. They do, however, note the high NOx emissions and difficulty in after-treatment for lean burn operation [24], which seems to have been prohibitive for more mainstream adoption of this technology.

Turbo expansion

Turboexpansion is a novel concept that was introduced to improve knock limits in the mid 2000s by Turner et al [43–45]. The concept was based upon the thermodynamic principle that a gas undergoing expansion will drop in temperature. Since cooler charge temperatures can help to extend knock limits, this concept was devised to over-compress the fresh charge before then re-expanding it post-intercooler to further reduce the temperature at the inlet manifold on top of what is possible with heat exchangers alone.

The concept proved to be effective at increasing knock limits, but initial dynamometer tests fell short of performance targets, citing the isentropic efficiency of the expander as the critical element [44]. More recent work [46] again cites the importance of the expander efficiency in achieving targets with the turboexpansion concept, which appears to be an obstacle for the adoption of this technology.

Variable compression ratios

The efficiency of an engine is intrinsically linked to its compression ratio which is demonstrated by the efficiency relationship for an ideal gas:

$$\eta \propto 1 - \frac{1}{r_c^{\gamma-1}}. \tag{2.2}$$

For current engines the maximum achievable compression ratio is limited by knock at high loads. Variable compression ratio (VCR) concepts have been devised to combat this and enable lambda 1 operation across the operating range with increased thermal efficiency in regions that are not knock limited.

VCR concepts can be divided into three main groups, as identified by Wolfgang et al [47]:

- Variable effective distance between crankshaft and cylinder head
- Articulated multi-link crank trains
- Variable effective conrod length

An example of the first of these concepts is the Cooperative Fuels Research (CFR) engine, which is used for quantifying octane ratings of fuels. The CFR engine uses a rack and pinion method to raise or lower the cylinder head to reduce or increase the compression ratio – which is the method by which it is used to quantify the octane rating of a fuel [48].

The cost and complexity of this form of VCR concept is quite prohibitive to OEMs though, so more research has been directed at the other two methods of VCR operation.

Several concepts have been developed in the vein of articulated multi-link crank trains, one of which has brought to market the first production VCR engine [49]. The concept, developed by Nissan, uses a 2l GDI engine which is currently only incorporated into a couple of their vehicle lines. The VCR mechanism uses a link with a central bearing attaching to the crankshaft. One side of the link connects to the conrod, and the other side is raised or lowered by a control link. The position of the control link is operated by an electric actuator.

Nissan's concept is reported to achieve fuel economy equivalent to modern 1.4-1.6l turbocharged engines, but with torque output exceeding that of a 3.5l NA V6, by using a

continuously variable compression ratio from 8:1 to 14:1 across the operating map. It is, however, only currently available to US and Chinese markets, as the linkage parts require further development to fit smaller displacement engines that are more common in Europe.

Collée et al [50] have showcased a VCR concept which uses a similar mechanism to that of the Nissan VCR concept. Their concept uses a rocker system modification to the conrod that uses a secondary cylinder to actuate the control mechanism – actuated by oil pressure which is driven from either inertial forces (increasing CR) or combustion gas pressure (decreasing CR). Despite there still being a high level of complexity in this system, Collée et al are still confident that it provides a cost-effective opportunity to improve BSFC figures by up to 10 to 15%. The geometric compression ratio can be varied from 8:1 to 18:1 which, in combination with Miller cycle operation, can offer high efficiency benefits across the operating map whilst avoiding knock at high load with stoichiometric operation. Their development roadmap highlights the compatibility of this system with other technologies, including 48V mild hybridisation and EGR.

Variation of the conrod length typically dictates that a two-step approach must be used [47]. Options include using an eccentric bore for either the piston pin ([51]) or conrod big end ([52]), or using a telescopic conrod shank ([47, 53]).

Wolfgang et al [47] developed a telescopic oil pressure actuated conrod. They concede that it is 60% heavier than a standard conrod, but can switch compression ratios between 9:1 and 14:1, and can increase the CR over 10 cycles and decrease CR over 4 cycles. Schulze et al [53] developed a similar system that uses hydraulic switching between two chambers which fill due to the mass force of the crank on the conrod.

Gomecsys developed a concept that uses an eccentric bore at the big end bearing. They boast of it being a compact system, and it is electrically actuated and able to vary the compression ratio from 8.5:1 to 14:1 (on a demonstrator 1.6l GDI) to provide 8% reduction in CO_2 [52].

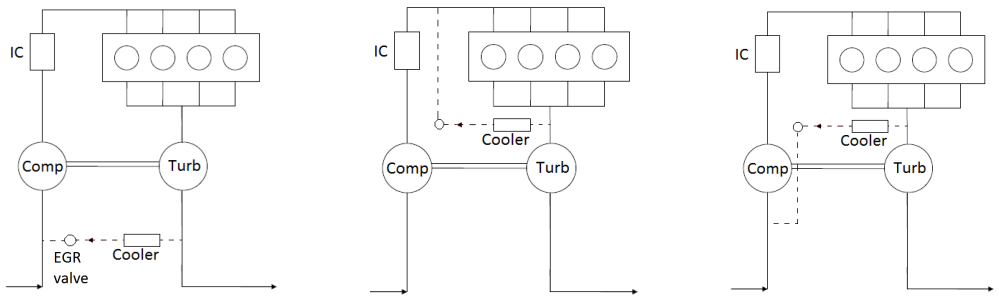

(a) Low Pressure Architecture

(b) High Pressure Architecture

(c) Mixed Pressure Architecture

Figure 2-1: Illustration of the three most common EGR architectures (the EGR route is shown by the dashed line, IC denotes intercooler)

The consensus on VCR technology seems to be that the benefits offered by VCR are well supplemented by Miller cycle operation, and that the emissions and BSFC benefits of the two technologies combined are greater than the sum of both in isolation.

2.1.4 EGR architectures

There are a number of potential architectures for EGR operation, which often prove to be the most pertinent aspect to EGR performance within a powertrain system. For the most part, these vary by the location from which the exhaust gases are sourced (pre or post turbine), and the location for the introduction of the exhaust gases to the inlet side (pre or post compressor). A large number of studies focus on either high pressure (HP – Figure 2-1b) – pre turbine to post compressor – operation or low pressure (LP –Figure 2-1a) – post turbine to pre compressor – operation, with some also including mixed (HP-LP) operation (Figure 2-1c).

Vítek et al [54] used simulation methods to compare the effect of four different cooled EGR architectures on a diesel engine over the NEDC cycle. Their results showed that during steady state operation at some points on the NEDC cycle the LP layout showed as much as an 8% BSFC reduction in comparison to the other architectures. Combining this with the capability of the LP architecture to provide sufficient EGR rates across the entire operating map showed a significant advantage for this layout, despite a poorer

transient response than the HP alternatives.

A similar study was conducted by Potteau et al [55] on an SI engine, which investigated four different EGR architectures via simulation before investigating an HP (Figure 2-1b) and LP (Figure 2-1a) architecture in more detail on an experimental engine. The LP EGR loop was, in fact, sourced from downstream of the catalyst to benefit from "favourable thermal properties and cleaner gases". This would change the chemical composition of the gases introduced to the inlet charge in comparison to the non-catalysed HP loop and therefore introduces a further variable when comparing the two architectures.

A common problem observed with HP architectures is the availability of a positive pressure differential across the operating map between the inlet and exhaust manifolds to drive the EGR flow. For this reason Potteau et al [55] used a throttle upstream of the EGR inlet to create a pressure differential to drive the EGR flow in HP mode. Despite this, they still found the system incapable of producing the required pressure differential at low speed, high load conditions. They observed a 6.6% BSFC improvement for the HP architecture over non-EGR operation, which compared to a 13.6% improvement for the LP architecture at similar conditions (5500 rpm, 12.9 bar BMEP). A large part of this may be attributable to the knock limited spark advance being only improved by 5°CA for the HP layout, compared to 10°CA for the LP architecture. They concluded that this could be due to both cooler recirculated exhaust gases in the LP layout, and the effect on combustion of the decreased HC and CO levels due to catalysis of the recirculated exhaust gases.

Alger et al investigated the use of an uncooled HP EGR loop at low loads, and a cooled LP loop for high loads on an SI engine [13]. Although its significance is not mentioned in the study, the LP architecture used the same configuration as that in Potteau et al's study [55] and sourced the exhaust gases from downstream of the catalyst. The chemical effect of this is not discussed but, despite this, the authors conclude that the

cooled LP EGR configuration is preferable for knock prevention at high loads[2], and the hot HP EGR at part loads to help maintain combustion stability whilst also thermally de-throttling the engine [3].

Turner et al [56] focused their investigation on the high load operation (at 5000rpm) of an SI engine employing an integrated cooled exhaust manifold with a comparison of an HP, LP and an HP-LP EGR configuration. Their data were for comparatively low EGR rates (up to 6%) which are significantly lower than those used previously in the literature. They concluded that the different architectures had a larger impact on the charging system than they did on the combustion system, and that the LP architecture appeared to offer the least benefit. They also noted that the turbocharger was not well matched to the engine, and that with a less restrictive turbine the EGR benefits may have been significantly improved. Furthermore, the matching of the turbocharger to the engine could have differing effects for each of the EGR configurations. This further highlights the complexity involved in the comparison of different EGR systems.

2.1.5 High and Mixed Pressure EGR Systems

Several studies have focused purely on HP EGR to ascertain its benefits versus either lean operation or overfuelling. Galloni et al [57] and Hattrell et al [58] used simulation methods to confirm the advantages of EGR, and experimental investigations by Grandin et al [24, 59] and Fontana et al [60] provide further confirmation that cooled HP EGR can provide significant fuel consumption benefits[4] where the engine speed is high enough to provide a sufficient pressure differential between the exhaust and inlet ports to drive the EGR flow.

Cairns et al [42] compared EGR supplied post compressor (HP) to that supplied pre-compressor (HP-LP) and concluded that although the HP loop was favourable for transient response, it was not possible to drive the EGR rate through the full operating

[2] At high loads a BSFC reduction up to 26% was observed due in large part to the elimination of over-fuelling

[3] At low loads a BSFC reduction of up to 3% was observed

[4] These benefits vary between 6% and 15% BSFC reduction at high load between the different studies.

range due to an insufficient pressure differential between the exhaust and intake manifolds. They go on to say that although an LP EGR architecture was not investigated, it may improve on the HP-LP architecture that they did test due to lower cooling demands of the post-turbine gas.

2.1.6 Low Pressure EGR Systems

Low pressure EGR systems are a very active area of research, but research has primarily focused on the dilution effects of EGR rather than the chemical effects on combustion.

Kaiser et al [61] investigated an LP EGR architecture on a twin turbocharged V6 SI engine, citing the main advantage of LP EGR as "it enables EGR to flow at lower engine speeds where engine knock limited combustion is more of a problem". Bourhis et al [62] investigated a similar architecture but with post-catalyst sourced EGR in combination with internal EGR (IGR) through variation of the valve overlap. They found significant fuel consumption benefits of up to 20g/kWh at part load which they attributed more to VVT optimisation rather than the effect of the EGR.

Hoepke et al [63] also investigated an LP EGR system on a boosted GDI SI engine and confirmed that it extended the knock limit due to lower end gas temperatures. Their experimental investigations showed maximum fuel consumption benefits of 3%, which compared to 5% predicted by simulation.

Evidence from the literature suggests that any EGR architecture involves a certain extent of compromise, be it the slower transient response of LP EGR, or the insufficient pressure differential to provide HP EGR flow across the full operating map. Furthermore, the different aspects of high and low pressure EGR systems can favour either purpose for EGR application. Hotter EGR gases can benefit combustion stability whilst de-throttling an engine at part-load, whereas cooler EGR provides more potential for extending knock limits at high load [64]. Chao et al [65] confirmed this with a direct comparison of HP and LP EGR over a mini-map from 1500 to 3000 rpm and loads

ranging from 2 to 16 bar BMEP.

2.1.7 Studies focussing on post-catalyst EGR

Although most publications concerning EGR treat it as an inert substance, some of the components within EGR are chemically active and can influence combustion chemistry. For this reason the location for sourcing the EGR gases – whether pre- or post-catalyst – can be significant in how it affects combustion. This presents a further aspect for consideration during selection and analysis of an EGR architecture.

The conversion of NOx, CO and HCs in a catalyst reduces the number of chemically active ingredients in EGR, thereby altering the availability of radicals in the end gas during combustion relative to pre-catalyst EGR.

Several studies investigate the use of a catalysed EGR system in an LP architecture without any mention of the chemical significance of this and without any comparison of performance between the catalysed loops and equivalent uncatalysed loops [13, 55, 62]. Only a few examples can be found in the literature where this kind of comparison has been made.

Roth et al [66] considered the advantages of operating an SI engine with BMEP values reaching 17 bar with both LP and HP EGR configurations available to cover the full operating range. Within this study the authors experimentally compared the effect of post catalyst versus pre catalyst EGR for the LP loop. They concluded that pre-catalyst EGR was preferable to catalysed EGR because:

- The average BSFC was improved by 1.5-3.5%, with a higher power production observed for all points despite having up to 5°CA less favourable combustion phasing due to knock.
- The combustion rate was faster.
- HC emissions were lower by 30-40%.

- PMEP was reduced by 5-15% at higher speeds and loads.
- The pressure differential available to drive the EGR was larger due to the pressure loss over the catalyst, allowing a reduced EGR valve size and larger delivery range.

Roth et al [66] do mention that a significant amount of internal EGR, which is of course uncatalysed, was present at some of their test points and therefore could have affected the data produced. At a reference 10% external EGR rate they record an internal EGR fraction from 8% up to 48%, dependent on speed, load, and valve timing. Evidence discussed later in this chapter on effects of NO suggest that this level of RGF could significantly impact the comparison here.

It must also be noted that, during their investigation, Roth et al [66] measured the external EGR rate by calculating the ratio of CO_2 measured in the intake to that in the exhaust manifold (Equation 2.3). This inherently carries an error when calculating the EGR rates with catalysed exhaust gases, since the CO_2 content increases after the exhaust manifold when the gases pass through the catalyst[5]. This error could mean that, for a given EGR rate, the total quantity of exhaust gases being recirculated could vary between pre and post-catalyst operation, which could impact the results being presented.

$$\text{EGR rate} = \frac{\text{Intake } CO_2 - \text{Background } CO_2}{\text{Engine out } CO_2 - \text{Background } CO_2} \tag{2.3}$$

Hoffmeyer et al [3] studied the effects of catalysed EGR with an HP EGR loop on a 2L 4 cylinder turbocharged SI engine and a catalyst within the EGR loop. They used a similar process to measure the EGR rate as Roth et al [66], but calculated that the catalytic process only introduced an error of less than 2% in their study. This is surprising, considering that one of their test points was not operated with a constant lambda, and air-fuel ratio is known to have a large impact on exhaust CO content [13] which would then affect the CO_2 increase post-catalyst.

[5]The level of increase of CO_2 content is dependent on the CO emissions.

In contrast to Roth et al's study [66], Hoffmeyer et al [3] found an improvement in fuel consumption of up to 2% with the catalysed EGR compared to that of the non-catalysed loop, which they attribute to earlier combustion phasing (1.5 - 3°CA) as a result of the increased knock tolerance of the engine. They cite the increased heat capacity of the inlet charge due to the increased CO_2, and the reduction of NO and HCs after catalysis as the primary reasons for the increased knock limit. The disparity between the findings of these two studies highlights the difficulty in achieving a fair comparison between the two EGR compositions. Inlet temperature and pressure cannot be controlled accurately whilst using a turbocharger and can have a significant impact on knocking behaviour. Additionally, engine operating conditions can impact the minor species concentrations in the exhaust, which in turn affects the impact of catalysis. Details of these factor are not shared in either study, but they are possible causes for the disagreement between the two research groups.

In addition to their experimental work Hoffmeyer et al analysed the chemical interactions using a reduced PRF mechanism (from [67] – 233 species, 2019 reactions) blended with an early version of the GRI-Mech NO sub-model [68] in a homogeneous reactor model. They conducted a sensitivity study with this model to evaluate the contribution of each EGR component on ignition delay time. Their results are shown in Figure 2-2, where it can be seen that after catalysis the increase in ignition delay stems primarily from the reduction of NO and C_2H_2.

More recently, research has been conducted at the University of Bath by Lewis et al [69] on an SI engine with BMEP levels reaching 26.5 bar and a catalyst installed in the EGR loop. Concerns over errors introduced by measuring the EGR rate via the CO_2 ratio between the inlet and exhaust manifolds prompted them to use the mass air flow into the engine as a measure instead. This means that their investigation is carried out with a constant total air flow into the engine (air + EGR) rather than a constant load on the engine and, as such, the load and fuelling decreases with higher EGR rates due to the reduction in oxygen in the charge and the ECU being set to

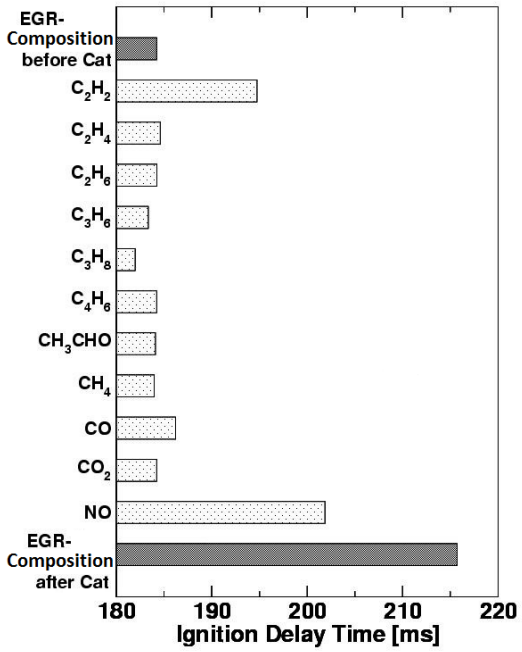

Figure 2-2: Results of a sensitivity study by Hoffmeyer et al comparing the predicted ignition delay time contribution for each of the minor species present in EGR (operating at 17.5 bar IMEP and 2500rpm). Reproduced from [3].

maintain stoichiometry.

Lewis et al [69] found an increase in the knock limit of up to 6°CA with catalysed EGR for equivalent EGR mass flows, but at equivalent BMEP values the BSFC was found to increase by up to 10%. This is attributed to the lower calorific value of the charge for catalysed EGR due mainly to the oxidation of HCs and CO in the catalyst. One point that was highlighted was that the engine-out CO and HC emissions were considerably higher than would be expected for stoichiometric in-cylinder operation. They concluded that this was due to the blow-through of fresh air due to valve timing overlaps, causing the engine to be running rich in-cylinder despite the exhaust lambda sensors showing it to be running at stoichiometry. Another effect of rich in-cylinder conditions is that NOx emissions are relatively low, so the catalysis of the exhaust gases in this study would have offered little benefit from the reduction in EGR NOx content.

Whilst most studies utilising post-catalyst EGR focus on low pressure architectures,

the possibility of utilising a catalytic gasoline particulate filter in a high pressure EGR loop was investigated by Fischer et al [70]. This concept was devised to reduce fouling of the EGR cooler (very much similar to a concept devised by Lu et al [71] for diesel engines) and was found to provide efficiency improvements of up to 8%, which were further improved by cooling of the EGR gases down to 50°C. In addition the particulate emissions were greatly reduced – in the order of 75% – compared to operation of the engine without EGR.

2.1.8 Reformed EGR

A study by Topinka et al [72] focused on the effect of H_2 and CO on combustion, both in isolation and combined. They found a potential for increased knock limits with both components, attributing this to higher octane ratings of each of these substances – estimating CO to have an octane number around 106, and H_2 an octane number of 130 [73].

This phenomenon has led to some researchers seeking to exploit the benefits of hydrogen on combustion by hydrogen reformation. One such method, demonstrated by Fennell et al [74], uses reformed EGR gases to improve combustion stability at high EGR rates. A common issue with reformation, which is also mentioned in this study, is the energy loss associated with the reformation process, which offsets the benefit to combustion in the engine.

This problem has been circumvented to some degree with the dedicated EGR concept devised at the Southwest Research Institute [75, 76] which separates the exhaust ports of one cylinder to divert the entirety of the exhaust gases from this cylinder back to the inlet. This allows very rich conditions to be run in this cylinder, increasing CO and H_2 production to effectively produce reformed EGR. In a comparison between this concept and a LP EGR system, the D-EGR concept was found to improve EGR tolerance at part load and also improved knock limits at high load [77].

A development to the D-EGR concept by Chang et al [78] introduced a catalytic reformer

in the EGR leg and separated the intake for the dedicated EGR cylinder from that of the other cylinders.

Both concepts claim to have improved BSFC by a significant amount (8% [78] and 10% [76]) at part load with significantly increased EGR tolerance.

2.1.9 Comparison of benefits found with EGR

Table 2.1 gives a summary of the literature on experimental results of EGR effects on engine performance and efficiency benefits. As can be seen, the ability of EGR to improve knock limits and reduce harmful emissions is undisputed but its effectiveness, when combined with alternative technologies, is not always so clear cut. The benefits associated with EGR operation give varying impacts depending on EGR architecture and calibration/configuration with other technologies and fuels. This means that the impact of EGR is system-specific and as such cannot be treated as a plug-in solution, but must be considered with the system as a whole. The offset of cost when considering EGR systems is also a significant factor which OEMs must consider when deciding which technology to adopt for production. As such, reliable simulation methods to assess EGR performance within an entire powertrain system are invaluable in order to guide the decision-making process for future powertrain design.

Table 2.1: Summary of experimental work in the literature concerning EGR efficiency benefits (denotes pre-catalyst EGR, denotes post-catalyst EGR, denotes reformed EGR)

Author	**Speed**	**Load**	**EGR Architecture**	**Combustion System**	**BSFC Improvement**
	rpm	bar			
Alger et al [13]	1500	3 & 8	HP hot up to 20%	1.6l I4 GDI with split injection for low load	
	2000	2 & 5			3%
Potteau et al [55]	5500	12.9	HP hot up to 11.5%	2l I4 GDI	6.6%
Chao et al [65]	1500-3000	2-16	HP cooled up to 20%	1.3l I4 GDI	7%
Kumano et al [79]	4000	high load	HP cooled up to 5%	2.3l I4 GDI	2%
			LP cooled up tp 6%		1.2%
Zhang et al [80]	1500	2.2	LP cooled up to 30%	1.8l I4 GDI with high tumble modification for EGR experiments	18%
	1500	3.5			17%
	2000	2.2			19%
	2000	3.5			13%
Cairns et al [42]	5000-6000	10-18	HP-LP cooled up to 13%	2l I4 GDI	10%

Continued on next page

Continued from previous page

Author	Speed	Load	EGR Architecture	Combustion System	BSFC Improvement
	rpm	bar			
Cairns et al [42]	1600-5000	14-22	LP cooled up to 8%		16%
Liu et al [81]	1000-3000	100Nm - 250Nm	LP cooled to 25%	2l GDI, cam phasing optimised for EGR	4.9%
	1000-3000			Same with higher CR	7.3%
Hoepke et al [63]	1500	14	LP cooled up to 12%	2l I4 GDI	-0.5%
	2000	14			2.8%
	2500	14			3.2%
Grandin et al [24]	5000	16.5	HP cooled vs uncooled up to 13.8%	2.3l I4 gasoline	7.3%
Ivanic et al [82]	1500	3.5	NA - H2 enhancement also tested	1 cylinder running on indolene	6%
Park et al [83]	Idle to 4500	low/transient	HP cooled	2.4l I4 GDI	3.6%
Francqueville et al [84]	2000	19	Rig, cooled EGR up to 30%, compares CO2/N2 dilution as well	350cc single cylinder GDI	19 g/kWh
Kaiser et al [61]	1000-5000	1-32	LP cooled	3.2l V6 GDI with E0 fuel	4.2%

Continued on next page

Continued from previous page

Author	**Speed**	**Load**	**EGR Architecture**	**Combustion System**	**BSFC Improvement**
	rpm	bar			
Kaiser et al [61]	1000-5000	1-32	LP cooled	3.2l V6 GDI with E85 fuel	3%
Turner et al [56]	5000	17.5	LP cooled to 8%	1.5l I3 GDI	2.2%
			HP-LP cooled to 8%		5.1%
			HP cooled to 6%		5.9%
Siokos et al [85]	1800	3	LP cooled	2l I4 GDI	1.5%
	1500	4			2.4%
	2500	5			2.1%
Liu et al [86]	2000	2	HP cooled	1.3l I4 GDI	3.4%
		4			4.6%
		6			3.5%
		8			3%
		10			5.3%
Yin et al [87]	2000	2	LP cooled up to 16%	1.5l I4 PFI	3%
		4			4%

Continued on next page

Continued from previous page

Author	Speed	Load	EGR Architecture	Combustion System	BSFC Improvement
	rpm	bar			
Yin et al [87]		6			3%
		8			4%
		10			6%
		12			7%
		14			11%
		16			11%
		18			4%
		20			18%
Su et al [88]	1000	7.9	LP cooled	2l GDI, with increased compression ratio for EGR points	2.4%
	2000	9.4			2.1%
		9.4			2.8%
		12.6			2.8%
		15.7			3.5%

Continued on next page

Continued from previous page

Author	Speed	Load	EGR Architecture	Combustion System	BSFC Improvement
	rpm	bar			
Su et al [88]	3000	9.4			2.2%
		12.6			2.3%
		15.7			2.2%
Lewis et al [69]	1500	26	Rig, cooled	2l I4 GDI	16%
		24			5%
		22			11%
Alger et al [89]	1500	12	LP cooled up to 25%	1.6l I4 GDI	8.9%
Song et al [90]	2000	5	LP cooled up to 25%	1.5l I4 PFI	4.7%
	3000	10			10.1%
Duchaussoy et al [91]	5000	16	HP cooled to 17.5%	2l I4 GDI	3%
Fontana et al [60]	1500	WOT	HP cooled	1.2l I4 gasoline	2.3%
	2000				5.3%
	2200				5.7%
	2500				6.5%

Continued on next page

Continued from previous page

Author	Speed	Load	EGR Architecture	Combustion System	BSFC Improvement
	rpm	bar			
Galloni et al [92]	4000	WOT (1.5 bar MAP)	HP cooled up to 8%	1.4l I4 PFI	7.6%
	5000	1.57 bar MAP		7.1	7.1%
Hoffmeyer et al [3]	2500	17.5	HP cooled up to 13%	2l GDI	1%
	3000	19			
Tornatore et al [31]	3000	16	LP cooled up to 10.8% at high load and 19.5% at low load	2 cylinder 0.9L PFI	2.8%
	3000	5-7			3.2%
Potteau et al [55]	1500	11.3	LP cooled 8% ans 12.2%	2l I4 GDI	7.4%
	5500	12.9			13.6%
Alger et al [13]	2000	14	LP cooled up to 19%	1.6l I4 GDI	7.5%
	2000	18			7%
	3000	18	LP cooled up to 19%	1.6l I4 GDI	4%
	4000	18			19%
	4500	17			16%

Continued on next page

Continued from previous page

Author	Speed	Load	EGR Architecture	Combustion System	BSFC Improvement
	rpm	bar			
Alger et al [13]	5500	15			24%
Chao et al [65]	2000-3000	2-16	LP cooled up to 20%	1.3l I4 GDI	8%
Song et al [90]	2000	5	LP cooled up to 20%	1.5l I4 gasoline	4.3%
	3000	10			9.6%
Takaki et al [93]	1200-3200	7-15	LP cooled up to 20%	1.6l I4 gasoline	5%
Fischer et al [70]	2000-4750	4-20	HP cooled up to 22%	1.4l GDI	12%
Lu et al [2]	1250-4000	1-17	LP cooled up to 20%	1.3l I4 PFI with increased CR for EGR tests	12%
Lewis et al [69]	1500	26	Rig up to 15%	2l I4 GDI	12.9%
	1500	24			5%
	1500	22			7.6%
Hoffmeyer et al [3]	2500	17.5	HP cooled	2l GDI	2.5%
	3000	19			
Bourhis et al [62]	3000	6	LP cooled up to 10%	2l I4 GDI also incorporating VVT tests to analyse IGR effects	4 g/kWh

Continued on next page

Continued from previous page

Author	**Speed**	**Load**	**EGR Architecture**	**Combustion System**	**BSFC Improvement**
	rpm	bar			
Bourhis et al [62]	3000	10			1 g/kWh
Chadwell et al [76]	1000-5000	2-17	D-EGR concept	2l I4 GDI	13%
Alger et al [75]	2000	2/4	D-EGR concept -25%	1.6l I4 GDI	10%

2.2 The chemistry of exhaust gas recirculation

To fully understand the chemical interactions of EGR, the hydrocarbon oxidation mechanisms present in gasoline combustion must first be considered. This section will summarise the mechanism by which hydrocarbons are oxidised before explaining how this process is impacted by EGR constituents. The most volatile species in EGR is NO, and the mechanisms by which it displays this volatility are discussed.

2.2.1 A brief summary of hydrocarbon oxidation characteristics and mechanisms of knock

Hydrocarbon oxidation is by nature a highly complex subject. In essence, the combustion process is a chain reaction, where the principle reactants do not react directly but dissociate to form radicals which then initiate a chain of steps. The formation of these radicals is therefore an important aspect of combustion, and can dictate the combustion rates as well as the likelihood of autoignition occurrences. The radical pool can be composed of a number of different radicals which can be formed by competing reaction paths – the activity of each path depends on the pressure and temperature as well as the available compounds. Detailed kinetic models of these mechanisms can run into thousands of species, with tens of thousands of reactions.

The temperature regimes

Typically the reaction paths are divided into three temperature regimes: low, intermediate, and high. The low temperature regime typically occurs at less than 800K, and the high temperature regime above 1100K, with the intermediate regime sitting between the two. For some fuels, the intermediate regime exhibits a negative temperature coefficient (NTC) behaviour, where further increases in temperature result in an increased ignition delay (as demonstrated in Figure 2-3). Typically paraffinic fuels (such as iso-octane and n-heptane) exhibit strong NTC behaviour, whilst aromatics and oxygenates (such as toluene and ethanol) can show little or no NTC behaviour [4].

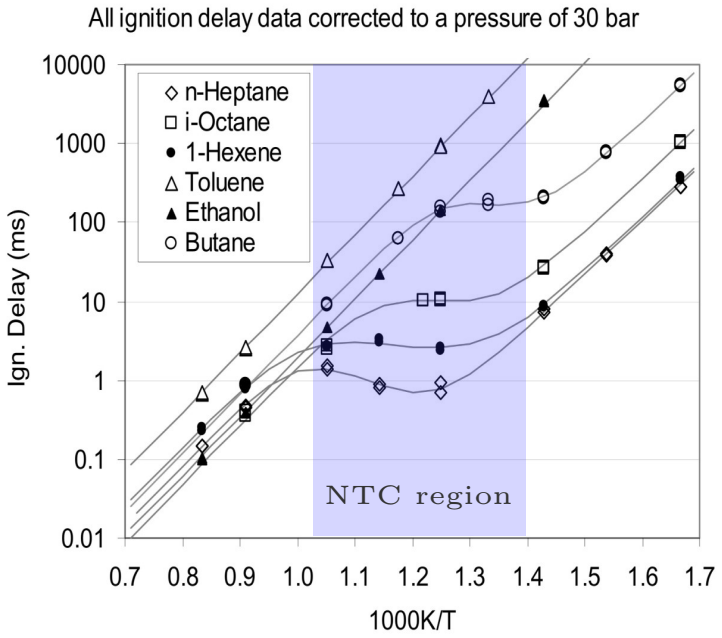

Figure 2-3: A demonstration of the NTC behaviour of different fuels reproduced from [4] . Note the pronounced NTC behaviour exhibited by the paraffinic fuels contrasting with the absence of NTC behaviour for the toluene and ethanol.

Semenov [94] proposed the existence of unstable intermediate species that undergo different reactions depending on temperature. The reduction in reactivity in the NTC region can be explained by the competition between these reactions acting on the intermediate species:

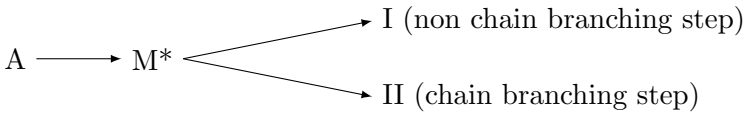

where M* is the unstable intermediate formed from fuel A, and route I requires a higher activation energy than route II.

Below the activation energy required for route I, the chain branching step (route II) is favoured and increases the radical pool[6]. Reaction path I is triggered as the temperature moves into the intermediate regime and the degenerate chain branching step

[6]The 'chain branching" step refers to a reaction by which two radicals are produced for each one consumed, thereby increasing the availability of reactive radicals. For example:

$$\dot{O} + H_2 \rightarrow \dot{O}H + \dot{H}. \tag{2.4}$$

becomes more dominant – resulting in a relatively slow increase in radical production and consequently a reduction in reaction rates. The intermediate temperature regime is dominated by HO_2 chemistry with branching occurring from the dissociation of H_2O_2, formed by H-abstraction by HO_2 [95].

Further increases in temperature into the high temperature regime move the reaction rate dependence away from peroxy radicals, and decomposition of the carbon chain tends to occur through breakage of the weakest bonds, for example: $C_4 \rightarrow 2C_2$ [96]. This results in a much faster chain shortening process than the progressive scission reactions in the low temperature regime of the form: $C_4 \rightarrow C_3 \rightarrow C_2 \rightarrow C_1$.

The boundaries between temperature regimes are dependent on pressure and are not rigid – progression from one temperature to the other does not imply that reactions from the first stage cease to occur [96].

The dependence on a radical pool to propagate the chain reaction, especially in the low temperature regime, explains the induction intervals that are observed in the ignition of fuels, since the formation of the radical pool effectively incurs a delay period. This formation process can also exhibit what is known as the "cool flame" phenomenon, where the initial stage of ignition only releases a small amount of heat in the formation of stable radical species. This 'two stage' ignition has not been observed at high temperatures [96].

Knocking combustion

End gas autoignition is reported to occur most commonly in the low and intermediate temperature regimes [97, 98] – the initiation for which is described by the first step of Semenov's general mechanism for low temperature hydrocarbon oxidation mechanism [94]:

$$RH + O_2 \rightarrow \dot{R} + HO_2 \tag{2.5}$$

which produces R, an organic radical[7], by abstracting a hydrogen atom from a fuel hydrocarbon (RH).

Once a radical pool exists this process is sped up by the attack of radicals upon the fuel molecules:

$$RH + \dot{X} \rightarrow \dot{R} + XH \tag{2.6}$$

where X represents any radical.

The production of the radical pool is very dependent on the temperature regime and available reactants. Of the most reactive radicals, the general effectiveness of each is in the order: OH > O > H > CH_3, of which the first three all react very quickly.

The production of these radicals in the end gas will not be spatially homogeneous, since mixture inhomogeneities will result in hot spots.

2.2.2 Impact of NO

NO is a highly reactive substance and as such can have a significant impact on the combustion process. A large number of investigations have been performed to assess the volatility of NO addition to C_1-C_2 hydrocarbons [99–103], and to C_3-C_5 hydrocarbons [99, 104–106], but fewer studies have focused on the NO sensitisation effect on the larger hydrocarbon compounds that are used to make up gasoline surrogates. A summary of some of the data from these investigations has been compiled in Table 2.2. These results demonstrate how sensitive the combustion process is to initial NO concentration, the fuel being burned, and the initial temperature and pressure.

In general terms, NO has been observed to promote autoignition with increasing effect up to a certain threshold, beyond which it will retard the ignition. This promoting effect is observed for all fuels with the one exception in Table 2.2 being iso-octane in Burluka et al's investigation [107], where the NO showed an inhibitory effect on autoignition.

[7]The dot denotes an active radical.

Both Prabhu et al and Risberg et al's studies [108, 109] confirm that the initial temperature of the charge has a large impact on the autoignition promoting effect of NO on both SI and HCCI engines, with a higher initial temperature extending this effect to higher concentrations for all fuels. Risberg et al [109] go further in confirming that the initial temperature has a larger effect on the combustion chemistry than the initial pressure. When comparing the data from this study with that from Burluka et al on a ported SI engine [107], the trends in results seem largely similar for each different fuel, with toluene reference fuels (TRFs) displaying characteristics that are more similar to gasolines than those of PRFs.

The negligible effect of NO on PRF fuels found by Burluka et al [107] are not reflected in Risberg et al's study on an HCCI engine [109], where some autoignition promoting effect is observed. Risberg found the PRF to be sensitive to trace amounts of NO, but the promoting effect soon disappeared once the concentration was increased. This effect may be explained by the promoting effect NO has at low/intermediate temperatures on high-octane fuel components such as iso octane and toluene, as well as its inhibiting effect on low octane components such as n-heptane [110].

Table 2.2: Summary of data taken from the literature concerning the effect of NO on the oxidation of gasoline surrogate fuels and components

Author	**Experiment**	**Variables**	**MAT**	**Fuel**	**Speed**	**NO conc**	**Results**
			°C		rpm	ppm	
Burluka et al [107]	Experimental and simulation ported single cylinder SI engine with simulated EGR (CO_2, N_2, NO, & H_2O) Skip-fire ratio of 7	Fuel, NO concentration	70	3 PRFs TRF 2 gasolines iso-octane	1500 (WOT)	0-400	Iso-octane: increasing NO concentration from 0-400ppm resulted in a delay in knock onset time of up to 4°CA, so KLSA was advanced PRF: NO concentration had very little effect on knock (authors propose that repressive effect on iso-octane may have been offset by an autoignition promoting effect on the n-heptane in the mixture) ULG&TRF: knock onset advanced by up to 2°CA by introducing trace amounts (100-200ppm), further increase in NO concentration did not advance knock further.
Stenlaas et al [111]	Simulation	Lambda, NO concentration	137-159	PRF	?	0-1408	Simulation model finds maximum influence of NO on autoignition timing at 500ppm, but states that data must be taken qualitatively rather than quantitatively.
Kawabata et al [112]	Experimental Single cylinder gas engine	NO concentration	57	Natural gas	1000	0-400	NOx concentration increase advanced autoignition timing and increased knock intensity with almost linear relationship, by up to 7°CA and 170 kPa at 400 ppm.
Stenlaas et al [113]	Experimental 4 cylinder 2.3L SI engine	Lambda, NO concentration	?	Gasoline	1000-4000	100-1600	No effect on exhaust temp found with addition of NO Increased concentrations of NO resulted in increased knock intensity and advanced the angle of knock onset by up to 6°CA Lambda variations did not alter the effect of NO, but rich mixtures were more prone to knocking.
Prabhu et al [108]	Experimental Single cylinder 4 stroke SI engine compression ratios 5.2 and 8.2	Inlet charge temperature, NO concentration	60 74 127 172	PRF	900	0-400	Low Manifold Air Temperature (MAT): NO promoted autoignition up to 100ppm then retarded from then on, High MAT: promoting effect of NO extended up to 400ppm No pressure/combustion data from the lower compression ratio.

Continued on next page

Continued from previous page

Author	Experiment	Variables	MAT	Fuel	Speed	NO conc	Results
			°C		rpm	ppm	
Risberg et al [109]	Experimental Single cylinder HCCI engine	Fuel, MAT/MAP combination, NO concentration	40 100	PRF TRF Gasoline	900&1200	0-476	High MAP (2 bar, 40°C): PRF – NO advanced combustion by around 2°CA at 15-48ppm NO, at higher concentrations the promoting effect reduced and 448ppm retarded combustion TRF – all concs advanced combustion, up to 9°CA for 476ppm ULG – all concs advanced combustion up to 4°CA at 229ppm High MAT (1 bar, 100°C): PRF – all concs advanced combustion up to 8°CA at 240ppm TRF – all concs advanced combustion up to 12 °CA at 207ppm ULG – all concs advanced combustion up to 12°CA at 307ppm HCCI combustion reported to be more sensitive than SI combustion to NO addition.
Dubreuil et al [114]	Experimental 4 cylinder HCCI engine, one cylinder active	Fuel, simulated EGR addition, CO, CH_4, NO addition	53-118	n-heptane 75% n-heptane/ 25%iso-octane 80%n-heptane/ 20% toluene	1500	0-500	No effect of intake CO and CH_4 addition was found. NO had a maximum promoting effect on autoignition timings at 100ppm of 1.5°CA, beyond which the effect reduced with increased concentrations.
Roberts et al [115]	Experimental Single cylinder ported SI engine with skip-fire ratio of 9	Fuel type, simulated EGR addition, NO concentration	70-110	iso-octane PRF TRF ULG	1500	0-774	Iso-octane: knock onset was advanced by up to 1.9°CA at 387ppm of NO (7.5% sEGR) 95PRF: knock onset was advanced by up to 1.1°CA at 387ppm of NO (7.5% sEGR) 90PRF: knock onset time was not affected by 258ppm NO (5% sEGR), and was delayed at concentrations higher than this up to 0.8°CA at 774ppm NO (15% sEGR) 90TRF: knock onset was advanced by up to 3.2°CA at 762ppm NO (15% sEGR) 90ULG: knock onset was advanced by up to 3.9°CA at 768ppm NO (15% sEGR).

Continued on next page

Continued from previous page

Author	Experiment	Variables	MAT	Fuel	Speed	NO conc	Results
			°C		rpm	ppm	
Moréac et al [116]	Experimental, supplemented by simulation Jet stirred reactor at 10 bar with measured species concentrations	Fuel, NO concentration, temp	550-1000K	n-heptane iso-octane methanol toluene	NA	0-500	n-heptane: inhibiting effect of NO at low temperatures, accelerating effect at high temperatures iso-octane: Accelerating effect of NO low at low temperatures but stronger at higher temperatures. Stronger accelerating effect than on n-heptane methanol: Some accelerating effect observed with NO, but much weaker than for the other fuels. Noted that methanol interactions can be highly dependent on equivalence ratio toluene: strongest accelerating effect of NO found in intermediate temperature regime. This appeared to be pressure dependent as at atmospheric pressure the reaction required a much higher temperature to initiate.
Contino et al [117]	Experimental and simulation HCCI single cylinder engine	NO concentration	435K	iso-octane	1000	0-500	NO could significantly advance ignition by up 15 CAD at the highest concentration
Chen et al [5]	Experimental plus comparison with simulation Rapid compression machine	NO concentration, temperature, lambda = 1, pressure = 9 bar	650-1000K	n-heptane	NA	0-400	Promoting effect of NO observed up to 100ppm in low temperature regime, stronger promoting effects observed in the intermediate and high temperature regimes.
Chen et al [118]	Experimental CFR engine	Equivalence ratio = 0.91-1.43, intake temperature, fuel	52-200°C	One PRF, three TRFs, and three ERFs	600	0-800	Temperature: Increasing temperature increased the autoignition promoting effect of NO, and raised the concentration at which the promoting effect switched to an inhibitory effect. Equivalence ratio: leaner mixtures appeared to increase the promoting effect, but there were also interactions between equivalence ratio and residual gases Fuel: Higher contents of toluene and ethanol appeared to correlate with higher promoting effects of NO.

Roberts et al [115] expanded further on the mechanisms behind NO effects on different fuels and with different inlet temperatures. They highlighted the significance of the negative temperature coefficient region (NTC), which is more prominent for some fuels than for others. They found that for fuels exhibiting more pronounced NTC behaviour (for example PRFs) NO will suppress normal autoignition chemistry if the pressure temperature history of the end gas falls within the NTC region for a significant time before autoignition, with the opposite being true for fuels exhibiting little or no NTC behaviour (such as TRFs and ULGs). This could explain the variation in results obtained by various authors in Table 2.2, especially where the HCCI results differ from those obtained with SI ignition.

Surprisingly, lambda values were found not to have a significant impact on the effect of NO on combustion by Risberg et al [109]. Stenlaas et al [113] confirmed this with experimentation on an SI engine, but the lower lambda values did appear to show an advanced knock angle compared to lean operation. Findings by Chen et al [118] contradict this, although they do concede that the tests conducted at leaner equivalence ratios may have had a higher residual gas fraction which could have impacted the results.

An unexpected result from the work by Stenlaas et al [113] is that the inhibitory effect of NO was not observed at high concentrations. The inlet temperature is not divulged so it is hard to assess whether it may be a contributory factor, and the effect of the higher operating speeds in this study may also have had an impact.

As Chen et al mention in their study on NO addition in the octane rating engine [118], the mode by which these studies are conducted can be critical to the results achieved. Studies conducted with skip-fire operation such as [115] ensure extremely low residuals to influence the combustion results, but at the expense of cooler cylinder wall temperatures than would be seen during normal combustion. For this reason Chen et al conducted their study without skip-fire operation, but they do concede that the high ($\approx$10%!!) residuals will have affected results since the in-cylinder NO content will be the sum of both the residuals and that added to the inlet. In terms of real engine operation,

however, this is more representative.

In summary, NO sensitivity of autoignition has been documented for a range of fuels, but this effect is heavily dependent on temperature and fuel composition, with aromatics and ethanol displaying higher sensitivity to it in some studies. This has been attributed either to their higher octane ratings or to their lack of NTC behaviour by different research groups. Trace amounts of NO have been found to reduce the onset of hydrocarbon oxidation for paraffinic fuels by up to around 100-200K [119].

Chen et al [118] also highlight a requirement for new fuel-specific NO mechanisms to enhance the kinetic modelling of engine combustion after finding shortcomings in the existing mechanisms from the literature which they tested.

NO mechanisms

To fully understand the behaviour exhibited by NO addition to combustion, it is necessary to consider the kinetic effects. The following mechanisms describe NO interactions with hydrocarbon oxidation in the low temperature regime.

Faravelli et al describe the main influence of NO as "increasing the chain length and providing a more rapid build-up of the radical pool" [119]. NO combines with peroxy radicals via:

$$RO_2 + NO \rightarrow RO + NO_2 \tag{2.7}$$

where R can be either H or an alkyl group. Faravelli et al state that the conversion of HO_2 to OH is responsible for over 80% of the conversion of NO to NO_2.

In addition to this, NO promotes the conversion of the relatively unreactive HO_2 radicals into OH radicals via:

$$NO + HO_2 \rightarrow NO_2 + OH \tag{2.8}$$

NO is also formed from NO_2 by:

$$NO_2 + H \rightarrow NO + OH \tag{2.9}$$

The net effect of reactions 2.8 and 2.9 is:

$$HO_2 + H \rightarrow 2OH \tag{2.10}$$

which is more active than the recombination reaction:

$$HO_2 + H \rightarrow H_2O_2 \tag{2.11}$$

Equations 2.7 to 2.11 demonstrate the mechanism by which NO can increase the pool of reactive OH radicals – which then increase the reactivity of the end gas and therefore the propensity for autoignition to occur.

The inhibitory effect of NO at high concentrations indicates the presence of competing reaction paths which consume radicals during combustion. The following mechanisms, published by a number of researchers [108,109,113,114,119], describe this process:

The scavenging of OH radicals can occur by:

$$NO + OH + [M] \rightarrow HONO + [M] \tag{2.12}$$

$$HONO + OH \rightarrow NO_2 + H_2O \tag{2.13}$$

These two equations effectively equate to:

$$NO + 2OH \rightarrow NO_2 + H_2O \tag{2.14}$$

In addition, NO_2 can scavenge peroxy radicals (HO_2) to form HONO, which then con-

sumes more OH radicals:

$$NO_2 + HO_2 \rightarrow HONO + O_2 \tag{2.15}$$

The inhibiting effect is the result of both the competition between reactions 2.15 and 2.8 and the chain termination effect of reaction 2.13.

As the temperature rises further (>1000K), the importance of peroxy radicals diminishes, as alternative production paths for OH radicals become more active. This reduces the enhancing effect of NO [119] – meaning its impact on the OH radical pool is limited to the low temperature regime. This could be why NO is predominantly significant in the earlier stages of combustion where autoignition is a prominent issue, but has not been observed to have a significant effect on combustion duration or exhaust temperature [113].

2.2.3 Implications for post-catalyst EGR

The evidence for the fuel consumption benefits of catalysed EGR over uncatalysed EGR is not conclusive. There is compelling evidence, however, through the consideration of the species present, that post-catalyst EGR can improve the knock limit at high load. Whether this increased knock limit is offset by other losses within the system is as yet unclear and would most likely be dependent on individual architecture and operating regimes.

At low loads the pressure loss across the catalyst may offset some of the additional de-throttling that post-catalyst EGR can offer. Slower combustion rates with post-catalyst EGR, resulting from the decrease in CO content and increase in CO_2, may also have implications for low load points, where combustion stability may be affected by lower flame speeds at higher EGR rates [60].

The conversion in the catalyst of any components in the recirculated exhaust gases that may have resulted from incomplete combustion by equations 2.16, 2.17, and 2.18 can reduce the calorific value of the in-cylinder mixture. This reduces the available

energy for combustion (albeit by a small amount) so could potentially offset some of the advantage of the more favourable combustion phasing afforded by the use of post-catalyst EGR.

$$2NO_x \rightarrow N_2 + xO_2 \tag{2.16}$$

$$2CO + O_2 \rightarrow 2CO_2 \tag{2.17}$$

$$C_xH_{2x+2} + \left(\frac{3x+1}{2}\right) O_2 \rightarrow xCO_2 + (x+1)H_2O \tag{2.18}$$

Previous studies have highlighted that the most significant change brought about by catalysing the EGR gases is most likely to be the NOx conversion. Although this does not offer much in the way of calorific value, there is evidence that it can play quite a significant role in promoting autoignition within the end gases.

2.3 Analysing EGR effects on combustion by simulation methods

As engine optimisation has become ever more critical in satisfying legislation on emissions control the demand for improved simulation methods has grown in an effort to enable more cost and time-effective optimisation of combustion systems.

There are a number of methods which have been employed to model the effects of EGR in SI engines, but most of them take an empirical form and therefore are not reliable for conditions which have not previously been visited experimentally.

This section will discuss the various methods employed to model EGR effects in relation to knock limits after first outlining the different modelling methods described in the literature.

An outline of the factors around kinetic mechanisms and fuel considerations relevant to the modelling work in this thesis follows.

2.3.1 Types of combustion model

Verhelst et al [120] separate combustion modelling methods into three main categories:

- zero dimensional – also known as single zone models, they employ a Wiebe function to describe the burn rate, these models require extensive empirical calibration before they can be validated, but also offer the most computationally efficient method of combustion modelling. Zero-dimensional combustion models are widely used in 1-D simulation tools in order to model engine architecture. Their low computational cost allows for high speeds of simulation which can allow time-efficient comparisons of different architectures.
- multi-zone – these models divide the cylinder into burned and unburned zones[8] and employ chemical kinetic mechanisms to model reaction rates.

[8]The entrained zone is also included for three zone models.

- multi-dimensional – these models are the most computationally expensive and use computational fluid dynamics (CFD) to model turbulence and distributions within the cylinder. This makes them very powerful in being able to model complex in-cylinder effects such as turbulence effects of port or piston designs, and spray characteristics of fuel injectors, but at the expense of computing time.

Zero dimensional models

Zero dimensional combustion models are very common in 1-D engine simulations and provide a very time-efficient method to model combustion. The Wiebe functions are defined by parameters that are derived empirically from experimental data describing combustion phasing and duration. They are an effective way to model complete power-train systems but are limited to conditions at which experimentation has been performed, and their accuracy relies upon that of the experimental data.

Modelling of EGR effects with these models relies upon calibration of the Wiebe function parameters to incorporate EGR rate correlations and is most commonly achieved by fitting parameters to previously measured experimental data.

Since this thesis is concerned with the chemical impact of EGR components, these models are not considered further.

Multi-zone models

Multi-zone combustion modelling can take the form of predictive modelling – i.e. calculating flame propagation and heat release from initial conditions, or it can be retrospectively applied to experimental data to provide a model of the chemical interactions during the combustion process. The latter applies a mass fraction burned (MFB) profile that has been derived from experimental data to provide the boundary conditions for the chemical model at each time step. In essence this is the application of a kinetic model to a zero dimensional combustion model, although the burn rate is directly derived from experimental data.

Predictive multi-zone models can consist of a large number of sub-models to describe the various processes that affect combustion rates, such as heat transfer and turbulence. These sub-models often approximate the complex geometries of the cylinder and flame front into 1-dimensional representations, hence earning the name "quasi-dimensional" models. This allows time-efficient calculation of the 3-dimensional processes albeit without the same level of fidelity achieved by CFD models.

Tornatore et al [121] employed a two zone model with an "in-house developed" fractal combustion model to successfully model EGR response in a twin-cylinder PFI engine. Their model involved a certain amount of empirical fitting, which included an empirical correlation to estimate the flame kernel duration, and a look-up table for the laminar flame area. Their model achieved an advance in the predictive capabilities of multi-zone models incorporating external EGR, but still relies heavily on empirically derived correlations.

PDF models are an emerging form of quasi-dimensional modelling which use stochastic parameters to account for processes which we cannot measure or predict with confidence such as turbulence and mixture inhomogeneities. The mixture within the cylinder is represented by a number of stochastic particles, each with a mass, volume and temperature but no spatial determination within the cylinder.

The initial particle ensemble is represented by a probability density function, this evolves according to a transport equation which is solved numerically using a Monte Carlo method with time-splitting techniques. The various terms of the transport equation relate to the different processes within the cylinder, such as turbulent mixing, injection, piston movement, heat transfer and chemistry.

Multi-dimensional models

Multi-dimensional models, using computational fluid dynamics (CFD), boast the capability to model the fundamental in-cylinder processes relevant to intake air flow, fuel spray and vaporisation, mixture preparation spark ignition, flame growth, turbulent

flame propagation, and exhaust flow. In simulating combustion one of the most prominent aspects is turbulence modelling [122]. In this field there are three distinct approaches to solving the chemically reacting turbulent flow fields:

- Reynolds-averaged Navier-Stokes (RANS) equations
- Large eddy simulation (LES)
- Direct numerical simulation (DNS)

RANS based methods are the most popular in the literature, and are expected to continue to to be due to their effectiveness and simplicity [123].

More recently LES based models have gained in popularity due to their greater capacity to account for cycle-to-cycle variability [124–126]. DNS methods are deemed impractical for complex engine modelling due to their enormous computational cost when chemical kinetics are coupled with them [122].

Multi-dimensional models provide the most detailed physical representation of a combustion system, CFD methods can model the 3-D interactions associated with the valve flows, in-cylinder turbulence, and fuel spray characteristics. This detail comes at the expense of computing time, with the fine meshes required for accurate CFD representation multiplying the number of calculations for a model quite significantly – for this reason the use of full chemical mechanisms in CFD modelling is impractical. Generalised lumped models are often used to represent the kinetic mechanisms, where specific species are not identified but are represented by a generalised equation. The "Shell" model from Halstead et al [127] has long been the most popular of these [128].

2.3.2 Evaluating knocking combustion by simulation

Modelling methods can use either numerical or kinetic techniques to predict the occurrence of autoignition.

Numerical methods rely on empirical models and are generally based on the concept of

ignition delay coefficients (IDCs) pioneered by Livengood and Wu in 1955 [129] which uses a single step Arrhenius function to predict the overall ignition delay time. These correlations must be empirically calibrated in order to accurately represent experimental systems and are commonly, but not exclusively, used with zero dimensional combustion models.

This method uses Equation 2.19 to predict the ignition delay time, τ, with A, n and b being empirical constants which can be calibrated to represent the octane rating of the fuel, equivalence ratio, and the combustion system characteristics.

$$\tau = A.P^{-n}.e^{b/T} \tag{2.19}$$

The angle of autoignition onset can then be calculated by solving equation 2.20, where t_0 is the time at the start of compression, and t_c is the time of autoignition onset.

$$\int_{t=t_0}^{t=t_c} \frac{dt}{\tau(t)} = 1 \tag{2.20}$$

Developments of this method to incorporate EGR effects have been presented by Hoepke et al [63] (Equation 2.21) which Chen et al [130] then tested before adding a term for λ to account for non-stoichiometric mixtures (Equation 2.22).

$$\tau = A\left(\frac{P}{T}\right)^{-a}(1 - x_{EGR})^{-b}e^{\left(\frac{E}{T}\right)} \tag{2.21}$$

$$\tau = C_1\left(\frac{P}{T}\right)^{-C_2}(1 - x_{EGR})^{-C_3}\lambda^{-C_4}e^{\left(\frac{C_5}{T}\right)} \tag{2.22}$$

where a, b and $C_1 - C_5$ are empirical constants and x_{EGR} is the EGR fraction.

Extensions to IDC methods have been developed to try and capture more detail in the combustion process, including a two-stage model developed by Fandakov et al [131] which attempts to emulate the low and high temperature ignition phenomena exhibited by

most fuels. This model accounts more accurately for the NTC behaviour exhibited by the paraffinic components of gasoline fuels by defining different IDCs for the low temperature and high temperature reactions. These IDCs are applied sequentially to emulate the temperature increase resulting from each regime. The coefficients of the model are functions of the pressure, equivalence ratio, EGR rate, and fuel properties.

IDC methods are often employed due to their relative simplicity and ease of use, however their accuracy is very dependent upon the calibration of their parameters to capture results seen experimentally which limits their predictive capability somewhat.

Conversely, kinetic models can provide a prediction of autoignition simply by observation of heat release in the end gas. The accuracy of this depends on both the pressure and temperature history predicted in the end gas, and the mixture composition and accuracy of the kinetic mechanism for those conditions.

Whilst the prediction of autoignition provides valuable information on the expected combustion behaviour, the presence of autoignition does not necessarily indicate the occurrence of knock. This is often accounted for by assuming that no knock can occur after a pre-defined MFB point [132]. Fandakov et al developed a method to define this boundary more accurately by defining a boundary layer at the exposed surfaces in the cylinder [133]. They defined the thickness of the boundary layer by the Reynolds number, thermal diffusivity of the mixture, and the time during which the surface is exposed for. Their method proposed that if the unburned mass fraction in the boundary layer at the predicted time of autoignition was beyond a pre-defined threshold no knock could occur. The threshold itself was calibrated against experimental data at the knocking boundary.

Bradley et al proposed an alternative method to predict whether an autoignition event would trigger knocking combustion [134]. They related the propagation of an autoigniting centre to the resulting knock intensity in CFD models. The relationship depends

upon the speed of the autoigniting flame front and the speed of sound in the form:

$$\xi = \frac{a}{u_a} \tag{2.23}$$

where a is the speed of sound and u_a is the speed of the autoignition flame front, which is given by:

$$u_a = \left(\frac{\delta\tau_i}{\delta r}\right)^{-1} \tag{2.24}$$

where τ_i is the autoignition delay time, and r is the distance from the autoignition centre.

The value of ξ can indicate the mode by which the autoignition centre will propagate, with a value close to 1 meaning that the flame front can couple with the pressure wave generated by heat release. This creates a "developing detonation" which can cause a damaging pressure spike [134].

Netzer et al combine this method to ascertain the mode of autoignition propagation with the dimensionless term:

$$\epsilon = \frac{l}{a\tau_e} \tag{2.25}$$

which describes the the severity of a developing detonation event. Here l is the length of the initial autoignition kernel and τ_e is the excitation time, which is the time from 5% heat release to maximum heat release. Their work incorporated this theory into stochastic models to ascertain the severity of autoignition events. This parameter effectively describes the ratio between the autoignition kernel size and the distance travelled by the pressure waves during the autoignition event – higher values denote larger autoignition kernels and therefore more severe knock.

Bozza et al [135] describe a simpler method of quantifying knock in simulation models by observation of heat release in the end gas (Q_{ub}), as calculated in Equation 2.26 for

the unburned gas zone.

$$Q_{ub} = \int \frac{dQ_{chem}}{dt} dt \tag{2.26}$$

Their method, which they demonstrated in a two-zone model of an turbocharged SI engine, compares the total heat release from the end gas at the end of a cycle to a predefined threshold to determine whether that cycle is knocking. Their experiment uses a value of 40J (≈1% of the total heat released) as the threshold, but they describe it as a "tuning constant" which may require adjustment for different fuels and/or combustion systems. They do stress that their method is applicable for different operating conditions, although the level of calibration of the two-zone model that may be required for a change in operating conditions is not mentioned.

The approximation of the end gas to a homogeneous mixture can introduce error, considering that hotspots and inhomogeneities are often cited as the cause for autoignition. The increased fidelity that is available from CFD models can address this, as shown by a study completed by Zhen et al [136] on a methanol fuelled SI engine. Their model enabled them to locate common locations for autoignition in the cylinder and also identified OH, HCO and CH_2O radicals as common precursors to knocking combustion.

Shu et al [137] demostrated the capability of CFD methods to simulate knock via the pressure oscillations that result from autoignition. In order to minimise computational time of the model they used a reduced PRF kinetic mechanism consisting of only 41 species and 130 reactions and an automated adjustment of the time step to focus on the part of the cycle pertinent to knock. Despite this the running time of a knocking cycle still exceeded 70 hours. This model was further developed to investigate the effects of EGR in conjunction with variable compression ratio and supercharging on knock performance of a downsized engine [138]. Work by Galloni et al also demonstrated the use of CFD methods to predict knock via the pressure oscillations resulting from autoignition [139]. This demonstrates the power of CFD methods, and their versatility in analysing new technologies, but the time penalty associated with this method is still prohibitive to the

inclusion of more detailed chemical mechanisms.

PDF methods to model knock and EGR response

PDF methods were applied to combustion modelling by researchers from Cambridge in the early 2000s, in which detailed chemical kinetic models were combined with PDF methods to improve the accuracy of homogeneous two-zone models. Early iterations saw HCCI simulations performed with partially stirred plug flow reactor (PaSPFR) models which reportedly achieved good agreements with experimental data [140, 141].

This model was evolved to include a stochastic model for convective heat transfer, which was found to account for inhomogeneities more accurately than the deterministic model previously used. This method uses a jump process where a particle is selected according to a uniform distribution, which then transfers energy with the wall according to a fluctuation intensity, $h^{(n)}$, which takes the form:

$$h^{(n)} = (T^{(n)} - T_w)/C_h$$

where $T^{(n)}$ is the temperature of particle (n), T_w is the wall temperature, and C_h is a user defined parameter [142, 143].

Further research on HCCI engines was carried out with the Stochastic Reactor Model (SRM) from CMCL which involved co-simulation with 1-D simulation to supply the initial pressure, mass of residuals and initial temperature to the SRM for modelling of a six cylinder engine [144]. This was subsequently used to evaluate the engines EGR-AFR operating range [145]. This model incorporated a "Curl" mixing model, which replaced the deterministic "interaction by exchange with mean" model previously used (in [140–143]). The Curl model selects random pairs of particles between which mixing occurs, reportedly improving performance for multiple reacting scalars.

Whilst the SRM developed in Cambridge focused primarily on HCCI combustion, a research group at Lund University has used PDF methods to focus more on SI com-

bustion [146–149]. Their work has extended to knock prediction techniques which have been applied in a number of ways in recent publications [149–155].

Netzer et al [153] applied the detontation diagram method of Bradley et al [134] in one of these studies. Comparisons of this method with experimental results showed a good agreement.

The stochastic nature of knock is a significant factor in predictive modelling methods and Linse et al [151] addressed this by applying a distribution to the ignition probability, which they then combined with CFD methods to provide estimates for the number of knocking cycles in a given sample. They evaluated the onset of knock by comparison to a threshold on the high pass filtered heat release rate.

Pasternak et al [150] address the issue of knocking combustion simply by observation of heat release in the end gas. They describe this as an indicator for the propensity to knock, since more advanced autoignition and larger amounts of heat release in the end gas are more likely to result in knocking combustion. Whilst this method does not provide a definitive boundary to define knocking combustion, it does remove the relative subjectivity in defining thresholds to describe whether a cycle is knocking or not.

A large part of the work at Lund University follows on from the results obtained by Stenlaas et al [111] on the sensitisation effects of NO, and apply these results to further work on the effect of residual gas on SI combustion. The kinetic mechanisms used by this research group focus primarily on the n-heptane interactions – varying from reduced mechanisms developed in-house ([67,156]), to Curran et al's detailed mechanism ([157]).

The incorporation of EGR in most these studies extends as far as the inclusion of residual gases in the models. Work by Pasternak et al [154] is an exception to this where EGR rates from 0-25% are included in a model for GDI combustion using a PRF fuel. The response to EGR in this particular case is defined by a database of laminar flame speeds for iso-octane that is pre-loaded into the model.

Lauer et al [158] have used CMCL's SRM Suite to investigate knocking combustion in a DISI (direct injection spark ignition) engine, identifying the onset of knock simply by observation of the heat release spike associated with end gas autoignition. They report accurate representation of a range of operating conditions with the model with EGR rates up to 7% and speeds of 2000 and 4300 rpm, but did have to adjust the ignition timing in the model to achieve representative burn rates.

Simulation of EGR effects in PDF models has been included in work presented by CMCL in the context of its effect on HCCI combustion [145] but this has only extended as far as the fitting of a 2-D map to experimental data to guide the outputs of the model.

2.3.3 Kinetic models

Kinetic mechanisms form the basis for kinetic combustion modelling and as such have received significant attention in the literature.

The structure of hydrocarbon kinetic models are generally hierarchical, where the reaction mechanism for a large fuel molecule tends to be made up of the mechanisms for all of the possible smaller fuel molecules that can be derived from it. This has paved the way for many mechanisms for hydrocarbon fuels being built upon previous mechanisms incorporating smaller fuel molecules. Comprehensive mechanisms are designed to represent all of the elementary steps and intermediate species involved in the combustion process – for hydrocarbon molecules of 7 or more carbon atoms detailed mechanisms may have a few thousand reactions between up to a thousand intermediate species[9] [96]. Theoretical methods are often used to determine the reaction rates in these large mechanisms [128] for which there are now a number of software packages available.

Sarathy et al provide a fairly comprehensive review of recent detailed mechanisms available in the literature [163] which consist of either individual hydrocarbons (such as toluene) or blends of hydrocarbons to model more common surrogate fuels. The size

[9]One such mechanism devised by a research group at KAUST consists of 2315 species and 10079 reactions to model a nine-component fuel [159–162]. Such a large mechanism would require an inordinate amount of computing power and time to run.

of these mechanisms is prohibitive for their use in engine simulations, as described by Lu et al [164]: "there is a need to reduce the size and stiffness of mechanisms that are developed, with minimum loss of chemical fidelity, before they can be adopted for simulations".

Reduction of detailed chemical mechanisms is a time consuming process, so a lot of research has gone into improving the efficiency and accuracy of the process by evaluating various techniques. Naik et al [165] investigate the use of six different techniques that they found in the literature, and go into more depth in the use of directed relational graph (DRG) and directed relational graph with error propagation (DRG-EP) techniques in order to produce skeletal mechanisms for CFD purposes. A combination of the DRG-EP approach in combination with sensitivity analysis has been found to shorten the computing times required for mechanism reduction [166, 167] but, in essence, these methods follow the principle of removing the reactions which have little or no impact on the performance of the mechanism whilst keeping the accuracy within a defined tolerance. Needless to say, the accuracy of a reduced mechanism is limited by that of the detailed mechanism from which it is derived.

Mechanisms can be further reduced by the lumping of their chemical processes to form generalised equations to represent the combustion process. These "lumped" mechanisms are calibrated via correlations with experimental data to give the total heat release of the system – specific intermediate species and reactions are not considered [128]. The most common of these is the "Shell" mechanism, developed by Halstead et al in 1975 [127] and adapted further by Hu and Keck [168], which is commonly used in CFD applications where more complex chemical mechanisms are impractical.

TRF mechanisms with NO sub-models

With the most common gasoline surrogates consisting of either PRFs – iso-octane and n-heptane blends, or TRFs[10] – PRFs combined with toluene to increase the sensitivity

[10]Sometimes referred to as TPRFs.

of the fuel, these fuels have received the most attention in the literature. Increasingly ethanol is also being included in these models – in line with the increasing trend for ethanol inclusion in real gasolines, but the maturity of ethanol's kinetic mechanisms, especially in relation to NO interactions, is still fairly low [128].

A large number of researchers have used TRFs as surrogate fuels to represent gasoline behaviour, and consider it to emulate the behaviour of gasoline sufficiently. The PRF part of these mechanisms is still commonly derived from the detailed mechanisms that Curran et al developed almost 20 years ago [157, 169].

Detailed mechanisms have been considered too time intensive to be considered for this work, so the focus of this section rests more with reduced TRF mechanisms.

A number of reduced TRF mechanisms that are available in the literature are summarised in Table 2.3. There are only a small number of reduced TRF mechanisms which include NO submodels, most of these targeted at predicting the NOx emissions at the end of combustion rather than the sensitisation effect of NO on the fuel molecules. GRI-Mech 3.0[11] [68] is a common source for NO mechanisms which are blended into surrogate fuel mechanisms. It contains interactions with just C_1 and C_2 hydrocarbons, developed for modelling natural gas combustion with NO interactions.

Anderlohr et al's work [170] builds on the GRI-Mech 3.0 mechanism and work by Glaude et al [104] to include interactions of NO with alkanes, benzene and toluene. Most of these are estimated computationally, and some are adapted from other works in the literature. This mechanism has become widely used in the field where NO sensitisation is concerned, and consists of 536 species and 3000 reactions. Chen et al [5] assessed its performance in relation to NO effects on n-heptane autoignition and found that revising some of the rate constants improved the mechanism's accuracy.

Andrae et al [171] also adjusted some of the rate constants from Anderlohr et al's NO mechanism whilst incorporating it into their semi-detailed TRF mechanism.

[11] The GRI-Mech series of mechanisms originate from the Combustion Laboratory at the University of California, Berkeley.

The final mechanism from Table 2.3 that was devised with NO's sensitisation effects in mind was that of Zheng et al [172]. They heavily reduced Anderlohr's mechanism to produce one of the smallest TRF-NO mechanisms in the literature, which showed a good correlation with experimental data on NO influence of ignition delay times in HCCI combustion but overestimated peak pressures. Zheng et al compared their mechanism's performance against that of Andrae et al [171] at the same HCCI conditions proving a similar accuracy for those conditions.

Machrafi et al did add an NO submodel (consisting of 12 species and 21 reactions) for sensitisation of hydrocarbon fuels to their TRF mechanism in one of their publications [173], which originated from Machrafi's PhD thesis[12].

In the context of knock the most relevant chemical mechanisms relate to the development of the end gas mixture and how readily it will ignite. This serves as some reassurance on the applicability of gasoline combustion mechanisms that have been developed with HCCI combustion in mind – which encompasses the vast majority of them. Previous studies on SI combustion [150, 154, 189] have employed these same mechanisms, despite their validations being performed at pressures and temperatures slightly below those which can be exhibited by SI combustion.

[12] An attempt was made to contact this author to enquire about the source of his NO sub model, but was unsuccessful.

Table 2.3: Reduced TRF mechanisms from the literature

Author	Species	Reactions	NO submodel	Validation Method
Machrafi et al [173–175]	49	62	NA[1]	Shock tube, RCM and HCCI
Kim et al [176]	44	59	NA	RCM at 890-1000K and 18 bar
Lee et al [177]	48	67	NA	RCM at 890-1000K and 18 bar
Raj et al [178]	226	2121	NA	Premixed laminar flames
Liu et al [179]	56	168	NA	Shock tube, jet-stirred reactor, flow reactor compared to experimental data and a detailed mechanism from [180]
Andrae et al [181, 182]	137	635	4 species, 24 reactions	Ignition delay times in shock tube, RCM, HCCI engine, and laminar flame speeds[2]
Andrae et al [171]	155	777	21 species, 164 reactions[3]	Ignition delay times and fuel conversion in jet-stirred reactor and HCCI engine
Wang et al [183]	109	543	4 species, 12 reactions[4]	Laminar flame speeds, and ignition delay times in shock tube and HCCI engine
Zheng et al [172]	80	184[5]	23 reactions[6]	Ignition delay times in a shock tube and HCCI engine
Stagni et al [167]	115	856	NO production model	Laminar flame speeds compared to detailed models
An et al [184]	219	1229	NA	Ignition delay times and laminar flame speeds
An et al [185]	85	232	NA	Ignition delay times and laminar flame speeds
Sarathy et al [163]	79	383	15 species, 103 reactions[7]	Ignition delay times and laminar flame speeds plus simulation of a heavy duty diesel engine

[1] Machrafi et al do add an NO submodel in [173] which has 12 species and 21 reactions, reporting it as being "qualitatively acceptable" on observations of ignition delay times in an HCCI engine.

[2] Liu et al [179] include Andrae's mechanism along with some detailed mechanisms in a comparison against experimental data from shock tube experiments for ignition delays and CO and CO_2 concentrations. Andrae's mechanism does not perform as well as the other mechanisms for CO+CO_2 concentrations, but the ignition delay data agrees well.

[3] Adapted from [68, 170, 186]

[4] This NO model was developed for NOx formation in a Diesel engine by [187]

[5] The PRF mechanism was based on that used by [171] and the toluene model came from [174]

[6] Reduced by sensitivity analyses on Anderlohr's NO submodel [170]

[7] The NO model was added from [8], which in turn used the NO model developed by [188] which was targeted at improving NOx emissions predictions

2.3.4 Fuel considerations

Quantifying knock properties of a fuel

The tendency of a gasoline to autoignite is quantified by its octane rating. A standardised process for ascertaining the octane rating of a fuel was developed by the Cooperative Fuel Research (CFR) Committee in 1928 [48] which became known as the "Research Method". Further work in 1932 on correlating the Research Octane Number (RON) of a fuel with real driving conditions resulted in changes to the Research Method, giving rise to the "Motor Method" of octane rating. The Motor method consists of more knock-prone conditions and so the Motor Octane Number (MON) tends to be lower than the RON.

Both the RON and MON rating methods are based on the standard CFR engine[13], with the test conditions defined by the American Society for Testing Material (ASTM). The octane rating scale is defined by the performance of iso-octane and n-heptane, which have a rating of 100 and 0 respectively for both tests.

Composition of surrogate fuels

Gasolines are composed of a blend of hydrocarbons which are classified according to their structure. The main groups are:

- paraffins (alkanes)
- olefins (alkenes)
- aromatics (arenes)
- naphthenes (cycloalkanes)
- oxygenates (alcohols and ethers)

For the purposes of modelling it is unrealistic to attempt to match the composition

[13]The CFR engine is a PFI variable compression ratio engine originally designed and built by the Waukesha Motor Company in 1928 [128]. The engine uses a magnetostrictive pickup sensor which responds to the rate of pressure rise rather than the pressure oscillations. For this reason some authors have urged caution when relating RON and MON to autoigntion [190, 191]

of a gasoline exactly, due to both the complexity involved and the confidentiality that is often associated with commercial gasoline blends. Surrogate fuels are an effective way to represent gasolines with simpler hydrocarbon blends. The simplest of these are primary reference fuels (PRFs) which consist of just two components, iso-octane and n-heptane. By definition the RON and MON of these fuels is equal to the fraction of iso-octane that they contain. A major challenge in combustion modelling is the selection of surrogate fuels to model the combustion chemistry with sufficient accuracy whilst keeping complexity within reasonable limits.

By definition the sensitivity of PRFs is 0, which is not true of gasoline, so toluene reference fuels (TRFs) are commonly used in order to more closely emulate the sensitivity seen in commercial gasolines.

To model SI combustion, a fuel's propensity to autoignite is of paramount importance, so matching the RON and MON of a fuel is the primary concern for surrogate development. Sarathy et al [163] describe the motivation for matching the different qualities of the fuel:

- The octane rating will capture the fuel's combustion phasing and knocking characteristics.
- The LHV will determine the cumulative heat released during combustion.
- The H/C ratio will determine the emissions characteristics – Mehl et al [192] add that flame speed, flame temperature and heat of combustion are also influenced by the H/C ratio.

Additional physical properties of the fuel can be important in assessing the spray and evaporation behaviours in models for which these are applicable, but the number of components required to match all of these characteristics can quickly escalate.

Pera et al [9] compare a number of surrogate blends with a commercial gasoline both experimentally and via simulation. Their focus was mainly on the autoignition properties

Table 2.4: Comparison of the surrogate fuels investigated by Pera et al [9], with compositions being defined by molar fractions.

Gasoline	ULG95	Surrogate	Sur95t
Linear paraffins	10.7	n-Heptane	13.7
Branched paraffins	35.1	Iso-octane	42.8
Cyclic paraffins	10.9	cyclohexane	-
Aromatics	31.7	Toluene	43.5
Olefins	5.7	Cyclohexane	-
Oygenated	5.9	Ethanol	-
RON	95		95
MON	85		87.8
H/C ratio	1.801		1.801
O/C ratio	0.011		0
Molar weight (g/mol)	94.3		102.7
Density at 298K (kg/m^3)	749		750
LHV (kJ/kg)	42801		42893

of the fuel, since application to knock modelling was their primary concern. As an outcome they managed to reproduce the behaviour of a commercial gasoline (sampled from 2005-2009) with a TRF consisting of only three compounds: n-heptane, iso-octane and toluene – as shown in Table 2.4.

Octane rating correlations are particularly relevant in the context of emulating gasoline behaviour with surrogate fuels. A number of researchers have developed correlations which use data from the literature to produce empirical models to predict RON and MON values from the composition of a surrogate fuel. One such study, which has been cited many times, was conducted by Morgan et al [193] and compares a linear blending method for TRF surrogates with a seven term second order correlation, and a "modified linear" model which essentially consists of a reduced version of the second order method. Their study revealed that a simple linear blending method is not sufficient for calculating RON and MON values of TRF mixtures due to the interaction of the toluene with the n-heptane and iso-octane.

Yuan et al [194] and Foong et al [195] examined the octane effects of adding ethanol to TRF surrogates. The latter used Morgan et al's [193] modified linear blending correlation, whereas the former assumed a linear blending method for the TRF constituents

with second order interactions for the ethanol addition.

Cai et al [8] developed Morgan et al's model further to incorporate a term for the H/C ratio of the fuel, and inverted the operation to deliver the ratios of toluene, iso-octane, and n-heptane corresponding to a desired RON, MON, and H/C ratio.

Alternative methods to determine octane ratings have included work by Badra et al [196] on relating ignition delays computed by simulation of the CFR engine, similar to an approach which was investigated by Smallbone et al [197] and Mehl et al [192]. Westbrook et al [198] are the most recent researchers to present a kinetic modelling method to compute the octane ratings of surrogate fuels. A high level of confidence in the accuracy of said kinetic models is required for this approach.

Puduppakkam et al [199] presented a generalised method for surrogate fuel formation, which aimed to minimise error for a number of chemical and physical fuel properties for multi-component blends. A similar approach was developed by Su et al [200] which optimised the surrogate formation process computationally. These studies focused on multi-component fuels, hence the requirement for computational optimisation strategies.

2.4 Conclusions

This literature review has focused on three distinct areas which are important to the research in this thesis.

The first of these areas summarises EGR studies relevant to SI engine operation, and specifically knock control. It describes the evolution of EGR technology up to the present day, and alternative knock control technologies which can be used in parallel with, or in place of, EGR.

The second area focuses in more detail on the chemical effects of EGR, and the relevance of this in relation to EGR composition – i.e. whether it is sourced from before or after the catalyst. There is overwhelming evidence in the literature that NO is the most active ingredient in EGR with respect to knock propensity, but very few studies expand on what the implications of this are on the benefits or drawbacks of using post-catalyst EGR as opposed to pre-catalyst EGR. The few studies that do directly address the topic of EGR compositional effects do not reach a consensus on the merits of catalysed EGR [3, 66] and an experiment with more precisely controlled boundary conditions on the combustion system (such as manifold pressures and temperatures) could shed more light on this topic.

The third part of this chapter has reviewed work on modelling methods for predicting EGR effects on combustion. Of the various methods of combustion modelling, PDF methods have stood out as boasting potential to bridge the gap between simple one dimensional models and much more complex and computationally expensive CFD models. PDF models have successfully been applied to GDI engines to predict knocking combustion, and their integration of kinetic mechanisms may help in their ability to predict the effects of EGR with consideration of its composition.

The chapter ends with a review of relevant chemical mechanisms that are available in the literature and key points in the composition of surrogate fuels for use with these mechanisms.

CHAPTER 3

INITIAL PRE-/POST-CATALYST EGR COMPARISON ON A HIGH LOAD GASOLINE ENGINE

This chapter details a preliminary study on the pre versus post-catalyst effects on high load combustion. The tests are performed on an artificially boosted engine, which enabled more accurate control of the airflow through the engine in order to be able to analyse the combustion system in greater detail.

The engine and test facilities are detailed in the first section, followed by a description of the testing procedure in Section 2. The third section divides the results into those relating to engine performance and emissions before then focusing on the characteristics observed during knocking combustion.

It was expected that the reduced NO content of the post-catalyst EGR would enable increased knock limits when compared to equivalent pre-catalyst EGR operation, and whilst they were advanced considerably with post-catalyst EGR it was suspected that a large part of this improvement was derived from the reduction of load resulting from conversion of the oxygen in the EGR gases by the catalyst. Despite this, intermittent catalyst light-off did reveal evidence to support previous findings in the literature that NO is one of the most active minor species in EGR gas.

The conclusions drawn from this work were used to advance the experimental techniques for the experimentation conducted in Chapter 4.

3.1 Introduction, aims of testing and experimental hardware

Whilst some studies do focus on the benefits and trade-offs between pre and post-catalyst EGR, the evidence for the benefits it could provide to GDI combustion systems is still inconclusive. This chapter details a preliminary study on the comparison between pre and post-catalyst cooled EGR, with details of potential pitfalls and complications in attempting to compare these two operation modes.

Since engine architecture is such a significant factor in the evaluation of EGR effects on boosted engines, this experiment aims to somewhat neutralise that factor by using an artificial boosting system. This system replaces the turbocharging hardware on the engine and allows independent control of manifold pressures to isolate the combustion system from the effects of turbocharger behaviour.

The absence of a turbocharger makes consideration of high or low pressure EGR architecture irrelevant for this experiment, with it instead just taking the form of "cooled EGR".

Since this arrangement allows for no low pressure introduction point for EGR gases, a rig was used to provide the driving pressure for the EGR flow. This also provided the opportunity to put a catalyst in the EGR leg without affecting any of the flow conditions for the engine.

The main aims of this experiment are:

- to design an experiment to investigate the effects of EGR catalysis on diluted high load combustion.
- to analyse the effects of pre and post catalyst EGR on knock limits and engine performance at high load.

Table 3.1: Table of engine details

Engine Type	In-line 4 cylinder, 4 valves per cylinder
Capacity(cc)	1991
Bore/Stroke (mm)	83/92
Compression ratio	9.0:1
Firing Order	1-3-4-2
Construction	All-aluminium AJ133 cylinder block converted to single bank operation)
Combustion system	Pent-roof combustion chamber Asymettrical central DI and spark plug High-tumble intake ports Auxiliary port-fuel injection (not used in these experiments)
Valve train	Chain-driven double overhead camshafts (DOHC) Dual continuously variable camshaft phasers (DCVCP) Cam profile switching (CPS) tappets on inlet and exhaust
Specific power(kW/l)	142 @ 6500 rpm
Specific torque(Nm/l)	255 @ 3500 rpm
Other	External cooled EGR Water cooled exhaust manifold 130-145 bar peak pressure limit

3.1.1 The Ultraboost engine

The engine under investigation in this chapter was the Ultraboost engine, a prototype two litre four cylinder GDI engine derived from Jaguar's V8 AJ133 engine, which incorporates a number of technologies in an attempt to match the torque curve of the original naturally aspirated five litre engine.

The prototype engine operated as a four cylinder in-line engine, using one bank of the AJ133 engine block, with a flat-plane crankshaft reducing the engine stroke and a liner pack reducing the bore diameter of the engine block to achieve the desired displacement and compression ratio.

The continuously variable camshaft phasers of the original V8 engine were kept, but for these tests the cam phasing was kept constant. Details of the engine are provided in Table 3.1.

The engine was operated at boosted conditions without the use of turbomachinery. Pressurised air was supplied to the inlet of the engine by a forced induction simulator (FIS), allowing precise control of manifold pressure across operating conditions in order to look more closely at the combustion system. Compressed air at 7 bar was supplied to the FIS which passed it through a filter and regulator to provide dry, clean air at 5 bar. Air temperature was controlled between ambient and 85°C by a 15kW electrical heater and closed loop control. Total mass airflow into the FIS was measured by the pressure drop across an orifice plate before the heater.

A butterfly valve controlled by a closed-loop PID controller regulated the intake manifold pressure, and excess air passed through an ABB Sensyflow mass flow meter before being dumped into the cell. Total engine flow was therefore calculated by the difference between the total flow into the FIS and the discarded airflow.

Another butterfly valve on engine exhaust provided back pressure to simulate the presence of a turbocharger. The target pressure values were derived from 1-D simulations of the engine operating at steady state with both a turbocharger and supercharger in series.

Further details of this engine are provided in [201].

3.1.2 The EGR rig

The driving force for the recirculated exhaust gases was a 2.4L diesel engine with a modified valve train to convert it to two-stroke operation, effectively operated as a positive displacement pump. The pump was powered by a variable speed electric motor which enabled delivery of up to 20% EGR throughout the operating range of the engine. The exhaust gas was sampled from after the exhaust back pressure (EBP) valve before passing through a heat exchanger either side of the pump and being reintroduced upstream of the inlet manifold via a 'colander' nozzle protruding into the air flow. The coolant for the heat exchangers was independent of the engine coolant system and so had no impact on the rest of the engine.

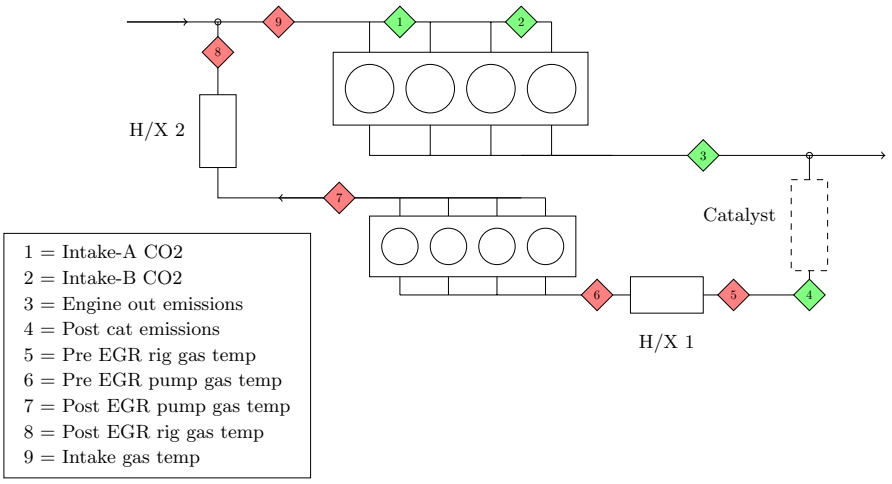

Figure 3-1: UB100 engine setup and measurement points. The catalyst is shown by a dotted line as it was installed only for the catalysed tests.

Figure 3-1 shows the layout of the engine and EGR rig, with sampling points denoted by the numbered diamonds.

Whilst the EGR rig provided a unique opportunity to investigate dilution effects on boosted combustion without consideration of turbomachinery effects, these tests were performed with a relatively early specification of the equipment.

The cooling of the exhaust gases both before and after the pump was taken care of by two Bowman heat exchangers, which were supplied with a facility supply of cold water. The cooling power of these heat exchangers exceeded that required by the EGR gases, so cooled the gases well beyond their dew point, which in turn deposited much of the water either in the EGR pump[1]or in catch pipes in the heat exchangers. Some of this water was returned to the engine, evidenced by markings along the lower surface of the inlet runner. These markings were only observed on cylinder 4's inlet runner, being the first cylinder to see the incoming fresh air.[2]

[1]The leakage of water past the piston rings of the pump engine raises a question over whether oil could have leaked in the opposite direction from the sump. None of the data indicated any pre-ignition events that oil droplets could have triggered, but having said this the effect would have been mitigated by the EGR gases. Inspection of the hardware revealed no signs of oil residue in the EGR pipework.

[2]A later iteration of this rig included a temperature control unit for the heat exchanger coolant to avoid excessive cooling of the EGR gases. It could be argued that maintaining the water content of the EGR gases would have resulted in less consistent results, since a larger quantity of water would have condensed out of the EGR gases on mixing with the cooler fresh charge and would likely be unevenly distributed between the cylinders.

Gas mixing

The mixing of the EGR gases with the fresh charge air is an important consideration in the accuracy of this experiment, since variability in the inlet charge distribution between cylinders, and the consistency of inlet charge composition over time, can have a significant effect on the combustion behaviour.

This has been highlighted by the work of Siewert et al on a 2L diesel engine [202] where premixed EGR was compared to manifold mixed EGR. Variations in the concentrations of the EGR gases seen by each of the cylinders were found to vary by up to 10% (of the measured values) for premixed EGR, in contrast to a value of up to 45% for manifold mixed EGR.

Since premixed EGR is not feasible in many applications the method and location of EGR delivery to the inlet is important to improve mixing of the EGR gases before entering the cylinder.

Pressure pulsations due to valve events at both the inlet and exhaust side have been found to influence the uniformity of EGR distribution in the inlet charge [202–204]. This can cause the EGR to be delivered in "packets" rather than as a continuous flow, so caution should be taken to avoid introducing EGR too close to the inlet manifold and thereby not allowing sufficient mixing opportunity.

Since the EGR supply is being delivered artificially at consistent rates for this investigation it is only the inlet valves that will contribute in the pressure fluctuations that could influence EGR flow. An attempt to mitigate this has been made by locating the EGR delivery point 0.5m upstream of the inlet manifold and throttle body, which should allow for the gases to be more completely mixed before reaching the manifold[3].

Kim et al [205] found a simple single location EGR delivery to be just as effective for cylinder to cylinder distribution as bespoke EGR valves delivering the EGR flow to each

[3]Whilst this arrangement optimises EGR mixing, it also introduces further lag to transient response. Since this experiment was conducted at steady state conditions this is not a concern for the current work.

port. Importantly they do note that the eddy currents and reverse flow induced by the throttle were particularly beneficial for EGR mixing.

Dimitriou et al [206] investigated the effect of different nozzle designs on EGR mixing with 1D and 3D co-simulation techniques; using the CoV between cylinders as an indicator for mixing effectiveness. They compared ten nozzle designs, finding the most effective one to be a simple probe inserted at a right angle to the direction of flow, with holes along its length.

The EGR nozzle design for this study was selected to emulate that found most effective by Dimitriou et al, referred to earlier in this section as a "colander nozzle". It consisted of a straight pipe protruding into the incoming flow, with multiple holes around its circumference and length. It was positioned before the throttle body, with 300mm of inlet pipe before the throttle body to maximise the turbulence – and therefore mixing effectiveness of the diluent gases. Direct assessment of the mixing effectiveness of this setup was not possible with the available hardware, but could be inferred by comparison of the IMEP values measured for each cylinder.

A summary of the comparison of IMEP values between the cylinders for all of the test points recorded is given in Figure 3-2. For each EGR rate this plot compares the difference in the IMEP of each cylinder against the mean of all four cylinders. The fourth cylinder appears to be the only one that is noticeably affected by the introduction of EGR. The rise in IMEP relative to the other cylinders would suggest that cylinder 4 receives less EGR than the other cylinders. The most constant cylinder relative to the mean of all four cylinders is cylinder 1.

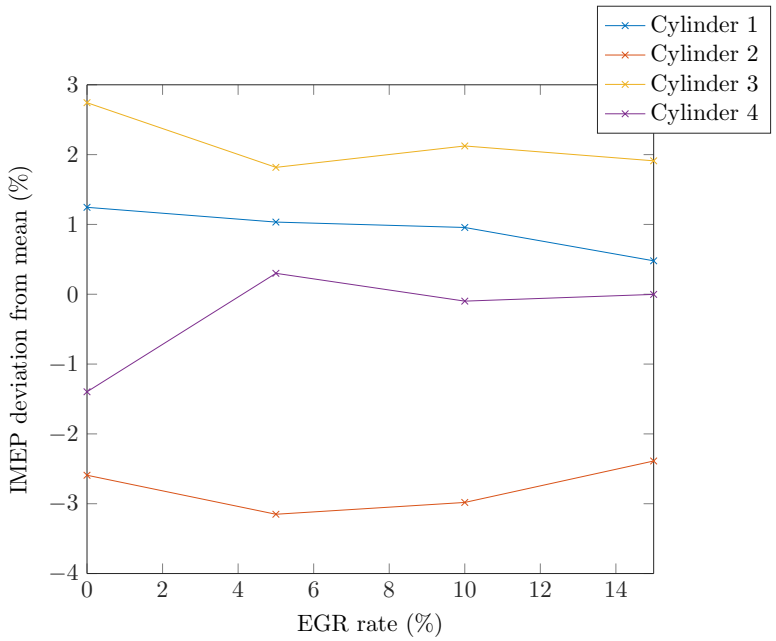

Figure 3-2: Average percentage variation from the mean IMEP across all four cylinders at each EGR rate. Aside from cylinder 4's rise in IMEP relative to the other cylinders when EGR is introduced, the EGR does not seem to affect IMEP distribution between cylinders greatly.

3.1.3 Test cell facilities

The engine was coupled to a twin dynamometer arrangement with a total 400 kW capacity – a 200 kW AVL AC dynamometer was supplemented by a Froude eddy current dynamometer. An AVL Indicom system communicated with the Kistler air-cooled in-cylinder pressure sensors and port pressure sensors for combustion analysis.

Aside from the high resolution pressure data, all control and data acquisition was performed with a Sierra-CP CADET V14 system. This included 32 K-type thermocouples and 16 pressure channels for both the air and coolant paths, the data from which was collected for 10 second averaged samples at each test condition.

Two Horiba MEXA 7000 emissions analysers measured the exhaust emissions both pre and post-catalyst. A summary of the test equipment is given in Table 3.2.

Table 3.2: Table of test cell facilities

Dynamometer	Twin dynamometer arrangement: AVL 200 kW AC dynamometer and Froude AG250 eddy current dynamometer
Speed measurement	1024 pulse/rev encoder
Torque measurement	1 kNm torque measurement flange
Combustion analysis	AVL Indimaster advanced 16 channel system AVL 3600 pulse/rev optical encoder Kistler 6054A in-cylinder transducers Kistler 4049A water-cooled exhaust pressure transducer Kistler transducer cooling module and amplifiers
Air flow measurement	ABB Sensyflow 1200 kg/h
Fuel flow measurement	CP Engineering FMS-1000 1 litre gravimetric fuel weigher Coriolis flow meter
Emissions	2 off MEXA 7100 DEGR exhaust gas analysers for simultaneous pre and post-catalyst sampling AVL 439 Opacimeter Cambustion DMSA 500 particulate sizer/counter
AFR	ETAS LA4 lambda meter
Intake O_2 %	Labcell pressure-compensated lambda CAN
Engine blowby	Labcell blowby meter
Other measurements	Up to 32 K-type thermocouples, 16 PRTs and 16 pressure channels, coolant flow rate (Krone magnetic flow meter)

3.2 Testing procedure

The engine was operated at steady state test points as detailed in Table 3.3. The inlet temperature was fixed at 40°C and cam phasing was fixed for all operating points. A warm up procedure was followed to ensure consistent starting conditions for the tests, with a daily test point providing an alert if any parameters were to deviate significantly.

The cam phasing was selected to maximise the scavenging effects, thereby minimising residuals, with a high pressure gradient from the inlet to exhaust assisting with this [4]. This combination did however result in there being high oxygen content in the exhaust gases of up to 3%. As is discussed later in this chapter, this oxygen was removed by the catalyst, and therefore altered the load slightly between equivalent pre and post-catalyst EGR operating points.

Spark sweeps were performed at each EGR rate and 10 second averaged logs were taken as well as 300 cycle in-cylinder pressure logs at a resolution of 0.1 °CA for each spark angle.

Knock tends to be most prevalent at lower speeds and high loads so speeds of 1500 and 3000rpm were selected. Collection of the majority of this data was performed by a colleague at the University of Bath, and the data features in [69] and [14].

Table 3.3: Table of test variables

Parameter	Values
Speeds (RPM)	1500 & 3000
Inlet Manifold Pressures (bar)	1.8 & 2 & 2.2
EGR rates (%)	0 & 5 & 10 & 15

[4]The high pressure gradient between the inlet and exhaust manifolds was a result of 1-D simulation results done during the Ultraboost project to mimic operation with both a turbocharger and supercharger. The test points used for this data were taken during a phase of testing in which the Ultraboost manifold pressures were selected to simulate a supercharger bias.

3.2.1 Experimental conditions and EGR rate evaluation

EGR rates are traditionally calculated by the ratio of CO_2 at the inlet and exhaust sides of the engine (as shown in Equation 3.1), which stems from diesel combustion where near complete combustion occurs. Gasoline combustion often does not result in complete combustion, so more carbon monoxide and hydrocarbons are present in the exhaust. A three way catalyst oxidises these species to carbon dioxide and water, as well as enabling the reduction of nitric oxides (NOx) to nitrogen and oxygen. The change in CO_2 content can complicate the evaluation of EGR rates with the presence of a catalyst, and sampling positions can have a very large impact on the reported rates due to this.

$$\text{EGR rate} = \frac{\text{Intake } CO_2 - \text{Background } CO_2}{\text{Engine out } CO_2 - \text{Background } CO_2} \tag{3.1}$$

In order to keep the EGR rates as comparable as possible between the pre and post-catalyst EGR tests it was decided to fix the mass flow rates for the two experiments. Due to the unique nature of the engine setup it was possible to maintain constant manifold pressures for each EGR condition using the FIS. The pre-catalyst EGR rates were targeted at 0,5,10 and 15% using the traditional method outlined in Equation 3.1. The post-catalyst EGR tests were then performed targeting the mass flow rates measured during the pre-catalyst EGR tests. At each steady state condition the mass flow through the FIS was recorded and the duty on the EGR rig was adjusted so that the fresh air mass flow matched for both conditions. In reality this resulted in a “mass of air displaced by EGR” rate.

Figure 3-3 plots a comparison between the various methods of quantifying EGR rate against the mass of inlet air displaced for the post-catalyst EGR test points. The values for post-catalyst CO_2 ratio and calculated mass have a maximum deviation of 2%, but are within 1% for the majority of test points. These deviations may in fact be magnified

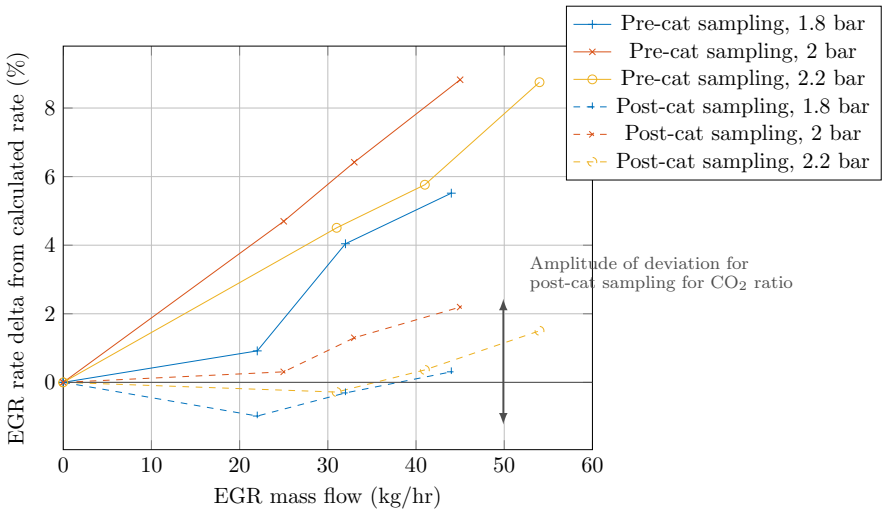

Figure 3-3: A comparison of the effect of sampling location (pre or post-cat) on post-catalyst EGR rates. The orange, yellow and blue lines correspond to boost pressures of 1.8, 2, and 2.2 bar (abs) and the solid lines represent pre-cat sampling of the EGR gases, whilst the dashed lines denote post-cat sampling.

by the error margin present in the mass flow measurement of the boost rig.

3.2.2 Knock limit evaluation

Accurate identification of knocking combustion is important for engine optimisation, and is an area that is often reviewed by researchers. This has resulted in a number of methods being devised to identify knock onset, usually based on either time domain or frequency domain metrics. Unfortunately there still seems to be no consensus on the most appropriate of these methods. Giles [207] compares a number of knock evaluation methods, finding that they broadly come down to subjectivity on defining thresholds at some stage of the process.

The initial stage in most knock quantification processes involves filtering the in-cylinder pressure trace to isolate the pressure oscillations arising from autoignition. Since the most common oscillation frequencies will depend on the natural oscillation modes – and therefore the geometry – inside the cylinder, they can be estimated by Draper's Equation [208]:

$$f_R = c\left[\left(\frac{\rho_{m,n}}{B}\right)^2 + \left(\frac{P}{2L}\right)\right]^{1/2} \tag{3.2}$$

Where B is the cylinder bore, $\rho_{m,n}$ is a constant defined by the Bessel function according to the type of vibration mode, P represents the axial resonance mode and L is the axial distance.

As autoignition occurs when the piston is near TDC, knock oscillations occur in a disc shaped region in the cylinder, so the axial component of Equation 3.2 can be neglected [139]. The calculated oscillation modes are shown in Table 3.4. Galloni et al state that the most prominent knock frequencies tend to lie in the range from 6-20 kHz [57], it is often observed that the first resonant mode is the strongest of these. From Equation 3.2 and the Eigenvalues from Table 3.4, the theoretical resonance frequency for each mode can be approximated[5]. Estimations for the resonant frequencies are given in Table 3.4 assuming an end gas temperature of 700-800K. When compared to the frequencies seen later in Section 3.3.3 it appears that this method tends to overestimate the natural frequencies, which most likely stems from the simplification of the combustion chamber into a homogeneous volume for the purposes of Equation 3.2.

For the data collected in this experiment a band pass filter was selected to isolate oscillations from 4 to 25 kHz in the crank angle window in which combustion occurs.

One of the most common methods to define knock intensity is the amplitude of the oscillations in the band pass filtered pressure trace – often referred to as the maximum amplitude of pressure oscillations (MAPO). This can take the form of either the peak-to-peak amplitude, or the amplitude of the absolute values of the oscillations – both of these methods have been used in the literature and they are illustrated in Figure 3-5 on the band pass filtered pressure trace from Figure 3-4. The knock peak (amplitude of absolute values) tends to be around half of the peak-to-peak value so it important to make clear which method is being used. The MAPO values throughout this thesis are defined as the amplitude of the absolute values, as illustrated in Figure 3-5b.

[5]This is only an approximation since the estimation of the ratio of heat capacities – and therefore the speed of sound – is only known approximately, and is not expected to be homogeneous across the cylinder.

Table 3.4: Table of the first few resonance modes and their associated eigenvalues (recreated from [10]). The '+' and '-' in the theoretical mode shape diagrams denote the positive and negative nodes of the standing resonant wave patterns – viewed from the top of the cylinder.

(α, β)	ρ	$f_{theoretical}$ (kHz)	Theoretical Mode Shapes
(1,0)	1.841	11.5	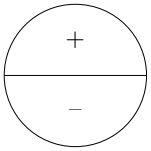
(2,0)	3.054	19.1	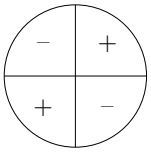
(0,1)	3.831	24.0	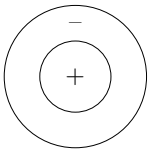
(3,0)	4.021	25.2	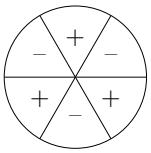
(4,0)	5.318	33.3	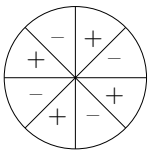

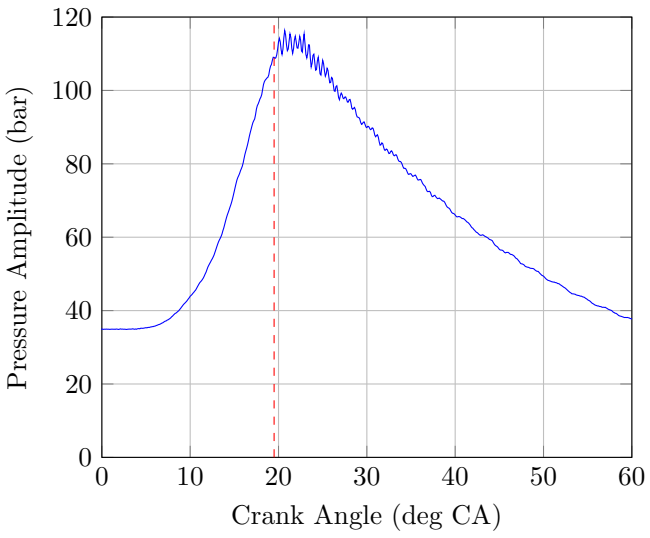

Figure 3-4: A pressure trace from a single knocking cycle in the crank angle window from 0 to 60 °CA ATDC. The red dashed line indicates the onset of knock for this cycle.

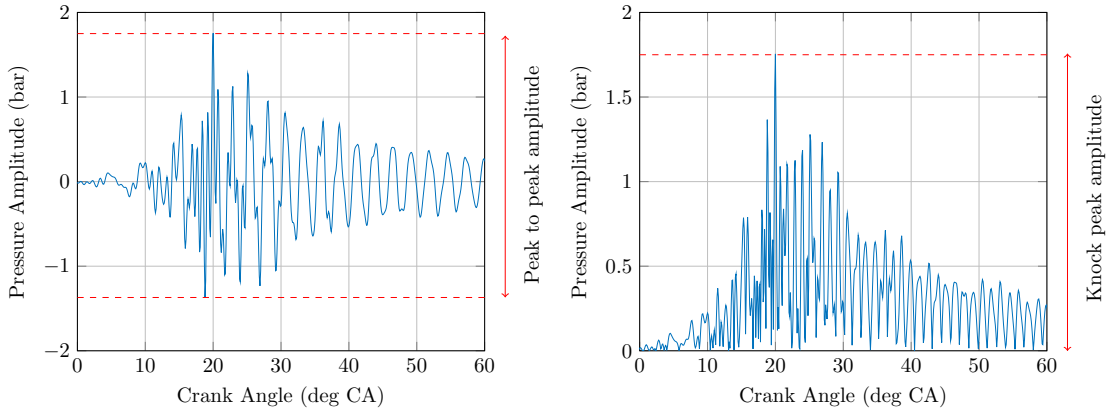

Figure 3-5: The resulting band pass filtered trace of the pressure signal in Figure 3-4 to show the pressure oscillations resulting from knock in a single cycle. The peak-to-peak amplitude is illustrated in (a), and the absolute amplitude is illustrated in (b).

The knock peak limit for this experiment was defined as 1 bar per 1000 rpm[6], but since knock tends to be a stochastic phenomenon there is usually a spread of MAPO values over a given period during steady state operation. For that reason, knocking combustion was identified with the help of a histogram in AVL Indicom software in which limits were set corresponding to those given above. An operating point was considered to be knocking if over 10% of cycles during a 1.5 second period exceeded the threshold. This method has been used for data from this engine in a number of published papers [69, 209].

Spark sweeps were performed between the retardation limit – defined by either a CoV exceeding 5% or exhaust temperatures exceeding 1000°C – and the knock limit.

At the conditions tested for this engine the window for altering the spark angle between the knock limit and exhaust temperature limit was very small without altering the equivalence ratio. It was for this reason that the KLSA were defined simply by the threshold for the knock peak values.

[6]Defined by the maximum amplitude of the absolute oscillation values rather than peak-to-peak.

3.3 Results of experimental work

3.3.1 Comparison on engine performance

This section discusses the BSFC, IMEP, emissions and combustion phasing of the engine. Comparisons between the pre and post-catalyst architectures are made, but being mindful of extra factors that are influencing performance when comparing the two architectures. All of the following plots show significant impacts between the pre and post-catalyst test conditions, but they are all significantly affected by the change in engine load brought on by the reduction in manifold O_2 content with post-catalyst EGR – which has been briefly mentioned in Section 3.2. This effect is considered to have a larger impact than the chemical or thermodynamic effects introduced by the change in EGR composition.

In agreement with previous studies on EGR, the knock limit was advanced at higher EGR rates with a corresponding advance being evident in combustion phasing. This improved BSFC and emissions characteristics of the engine with both pre and post-catalyst EGR.

Figure 3-6 compares pre and post-catalyst effects on KLSA, IMEP, and BSFC, plus inlet oxygen concentration to show the discrepancy between the pre and post-catalyst conditions.

Figure 3-6b demonstrates how the inlet oxygen concentration is reduced for post-catalyst EGR – denoted by the dashed lines – by up to 0.5% for all of the boost conditions shown. This is believed to be the primary factor in the load reduction displayed in Figure 3-6c between the pre-and post-catalyst conditions.

Although the reduction of radical availability resulting from catalysis of the EGR would be expected to improve the knock limit, the extent of the improvement exhibited in Figure 3-6a can be largely attributed to the load reduction.

With improved combustion phasing a corresponding improvement in BSFC is often ob-

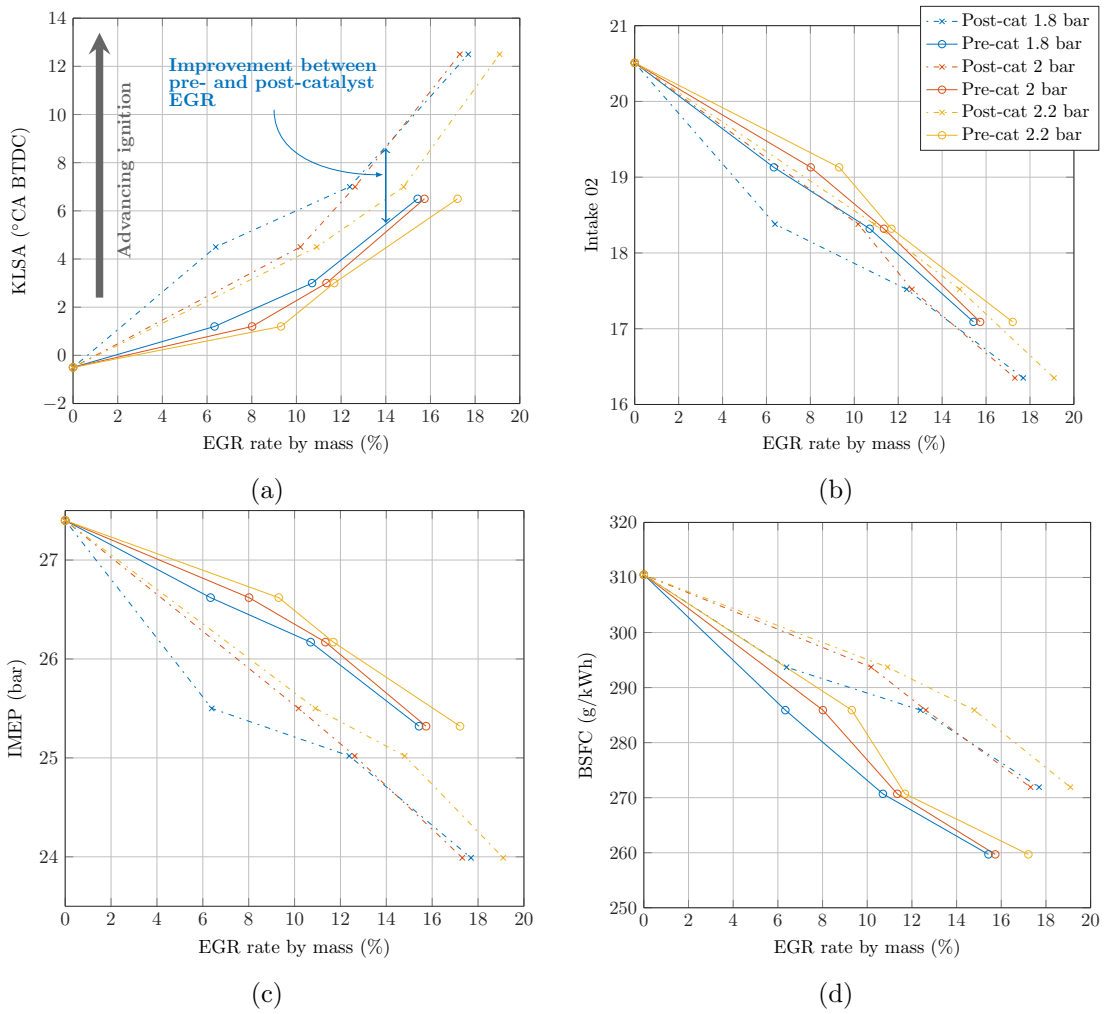

Figure 3-6: Absolute effects of EGR, both pre and post-catalyst, at 1500rpm on KLSA (3-6a), IMEP (3-6c) and BSFC (3-6d). Inlet oxygen concentration is included in 3-6b to show the difference between pre and post-catalyst operation. Solid traces represent pre-catalyst EGR and dashed traces represent post-catalyst EGR.

served, however the evidence from Figure 3-6d shows the opposite trend between the two EGR compositions. A part of this can be attributed to the increased calorific value of the uncatalysed EGR gases due to the unburned HCs and CO content, which would supplement the fuel to some extent. The discrepancy between the inlet oxygen concentration, and therefore IMEP, for the two EGR compositions will also contribute to this fuel consumption trend. Since the frictional and pumping losses are constant[7] the relative proportion of these losses increases at lower IMEPs. This increases the fuel consumption for a given brake output.

The direct effects of the dilution and resulting advanced combustion phasing are illustrated in Figure 3-7 for one boost condition at 1500 rpm. Whilst it must be conceded that the reduction in load with increasing EGR rates is a factor – exhibited by the lower total heat release – these plots do illustrate the reduced heat release rate and advanced phasing enabled by the dilution and resulting knock limit advance.

The reduction in the heat release rate with EGR addition can be observed by the decreased amplitudes in comparison to the blue trace in Figure 3-7c and decreased gradients in comparison to the blue trace in Figure 3-7b. The advanced phasing, shown by the shift to the left of the yellow trace in all three plots, corresponds to an advance in cylinder pressure rise, which in turn advances the mechanical work exerted on the piston and therefore the efficiency of that cycle. The optimum phasing of this heat release for efficiency is dependent on the engine operating mode. Earlier phasing results in higher peak pressures due to the piston position being closer to TDC, whilst later phasing results in a longer effective crank lever to exert a torque on the crankshaft. MBT occurs at the position where the product of these two factors is at a maximum.

Before looking too deeply into the comparison between pre and post-catalyst EGR it must be noted that the NOx catalyst conversion efficiency was very poor for most of the post-catalyst EGR tests. This was most likely caused by poor light-off of the cata-

[7]These losses are constant due to their being no change in speed or manifold pressures at equivalent test points.

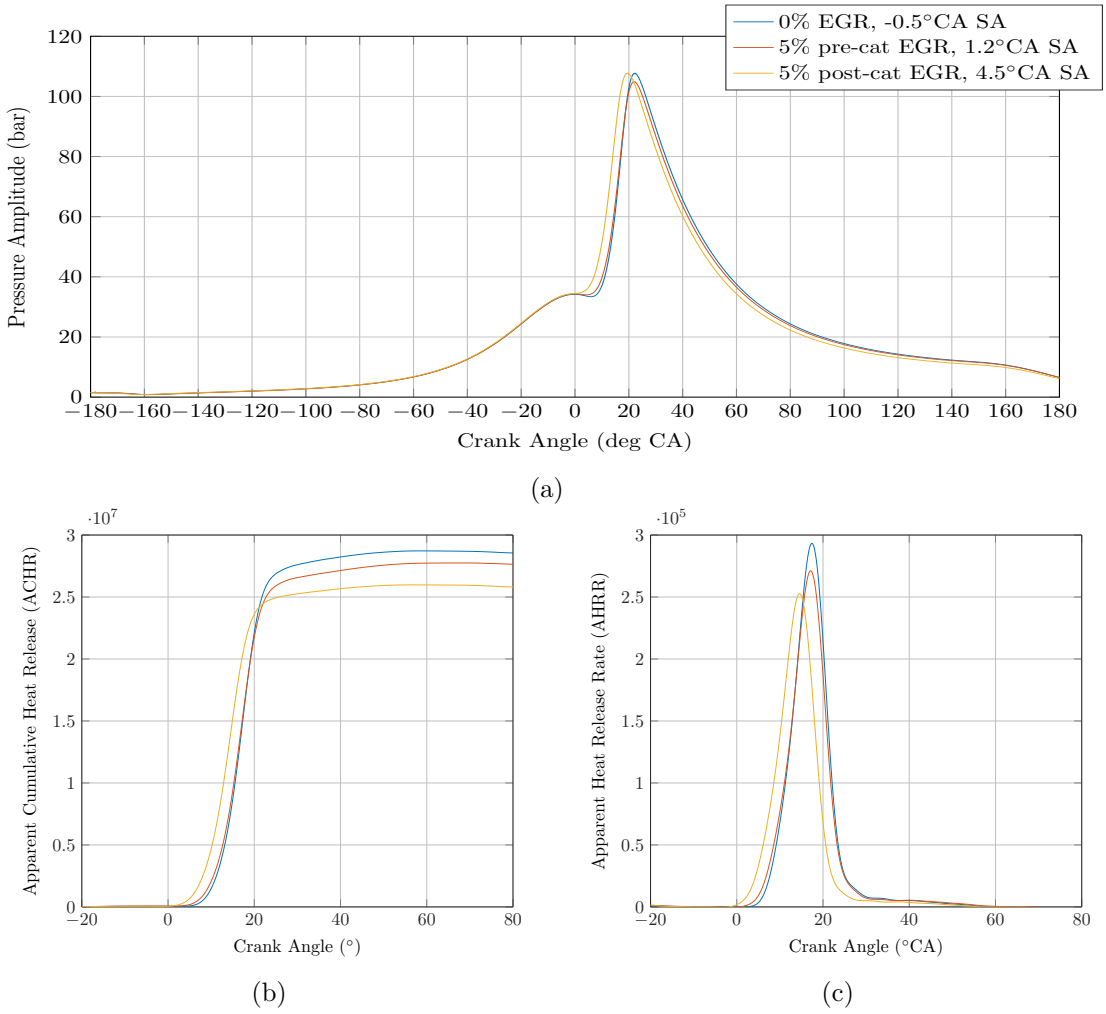

Figure 3-7: Example cylinder pressure trace (Figure 3-7a), apparent heat release rate (Figure 3-7c) and cumulative heat release (Figure 3-7b). These plots illustrate the two opposing combustion effects of dilution and spark advance for a single boost condition at 1500 rpm.

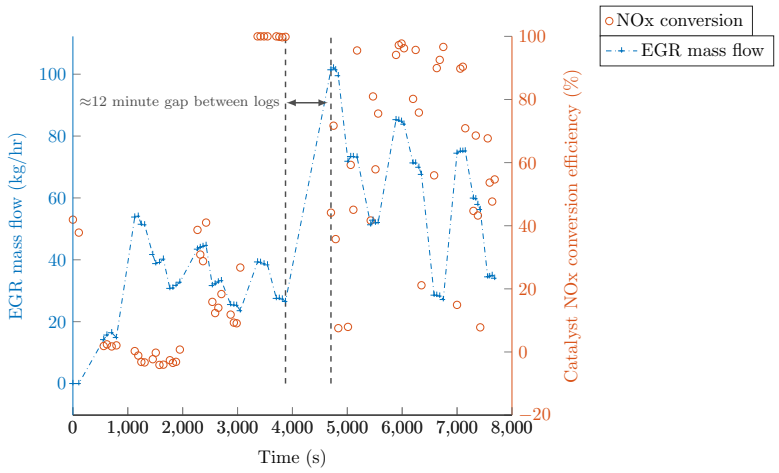

Figure 3-8: Comparison of the catalyst conversion efficiency (right axis) and the EGR mass flow (left axis) plotted against time in seconds. Whilst there doesn't appear to be an obvious correlation between the mass flow and conversion efficiency, a large gap between logs in the middle of the test appears to be a significant factor in the catalyst performance.

lyst[8].

This is demonstrated in Figure 3-8 where the NOx conversion has been plotted alongside the EGR mass flow through the catalyst. Since all of the catalysed EGR data was collected during one test these can be plotted against time, where zero seconds corresponds to the start of the test.

It is hard to see a correlation between the mass flow through the catalyst and the NOx conversion, but a large gap of around 12 minutes is apparent in the middle of the test where no logs were recorded. Before this pause it appears that the catalyst had reached light-off, but following the pause the conversion is inconsistent. Maintaining catalyst light-off with the catalyst not positioned in the main exhaust flow is difficult considering the intermittent nature of the exhaust flow it receives[9] and the fact that the catalyst was not sized correctly for such low flow rates.

As much of the literature shows [115] NO can be a potent autoignition promoter at certain concentrations, so its removal would in theory enable extended knock limits for

[8]Bartley et al [210] and Theis et al [211] do show that NOx conversion efficiency is the slowest to respond during catalyst light-off, and does require higher temperatures than CO and HCs.

[9]Intermittent in nature due to the EGR rates being changed fairly regularly.

post-catalyst EGR. The post-cat EGR data does show extended knock limits, but the extent to which this is due to the reduced NO content rather than the reduced load cannot be stated with confidence.

Of the post-catalyst EGR logs collected at KLSA, only three have a NOx conversion rate better than 90% with one additional test point above 80% NOx conversion efficiency. Figure 3-9 provides a visualisation of the reduction in the NOx concentration in the inlet charge air for post-catalyst EGR, as compared to pre-catalyst EGR for this test.

The similarity between the trends shown in Figures 3-9 and 3-10 are quite striking, suggesting that the NOx content of the EGR has a significant effect on the knock limit. To rule out any other impacting factors an investigation into the temperature and pressure deviations at the inlet manifold show that they both stay within reasonable tolerances ($\pm$ 0.5 °C and $\pm$ 0.5 kPa respectively) and so are unlikely to have had a significant effect on the data produced; and CO and THC concentrations at the inlet show quite different trends to those seen for spark advance and NOx concentration.

The similarities between Figures 3-9 and 3-10 support previous findings in the literature that NO can have a promoting effect on autoignition in concentrations between 0-500ppm [3, 84, 107, 108, 111, 117, 212]. All of the pre-catalyst EGR tests in this investigation introduce NOx to the engine at concentrations within this window.

The difference in KLSA between the pre and post-catalyst EGR is presented in Figure 3-10, showing that on top of the base improvement in spark advance the post-catalyst EGR allows further advancement of up to 8 CAD at around 15% EGR. This improvement is reduced for higher EGR rates at 3000 rpm and 1.8 bar boost pressure since the target knock peak values were not reached and MBT timing had been exceeded. The effect of this is evident in the fuel consumption (Figure 3-12), IMEP (Figure 3-11) and emissions (Figures 3-14, 3-15, 3-13 and 3-16).

As previously mentioned for the condition shown in Figure 3-6d the effect of the improved combustion phasing was overshadowed by the increased calorific value of the

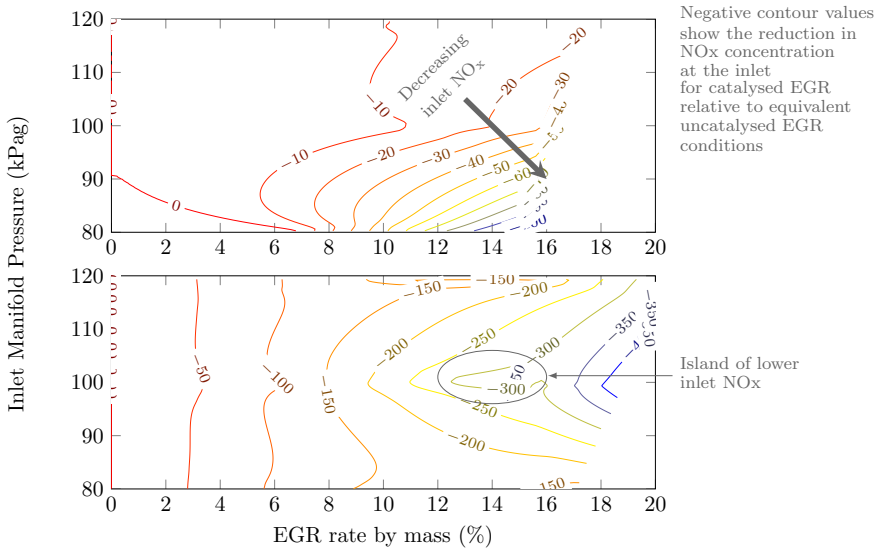

Figure 3-9: Contour plot showing the reduction in NOx concentration (ppm) at the inlet due to EGR catalysis. The trends in these plots are astoundingly similar to the trends shown in Figure 3-10, suggesting that the NOx reduction in the post-catalyst EGR could be a significant factor in extending knock limits.

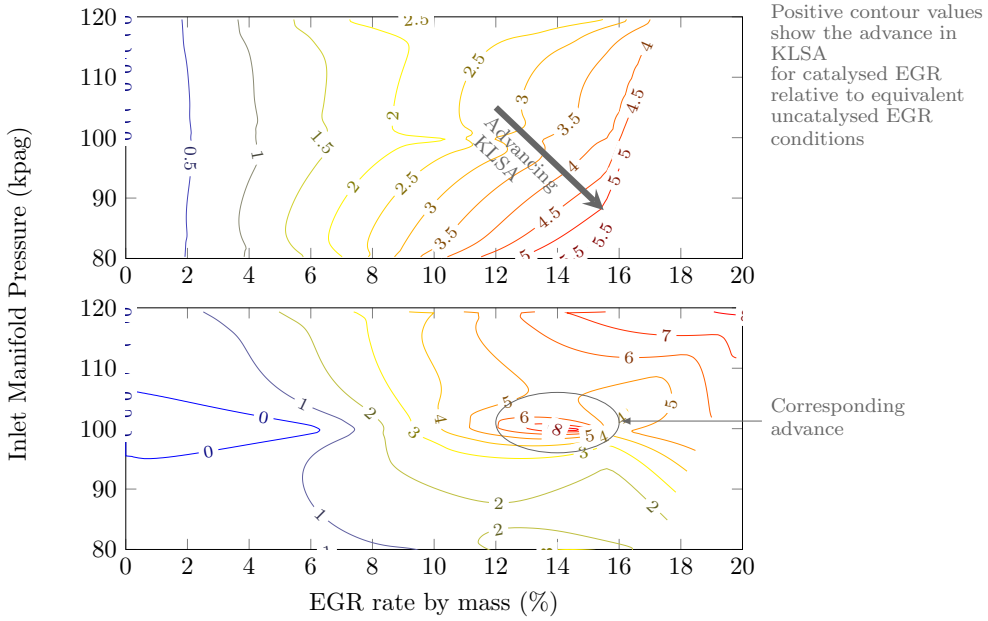

Figure 3-10: Contour plot showing the change in KLSA for post-catalyst EGR compared to that seen for pre-catalyst EGR at 1500rpm and 3000rpm.

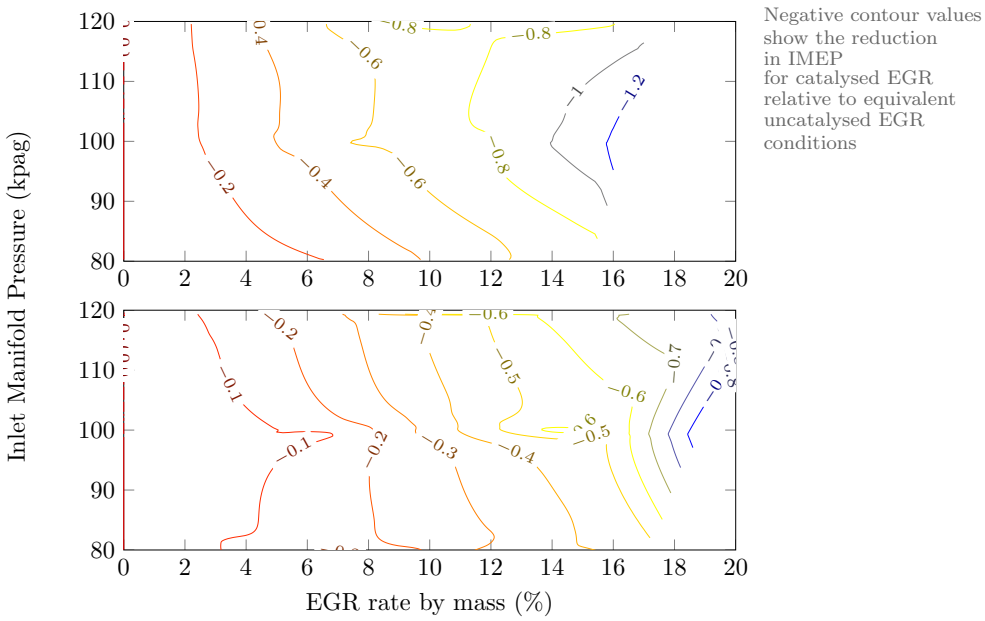

Figure 3-11: Contour plot showing the decrease in IMEP in bar as a result of post-catalyst EGR compared to that seen for pre-catalyst EGR at 1500rpm and 3000rpm.

uncatalysed EGR gases, and the lower load at the catalysed EGR conditions. Figure 3-12 demonstrates that this is the case across the entire range of conditions tested.

The emissions effects of post-catalyst EGR as compared to pre-catalyst EGR are shown in Figures 3-13, 3-14, 3-15, and 3-16. Paradoxically most of the emissions trends are different for the two different speeds tested – although this may be explained partly by MBT spark timing being exceeded – and therefore not advanced further for high EGR rates – at 3000 rpm, 1.8 bar boost, and by poor catalyst NOx conversion efficiency at that test point.

At 1500 rpm there is only a small change in NOx emissions between the two EGR compositions, similarly there is a small reduction in carbon monoxide for post-catalyst EGR, with a corresponding increase in CO_2. The hydrocarbon emissions are reduced for both the 80 and 100 kPag manifold conditions, but increase at the highest boost pressure. It is unclear what is causing this trend, but a tentative explanation could be that the increased in-cylinder mass for pre-cat EGR conditions (due to the extra oxygen content and therefore fuel) does not burn as completely at the lower boost conditions. The faster flame speeds associated with higher boost levels could enable this extra mass

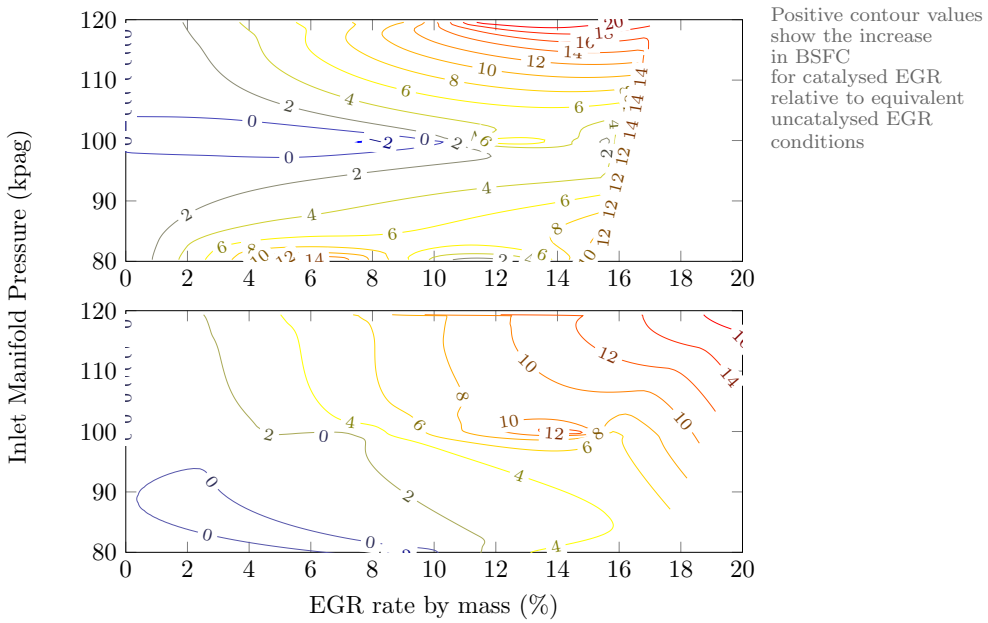

Figure 3-12: Contour plot showing the change in BSFC in g/kWh for post-catalyst EGR compared to that seen for pre-catalyst EGR at 1500rpm and 3000rpm. Contrary to expectations the BSFC is actually increased for post-catalyst EGR operation, a trend which is more apparent at higher boost levels.

to be burned more completely, therefore causing the boost pressure dependence that appears in Figure 3-13.

Amongst all of the emissions effects between pre and post-catalyst EGR the hydrocarbon emissions at 1500 rpm appear to be the only exhaust species that are affected by more than negligible amounts.

At 3000 rpm Figures 3-13 and 3-14 appear to show an island of higher emissions for post-cat EGR at around 14% EGR which corresponds to that found on the KLSA plot (Figure 3-10) and inlet NOx plot (Figure 3-9). Higher CO and HC emissions usually indicate that the combustion is less complete, which is the reverse to what would be expected with the more advanced combustion phasing with post-cat EGR – and particularly in this island of increased spark advance where the inlet NOx is reduced. The corresponding combustion duration delta between pre and post-cat EGR, illustrated in Figure 3-17 shows a reduced combustion duration in this island of increased spark advance – which would be expected to correspond with more complete combustion.

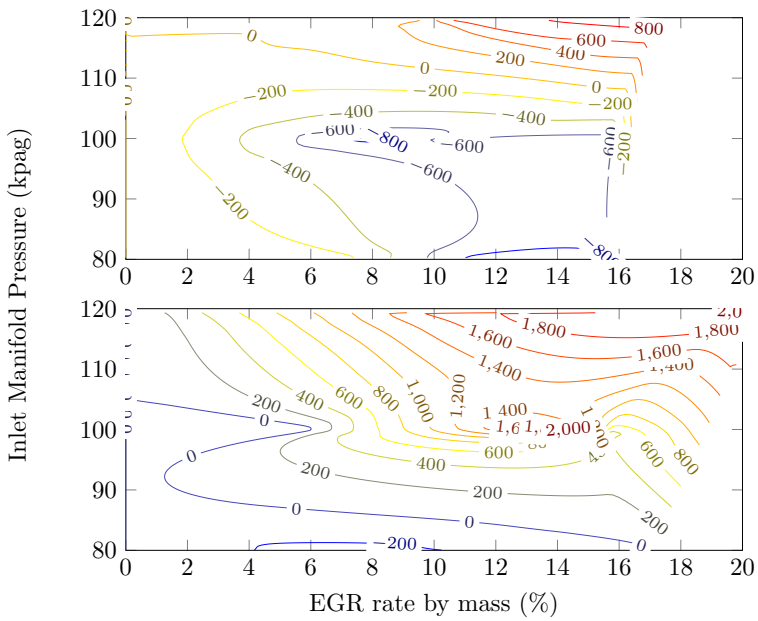

Figure 3-13: Contour plot showing the change in hydrocarbon emissions in ppm as a result of post-catalyst EGR compared to that seen for pre-catalyst EGR at 1500rpm and 3000rpm.

This evidence suggests that the reduced NOx content may be impacting the combustion chemistry to increase HC and CO emissions – meaning that the NO interactions may assist in achieving more complete combustion.

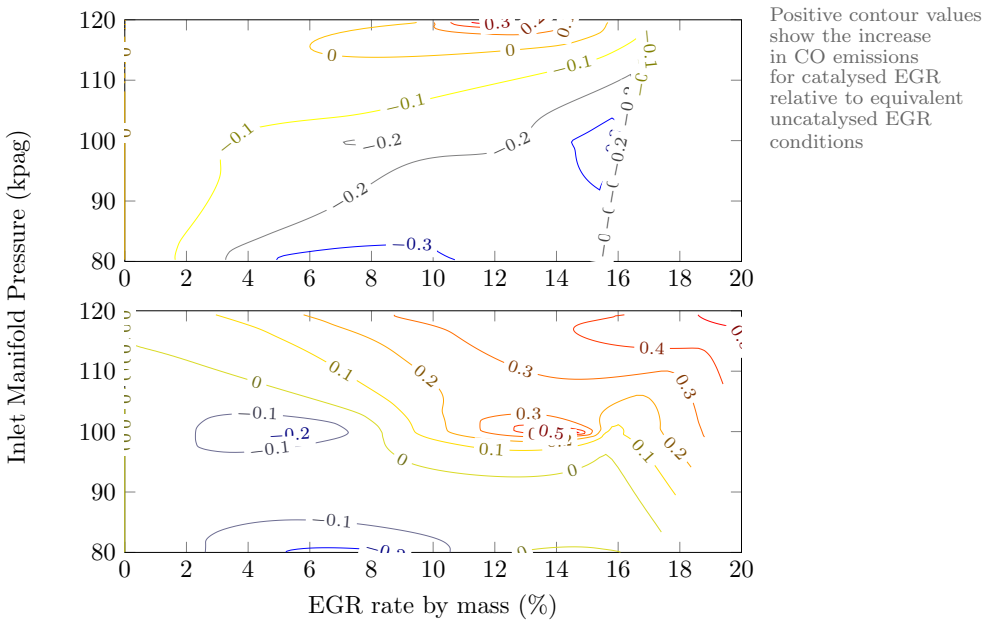

Figure 3-14: Contour plot showing the change in carbon monoxide emissions in % of total exhaust volume as a result of post-catalyst EGR compared to that seen for pre-catalyst EGR at 1500rpm and 3000rpm.

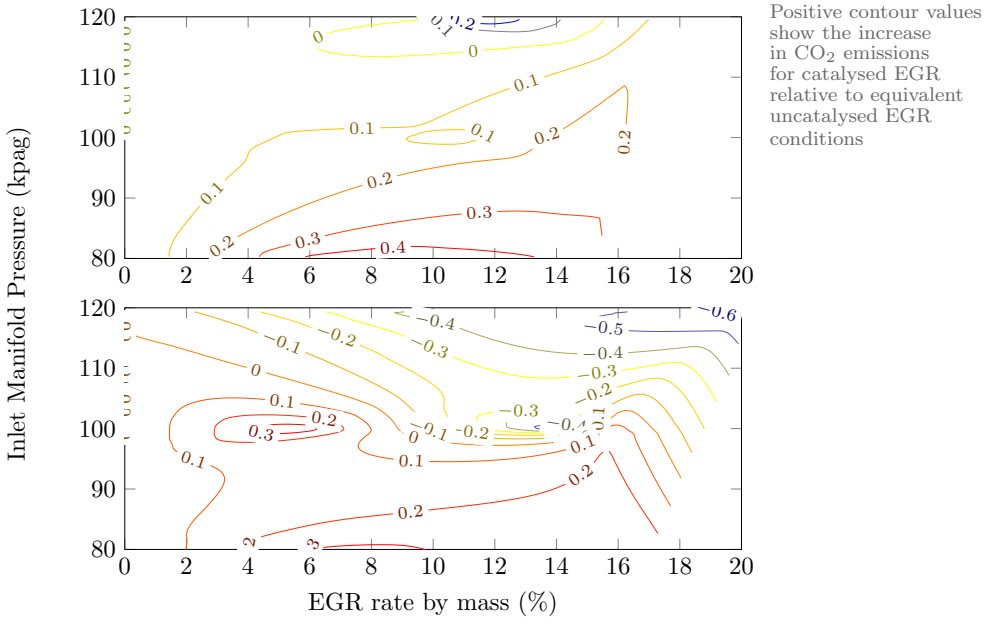

Figure 3-15: Contour plot showing the change in carbon dioxide emissions in % of total exhaust volume as a result of post-catalyst EGR compared to that seen for pre-catalyst EGR at 1500rpm and 3000rpm.

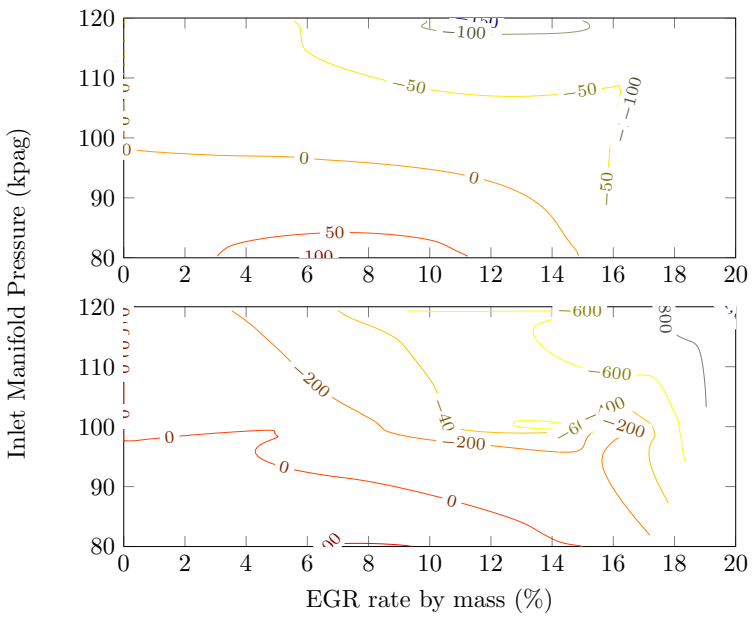

Figure 3-16: Contour plot showing the change in NOx emissions in ppm as a result of post-catalyst EGR compared to that seen for pre-catalyst EGR at 1500rpm and 3000rpm.

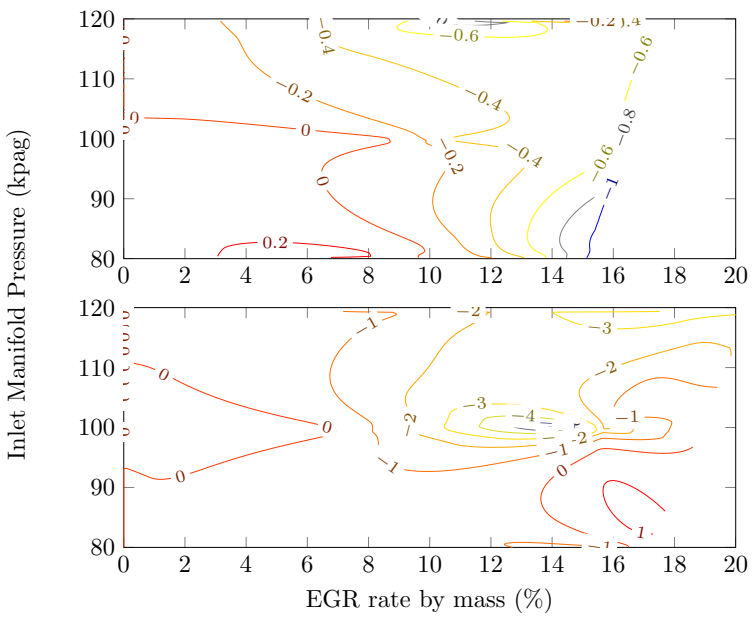

Figure 3-17: Contour plot showing the change in combustion duration as a result of post-catalyst EGR compared to that seen for pre-catalyst EGR at 1500rpm and 3000rpm. The shorter combustion durations seen for catalysed EGR will be due to the more advanced spark timing.

3.3.2 Estimations of in-cylinder lambda

The high levels of scavenging from the high valve overlaps and inlet to exhaust manifold pressure gradient would have resulted in some of the fresh charge blowing straight through the cylinder to the exhaust. The lambda meter in the exhaust did read stoichiometry but this was likely to be an average lambda value for the bulk exhaust flow. In reality it is expected that the exhaust flow contained "packets" of fresh charge which balanced out the rich burned gases.

The CO emissions provided an indicator that the in-cylinder conditions were rich – the CO emissions of 2-3% that were recorded for the entire dataset are significantly higher than expected quantities for stoichiometric combustion.

To investigate this a GT Power model of the engine was used to estimate the flow through the valves during each cycle and therefore the in-cylinder equivalence ratio. The model exists as part of the Ultraboost project, and features in publications such as [209, 213].

The model was adjusted to use a three pressure analysis using pressure data from the ports and in-cylinder transducers. From this the valve flows were estimated by 1-D calculations, the results showing that the trapped charge was only around 85% of the total charge.

Since this chapter is focusing mainly on the in-cylinder effects of the different EGR compositions, the fact that the in-cylinder lambda is quite significantly rich is not absolutely critical since it is consistent for all of the test points recorded.

3.3.3 Analysis of in-cylinder pressure oscillations

The recorded cylinder pressure traces give the richest information on combustion and phenomena associated with knocking combustion.

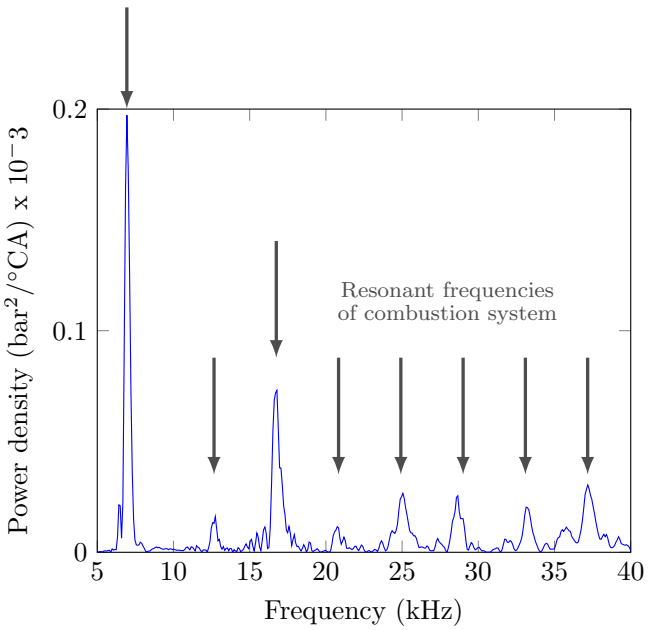

Figure 3-18: Illustration of a Power Spectral Density plot of a single cycle, showing the dominant frequencies for the main modes of oscillation. This example is from cylinder 2 at 0% EGR and 2.2 bar absolute manifold pressure at KLSA.

Oscillation Power

In addition to the oscillation amplitude (discussed in Section 3.2.2), the power of the pressure oscillations can also provide information on the knock intensity of a cycle. A power spectral density (PSD) plot is essentially a Fourier Transform of the windowed data, and gives an indication of the modes of oscillation present. Figure 3-18 gives an example of a PSD plot for a single cycle, illustrating the main modes of the oscillations by the peaks of the trace (corresponding to the modes shown in Table 3.4).

A spectrogram can be used to analyse the time during the cycle at which these oscillation modes are present, providing a form of "heat map" of oscillation frequency, power, and phasing during a cycle. Figure 3-19 illustrates how the stronger oscillation modes, denoted by the darker regions, are distributed. The higher frequency oscillations tend to decline in frequency as the piston moves down, due to the decline in temperature and increase in volume, and are the first to decay. The lower frequency oscillations extend further into the expansion stroke, showing more resilience to the reduction in pressure and temperature during the expansion stroke.

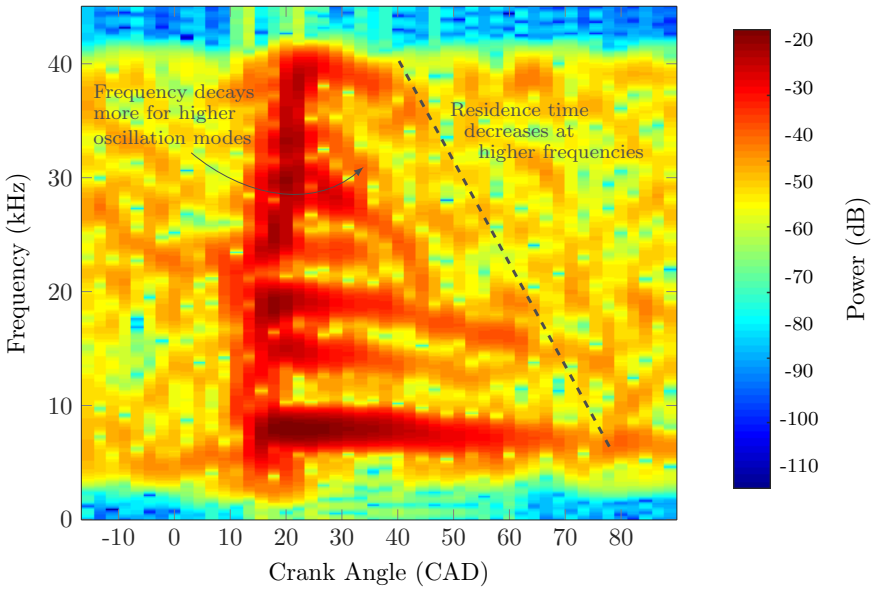

Figure 3-19: Heat map of the oscillation power during a cycle, with the higher frequency oscillations decaying more rapidly than the lower frequency ones, and showing a reduction in frequency during expansion. This example has been taken from cylinder 2 at 0% EGR and 2.2 bar absolute manifold pressure at KLSA.

The mechanism for this can be explained by considering the theoretical natural frequency from Draper's equation (Equation 3.2), which is directly proportional to the speed of sound. For an ideal gas the speed of sound is given by:

$$c = \sqrt{\frac{\gamma RT}{M}} \tag{3.3}$$

Where γ is the ratio of specific heats, R is the gas constant, M is the molecular mass of the gas and T is the temperature.

During the expansion stroke the in-cylinder mixture cools, which reduces the natural frequencies for all modes. For a given reduction in the speed of sound the change in natural frequency for higher resonant modes is larger than that for lower modes – thus explaining the decay at higher frequencies and explaining the longer residency time of the low frequency oscillations.

An unusual phenomenon was observed in some of the PSD plots for this engine, with

certain cycles exhibiting an exceptionally high peaks at 30-35kHz, as illustrated in Figure 3-20. This is contrary to what is most commonly observed, with the first mode of resonance being the dominant frequency for pressure oscillations in the cylinder. The majority of cycles observed during this experiment followed a more normal trend, with only some from each 300 cycle sample exhibiting these unexpected high frequency occurrences.

Possible aliasing of the natural frequency of the pressure transducers was ruled out by inspection of data from 6500 rpm tests[10]. The 30-35 kHz excitation was still present in this data, therefore ruling out resonance of the instrumentation as a possible source.

With a resolution of 0.1°CA the in-cylinder pressure data allowed analysis of frequencies up to 90 kHz for the 3000 rpm test points, and 45kHz for the 1500 rpm test points. The natural frequency of the pressure transducers is quoted at being ≈ 150 kHz – so aliasing of the transducers natural frequency could produce phantom ≈30kHz frequencies with the sampling rates used here.

This possible cause was ruled out by analysis of some data collected at 6500 rpm on the Ultraboost engine – which equates to a sampling frequency of 390 kHz and therefore high enough to avoid aliasing effects from a 150 kHz signal. At this operating condition the 30-35 kHz excitation was still present.

The following plots display data from cylinder 1, and show complete spark sweeps for each condition.

Figure 3-21 displays the variation in the fraction of knocking cycles exhibiting this high frequency excitation in each log. It is hard to discern any trends in the 1500 rpm data, but the 3000 rpm data in the lower plot does appear to show a slight reduction in high frequency events for higher EGR rates.

The quantity of high frequency events is also compared to the knock intensity in Figure

[10]This increased the sampling rate from 90 and 180 kHz (for the 1500 rpm and 3000 rpm tests respectively) to 390 kHz, which is sufficient to avoid aliasing of the 150 kHz natural frequency of the pressure transducers.

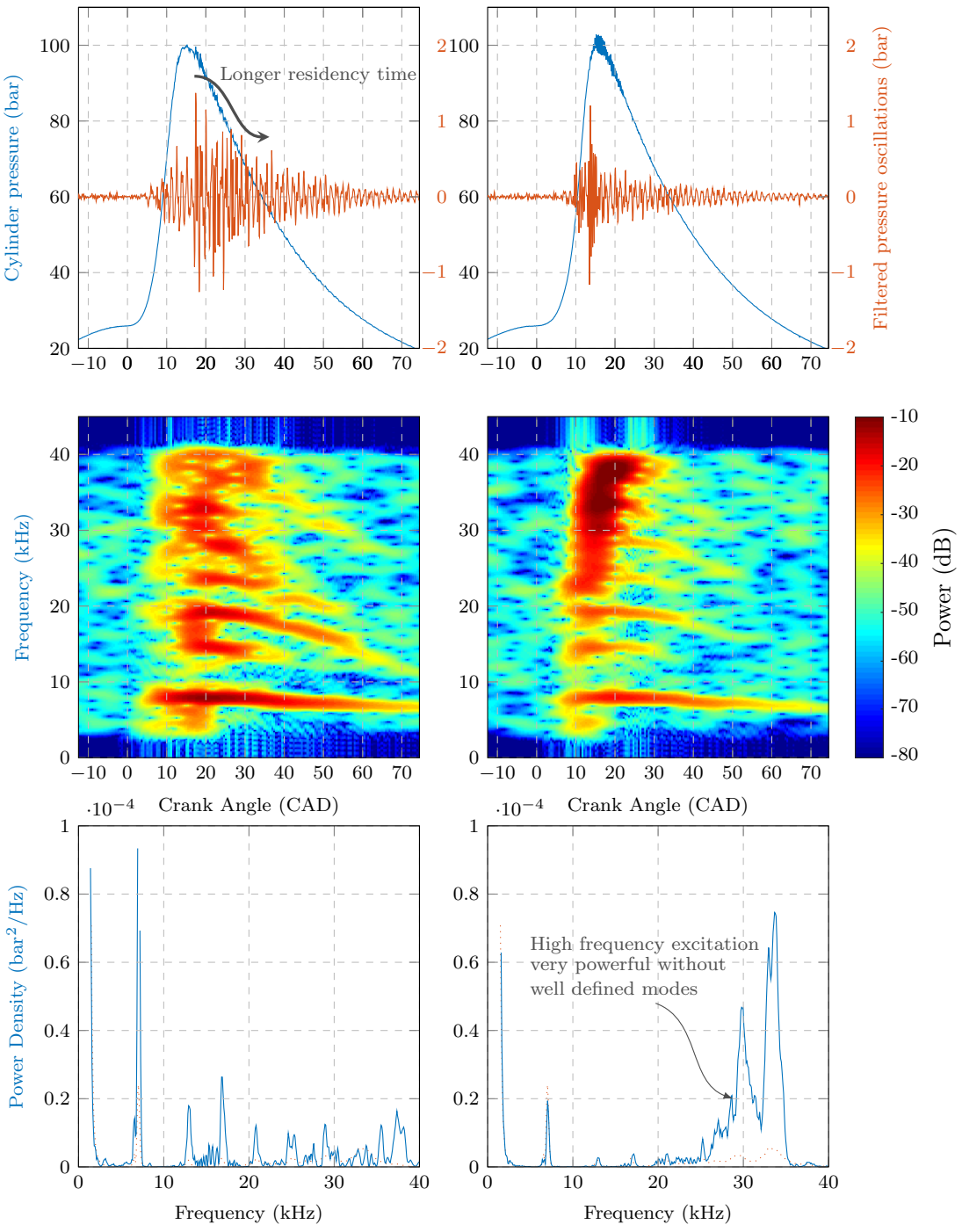

Figure 3-20: An illustration of the in-cylinder oscillations occurring during a cycle exhibiting high frequency excitation (right column), with the left column providing a comparison with a more common knocking cycle – both are from the same log at 0% EGR and KLSA.

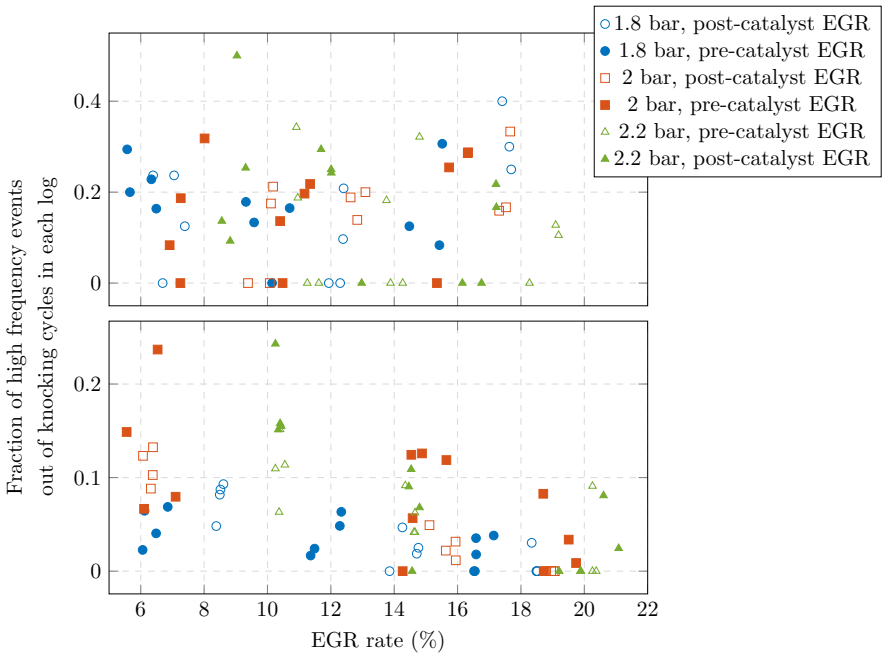

Figure 3-21: Scatter plot showing the fraction of knocking cycles exhibiting high frequency events for each log against EGR rate for 1500 rpm (top) and 3000 rpm (bottom). The fraction of high frequency events does appear to reduce slightly at high EGR rates, especially at 3000 rpm.

3-22 to assess whether this could be impacting the results from Figure 3-21. The knock intensity clearly has an influence on the number of high frequency events in a log, especially at the higher speed of 3000 rpm where the knock limit is higher. This relationship could be due to either the way that autoignition occurs at more knock-prone conditions, or it could be due to a resonance that is more easily triggered by these more powerful autoignition events.

The knock intensity during each log is directly affected by the ignition timing and Figure 3-23 illustrates how the knock intensity is not as high for the higher speed, high EGR conditions. This is most likely due to the test procedure rather than any physical effect of the EGR.

Whilst these high frequency events are an unusual phenomenon they do not appear to be dependent upon EGR rates. The correlation that seems to be evident between high knock amplitudes and the number of events suggests that this is the main contributor. To the knowledge of this author there is no other mention of this phenomenon in the

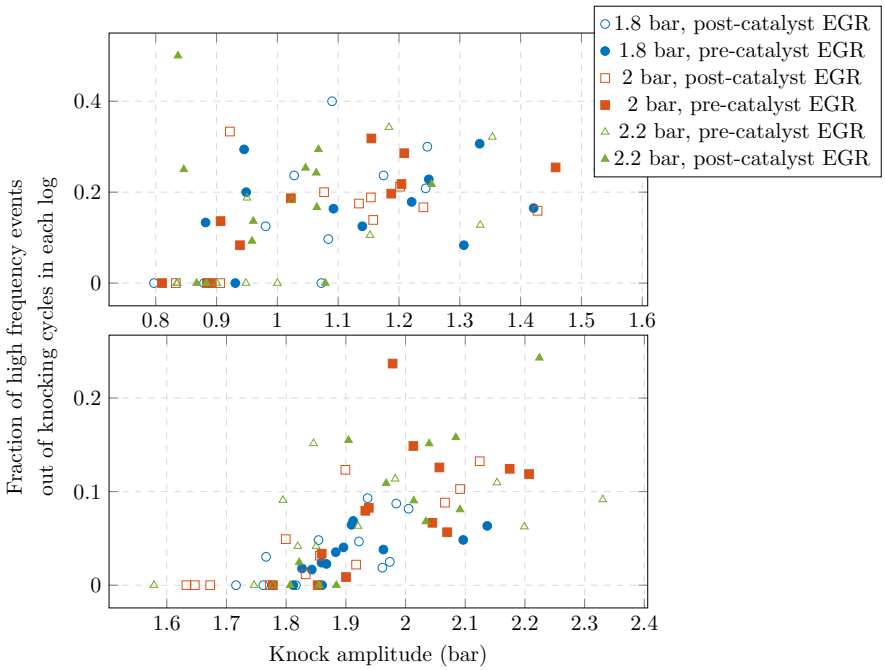

Figure 3-22: Scatter plot showing the fraction of high frequency events for each log against EGR rate for 1500 rpm (top) and 3000 rpm (bottom). The increase in high frequency events is apparent for conditions exhibiting higher knock intensities.

literature, so it may be a characteristic unique to this engine – potentially brought about by resonances in the pressure transducer tappings and locations.

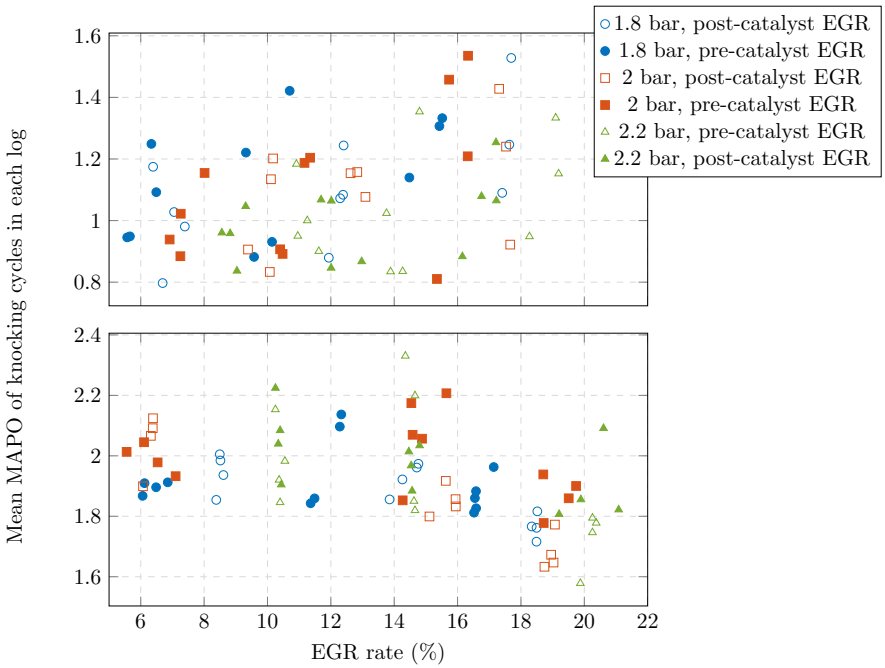

Figure 3-23: Scatter plot comparing the knock amplitude against the EGR rate The knock amplitude is directly a result of the ignition angle at each test point, so the drop in knock intensity at high EGR rates at 3000 rpm is most likely due to the test procedure.

3.4 Conclusions

The main aim of this testing was to assess the effects of EGR catalysis on high load combustion. Whilst this aim was not fully achieved due to disparities in the test conditions between the two EGR compositions, some conclusions have been drawn from the analysis of the data.

The following points summarise the findings from this analysis:

- This experiment was performed with constant manifold pressures, providing a consistent initial pressure and exhaust back pressure for each operating condition. Whilst this provides a consistent basis to observe the effects on changes in spark advance for a given condition, it does also mean that the engine load must decrease with a rise in EGR rate due to the displacement of the fresh air in the inlet charge.

  Both the post-catalyst EGR and pre-catalyst EGR tests were targeted at mimicking the same quantity of fresh air being displaced in order to allow comparison of

their effects. The pre-catalyst EGR gas did however contain some oxygen, resulting from the high valve overlap and large manifold pressure gradient employed on the engine for scavenging. This increased the oxygen availability to the engine when using pre-catalyst EGR compared to the post-catalyst EGR conditions, therefore increasing the fuel rate slightly to maintain lambda 1 at the exhaust.

The effects of this imbalance between the pre and post catalyst EGR tests outweighed most of the more subtle effects on engine performance that would've been expected by the reduction in NOx, CO, and HCs.

- Despite the lambda meters reading 1 at the exhaust, the in-cylinder lambda is estimated to be closer to $\lambda = 0.85$ (using 1-D simulation of the airflow through the inlet and exhaust valves) due to the large amount of blow-through. The exhaust lambda meter was effectively reading an average lambda value of 1, with the fresh air blown through during valve overlap offsetting the rich exhaust gases being expelled. The effect of these very rich in-cylinder conditions can be observed in the high THC and CO emissions and the relatively low NOx emissions. This means that the composition change due to catalysis of the EGR gases is slightly different to that expected for stoichiometric in-cylinder conditions, but is not expected to impact the trends significantly.

- Due to its size and location, the flow through the catalyst was below its design specification and inconsistent. This resulted in poor NOx light-off and therefore inconsistent NOx conversion for the post-cat EGR gases. Whilst this was not optimal for the comparison of pre and post-catalyst EGR operation, it did inadvertently provide some evidence that decreasing the NOx content of the EGR could extend knock limits. HC and CO emissions trends mirrored those seen with the improved knock limits, but were opposite to those expected for more advanced combustion. This could be further evidence that NO could impact the mixture preparation of the end gas, not only making it more liable to autoignite but also improving its combustible behaviour when it is consumed by the flame.

The results indicate that accurate predictions of EGR effects on engine combustion should also account for NOx content of exhaust gases where possible.

This experiment gives some insight into pre versus post-catalyst effects on combustion, especially with the inadvertent confirmation of NO effects in the context of real EGR operation that was brought about by poor catalyst light-off. The comparison is hindered by the high engine-out exhaust oxygen content though, which limits the conclusions that can be made about the overall effects of EGR composition.

The outcomes of this experiment highlight where the test process could be improved to give a better comparison between the two EGR compositions and these lessons are applied to the design of the experimental test procedures detailed in Chapter 4.

CHAPTER 4

CATALYSED EGR COMPARISON ON A HIGH BMEP PRODUCTION GASOLINE ENGINE

This chapter expands on the experimental work from Chapter 3 by conducting further comparisons between pre-and post-catalyst EGR on a high load engine. The engine in question was a production 1 litre Ford Fox Engine, with an artificial boost rig and EGR rig to remove the variables associated with turbocharger performance. Details of the engine and test facilities are given in the first section of this chapter.

The lessons from the previous chapter were used to refine the testing methods for this experiment – detailed in section 2 – which allowed the effect of EGR catalysis to be isolated more effectively.

Section 3 discusses the results of this testing, both in terms of the knock characteristics observed and also the engine performance at KLSA.

Improvements in knock limit were observed, but their benefit to outright performance is arguable. For a given spark timing the effect of EGR catalysis was observed to have some effect on the angle of knock onset, but also had a much larger effect on knock intensity even for cycles with equivalent knock onset times.

These results prompted a modelling based investigation into the dilution effects on GDI combustion, and the related NO interactions, which is detailed in Chapter 5.

As mentioned earlier in this thesis, the primary factor in EGR performance is the architecture employed. This study negated that effect to isolate the combustion system, showing that the combustion effects of EGR composition – apparent in the extended knock limit and advanced combustion phasing – could be significant in assessing the value of an overall system.

4.1 Introduction, aims of testing and experimental hardware

This chapter details the testing process on a 1 litre GDI 3 cylinder engine, with a comparison being made between pre and post-catalyst operation. The target of this testing is to quantify the potential benefit to high load combustion that can be achieved with catalysed EGR in comparison to uncatalysed EGR. The procedure will be similar to that detailed in Chapter 3 but with modifications to the process to overcome some of the hurdles previously encountered in making a fair comparison between the two EGR configurations.

The confirmation on the impact of NOx on combustion that was found in Chapter 3 has led this stage of testing to be more focused on precise inlet compositions. Previous issues of oxygen content mismatching (between the two EGR compositions), and poor catalyst NOx conversion have been addressed to allow a more consistent comparison between the two architectures.

4.1.1 The Fox engine

The investigations in this chapter were performed on a production Ford Fox XM engine. The engine is a proven production line engine, with much more mature ECU calibrations than the Ultraboost engine detailed in Chapter 3. For this testing the inlet and exhaust valve phasing was kept constant to maximise the consistency of combustion conditions for each test point. Further details of the engine are given in Table 4.1.

Table 4.1: Table of engine details

Engine Type	In-line 3 cylinder, 4 valves per cylinder
Capacity(cc)	999
Bore/Stroke (mm)	71.9/82
Compression ratio	10.5:1
Firing Order	1-2-3
Valve train	Dual continuously variable camshaft phasers
Specific power(kW/l)	92 @ 6000 rpm
Specific torque(Nm/l)	170 @ 1400-4500 rpm
Other	External cooled EGR Water cooled exhaust manifold

4.1.2 Test cell facilities

The test cell was equipped with a forced induction simulator which functioned in an almost identical way to that detailed in Chapter 3.

A 7 bar supply of dry compressed air was filtered and regulated down to 3.5 bar. A heater on closed loop control regulated the temperature of the air, with the feedback coming from a thermocouple installed in the engine manifold. The air supply to the engine was throttled to maintain the required manifold pressure and excess air was released through a dump valve.

The mass airflow was measured by two Sierra 'FastFlo' thermal gas flow meters, one measuring total flow into the rig and the other measuring the flow to the engine. The dump flow was calculated by the difference of these two values. During the test programme it was observed that the engine airflow values were not consistent across equivalent operating points. The culprit for this was identified as the accuracy of the flow meters measuring the mass of air expelled from the rig[1]. Since the available time and funding for this project did not allow for replacement of these flow meters, the engine airflow was instead calculated by the fuel flow and combustion stoichiometry during post-processing.

[1]The specifications of the flow meters revealed a quoted accuracy of ±1% of full scale with a repeatability of ±0.2% of full scale. Since they were calibrated to operate to a range of 1400 kg/hr this meant the potential error was as much as ± 14 kg/hr, with a variation of ±2.8 kg/hr from true values.

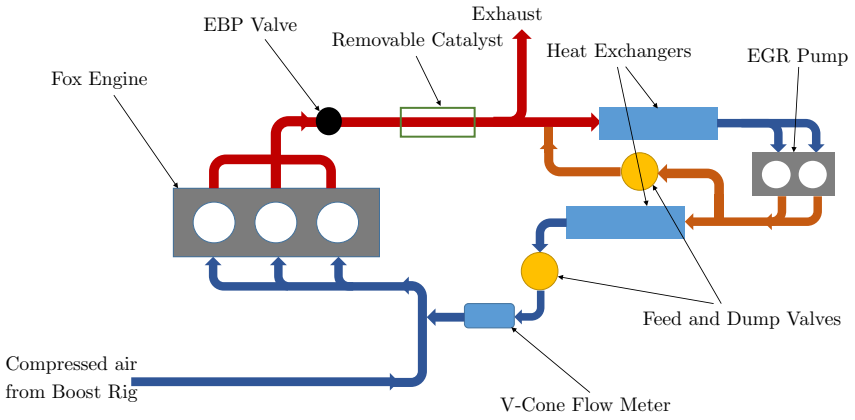

Figure 4-1: Schematic of the engine and EGR rig setup

Table 4.2: Table of test cell facilities

Dynamometer	300 kW AC dynamometer
Speed measurement	1024 pulse/rev encoder
Torque measurement	1 kNm torque measurement flange
Combustion analysis	AVL X-ion 6 channel system Kistler 3600 pulse/rev optical encoder Kistler 6054A in-cylinder transducers Kistler 4049A water-cooled exhaust pressure transducer Kistler transducer cooling module and amplifiers
Fuel flow measurement	CP Engineering FMS-1000 1 litre gravimetric fuel meter
Emissions	2 off MEXA 7100 DEGR exhaust gas analysers for simultaneous pre and post-catalyst sampling
AFR	UEGO lambda sensor
Other measurements	Up to 32 K-type thermocouples, 16 PRTs and 16 pressure channels, coolant flow rate (Krone magnetic flow meter)

4.1.3 The EGR rig

An updated EGR rig was used for this testing, essentially working on the same principle as that detailed in Chapter 3 but with several modifications. A Tata Nano 600cc engine was used as a positive displacement pump to drive the EGR flow, motored by an 11kW three phase induction motor. Two ball valves controlled a recirculation loop in the rig, allowing more precise control of the pump outlet pressure and delivery rate of EGR gases to the inlet. The layout of the rig is included in Figure 4-1[2].

A heat exchanger was positioned before the EGR pump to cool the incoming exhaust gases, with a secondary heat exchanger positioned in the feed line from the EGR pump. The pump engine and the secondary heat exchanger were connected to the coolant supply of the test engine in an attempt to regulate both the pump oil temperature and the feed EGR gas temperature.

Following the issues with catalyst light-off seen during the test process for Chapter 3, the catalyst was positioned closer to the engine and before the sampling point for the EGR rig. A blank pipe section replaced the catalyst for the pre-catalyst EGR test points.

An attempt was made to use a V-Cone differential pressure mass flow meter to give an accurate indication of the EGR supply rate to the engine. Ultimately this method proved ineffective, due to the pulsating nature of the supplied gas skewing the pressure differential observed across the V-Cone meter. Instead the ratio of the CO_2 concentrations between the feed gas and the inlet manifold were used to calculate the EGR rate.

4.1.4 Synthetic EGR rig

A simple rig to inject CO_2 and N_2 blends to the engine inlet as diluents was installed in the test cell to allow some data collection on synthetic EGR effects. The rig comprised

[2]The rig performance was characterised across its operating range to allow functionality with transient test cycles, although for this investigation only steady state test points were used.

of two M+W Mass Stream flow controllers, which allowed independent control of the CO_2 and N_2 gas supplies. The total equivalent EGR rates with this equipment were limited to 9% at the engine speed tested. This was imposed by a CO_2 flow limit to avoid freezing of the regulator.

The ratio of synthetic diluent gases

Without having data for the exact heat capacities of the exhaust gases from the engine, a simplified equation for combustion was used to estimate the typical ratios of the main constituents of EGR [214]:

$$\begin{aligned} C_xH_yO_z + \lambda(x + y/4 + z/2)\left\{O_2 + \frac{79.05}{20.95}N_2\right\} \\ \rightarrow aCO_2 + bCO + cH_2O + dH_2 + eO_2 + fN_2 \end{aligned} \tag{4.1}$$

where x, y and z are derived from the average molecular formula for the fuel[3], and λ=1 for stoichiometric combustion.

If the assumption of complete combustion is made for stoichiometric conditions then this equation can be simplified by assuming that there are no carbon monoxide, oxygen, or hydrogen products in the exhaust gas [214]. This provides a greatly simplified formula of:

$$\begin{aligned} C_xH_yO_z + (x + y/4 + z/2)\left\{O_2 + \frac{79.05}{20.95}N_2\right\} \\ \rightarrow xCO_2 + y/2H_2O + (x + y/4 + z/2)\left(\frac{79.05}{20.95}\right)N_2 \end{aligned} \tag{4.2}$$

This provided an estimated exhaust composition of: 13.5% CO_2, 73.8% N_2, and 12.7% H_2O[4].

The synthetic EGR rig was only capable of providing dry gas mixtures, so the ratio of CO_2 to N_2 was the only factor in determining the heat capacity of the synthetic mixture.[5]

[3] A detailed fuel analysis provided the C/O and C/H ratios for the experimental fuel

[4] It is appreciated that minor species are also present in real exhaust gas, but their impact on the heat capacity of the mixture was considered to be negligible due to their very low concentrations.

[5] A water injection element was designed and installed on the synthetic EGR rig, but unfortunately

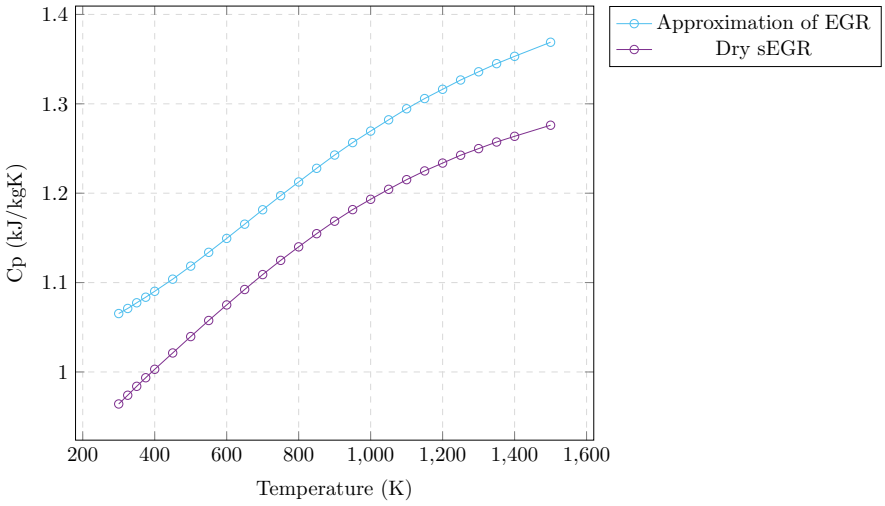

Figure 4-2: Cp values for the sEGR mixture compared to that estimated for real EGR in equation 4.1 for temperatures ranging from 300 to 1500K

The quantities of CO_2 and N_2 were determined by minimising the difference between the estimated EGR heat capacity and those of synthetic EGR compositions through a range of CO_2:N_2 ratios and over a range of temperatures to enclose those expected in the unburned gas mixture.

From this a CO2:N2 ratio of 29:71 was selected, which is plotted against the simple EGR model in Figure 4-2. The heat capacity of the dry mixture is lower than that estimated for EGR by a constant amount (around 0.1kJ/kgK) for the entire temperature range that is shown. This cannot be overcome by CO_2/N_2 mixtures alone due to the much higher heat capacity of water vapour.

4.2 Testing Procedure

A warm-up procedure was followed for both the engine and the EGR pump to allow the oil and coolant to reach stable values[6] before starting the test procedure. Repeatability points were taken at the start and end of each test session to confirm the repeatability of the testing process.

its use was curtailed by a poorly timed malfunction.

[6]The target temperatures for the oil and coolant were 90°C and 85°C respectively, which were maintained via PID controlled heat exchangers once they had been reached.

Table 4.3: Table of test points performed on Fox engine

EGR composition	EGR Rate (%)
N/A	0
Pre-catalyst	2.7-16.2%
Post-catalyst	2.7-16.2%
Synthetic	2.7-16.2%

For the test points the engine was boosted to 1.7 bar (absolute) at the inlet manifold, chosen to allow a large enough spark sweep window at zero EGR conditions to perform a comprehensive KLSA analysis during post-processing. The EGR rate was swept from 0-16% at 2.7% increments[7], with a spark sweep at each EGR rate. The limit on spark retardation was dictated by the exhaust temperature limit of 900 °C (or the CoV of IMEP reaching 3% for less temperature limited test points).

Thresholds for the knock peak limit were advised in a dyno debug document provided by Ford, which were incorporated into a knock histogram on AVL Indicom to guide the test process. The histogram limits comprise of two parameters – the lower threshold and the higher threshold. The higher threshold corresponds to a limit for any single cycle to reach, whilst the lower threshold corresponds to the limit for 10% of the previous 30 cycles. For this test the upper threshold was set to 3.25 bar and the lower threshold to 2 bar for the test speed of 2200 rpm[8].

The cam phasing was adjusted to provide the maximum allowable overlap without the oxygen content exceeding that measured for no overlap[9], in an effort to maximise scavenging without excessive blow-through. The cams were then fixed at these positions for the duration of the experiment. Fuel pressure was fixed at 2500 psi ($\approx$ 172 bar), injection timing was fixed at 300°CA, lambda 1 operation was maintained for the experiment and the intake temperature was fixed at 30°C via a PID control on a heater and bypass in the boost rig. The exhaust pressure was fixed at 1.5 bar by way of a cable controlled

[7] 3% increments were targeted, but this was skewed by an internal setting in the MEXA unit.

[8] The knock peak was defined by the amplitude of the absolute oscillation power as demonstrated in Figure 3-5b

[9] In practice the minimum oxygen content at this speed and load was 0.3%

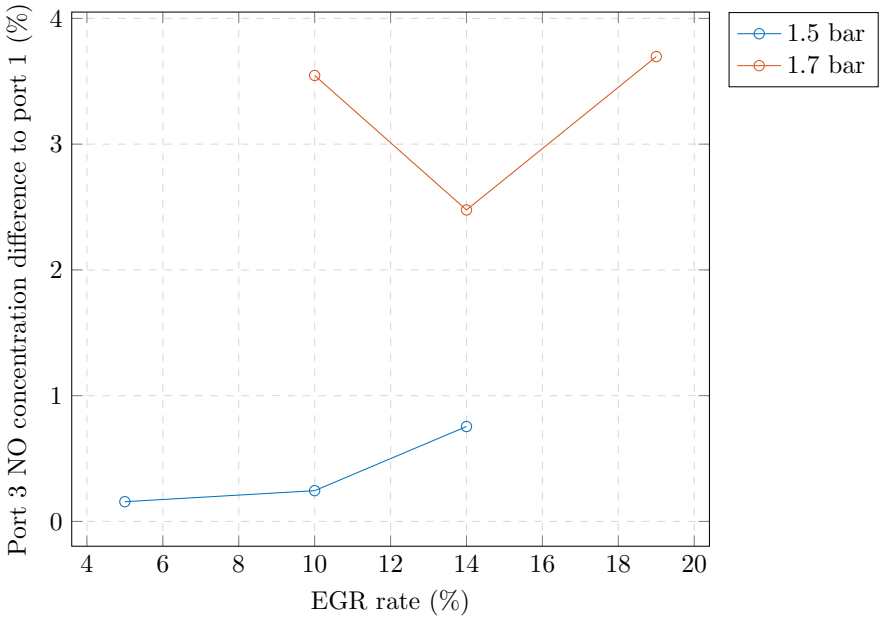

Figure 4-3: Comparison between NO concentrations at port 3 and port 1 for the engine operating with 1.5 and 1.7 bar at the inlet manifold. Positive percentage denotes higher concentration at port 3

back pressure valve[10].

4.2.1 Mixing of the diluents

The EGR mixer was designed according to evidence in the literature on the effectiveness of nozzle design concepts for gas mixing (discussed in more detail in Section 3.1.2). Once installed, verification of the EGR distribution between the cylinders was sought. A MEXA 1400FR fast analyser was connected to each of port 1 and port 3 sequentially to measure the concentration of NO in the inlet charge. Measurements taken at 0% EGR confirmed that no burned gas was being detected at the inlet side.

For inlet manifold pressures of 1.5 bar and 1.7 bar, EGR rates of 5, 9 and 13%, and 9, 14 and 19% were compared respectively with the NO concentration at the ports being measured. The average port NO reading over a 15 second period was then normalised by dividing by the MEXA engine out NOx measurement and EGR rate to allow for small variations in emissions and EGR rate between comparable test points.

[10]This value was selected to provide enough pressure gradient to assist scavenging whilst also enabling the blow-through of fresh air to be minimised by alteration of the cam phasing.

The results in Figure 4-3 show a fairly good match between port NO concentrations for the 1.5 bar boost condition, with only a deviation of up to 0.75% higher concentrations at port 3. However at the higher manifold pressure the concentration is more biased towards port 3, with the NO concentration between 2.5% and 3.7% higher. This means that for an EGR rate of 10% at cylinder 3, cylinder 1 potentially would see an average EGR rate of 9.65%.

4.3 Results of experimental work

The results presented in this section address both global outputs such as fuel consumption and torque, and in-cylinder pressure analyses to draw conclusions on the combustion behaviour.

A short note on the repeatability of the data collected is followed by an in-depth look at the knock behaviour of the engine, after which the engine output results are addressed.

4.3.1 Repeatability of data

Observations during the test process revealed some deviations in the PID controllers operating the boost rig temperature and pressure controls. Fluctuations of up to ± 1°C were observed in the temperature control with a period of around 30 seconds, and fluctuations of up to 1 kPa were observed in the manifold pressure with a shorter period of only a second or so.

Due to the large number of inputs being being used to control the engine, and amongst the many instrumentation channels that were recording data, it is expected that there would be a certain amount of deviation across all of the data that was collected. This raises a question over the level of uncertainty in the results obtained.

Errors and uncertainties in measurements can be categorised into either systematic or random uncertainties. Systematic uncertainty describes the shift that a certain measure-

ment exhibits from its true value, and as such it is not possible to quantify the systematic uncertainty from a dataset without additional external information[11]. Random uncertainty can be derived from the spread of data points that are collected during repeated measurements of the same value – more repeats will give more accurate information on the level of random error that a given measurement will have [215].

Efforts were made during the test process for this project to minimise the level of random error in the measurements. These involved the calibration of the emissions equipment before each session, and the repeats of daily test points before each session to compare results against those previously collected and therefore highlight any issues that may be present before collection of the data. No attempt has been made to quantify the systematic error in this dataset, but it is hoped that the re-calibration of equipment for each test, where feasible, and the manual check of the test cell facilities before firing up is sufficient to minimise the systematic error.

The data from these daily test points provided an opportunity to analyse the variation in the test data from day to day. Since this data was collected on the same engine, at similar operating points and with the same instrumentation it was assumed to be a valid representation of the spread that would be expected for all of the test points, and therefore was used to calculate error bars for the entire dataset where appropriate.

A Gaussian distribution was assumed for the random error, and the sample standard deviation was calculated for each channel of the repeated test points. From this a 95% confidence interval was calculated for each channel. This method gives a fairly crude estimation for the expected error, which by no means qualifies as a statistical analysis but at least serves to give an indication of the variation present in each channel.

4.3.2 The onset of knock and resultant oscillation behaviour

The process to analyse pressure oscillations in the cylinder which was outlined in Section 3.2.2 was repeated for this dataset to analyse the autoignition behaviour of the

[11]Calibration certification for certain pieces of analysis equipment can provide information on the tolerance window for systematic errors for certain measurements.

Figure 4-4: Image of damage around the edge of piston 1. The missing material will have had an effect on both the breathing characteristics and possibly the compression ratio of cylinder 1.

engine.

One characteristic that was quite apparent was the lower pressures exhibited by cylinder 1 at TDC (illustrated in Figure 4-5). This was observed during the testing of the engine and is reflected across all of the data points collected. A pressure test on the transducer for cylinder one revealed no deviations in accuracy, so it was assumed that this phenomenon was genuine.

Inspection of the engine after completion of the test programme revealed damage to the top edge of piston 1 near the inlet ports (illustrated in Figure 4-4), which could have impacted the data in the manner observed.

Considering the damage to the piston two potential reasons were identified for this low pressure:

1. If the damage was sufficient to increase the cylinder volume, the compression ratio for cylinder 1 would be reduced, thereby reducing the pressure at TDC.

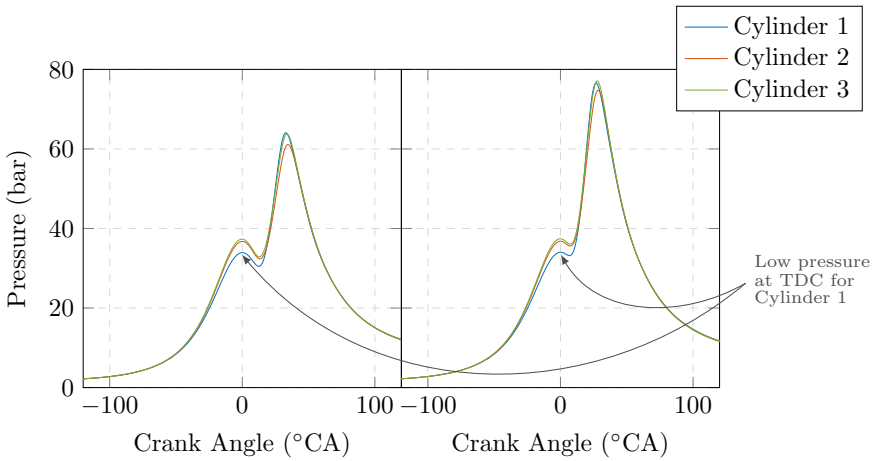

Figure 4-5: Comparison of the mean pressure traces for the three cylinders for spark angles of -5 and -1.5 degrees respectively. It can be observed for both advanced and retarded spark angles that cylinder 1 exhibits a lower pressure at TDC. These plots show the mean cylinder pressure for a full 300 cycle log.

2. Mixing of the fresh charge with a larger mass of warm residual gas would increase its temperature further, therefore resulting in a lower trapped mass in the cylinder volume.

The rate of combustion in cylinder 1, once initiated, is higher than the other two cylinders, allowing peak pressures to reach similar values to those seen in the other cylinders. This could be due to either or both of the above theories. Both a reduction in compression ratio and an increase in residuals would reduce the propensity for knock in that cylinder. A larger RGF would also increase the initial temperature of the cylinder charge, enabling a faster initial flame propagation and causing more heat release at earlier crank angles[12].

Modes of knock initiation

PSD traces for each test log were analysed to check for any results similar to the high frequency anomalies seen in the data from Chapter 3. The data provided a clear picture of the generation of oscillations at the different harmonic modes of the cylinder. High frequency excitation was present in some cycles, but at well defined frequencies and not so powerful that they dwarfed the lower frequency oscillations in such an extreme way

[12]The two opposing effects of increased dilution and increased temperature would be present here.

as those observed in Chapter 3.

The initiation of knocking conditions could be categorised into three groups by observation of the development of the oscillations during the cycle. These three categories are detailed below, and illustrated in Figure 4-6 (annotations refer to those in Figure 4-6).

Mode A: low frequency early initiation gradually builds into knocking amplitude, with no obvious transition point (annotation c). The other harmonic modes show very low levels of excitation (annotation b). It is likely that the autoignition process is less explosive in these cycles, which could indicate that it is occurring closer to the flame front, or that AI centres are more spaced out. The knock intensity for this mode is generally lower than that for the other modes of knock oscillation, and the most apparent indication for knock onset is revealed by inspection of the apparent heat release plot (annotation a). Shahlari et al's [216] SER method (described in Equation 4.3 on 150) does not predict knock onset angles accurately for this mode of knocking combustion, but instead identifies the very start of the low intensity oscillations.

Mode B: low frequency early initiation followed by sudden increase to knocking amplitude at either the same frequency or at different harmonic modes. The lower intensity oscillations usually begin at a similar point in the cycle as those described for mode A, but a significant transition point can be observed later in the cycle which indicates more violent autoignition in the end gas (annotation e). This transition point can consist of an increase in the power of the first harmonic mode, or the initiation of oscillations at another harmonic mode. It could be proposed that the lower intensity oscillations could be initiating the end gas ignition where propagating wave fronts meet reflected wave fronts to create areas of higher energy. The heat release rate exhibits a plateau during its fall at the corresponding crank angle to the onset of the high amplitude oscillations, where the autoignition event is most violent (annotation d).

Mode C: initiation at either one or (more commonly) multiple modes near P_{max}. These cycles exhibit a very abrupt onset of the pressure oscillations (annotation h) and usually consist of more than one harmonic mode ringing with considerable power. These are likely to be the result of hotspots or mixture inhomogeneities in the end gas triggering multiple AI centres as the temperature rises. In the example given by Figure 4-6 for this mode, the different harmonic modes are triggered simultaneously (annotation f) and the heat release accelerates at this point (annotation g) – which occurs very close to what would be the peak heat release rate, so extends this peak further.

Modes of autoignition relating to knock were investigated by Bradley et al [134] in a simulation context. They devised a dimensionless parameter, ξ, which related the ratio between the autoignition flame front speed and the local speed of sound to describe the mode of detonation as a result of autoignition. Unfortunately this dataset does not provide the opportunity to investigate the relationship between this parameter and the knock initiation modes described above, since more detailed information on the autoignition kernel growth would be required – details of which are only available experimentally from flame imaging methods.

Figure 4-7 shows a summary of the distribution of each initiation mode for all of the logs that were recorded exhibiting knock above an amplitude of 0.6 bar. It is clear that a large majority of the knocking cycles gravitate towards mode B – around 70% for all conditions except for one outlier. Conversely, mode A was the most rare, amounting to less than 10% of the knocking cycles for all conditions. From previous observation of the data it is suspected that this mode is very common in cycles exhibiting sub-knocking levels of oscillations.

There appears to be no correlation between the EGR composition and the distribution of knock initiation modes. It could be argued that Mode B sees a marginal increase, and Mode C decreases slightly with increasing EGR rates – but this correlation is not strong enough to be considered significant.

A further comparison between the knock initiation modes and the knock intensity is shown in Figure 4-8, which demonstrates the similarity between the results for both EGR compositions, confirming that the chemical change of the cylinder charge does not affect the initiation mode of the knocking oscillations. Further to this, it is apparent that cycles exhibiting heavier knock follow either Mode B or Mode C behaviour, which is unsurprising considering the gradual increase in oscillation power associated with Mode A.

Since the EGR composition does not appear to impact the initiation mode in this test,

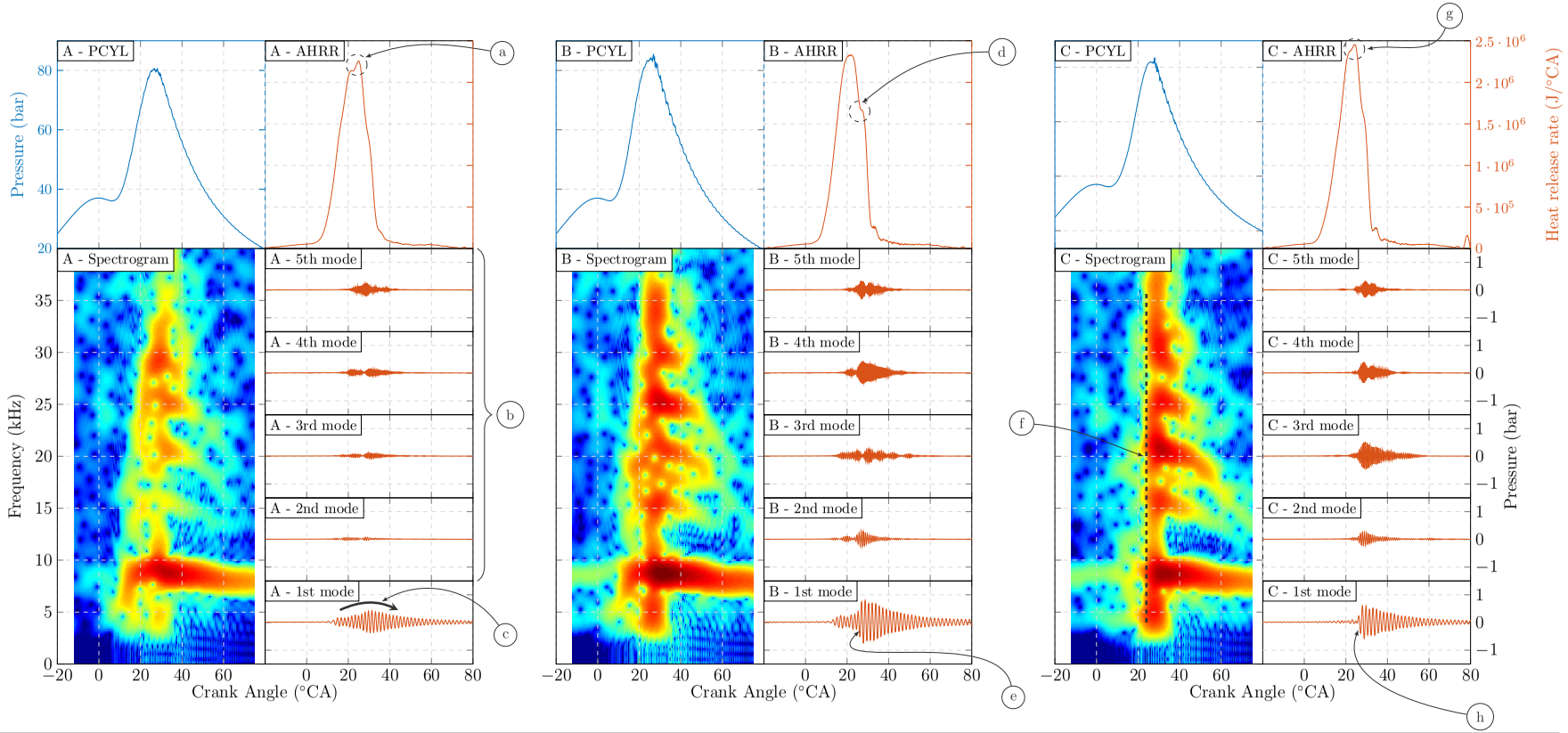

a	The most prominent sign of the knocking combustion for mode A is revealed in the heat release plot.	**e**	The amplitude of the first harmonic mode oscillations show a definitive transition point corresponding to the change in heat release rate gradient.
b	The amplitudes of oscillations at higher harmonic modes are very small.	**f**	The onset of the oscillations is almost simultaneous for all of the harmonic modes.
c	The amplitude of the first harmonic mode oscillations show a relatively smooth onset and decay, making it difficult to discern a definitive knock onset point from the filtered trace.	**g**	Due to the knock onset timing the extra heat release occurs near the heat release rate peak, effectively extending this peak higher.
d	The knock-causing autoignition event causes a change in the heat release gradient.	**h**	The oscillations have a very abrupt start from a very low level of excitation, contrary to the initiation of onset modes A and B.

Figure 4-6: Illustration of the three main modes observed in the onset of knocking oscillations. The plots shown are taken from a 0% EGR case with spark timing just beyond KLSA. The modes identified are: A - gradual onset of oscillations; B - gradual onset followed by sudden increase in oscillation power; C - sudden onset at multiple harmonic modes. These three modes could be divided further, but no additional insight was gained from doing so.

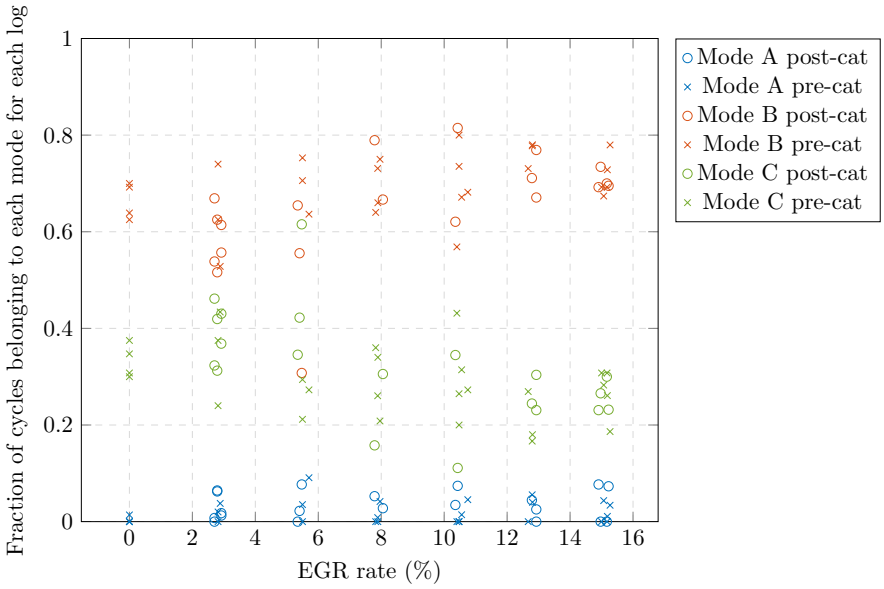

Figure 4-7: The distribution of the different initiation modes introduced in Figure 4-6 for all knocking cycles recorded during the test. The effect of EGR appears to be very marginal on this distribution.

it is not expected that the knock initiation mode is affected by kinetic interactions in the end gas. The slight affect with increasing EGR rate may be a result of the distribution of hotspots and the intensity of turbulent mixing as result of the increased dilution.

In a CFD-based study into knocking combustion Galloni et al mention that the frequency modes detected by a virtual sensor were dependent upon the location of the autoignition centre in relation to the position of the pressure sensor [139]. Although only done in the virtual realm, their findings suggest that the different knock onset modes observed in the current study could also relate to the location of the autoigniting centre.

An investigation into oil droplet formation and turbulent mixing effects may shed more light on the mechanisms behind this phenomenon, but that does not fall within the scope of this thesis.

The following points summarise the trends observed in the spectrograms for this dataset:

- the first harmonic frequency is usually the most powerful, but is also usually accompanied by the other modes for high knock intensities.

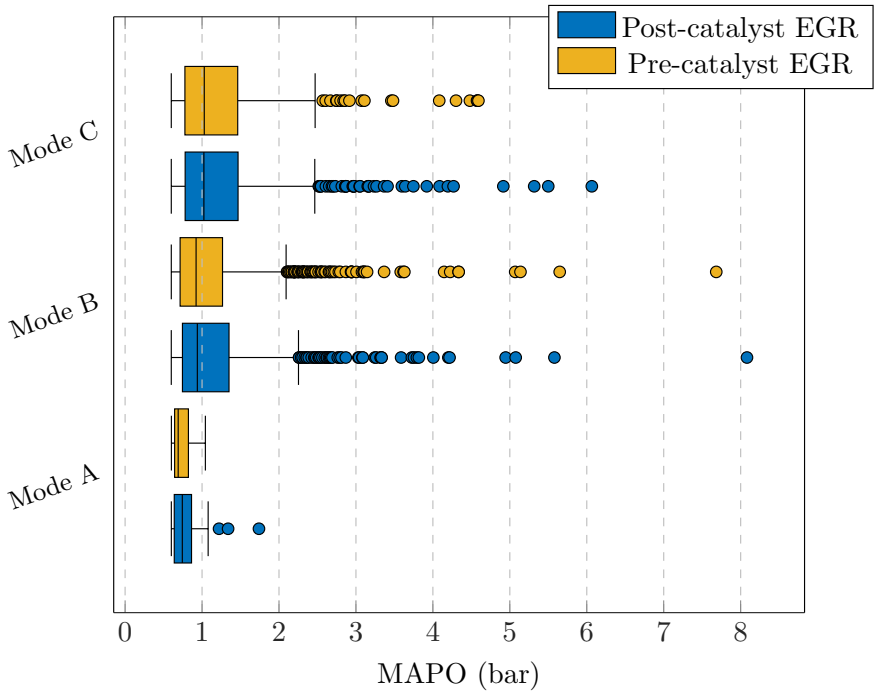

Figure 4-8: The distribution of the different initiation modes introduced in Figure 4-6 for all knocking cycles recorded during the test, plotted against the knock intensity for that condition. Mode A events are the most infrequent and tend not to reach high knock intensities. There does not appear to be a relationship between the EGR composition and the mode of the knock onset. The data for this plot includes around 1500 cycles for each EGR composition over the full range of EGR rates. The coloured dots indicate outliers for each set, these are defined as points that sit more than 1.5 $\times$ the inter-quartile range above the upper quartile value. The number of outlying points gives an indication of how the intensity of knocking cycles is generally distributed.

- the most powerful harmonic frequency can occur at any resonant mode (although the second mode is usually lower in power), oscillations do not always commence with the most powerful harmonic frequency.
- a large number of cycles exhibit low energy oscillations at the first harmonic mode before the onset of knock (close to MFB50).
- some cycles exhibit simultaneous excitement of all harmonic frequencies
- higher frequency oscillations decay to lower frequencies as the piston moves down and pressure decreases. This was also observed in the data for Chapter 3 and is suspected to be a result of the speed of sound reduction with lower pressure and temperature. The magnitude of this reduction is a scalar of the absolute magnitude, so higher frequencies have a more pronounced reduction – a more complete explanation of this is offered in Section 3.3.3 of Chapter 3.
- higher frequency oscillations have shorter residency times than lower frequency – suggesting that the standing half wave across the cylinder is the most stable form of resonance. Since this frequency is the lowest it will also suffer the least distortion by the reduction in the speed of sound during the expansion process.
- The distribution of the knocking modes appear to be more dependent on the knock intensity rather than the EGR rate or composition.

4.3.3 Comparison of knock onset angles

Comparing like-for like cylinder pressure traces can be difficult with multi-cylinder engines, due to the variation between cylinders causing some uncertainty on the exact charge composition distribution. For this reason a method has been devised to make as much of a like-for-like comparison as is possible for this data.

- to minimise error, comparative data points were chosen from the data where the inlet port temperature difference did not exceed 1°C (Seven conditions were found to be within this range whilst also having a large enough spark advance to provide

a good number of knocking cycles)[13].

- only cycles with a knock index (MAPO) exceeding 0.5 bar were selected, so that comparisons were being made between cycles that were actually knocking

- since the post catalyst conditions always showed fewer knocking cycles than their equivalent pre catalyst EGR condition, for each of the knocking post-cat EGR cycles a least square difference was performed between that cycle and all of the knocking pre-cat EGR cycles from IVC until 10°CA ATDC – to capture the deviation during the compression stroke and initial flame kernel growth. The pre-cat cycle that was the closest match was then paired up with that post-cat cycle – this way it was hoped that the comparison would be made for cycles with sufficiently equivalent initial conditions.

- knock onset was calculated for each of the cycles by the signal energy ratio (SER) method of Shahlari and Ghandhi [216] – this method calculates the signal energy of the pressure oscillations (SEPO) at each crank angle step by integration of the filtered pressure oscillations. The SER is then calculated by the square of the "forward" integral of the pressure oscillations over the following 5 crank angle degrees (SEPO_{fwd}), divided by the square root of the "backward" integral of the pressure oscillations over the previous 5 crank angle degrees (SEPO_{bwd}). This is more clearly described by Equation 4.3:

$$\mathrm{SER} \equiv \frac{\mathrm{SEPO}_{fwd}^2}{\mathrm{SEPO}_{bwd}^{1/2}} = \frac{\left(\int_{\theta_0}^{\theta_0+\Delta\theta} P_{filt}^2 d\theta\right)^2}{\left(\int_{\theta_0-\Delta\theta}^{\theta_0} P_{filt}^2 d\theta\right)^{1/2}} \tag{4.3}$$

  P_{filt} in this case is the band filtered pressure trace isolating the strongest harmonic oscillation ($f_{most-energy} \pm 1.5$kHz) – identified by examination of the power spectral density (PSD) for that cycle.

- the knock onset timing for each of the pairs was compared, and for each condition

[13]This temperature threshold was defined because temperature has previously been highlighted as a particularly important variable affecting NO response during combustion.

the distribution of onset angle differences was plotted.

Figure 4-9 illustrates this method by displaying a comparison of one of the pairs of cycles – the post-catalyst cycle on the left and the pre-catalyst cycle on the right. The shaded region in the top two plots denotes the part of the cycle which was considered in matching corresponding cycles for comparison.

The knock onset angle, denoted by the dashed black line in all plots, is demonstrated to be fairly accurate when compared to the band pass filtered traces (middle row). The SER[14] is included in this plot to reveal how the SER value evolves with increasing crank angle. The method of calculating the SER uses only the most powerful harmonic frequency – with Shahlari and Ghandi reporting that this reduces erroneous results due to the less well defined peak in the SER function that occurs when all frequencies are included in the signal to be analysed.

The pre-cat EGR cycle shows some well defined oscillations at the first resonant mode very early in the cycle, which are not powerful enough to qualify as knock. For this cycle the knocking pressure oscillations occur much later in the cycle at a higher resonance mode, which could have been initiated by the collision between the propagating wave and the reflected wave coming back from the wall.

Figure 4-10 illustrates the spread of the comparative knock onset angles between the paired pre/post-cat cycles, as well as the mean differences. Whilst the mean values do tend to show slightly later knock onset for post-cat EGR, the spread of values means that this is by no means definitive.

The mean improvements for each equivalent condition range from an improvement of 1.9 °CA down to an improvement of just 0.25 °CA for the EGR rates over 9%, but still with standard deviations in the region of 2 to 3 degrees. The predominantly earlier onset for catalysed cycles at 3% EGR could be due to the inherent variability in the data, which at such low EGR rates may have a larger impact than that of the minor species on the

[14] calculated as published by Shahlari et al [216]

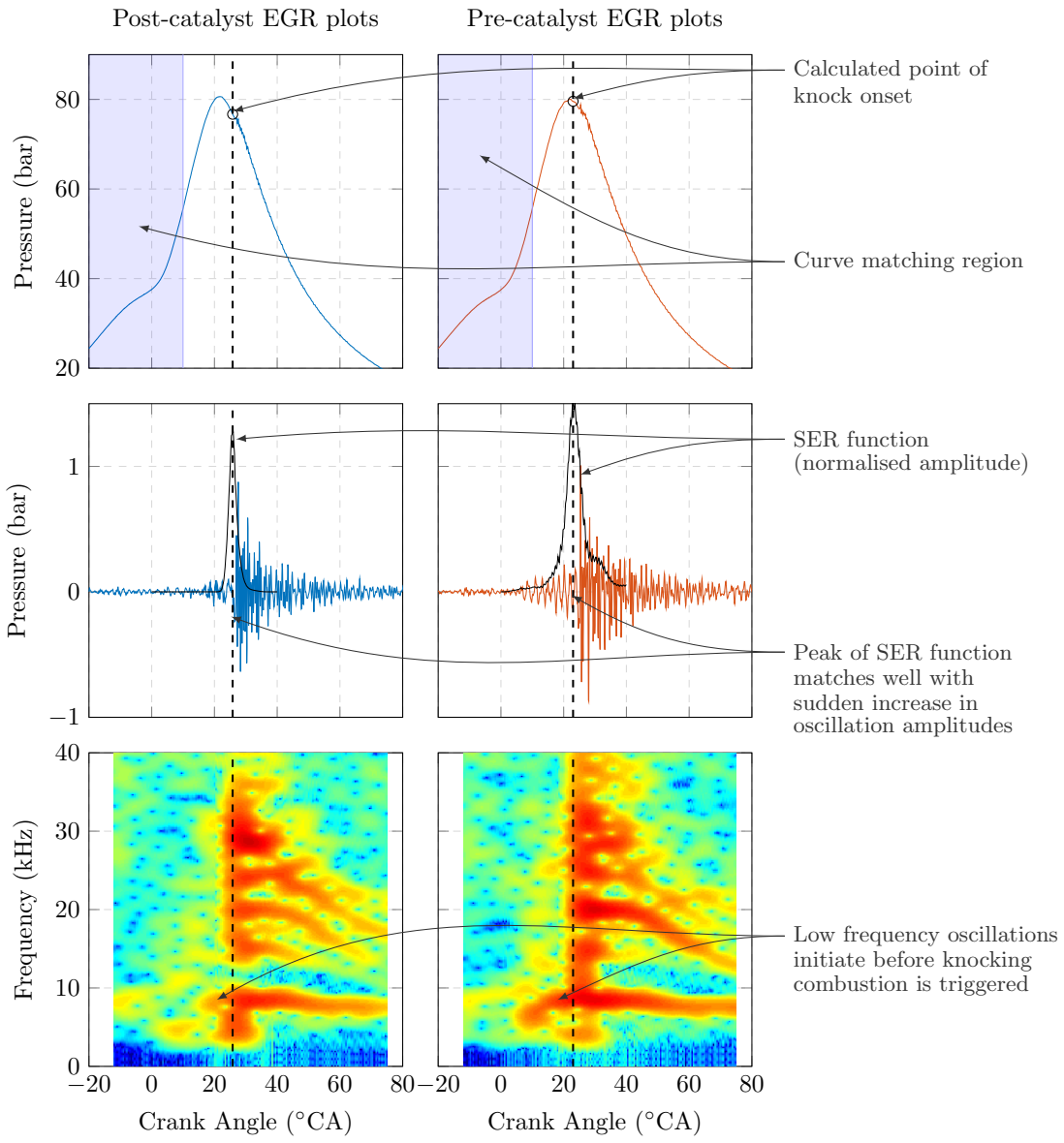

Figure 4-9: An illustration of the analysis method for comparing the angle of knock onset. From top to bottom these plots illustrate: cylinder pressure traces, filtered pressure trace (4 - 35 kHz band pass filter), power spectral density heat map showing oscillation power as a function of crank angle and frequency.

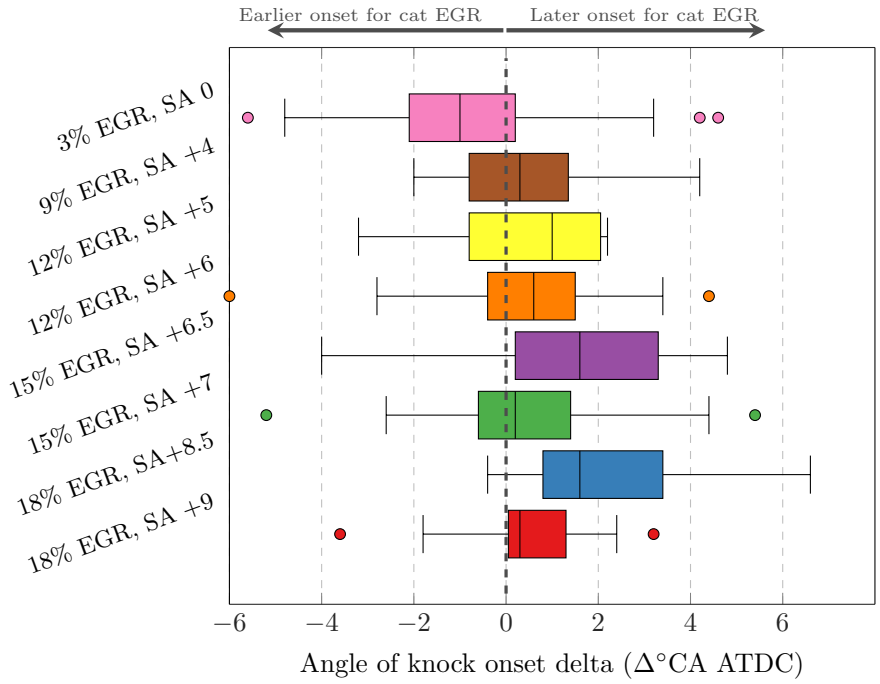

Figure 4-10: A comparison of the angles of knock onset deltas between equivalent pre and post-catalyst EGR pairs. Although the angle of knock onset seems to generally be more retarded for catalysed EGR conditions – particularly at higher EGR rates – there is a large spread in the onset angle deltas, with a large overlap between pre and post-catalyst values.

autoignition chemistry.

The data from Figure 4-10 suggests that at a given condition the probability of autoignition being delayed with post-cat EGR relative to pre-cat EGR is slightly higher – the mean improvement is 0.29°CA, which increases to 0.55°CA if the 3% EGR results are excluded. The relatively high standard deviation of the differences means that, if assuming a normal distribution, for a given pair of cycles only 54.4% would be expected to show a later angle of knock onset for catalysed EGR, this increases to 58.3% if the 3% EGR condition is excluded.

Another characteristic that differentiates the pre-and post-catalyst EGR conditions quite noticeably is the amplitude of the oscillations in the knocking cycles. This is illustrated in Figure 4-9 for the pair of cycles selected, but also becomes quite apparent when comparing the MAPO values between pre and post-catalyst conditions (shown in Figure 4-22 later in this section).

It has been well documented in the literature that at certain concentrations NO influences reactions that propagate OH radicals, as well as consuming OH radicals at high concentrations. It could be proposed from inspection of the current data that the increased NO available for pre-catalyst EGR conditions (when compared to equivalent post-catalyst conditions) may slightly increase the probability of knock onset being advanced, but more significantly promotes more powerful detonation when autoignition does occur. The mechanisms for this increase in intensity are likely related to the reaction paths involved with NO sensitisation of hydrocarbon oxidation, which may increase the abundance of reactive radicals in the end gas.

4.3.4 KLSA determination

The amplitude of the spark sweeps allowed a statistical method to be used to determine the knock limit during post-processing of the experimental data. This method was employed to improve the confidence in the KLSA values at which a large part of the comparison between EGR compositions is made.

Due to the spread of MAPO values during for a 300 cycle log, an average value is not representative of the level of knock during the log. This is illustrated in Figure 4-11 where the green dashed line, showing the mean MAPO value for each of the six logs, does not reflect the highly knocking conditions at more advanced spark angles. The 95th percentile values are also plotted, shown by the red dashed line, and show a much better response as the spark advances beyond -2.5 °CA.

Figure 4-12 shows a summary of the MAPO for all cycles logged during a spark sweep at 0% EGR, which illustrates how the MAPO values are distributed for knocking and non-knocking conditions. It can be seen that even at heavily knocking conditions there are still a large number of non-knocking cycles.

A piecewise linear regression (PLR) method (first used for KLSA determination by Giles [207]) was used to compare the 95th percentile MAPO values against the spark angle. For each test condition the spark advance was plotted against the 95th percentile

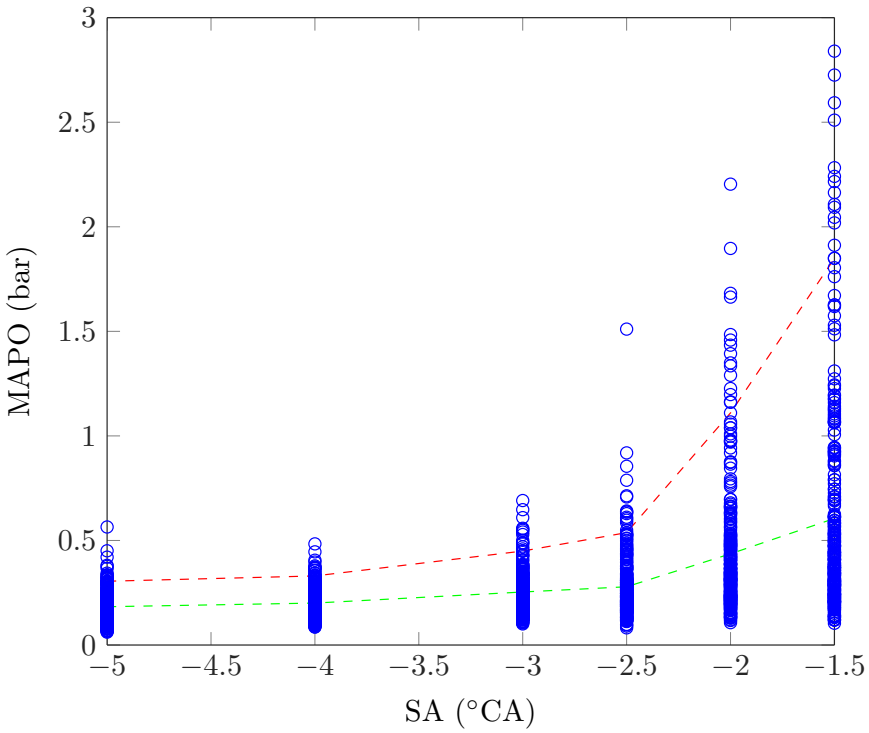

Figure 4-11: Example scatter plot of MAPO vs spark advance for all cycles at 0% EGR, with mean and 95th percentile values indicated by the green and red dashed lines respectively.

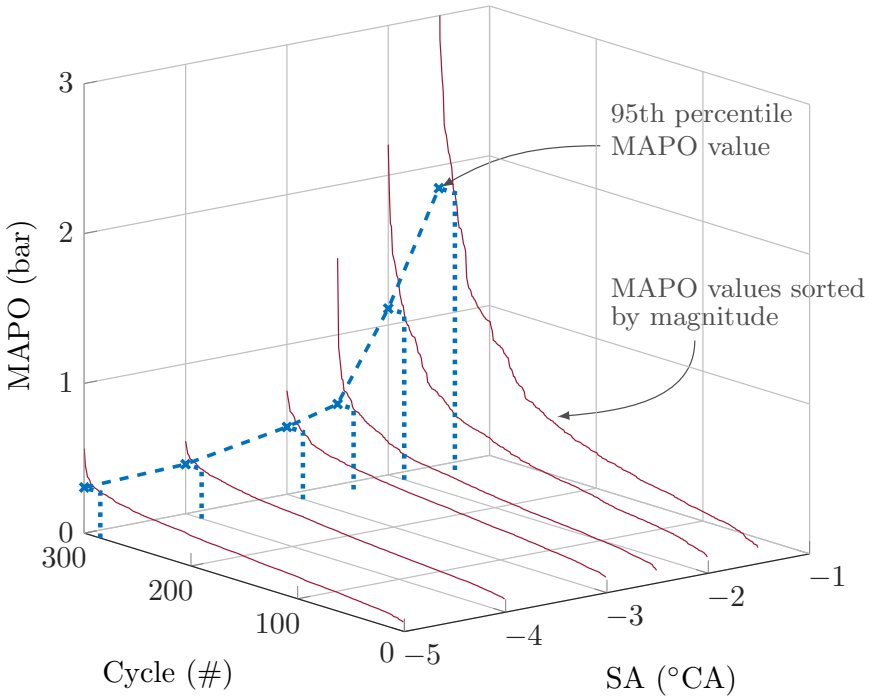

Figure 4-12: Illustration of the distribution of MAPO values and the 95th percentile amplitudes in relation to them. Even at highly knocking conditions it can be seen that a large number of cycles still have a MAPO below the threshold for knocking combustion.

MAPO, and a piecewise linear regression was performed to identify two lines of best fit (via the least squares principle) through the data points that have an intersection point at their common boundary, as shown in Figure 4-13. The intersection of these two lines then gives an impartial indicator for the spark angle at which the onset of knock occurs.

The outcome of this analysis can be skewed by the extent to which the spark was advanced during testing as the knock intensity increases exponentially for further spark advance past the knock limit. To account for this outlying high knock intensity logs (above 3 bar amplitude) were removed to limit the error of the best fit lines. The margin of error for this method is mostly defined by the size of the spark advance increments across a spark sweep, which for this investigation was set at 0.5°CA for spark angle close to the knock limit.

The results of this KLSA analysis appear to be more conservative than the thresholds that were recommended by the documentation, but do match very closely with the ignition angles that were observed during operation of the engine with automatic spark timing control enabled in the ECU. This mode of operation uses an accelerometer on the engine block to feed back to the ECU if knocking combustion is detected.

The lowest KLSA value across all three cylinders was used to define the absolute KLSA, in reality this was almost exclusively from cylinder 2 which displayed the highest knock intensities. This is suspected to be due to its location between the other two cylinders giving rise to higher wall temperatures.

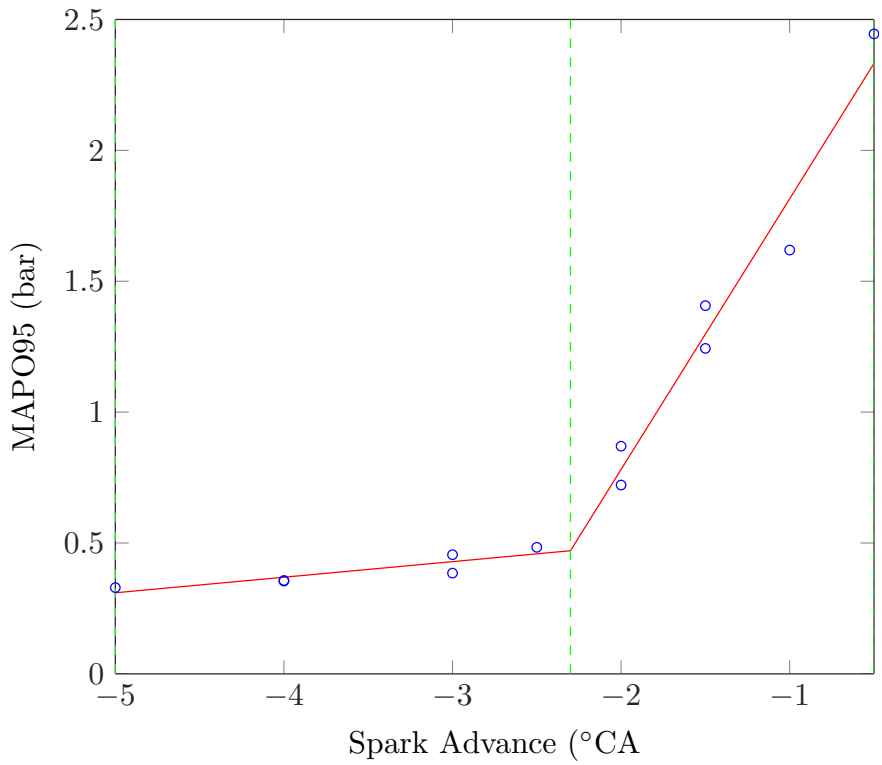

Figure 4-13: Example piecewise linear regression analysis (performed at 0% EGR on cylinder 3)

4.3.5 Performance and emissions effects of EGR composition

The data from these tests provide evidence to support advanced knock limits with post-catalyst EGR (Figure 4-14), albeit only by a small margin. This is contrary to the large improvements seen on the Ultraboost engine in Chapter 3, most likely due to the discrepancy in inlet oxygen content for the Ultraboost engine, and is potentially also impacted by the increased ethanol content of the fuel for the Fox engine[15].

The advanced knock limit provides an advance of combustion phasing of up to 1°CA for post-catalyst EGR as compared to pre-catalyst EGR at equivalent EGR rates over 6% (Figure 4-15). This also results in higher IMEPs, by up to half a bar (figure 4-16), and slightly higher torque (Figure 4-17). The fuel consumption does seem lower for the most part with post-catalyst EGR (Figure 4-18), interestingly though this is not evident at the higher EGR rates tested.

[15]If the literature reporting reduced response of ethanol to NO is valid for these test conditions and fuel.

The inlet temperature and airflow to the engine did deviate from their set points during the testing, which may reduce the accuracy of the results and provide some explanation for the discontinuity in some of the trends shown. Figure 4-19 shows how the inlet temperature varied between the test points, with up to two degrees difference between the pre and post-catalyst conditions at comparable EGR rates. The airflow showed a deviation of up to 3 kg/hr between the two EGR compositions (Figure 4-20) with a corresponding change in fuel flow to maintain lambda one (Figure 4-21). This is a change of up to 2.5%, which could be very significant in assessing the significance of the torque and BSFC effects – which are only improved by a similar margin to this.

The air and fuel flows do show a crossover point at 7% EGR which corresponds to a crossover point in the port temperatures. The similarity between these trends provides strong evidence that the dominant factor in producing these deviations is the fluctuation in temperature at the inlet. Since the torque and BSFC do not seem to follow a similar trend to the air flow data, it can be assumed that there are other factors, such as the difference in EGR composition, that are influencing the trends shown.

The magnitude of the difference between pre and post-catalyst EGR appears to remain constant for the entirety of the EGR rate sweep. This is slightly counter-intuitive considering the larger discrepancy between concentrations of minor species in the initial charge that would be present for higher EGR rates.

Focusing on the NO inlet concentration for pre-cat EGR, the inlet charge would contain ≈50ppm of NO at the 3% EGR condition, which increases to ≈300ppm for the 18% EGR condition. A plateau in the strength of the NO impact across this range of concentrations could explain the fairly constant difference between the pre and post-catalyst effects for this data.

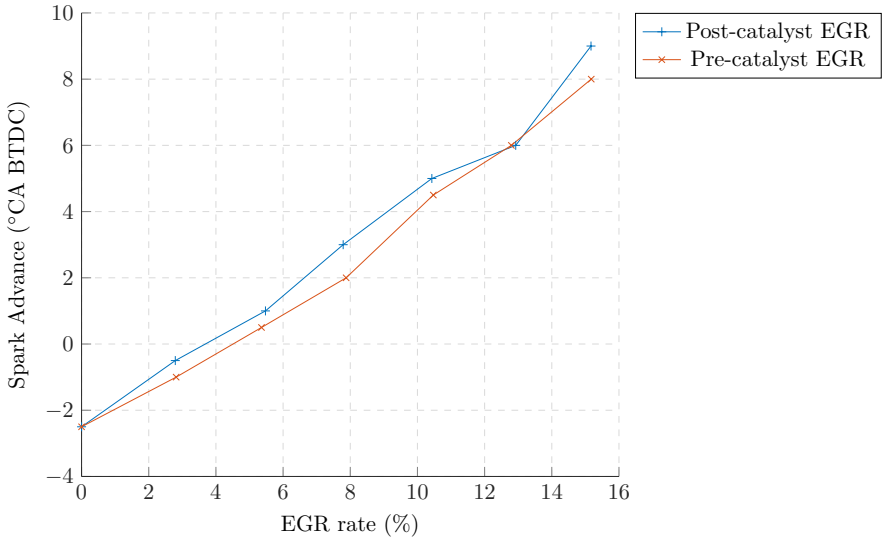

Figure 4-14: The comparison between KLSA improvements shown with post-catalyst EGR and pre-catalyst EGR show a marginal gain by using catalysed gases.

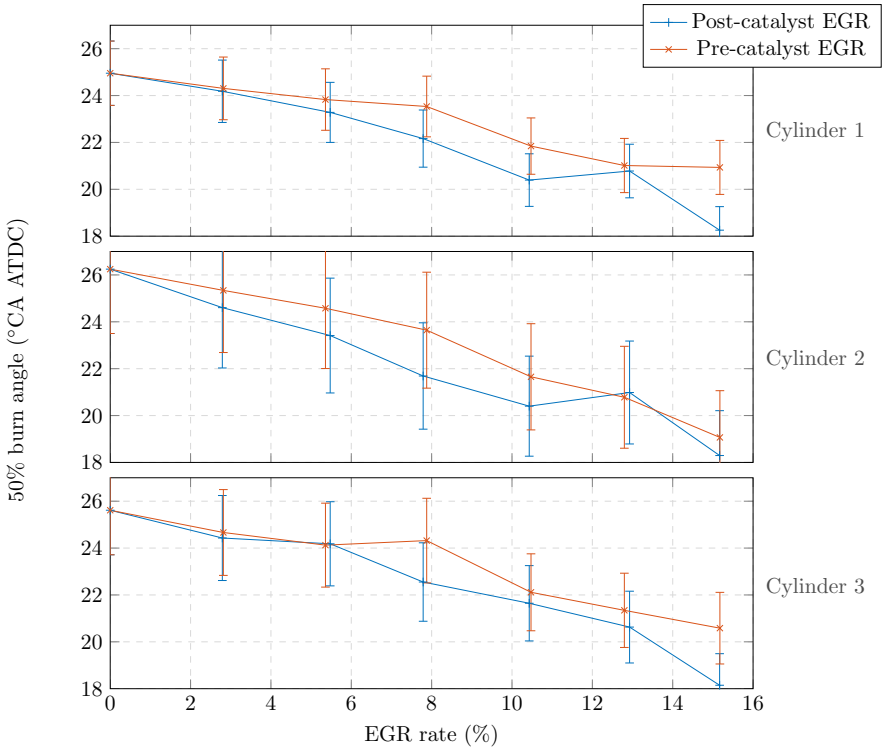

Figure 4-15: The marginal gain in catalysing the EGR gases results in improved combustion phasing by up to 2°CA at KLSA.

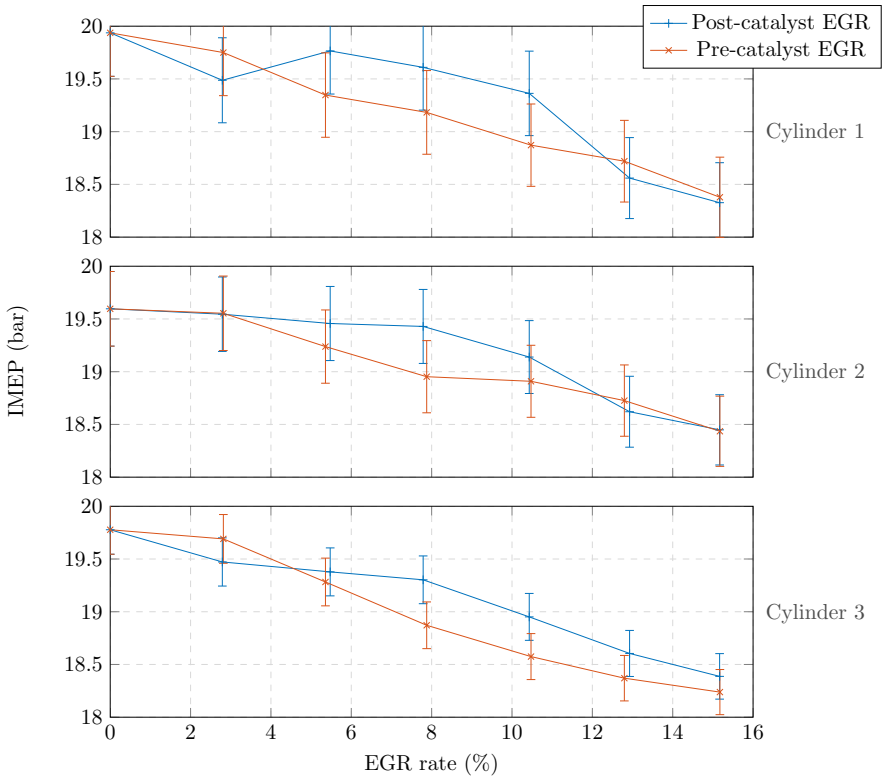

Figure 4-16: The IMEP is almost consistently higher for post-catalyst EGR across all three cylinders. This would be expected for the more advanced combustion phasing.

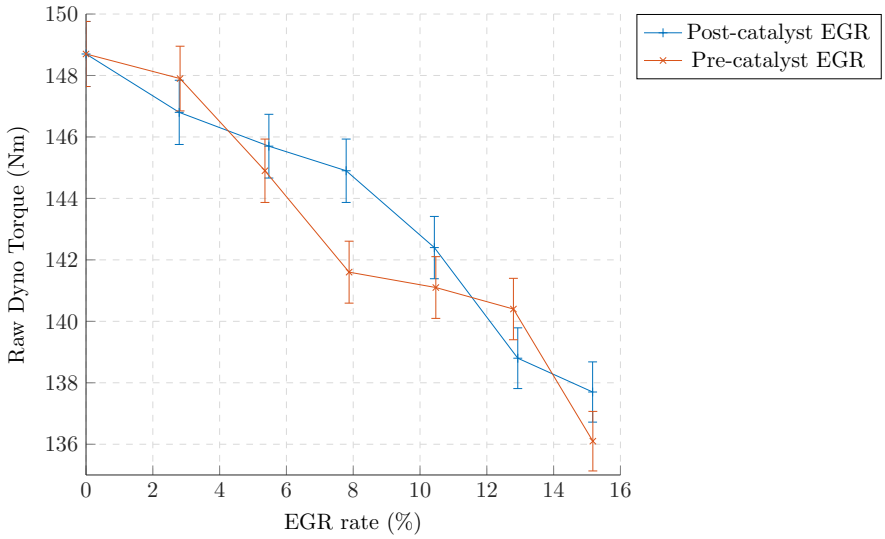

Figure 4-17: The torque output of the engine also follows the trends shown by the combustion phasing and IMEP, with a lower torque drop for post-catalyst EGR as compared to pre-catalyst EGR at KLSA.

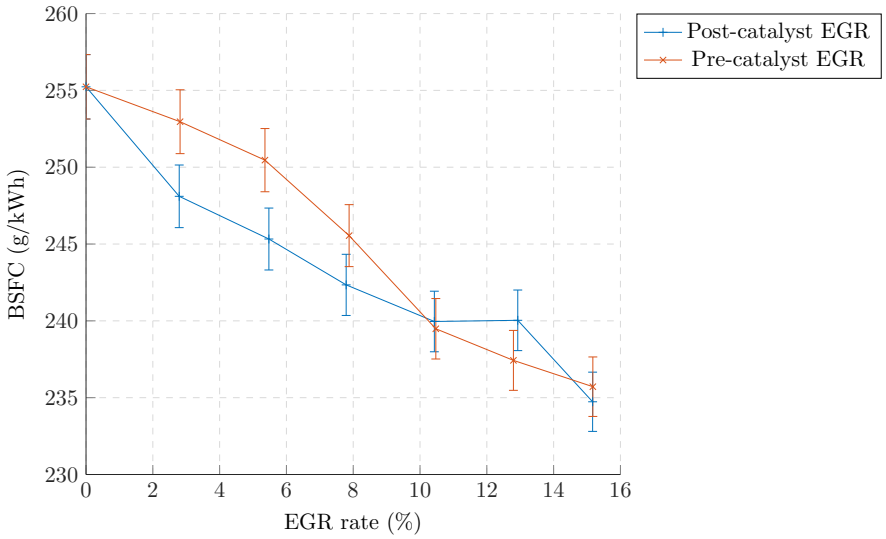

Figure 4-18: The BSFC at KLSA shows a greater reduction for post-catalyst EGR up to around a 10% EGR rate, beyond which the difference is negligible. This is slightly counter-intuitive considering the combustion phasing and torque improvements at these EGR rates for post-catalyst EGR.

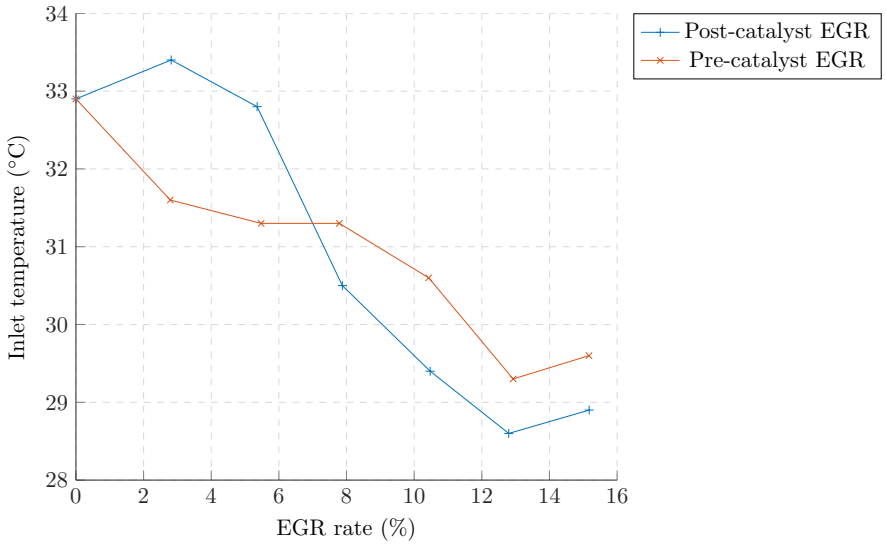

Figure 4-19: The temperature PID controller did not keep the inlet temperatures to as close a tolerance as was hoped, the difference between pre and post-catalyst points of up to 2°C could affect the engine airflow and therefore fuelling and load by up to 0.7% – which equates to around 0.8 kg/hr.

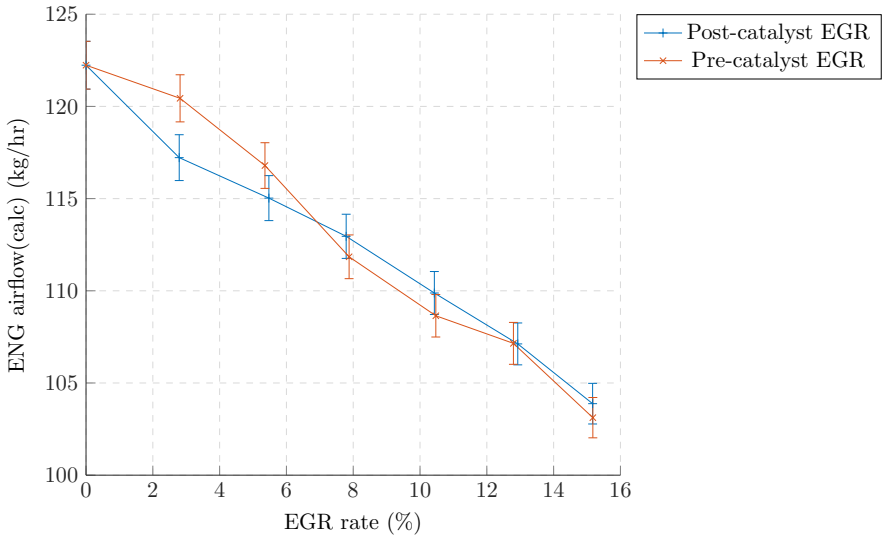

Figure 4-20: The engine airflow follows a very similar trend to that of the inlet temperature, indicating that the temperature is likely to be the primary factor in this deviation.

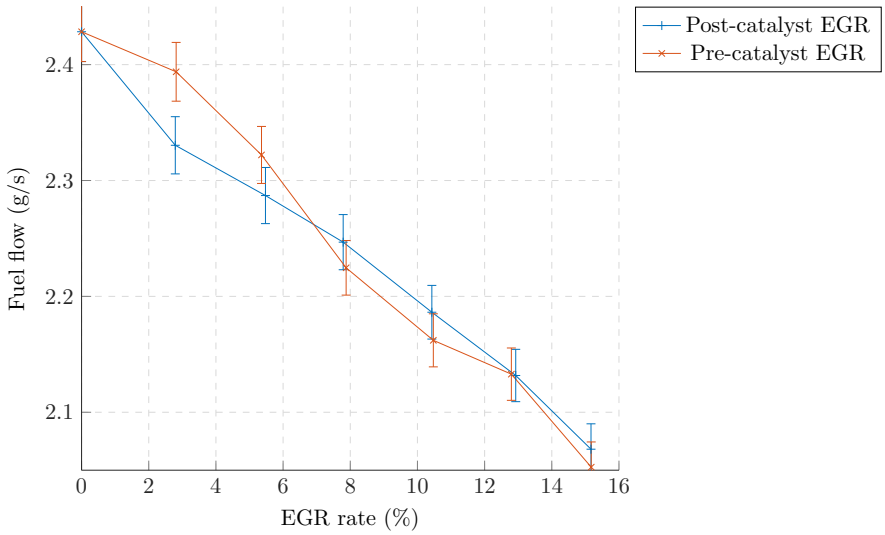

Figure 4-21: Lambda values were well controlled to stoichiometric, so fuel flow and airflow values correspond closely.

4.3.6 Effects of EGR composition on engine performance at equivalent spark angles

A comparison of results at equivalent spark angles can help to quantify the effects of different EGR compositions. Since the spark timing can have such a significant influence on the combustion results, the data across each spark sweep is presented in this section to provide a clearer picture of how the combustion rates and knock amplitudes are affected at equivalent operating points by EGR composition.

The most significant effect derived from post-catalyst EGR is the reduction in knock intensity. Figure 4-22 shows how the knock intensity develops as the spark is advanced for each EGR condition tested[16].

Comparison of the values presented does show a consistent trend towards the post-catalyst EGR (denoted by the solid lines) reducing the knock intensity versus the pre-catalyst EGR at a given spark angle beyond KLSA.

Cylinder two's higher propensity to knock is also demonstrated by the higher knock intensities displayed in Figure 4-22a, it is expected that this is due to higher wall temperatures due to its location between the other two cylinders.

Figure 4-23 gives a similar comparison on the combustion phasing as the spark angle is advanced for each EGR condition. It might be expected that the post-catalyst EGR would slow the combustion rates more, relative to the pre-catalyst EGR, since the minor species removed by catalysis such as CO and partially burned hydrocarbons have been demonstrated to increase flame propagation rates. The effects of these components on flame propagation are not significant enough to show any definitive trends in the data from this engine though, with the differences between flame propagation rates for pre and post-catalyst EGR most likely stemming from temperature fluctuations at the inlet.

[16]The variation between repeated points in this plot demonstrates the stochastic nature of knock, as well as the variation that was present in the inlet temperatures.

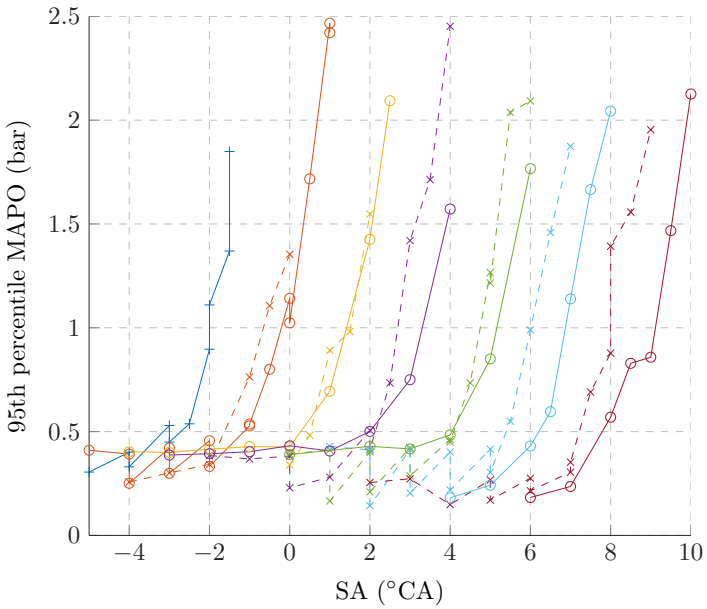

(a) Cylinder 2

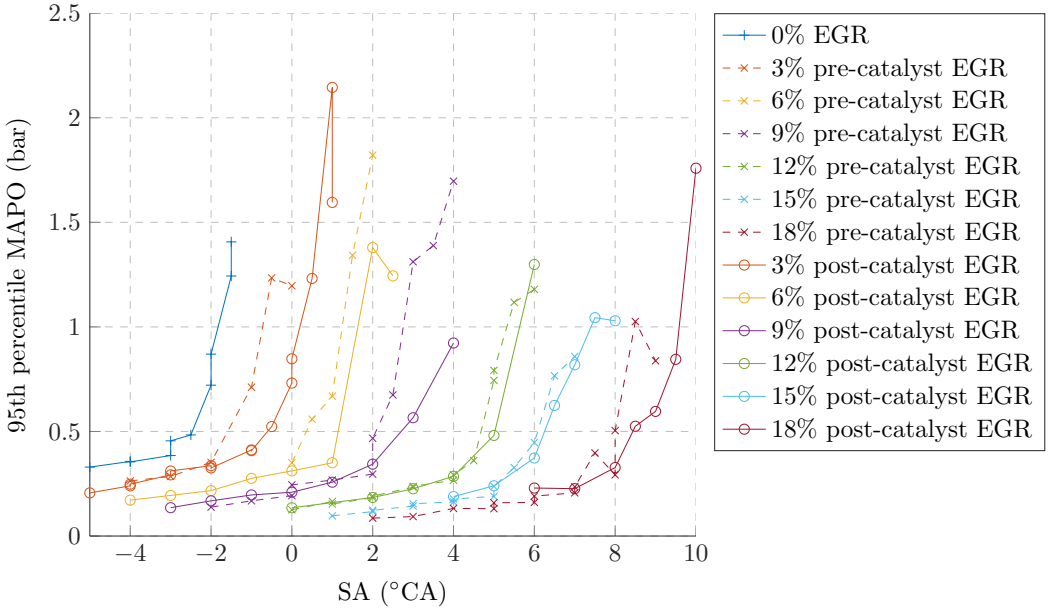

(b) Cylinder 3

Figure 4-22: Knock intensity for spark sweeps at both pre and post-catalyst conditions, for both cylinder two and cylinder three. The post-catalyst EGR conditions, shown by the dashed plots, quite clearly show a reduction in the knock intensity for comparative spark angles when compared to the solid traces for pre-catalyst EGR.

Chen et al [118] have observed that although NO can potentially affect flame propagation, this is far outweighed by its effect on knock onset. The data presented here certainly supports the theory that its effect on flame propagation is negligible relative to the variance observed due to other parameters.

Calculations for the heat capacity of both catalysed and uncatalysed EGR for typical species concentrations seen in this experiment reveal an increase in heat capacity for catalysed EGR of around 0.2%[17]. This would cause the heat capacity of the total in-cylinder mixture to change by less than 0.04% at the highest EGR rate tested. It is considered that the impact of such a small change in heat capacity would have a negligible impact on the thermal properties of the mixture, in fact small discrepancies in the fuelling rate would have a far larger thermal impact due to its much higher heat capacity.

[17]For the purposes of this calculation the unburned hydrocarbon emissions were approximated as methane.

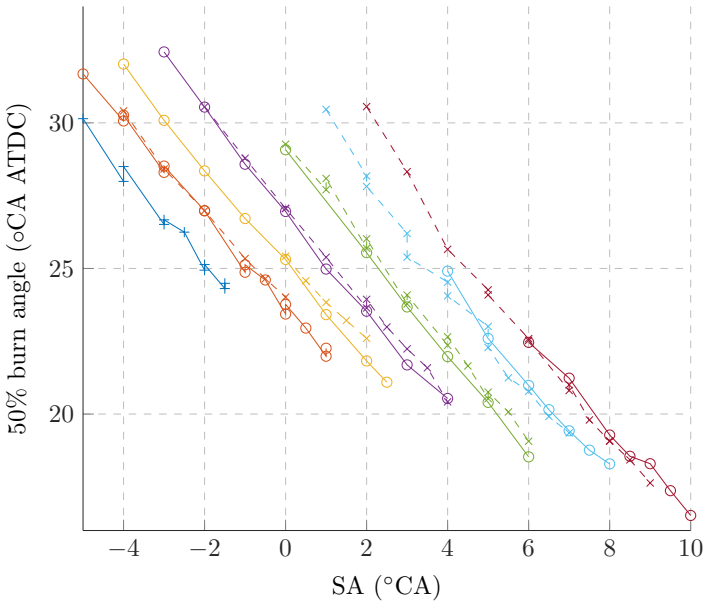

(a) Cylinder 2

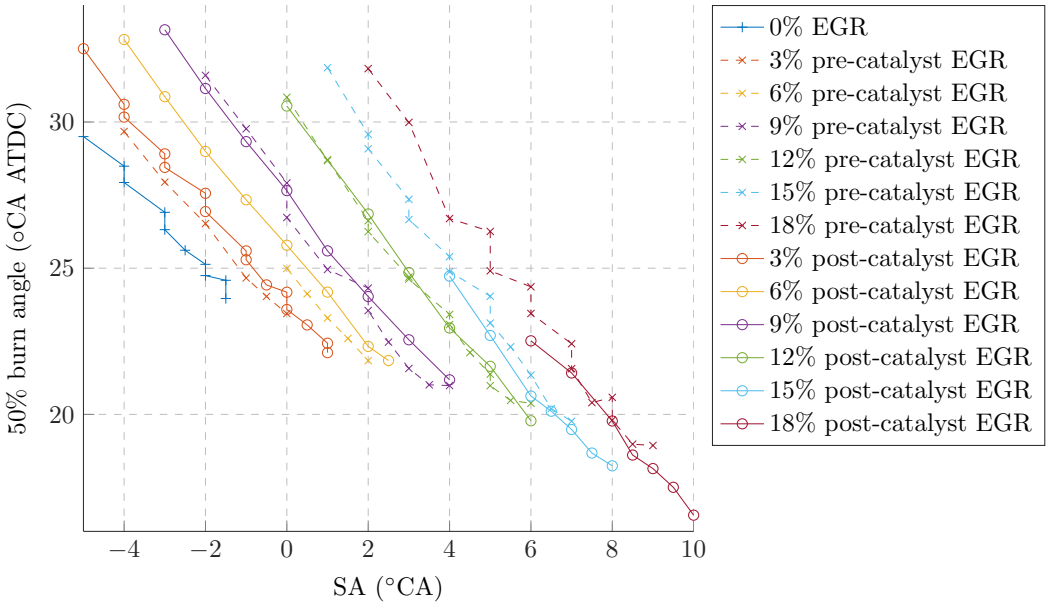

(b) Cylinder 3

Figure 4-23: Combustion phasing for spark sweeps at both pre and post catalyst conditions, for both cylinder two and cylinder three. The post-catalyst conditions, denoted by the dashed lines, do not seem to either advance or retard the combustion phasing significantly, with the variations that are seen most likely stemming from variations in the inlet temperature instead.

4.3.7 Comparison against synthetic dilution

A brief foray into the effects of synthetic dilution with the N_2/CO_2 blend devised in Section 4.1.4 was conducted to compare against the real EGR mixtures.

Although trace amounts of CO and HCs remained in the catalysed EGR gases (typical minor species concentrations are given in Table 4.5), it is anticipated that the main difference between that and the synthetic EGR is the presence of water. Unfortunately the exact quantity of water in the real EGR gases is unknown due to condensation along its path before being returned to the inlet manifold.

Table 4.5: Table of typical minor species content for each EGR composition.

Species	Uncatalysed EGR	Catalysed EGR	Synthetic EGR
NO	2500 ppm	2 ppm	0 ppm
CO	0.75%	0.2%	0%
HCs	1400 ppm	250 ppm	0 ppm

Evidence of the water condensing in the EGR rig was apparent by moisture along the pipe walls[18] and by emulsification of the oil in the rig pump[19] but the exact quantity of this could not be measured with the equipment available. There is some evidence of water condensing from the EGR gases on contact with the fresh air at the inlet manifold, which suggests that some water from the EGR was still present in the cylinder charge.

By contrast the synthetic EGR mixture enabled an investigation into EGR effects with knowledge of the exact diluent composition. Full spark sweeps were not taken due to the time limitations relating to the quantity of gas available from each bottle. It was felt prudent to err on the side of caution in this respect to avoid running out of diluent gas whilst the engine was running far beyond its knock limit for undiluted operation.

Therefore data was collected with predetermined ignition timing for each EGR rate

[18] A water catch pipe was installed on the rig in an attempt to collect any condensed water, but moisture was still present on the walls of the EGR feed pipe after each test period.

[19] As a re-purposed PFI engine, the EGR pump was running a lot cooler than its original design specification. This meant that the piston rings did not seal as effectively, so a large amount of condensate dropped into the oil. Regular oil changes were required to replace the emulsified oil.

so that data for equivalent spark angles could be compared. These ignition angles were:

3% EGR: -1°CA

6% EGR: 0°CA

9% EGR: 2°CA

The synthetic EGR (sEGR) results exhibited a stronger suppressive effect than the other two EGR compositions. The relative difference to pre-catalyst EGR is expected, due to the absence of any of the minor species, but the increased suppressive effect relative to catalysed EGR is surprising. It would be expected that the water content of the uncatalysed EGR would provide an increased dilution effect in comparison to the dry gases, whilst also increasing the C_p of the EGR mixture. This raised queries over the accuracy of the EGR rate evaluation methods, which were double-checked against the engine airflow and fuelling rates for each EGR rate. These measurements confirmed the equivalence of the EGR rates for the different EGR sources.

Figure 4-24 illustrates the suppressive effect of the sEGR on IMEP relative to the other two EGR compositions, which directly impacts the engine output. This lower IMEP was a result of the later combustion phasing (illustrated in Figure 4-25) arising due to the slower combustion rates displayed in Figure 4-26.

The reduced knock intensity with the sEGR, shown in Figure 4-27, will be primarily due to the slower combustion rates delivering a peak pressure further into the expansion stroke, and therefore reducing the peak end gas pressure and temperature.

Unfortunately the discrepancy between the EGR rates renders comparison of the cylinder pressure traces for specific logs invalid, so this is not displayed here.

The greater suppressive effect of the synthetic EGR relative to the other two EGR compositions is an unexpected result since water is widely regarded as having a suppressive effect itself, and therefore dry gases would not be expected to have such a strong dilution effect as wet gases. Therefore it is suspected that the difference observed between the

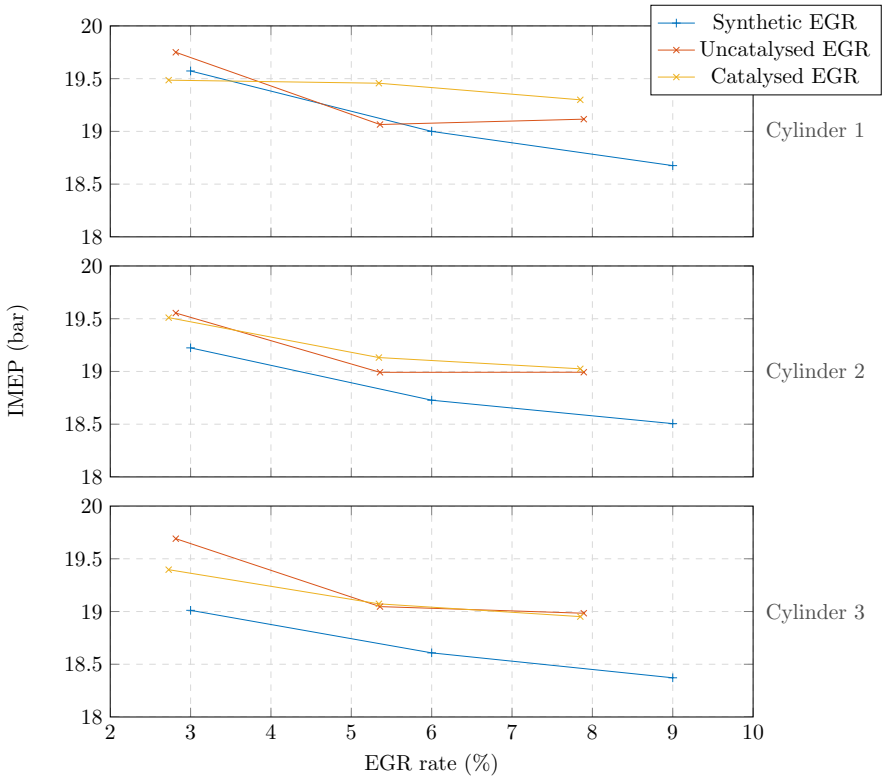

Figure 4-24: The average IMEP for cylinders 1 to 3 for each of the EGR compositions. It is particularly evident that the IMEP is lower for sEGR addition in cylinders two and three.

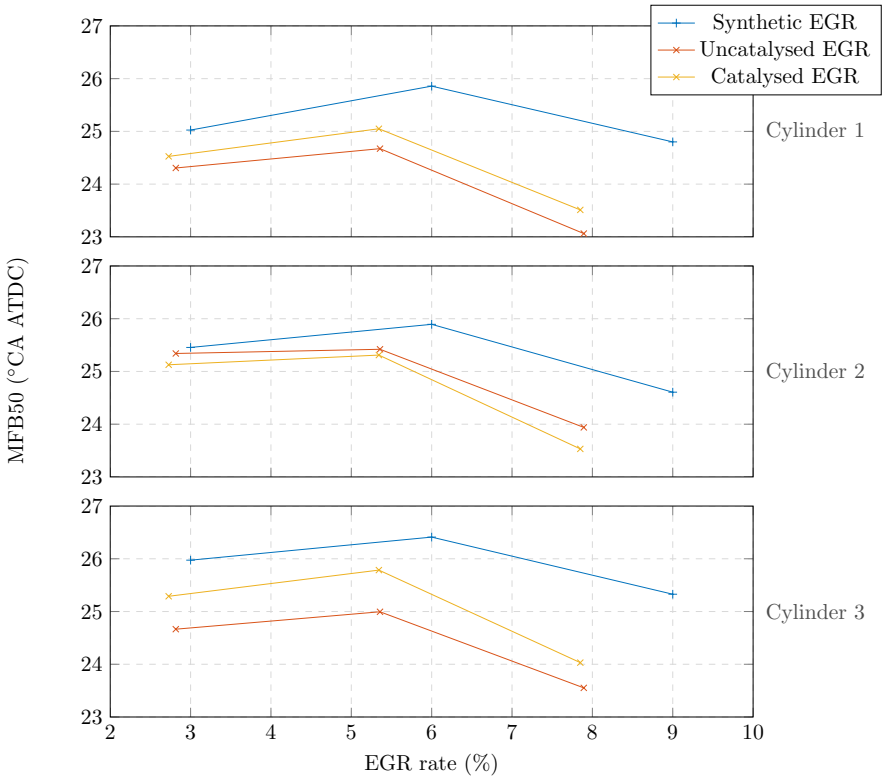

Figure 4-25: The average 50% combustion phasing for each cylinder, again showing an increased dilution effect of the sEGR to cause combustion phasing to be delayed by up to 1.5°CA compared to uncatalysed EGR.

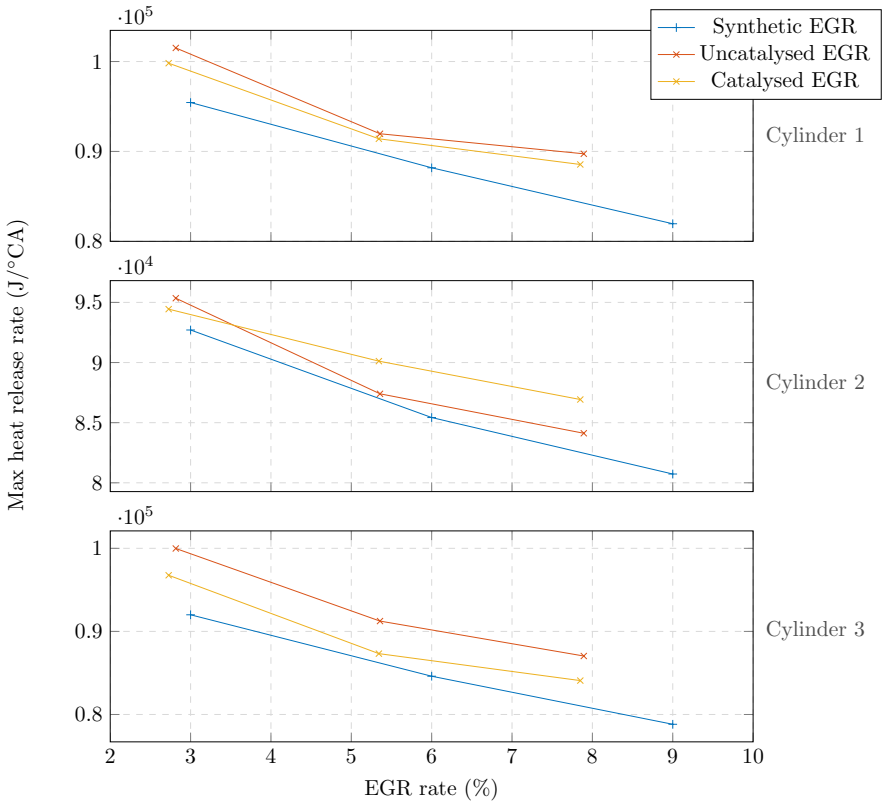

Figure 4-26: The maximum combustion rate for each cylinder and each EGR composition. Again illustrating the increased dilution effect of the sEGR in comparison to the two real EGR compositions.

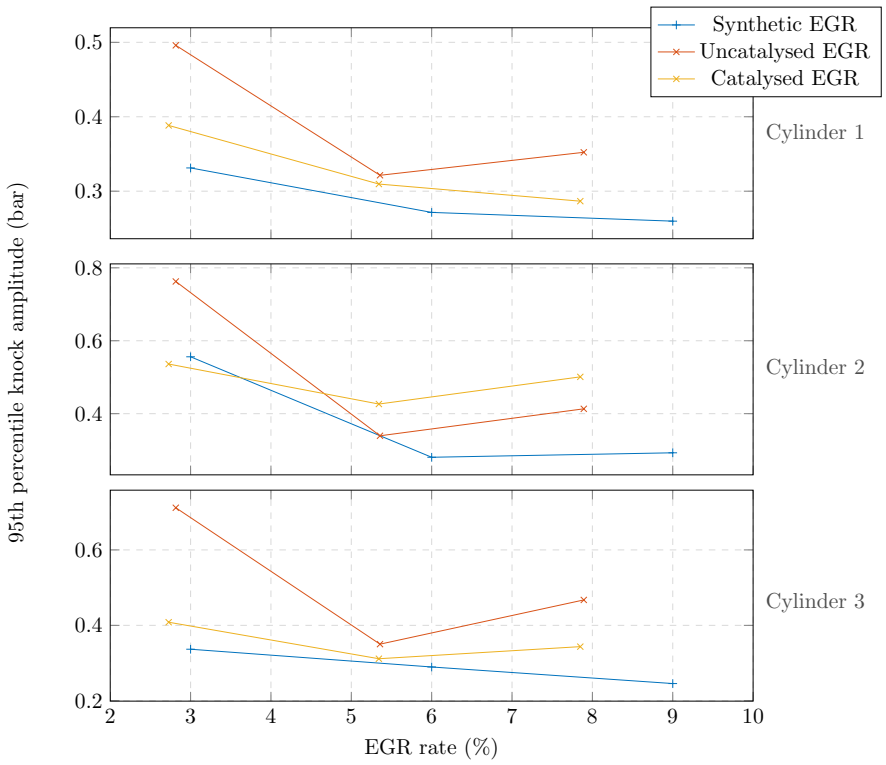

Figure 4-27: Comparison of the knock intensities for each cylinder with each EGR composition. The reduced knock intensity for sEGR will be primarily due to the slower combustion rates.

sEGR and the catalysed EGR has been impacted by the slight discrepancy in the EGR rates for the comparative test points.

4.4 Conclusions

The results presented in this chapter give a rich picture of the combustion behaviour of the Fox engine within the speed and load condition tested. The data confirm previous findings on EGR's ability to advance the knock limit whilst reducing NOx emissions for lambda 1 operation, although the outright knock limit advance due to EGR was lower than that reported in Chapter 3 and in the literature, where a generic value of 1 CAD per 1% of EGR is regularly reported.

Splitter et al [217] report, in a study comparing EGR effects with different fuels, that the anti-knock effects of EGR are reduced for fuels containing ethanol. This could potentially be due to the increased octane rating afforded by ethanol addition, meaning that the effective octane increase of EGR addition cannot provide as much of an improvement. Importantly the fuels investigated by Splitter et al compared E30 fuels with E0 fuels, which compares to a 10% ethanol content for the fuel used for the current work. Subsequently it is risky to make assumptions for these results based on the findings of Splitter et al. If the findings of Splitter et al do apply to fuels with lower ethanol contents this may mitigate the response to EGR slightly, which would explain the lower EGR response observed for this study in comparison to that found in the literature.

The data collected during this experiment provides strong evidence for the increased knock suppressing effect of post-catalyst EGR compared to pre-catalyst EGR, but the torque and efficiency benefits are less pronounced, and the effect on emissions does not seem significant. The efficiency improvements seen with post-catalyst EGR do not give compelling evidence to support its use over pre-catalyst EGR, especially with consideration of the error margins in relation to the improvement seen.

The increased knock suppressant effect afforded by catalysis of the EGR gases is evident

in the cylinder pressure data. Different initiation modes were observed in the cylinder pressure data but these appeared to depend more on the knock intensity than the EGR rate or quality. In a CFD based study Galloni et al [139] observed a relationship between the oscillation modes and the location of the AI centres in relation to a virtual sensor. Their findings could also be significant in interpreting the effects observed here.

The results from Chapter 3 along with evidence from the literature suggests that this increased suppressant effect stems mostly from the removal of the NO present in pre-catalyst EGR.

NO has a radical promoting effect and therefore can accelerate chain initiation reactions during the low temperature regime in the end gas. Despite this the measured knock onset angles only indicate a 58% chance of a later onset for catalysed EGR versus uncatalysed EGR. The effect of EGR catalysis on knock magnitude is much more striking though, with up to a 0.5 bar reduction in the amplitude of knocking oscillations at equivalent spark angles. This is fitting with the theory of knock being predominantly triggered by inhomogeneities and hotspots, with the magnitude appearing to depend more on the mixture preparation by NO interactions.

The analysis techniques employed to compare the data for pre and post-catalyst EGR have been designed to account for the variability inherent in knocking combustion. To the authors knowledge the knocking oscillation modes observed in Section 4.3.2 and the pairing method employed to compare the difference in knock onset angles between the two EGR compositions have not been published before. This pairing method could be a valuable technique for future research concerning stochastic phenomena.

Whilst the results of this investigation concur with those reported in the literature, it is apparent that the extent of EGR effects can be dependent on specific combustion systems and fuels. This points to a requirement for simulation methods to account for differences in combustion systems and the fuels they use in order to accurately predict EGR effects.

Simulation methods are employed in Chapter 5 to analyse the mixture effects further.

CHAPTER 5

MODELLING THE COMBUSTION CHARACTERISTICS OF A HIGH BMEP PRODUCTION GASOLINE ENGINE WITH CONSIDERATION OF DILUTION EFFECTS

This chapter uses a stochastic model to simulate combustion in the engine detailed in Chapter 4. The validity of the model is tested for spark sweeps and for diluted conditions before a comparison is made between the different EGR compositions.

The dilution response is tuned to better represent the performance observed experimentally in Chapter 4 and thus improvements to the model performance are suggested.

To compare the EGR compositions a model was calibrated for the 12% EGR condition, which effectively created a MFB profile with which to compare the kinetic effects that were predicted by the model. The effect of the two different EGR compositions was assessed in relation to knock limits by observation of heat release in the end gas and radical concentrations.

A sensitivity analysis that was performed for each of the most prevalent minor species in EGR confirmed NO to be the most volatile component for this model, which is in agreement with results from the literature.

5.1 Modelling goals

The platform used for the modelling work in this chapter is the Stochastic Reactor Modelling (SRM) Suite from CMCL Innovations. This platform was selected both for the potential that it boasts in achieving relatively fast computation times whilst accounting for variables arising from turbulence and inhomogeneities that we cannot measure or predict with confidence[1], and to assess its applicability for dilution effects in SI engine modelling – since stochastic modelling is still a relatively novel technology in the field.

The work in this chapter will endeavour to answer two questions:

- How well can the response to dilution for the test conditions reported on in Chapter 4 be reproduced by simulation methods, and what is the predictive power of these methods?
- Can these modelling methods shed more light on the mechanisms that are most pertinent when considering EGR composition?

The first of these questions is highly dependent on the performance of all of the sub-models in the model to represent the combustion phenomena displayed by the engine. The SRM provides a myriad of calibratable sub-models to represent processes in the engine relating to heat transfer, crevice modelling, blow-by – which can all be enabled or disabled where the user sees fit.

This can introduce questions over the validity of a given calibration:

1. If real performance is reproduced, how can the user be sure that the particular set of parameters used really does represent reality, and can a different combination of parameters reproduce the same result?
2. If the model fails to reproduce trends shown in experimental data, how can it be determined whether this is a shortfall of the model or simply a failure by the user

[1] These aspects are discussed in Section 2.3.

to calibrate the model accurately?

3. Since the model is only an approximation representing the real processes, where should the boundary be set to determine whether the model is performing satisfactorily?

The calibration process outlined in Section 5.4 and the selection process for the chemical mechanism outlined in Section 5.3 were designed to address the first two questions. The third of these questions is addressed by the process used to select a representative experimental cycle, from which a region was selected to illustrate an acceptable deviation for the simulated pressure trace. This process is also outlined in Section 5.4.

The chemical aspect of this modelling work is governed by the kinetic mechanism within the model. Kinetic modelling is an area that has received a lot of attention, resulting in a wealth of mechanisms being available in the literature. Section 5.3 outlines the process used to ensure that the chemical mechanism selected for this work is appropriate whilst also stating the limitations of the model.

The sections in this chapter will address the following topics:

- Justification for the choice of platform for the simulation work and a summary of the operation of the stochastic reactor model.
- The selection of an appropriate chemical mechanism to represent the processes occurring in SI combustion with a reasonable degree of accuracy whilst also minimising computational cost – this is an important consideration with respect to mixture composition effects.
- The methods used to calibrate the model and how the experimental data were used for this – this is important in addressing the previously mentioned questions over validity of the results.
- The comparison of the dilution effects in the model against experimental high load combustion data and identification of areas where there is potential to improve the

model performance.

- A comparison of the predicted effects of the different EGR compositions on the end gas species evolution and heat release.
- How this model could be improved with further work and ultimately how it could impact engine design and development, with consideration of the level of predictive capability that could be expected of it.

5.2 The Stochastic Reactor Model

PDF modelling of combustion is a relatively novel method of applying quasi-dimensional models. It is a method that has been successfully demonstrated by researchers from Cambridge, Germany, and Sweden over a variety of IC engine applications. The Cambridge research group has pioneered the application of PDF methods to combustion modelling and applied it to a number of studies on HCCI combustion based on the CMCL Innovations software that they have developed. Other research has been carried out with another software platform, called LOGEsoft, which operates in a very similar way to the CMCL platform. Their work has focused more on knock in SI combustion.

There is considerable evidence in the literature of the potential of PDF methods to bridge the gap between fully empirical modelling methods and computationally expensive CFD methods [145, 150, 151, 218]. The computation time benefit of SRM methods over CFD has been demonstrated by a number of studies, but perhaps the most remarkable example of this comes from a study on NOx and particulate emissions in partially premixed compression ignition (PPCI) [219, 220]. The SRM model achieved satisfactory results whilst boasting a reduction in computational time from 28 days to 10 minutes.

The basic premise of a stochastic reactor model is that it divides the cylinder up into "particles" which have no positional properties, but are defined by their species mass fractions and their temperature. The pressure, volume and total mass are global variables that apply to the whole in-cylinder mixture. Mixing and heat transfer can occur between

each particle and between the particles and the cylinder wall, each of these sub-models uses stochastic parameters to determine the mixing and heat transfer rates.

Both the CMCL and LOGE software are based on the same premise, the only discernible difference that is reported on in the literature is the quasi-dimensional flame propagation model that is employed by each software. For this work the CMCL software has been selected, it is considered that the difference between this and the LOGE software is not significant enough to alter the outcomes of this investigation. Mosbach et al performed a comparison of its performance for all of HCCI, SI, and Diesel operation and managed to match the pressure profiles for each operating mode with experimental data over a range of speed and load points [221]. This provides good evidence for the versatility of CMCL's SRM to model different combustion modes.

The particle number in the model is a significant factor in the level of inhomogeneity that can be modelled and therefore the accuracy of a given model. Bhave et al [142] demonstrated the accuracy of using 125 particles by comparing against models containing up to 1000 particles, which resulted in comparable accuracy of results with processing time being reduced from 8 hours (with 1000 particles) to 55 minutes (with 125 particles).

Su et al [222] developed an in-flow and out-flow model for the SRM, which accounts for breathing and injection phenomena. These processes added significant time to the computation processes, which they combated by evaluating how down-sampling affected the accuracy of the model in order to reduce complexity. Their analysis indicated that a 50 particle model provided sufficient accuracy for their application.

The optimum particle number is likely to be application specific but a majority of the work published on SRM models gravitates towards using 100 particles.

5.2.1 The PDF transport equation

Made up of a series of ODEs, the PDF transport equation governs the evolution of the species and temperature distributions during combustion within the SRM model and as such is the fundamental base upon which the model operates.

The model assumes statistical homogeneity – meaning the PDF is assumed to be the same throughout the cylinder. The model calculates the evolution of the N_S chemical species' mass fractions: $Y_1, ..., Y_{N_S}$, and the temperature T, as a function of time for each particle.

The N_S+1 random scalar variables are combined into the vector $\psi = (\psi_1, ..., \psi_{N_S}, \psi_{N_S+1}) = (Y_1, ..., Y_{N_S}, T)$ whose distribution is given by the PDF, f. The smoothness of the PDF is defined by the number of particles in the model. The PDF can be used to calculate mean quantities by:

$$\langle \psi_j(t) \rangle = \int_{j=1}^{j=N_{par}} \psi_j(f(\psi;t)d\psi \tag{5.1}$$

Since in-cylinder density varies during an engine cycle, it is more convenient to use the mass density function (MDF), $\mathcal{F}$, which relates to the PDF by:

$$\mathcal{F}(\psi;t) \equiv \rho(\psi)f(\psi;t) \tag{5.2}$$

where ρ is the density.

The evolution of the MDF in the stochastic reactor model is governed by the PDF transport equation, the right hand side of which describes the physical in-cylinder processes

labelled below:

$$\frac{\delta}{\delta t}\mathcal{F}(\psi;t) = \underbrace{-\sum_{j=1}^{N_S+1}\frac{\delta}{\delta\psi_j}[G_j(\psi)\mathcal{F}(\psi;t)]}_{\text{chemical reaction}} + \underbrace{\sum_{j=1}^{N_S+1}\frac{\delta}{\delta\psi_j}[A(\psi)\mathcal{F}(\psi;t)]}_{\text{turbulent mixing}} - \underbrace{\frac{1}{V}\frac{dV}{dt}\mathcal{F}(\psi;t)}_{\text{piston movement}} - \underbrace{\frac{\delta}{\delta\psi_{N_S+1}}[U(\psi_{N_S+1}\mathcal{F}(\psi;t)]}_{\text{convective heat transfer}} + \underbrace{\frac{\mathcal{F}_C(\psi;t)}{\tau_{crev}} - \frac{\mathcal{F}(\psi;t)}{\tau_{cyl}}}_{\text{crevice flow}} + \underbrace{\frac{\mathcal{F}_f(\psi;t)}{\tau_f}}_{\text{fuel injection}} \tag{5.3}$$

with the initial conditions:

$$\mathcal{F}(\psi;0) = \mathcal{F}_0(\psi) \tag{5.4}$$

Numerical solution

A Monte Carlo stochastic particle method is used to solve Equation 5.3. The PDF is approximated by equation 5.2 for N_{par} stochastic particles:

$$f(\psi;t) \approx \frac{1}{N_{par}}\sum_{i=1}^{N_{par}}\delta(\psi - \psi^{(i)}(t)) \tag{5.5}$$

where superscripts refer to individual particles.

This can combine with equation 5.1 to give an approximation of the mean in-cylinder quantities:

$$\langle\psi_j(t)\rangle \approx \frac{1}{N_{par}}\sum_{i=1}^{N_{par}}\psi_j^{(i)}(t) \tag{5.6}$$

An operator splitting technique is used to solve Equation 5.3, so that each term can be treated separately. The steps are described in Figure 5-1.

More detailed descriptions of the sub-models that make up the different parts of the PDF transport equation and the two-zone combustion model are included in Sections

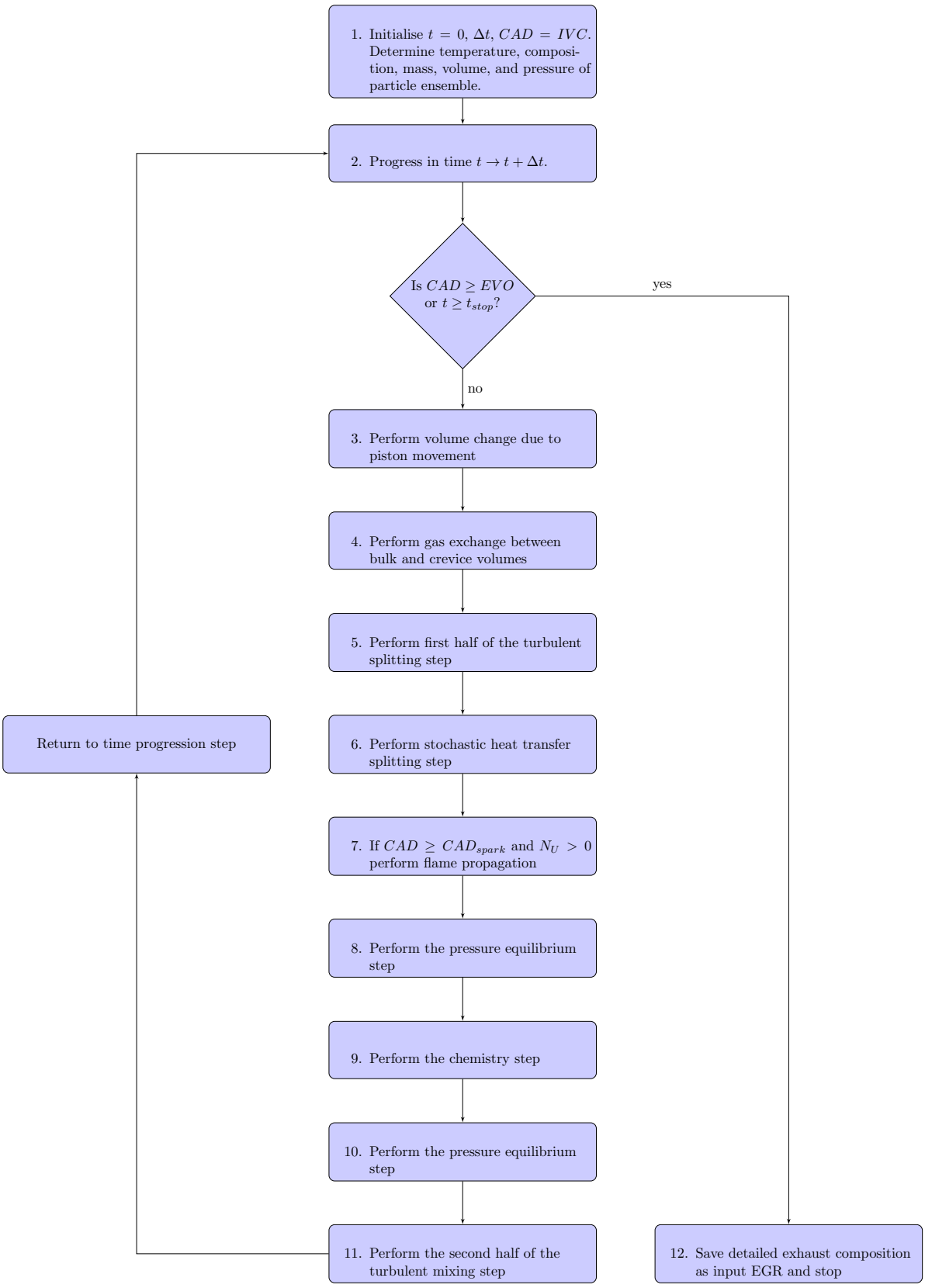

Figure 5-1: Process followed to solve Equation 5.3 by an operator splitting technique.

A.1 and A.2 of the Appendix.

5.3 Selection of kinetic mechanism

The choice of chemical mechanism is integral to the performance of a combustion model, as it describes the heat release and species development during the combustion process.

An important factor in the mechanism selection for this experiment was the computation time, and therefore the size of the mechanism. This moved the focus onto reduced mechanisms in order to achieve reasonable computation times[2].

As has been discussed in Section 2.3.4 commercial gasoline contains hundreds of different molecules which would be unrealistic to model in their entirety. So kinetic mechanisms are based upon surrogate fuels which represent the behaviour of gasoline. TRF mechanisms were considered for this investigation due to the large amount of work based on them in the literature, and their potential to model the NO interactions with both the paraffinic and aromatic components of gasoline. Despite the experimental fuel containing 10% ethanol it was decided not to use a mechanism incorporating ethanol since the interactions between ethanol and NO are not yet well understood [195].

A discussion of some of the available mechanisms in the literature that are appropriate for this project are discussed in Section 2.3.3 of the Literature Review chapter.

5.3.1 Evaluation of an appropriate chemical mechanism

Evidence from the literature, along with the required specifications for this work, guided the mechanism selection process.

Curran et al developed a detailed PRF mechanism which is widely used and validated across a wide range of operating conditions [157, 169]. Many researchers have used this mechanism as a benchmark with which to compare reduced mechanisms to quantify their accuracy.

[2] A semi-detailed TRF mechanism from Cai et al [8] consisting of only 339 species and 2791 reactions exceeded 15 hours during a test run.

A well validated mechanism developed by Sarathy et al [163] was trialled with the NO submodel from Cai et al [8] blended into it during some initial tests. The results of these tests revealed the potential for errors or misleading results if mechanism selection is not carried out prudently, and are presented in Appendix A.4.

The semi-detailed TRF-NO mechanism by Andrae et al [171] stands out as a well validated mechanism that has been developed with the impact of NO in mind, whilst keeping the mechanism at a manageable size.

Khan [96] states that Andrae's reduced TRF mechanism [181] performs just as well as Curran's detailed PRF mechanism [157, 169] after comparison between nine different mechanisms of varying orders of complexity on ignition delay data from shock tube experiments. He selected Andrae's mechanism along with two other reduced mechanisms for his work on SI autoignition.

The selected mechanism

The mechanism that was selected for this work is the semi-detailed TRF mechanism published by Andrae et al [171]. This mechanism is just small enough to keep simulation times within reasonable limits[3]. The detail of the NO model and its inclusion of the toluene interactions, plus validation across a wide range of operating conditions that included high pressure and temperature rapid compression machine data, served as motivation towards employing this mechanism. The lack of detail in the PRF reactions is a reason to proceed with caution in the analysis of these modelling results, but including more detailed models in this area would mean compromise would be required in the detail of the toluene/NO sub-models to keep the reaction number under 1000.

The mechanism of Zheng et al [172] was considered due to its size, but it was thought that the increased detail of Andrae et al's mechanism may provide more accurate insight into the relevant reaction paths for this study.

[3]Basic models used for calibration purposes could run in under 15 minutes, models with more detailed chemical outputs $\approx$ one hour.

Andrae's mechanism [171] was compiled from the following works:

- skeletal mechanism for iso-octane from a PRF model developed by Tanaka et al [223][4]
- skeletal model for n-heptane from Peters et al [224]
- Toluene model includes a detailed benzene sub-model by Alzueta et al [225] – with an oxidation subset for C1-C6 hydrocarbons, with a small subset involving NO.
- The C5 hydrocarbon subset has mainly been adapted from Zhong et al [226, 227]
- The C3-C4 subset is from Miller et al [228, 229] and Marinov et al [230]
- The C1-C2/NO subset comes from Glarborg et al [100]
- Extended to ethanol addition from Marinov et al [230]
- NO sub mechanism from GRI MECH 3.0 [68] (17 species,106 reactions)
- reactions involving HONO were added from Naik et al [186]
- TRF NO interactions were added from Anderlohr et al [170] with some reactions and rate constants modified to fit with the semi-detailed TRF mechanism[5]

Andrae et al validated the mechanism for conditions without NO using HCCI, RCM, and shock tube data with a focus on ignition delay times and pressure curve matches for the HCCI data. Laminar flame speeds were also compared between the experimental and simulated results [231]. For mixtures including NO validations were performed against HCCI and jet stirred reactor data [171].

[4] which itself is based on a model developed by Hu and Keck [168] which they describe as "remarkably successful" in knock prediction for SI engines

[5] Chen et al [5] also observed that the rate constants for some of the reactions in Anderlohr et al's mechanism did appear to be overestimated when compared to their data taken from a rapid compression machine

5.3.2 Fuel considerations

Although this work does use a TRF model to simulate the combustion effects, it is acknowledged that the fuel used to collect the experimental data did contain 10% ethanol. Dirrenberger et al [232] do claim that the addition of ethanol up to 15% does have a negligible effect on laminar burning velocities, but there is also evidence that it may influence NO interactions [118]. Evidence from the literature reveals that models for ethanol-NO interactions are not well developed [233], so this work was carried out with a TRF-NO mechanism that was well validated under the assumption that the exclusion of ethanol from the modelling work would not significantly affect its accuracy.

The selection of the surrogate fuel for this experiment was done using the correlation coefficients published by Cai et al [8] on octane number correlations for TRFs, which also contain a term for H/C ratio (R_{HC} in Equations 5.7, 5.8, and 5.9), and are detailed in Equations 5.7, 5.8, and 5.9. The octane numbers were then checked against the predictions of Morgan et al [193]. The resulting fuel composition is given in Table 5.1 with the details of the experimental fuel for comparison.

$$\begin{aligned}\text{Toluene [vol\%]} = {} & 1.9528 \times RON + 1.2987 \times MON - 5.3703 \times R_{HC} \\ & -0.0101 \times RON \times MON - 0.9047 \times RON \times R_{HC} \\ & -0.1244 \times MON \times R_{HC}\end{aligned} \tag{5.7}$$

$$\begin{aligned}\text{n-Heptane [vol\%]} = {} & -0.3592 \times RON + 1.9130 \times MON + 37.8896 \times R_{HC} \\ & -0.0097 \times RON \times MON + 0.2760 \times RON \times R_{HC} \\ & -0.9815 \times MON \times R_{HC}\end{aligned} \tag{5.8}$$

$$\text{iso-Octane [vol\%]} = 1 - (\text{Toluene} + \text{n-Heptane})\ \text{[vol\%]} \tag{5.9}$$

Table 5.1: Table of surrogate fuel properties versus the experimental gasoline

	Gasoline	Surrogate TRF
RON	95.5	94.3
MON	85.4	87.0
Paraffins	45.5% vol	77.9% vol
iso-octane	-	64.2% vol
n-heptane	-	13.7% vol
Olefins	7.3% vol	-
Naphthenes	8.7% vol	-
Aromatics	28.7% vol	22.1% vol
Ethanol	9.8% vol	-
C/H mole ratio	0.53	0.49
Stoichiometric AFR	13.97	16.1
LHV	41.21 MJ/kg	43.53 MJ/kg

5.4 Application of the model

The model was designed to simulate combustion in the Ford Fox engine presented in Chapter 4, with the experimental data presented in that chapter used for validation of the model. A brief recap of the engine parameters and test conditions is provided in Table 5.2.

Aside from the combustion system geometry, the SRM model has a large number of calibratable parameters to refine all of the sub-models which contribute to the PDF transport equation.

As the primary focus of this investigation was on EGR response and composition effects, the model was run from IVC to EVO and the injection model was not used. This choice was made in an effort to limit the number of variables that are introduced by the various sub-models, therefore limiting the potential error where exact boundary conditions are not well known.

The emissions data from Chapter 4 did not discriminate between NO and NO_2. A search through the literature revealed a study by Baronick et al [234] that measured gasoline NOx emissions to be composed of 99% NO, with the remaining NOx being NO_2. Initial simulations with the model supported this assumption, with the predicted

Table 5.2: Table of engine details and test conditions

Engine Type	In-line 3 cylinder, 4 valves per cylinder
Capacity(cc)	999
Bore/Stroke (mm)	71.9/82
Compression ratio	10.5:1
Firing Order	1-2-3
Specific power(kW/l)	92 @ 6000 rpm
Specific torque(Nm/l)	170 @ 1400-4500 rpm
Other	External cooled EGR Water cooled exhaust manifold
Speed	2200 rpm
EGR rate	0 - 18%
Inlet pressure	1.7 bar(abs)
Exhaust pressure	1.5 bar (abs)
Inlet temperature	30 degC

NOx emissions consisting of much less than 1% NO_2. This supported the decision to approximate the NOx content of the EGR as pure NO.

The model is calibrated to emulate the performance of the Fox engine investigated in Chapter 4; so the initial conditions have been selected to give equivalence between the experimental and simulation conditions. The fuel model was selected to give RON and MON values as close to the gasoline used for the engine as possible. This resulted in the LHV being slightly higher than the test gasoline, so the model has been adjusted to match the energy introduced to the cylinder during the experimental phase.

5.4.1 Selection of representative cycles for calibration

Since simulation models have very well defined initial conditions (most commonly at IVC for combustion models) they are usually validated against experimental methods which are designed to minimise the uncertainty in these initial conditions. These experiments are usually based on shock tube, rapid compression machine, and single cylinder engines – giving the most confidence in charge composition and initial temperature and pressure.

The use of a multi-cylinder engine for the experimental phase introduces a large amount of uncertainty in the initial conditions for individual cylinders. This makes the selection

of representative cycles more difficult when comparing against the data produced by simulation.

A brief look at the variation in data for a 300 cycle log (such as that displayed in Figure 5-2) demonstrates the difficulty in defining conditions for a model. This variation is of course also present for single cylinder experiments, but is magnified by the additional variability introduced by the extra cylinders – each cylinder interacts with the others to affect wall temperatures, breathing characteristics, and vibration of the cylinder walls and roof.

The target for the modelling results is therefore to emulate a representative cycle from the data rather than to match its behaviour exactly – this would require a far more complex model which is beyond the scope of this work.

A study by Chen et al [118] selected representative cycles by a cost function that minimised the distance from the means of both the combustion phasing and the knock peak. This was conducted on the octane rating engine, a single cylinder engine which gave much more accurate data for initial conditions and breathing characteristics.

Since the current study is concerned with knocking behaviour a mean pressure trace, or a cycle close to the mean, will not be representative of the limiting effect of knock for that condition. Even at heavily knocking conditions only a fraction of the cycles exhibit significant knocking behaviour[6] – so the selection of a representative cycle when considering the knocking behaviour of an engine is important.

To calibrate this model the experimental cycles making up the 90-95th percentile of peak pressures were averaged to give a target pressure trace. The mean was used in an effort to reduce the impact of any outlying cycles that could skew results. These cycles are illustrated in Figure 5-2 by the red traces, where the grey traces show all 300 cycles from a log taken at 0% EGR. The spread in pressure cycles seen in this plot is characteristic of the entire dataset.

[6] An example of the distribution of knock intensities in a given 300 cycle log at knocking conditions is given in Figure 4-12 in Chapter 4

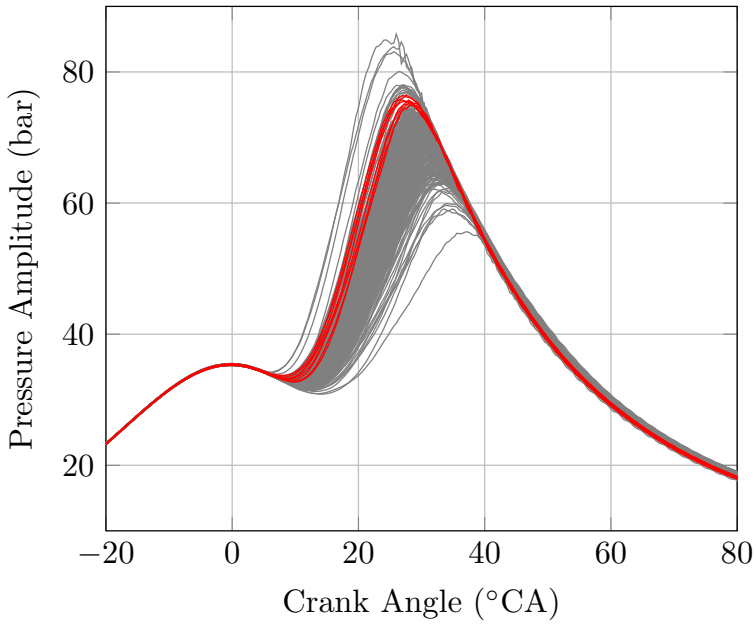

Figure 5-2: Illustration of the 90-95th percentile pressure traces in a 300 cycle log, ordered by peak pressure. It can be seen that the highlighted traces (in red) capture most of the cycles most prone to knock, whilst excluding any outliers with a more extreme pressure rise.

To assess the models performance a region of the pressure plot was defined for comparison. This was defined by the spread between the highest and lowest of the 15 cycles (top 5%) closest to the characteristic trace (judged by minimum RMSE). The peak pressure amplitude and phasing were considered the most important factors in assessing the match between the simulated and experimental data.

5.4.2 Significant parameters for the model calibration

Before constructing the combustion model the residual gas fraction was estimated using a 1-D model in GT Power that was provided by Ford, and previously validated at similar conditions. This value was assumed for the entirety of the EGR sweep data. The residual gas composition was blended into the oxidiser in the model to allow independent control of the external EGR composition.

The calibration was performed for a speed of 2200 rpm, with a boost pressure of 1.7 bar. Initial calibration was performed for the 0% EGR case at KLSA. This was then verified across a spark sweep for that condition before introducing dilution effects. Good

performance across a spark sweep was required since the spark sweep windows did not overlap across all EGR rates.

In initial tests with particle numbers of 5, 50 and 100 there were no discernible differences in cylinder pressure results, indicating that for this application the number of particles did not affect cylinder pressure results significantly. This is largely due to the model being initiated with a homogeneous mixture with no injection event, so the only significant impact of the particle number was on the end gas chemistry and species evolution. Inhomogeneities did develop during the simulation due to heat transfer and chemical effects but not to a significant enough degree for the bulk pressure to be affected.

In consideration of this the EGR response tests in Section 5.6 used five particles. The modelling assessments relating to end gas chemistry in Section 5.7 used 100 particles to improve the fidelity of the end gas chemistry in the model.

The calibration of the model parameters primarily pertained to those that affect the flame propagation model. The chemistry model is indirectly affected by their impact on local pressures and temperatures. The parameters that were primarily used for the calibration process are summarised in Table 5.3 and details of how they affect calculations within the model are provided in Section A.1 of the Appendix.

Agbro et al [218] describe an in-built optimisation tool in the LOGE SRM software to assist in the calibration of the initial conditions and mixing time parameters. Despite this the results that they present do not appear to achieve a very accurate match with the experimental pressure trace that they targeted.

In the absence of an in-built optimisation tool for the CMCL software, a calibration tool was developed in Matlab to accelerate the calibration process. This worked by calculating the RMSE for each simulated pressure curve and returning the parameter values that corresponded to the best matches. Iterations of sweeps were performed with the parameters relevant to the flame propagation model, mixing model, and initial

Table 5.3: Parameters used for the calibration of the combustion model. Details of how these parameters influence the calculations within the model are given in Section A.1 of the Appendix.

Calibration stage	Parameter	Effect
Motored portion	IVC Temperature	Higher temperatures reduce the charge mass
	Heat transfer multiplier	Larger multiplier decreases TDC pressure for given charge mass
	Compression ratio	Variations affect rate of pressure increase
Combustion	Flame scale constant	Larger values increase the flame propagation rate and advance SOI
	Characteristic time constant	Larger values decrease flame propagation rate and retard SOI
	Wall quenching constant	Larger values quench combustion further from the wall, mostly this only reduced AI propensity and increased unburned products
	Wall influence constant	Larger values reduce the peak pressure without affecting angle of P_{max}
	Pressure equilibration constant	Larger values reduce burn rate near end of combustion
	Turbulence dissipation constant	Larger values reduce burn rate after SOI

conditions[7] until a satisfactory match was achieved. This served as a rather basic brute force method to hone in on successful parameter value combinations.

An acceptable RMSE limit was derived from the spread between the 90th and 95th percentile pressure curves illustrated in Figure 5-2. The 0% EGR KLSA case that was used for this calibration gave an RMSE value of 0.5 with this method, so this value was used as the threshold during the calibration process. Once this threshold had been reached the following optimisation was performed by eye to ensure a good match in the timing and magnitude of the simulated pressure peak.

[7]The parameters that were focused on were those recommended in the calibration guide provided by CMCL Innovations.

5.4.3 The calibration process

The calibration process was broadly as follows:

1. Enter the engine geometry and test conditions such as speed, initial pressure and equivalence ratio into the model.
2. Run model to compare motored portion of pressure curve with experimental data.
3. Refine initial temperature, pressure and compression ratio to match motored portion of pressure curve, and to match the expected trapped mass as closely as possible.
4. Repeat steps 2 and 3 until motored pressure and trapped mass give a good match, the heat transfer multiplier can be used if required to obtain a good match.
5. Run a series of simulations with parameters relating to the flame propagation, turbulence, and pressure equilibration being swept through a coarse grid of expected values.
6. Compare the simulation results to the experimental pressure curve with the assistance of a plot of RMSE values against all parameter values, and refine the parameter sweeps according to the results that gave a minimum RMSE.
7. Repeat step 6 with an increasingly fine mesh until the RMSE is within the determined threshold. Make final adjustments by eye to match the timing and amplitude of P_{max} and the start of combustion.
8. Once the model represents a single condition well, run it over a spark sweep to compare its response against experimental data. Repeat steps 1-7 with small adjustments to the geometry and heat transfer if the behaviour during a spark sweep does not match the experimental data.

The calibration process is separated in this way to refine the fitting process, and therefore avoiding the fitting of false parameters in order to achieve a curve fit that is not repre-

sentative of the real system. The first step deals with the boundary conditions that can be measured with confidence and are therefore well known. Steps 2-4 refine the charge mass to be representative of the real system, and therefore provide the initial conditions for the start of combustion. Whilst the compression ratio for the engine is defined in the engine specification it is common for this to deviate by up to 0.5 points due to tolerances and rounding, so small adjustments to this in the model are not invalid.

Once the motored portion of the curve indicates a well matched charge mass, steps 5-7 refine the empirical parts of the combustion model to improve the burn rate. This is tested in step 8 to ascertain whether the model response is representative of the combustion system, or whether it has only been tuned to the specific operating point at which the calibration was performed.

Screen shots of the calibration tool in use are provided in Figures A-4, A-5 and A-6 in Section A.3 of the Appendix to illustrate an example of step 6 above.

In order to improve the response to a spark sweep the pent roof angle of the cylinder was adjusted to achieve a better match for the initial flame kernel growth. The cylinder roof in the model is a greatly simplified representation of the geometry of the real engine, so this adjustment was deemed acceptable since it replicated the surface area and clearance volume more accurately than the initial estimation of the cylinder pent roof angle.

5.5 Validation of the model over spark sweeps without dilution

A comparison was made between the simulated pressure traces during a sweep of spark angles against experimental data collected across the same spark sweep.

Calibration of the model was performed at KLSA since knocking combustion is the primary interest in this investigation. The resulting calibrated model was then applied to spark angles across the entire sweep performed at 0% EGR during the experimental phase (ranging from 5°CA after TDC (-5 in figure legend) to 1.5°CA ATDC (-1.5 in figure

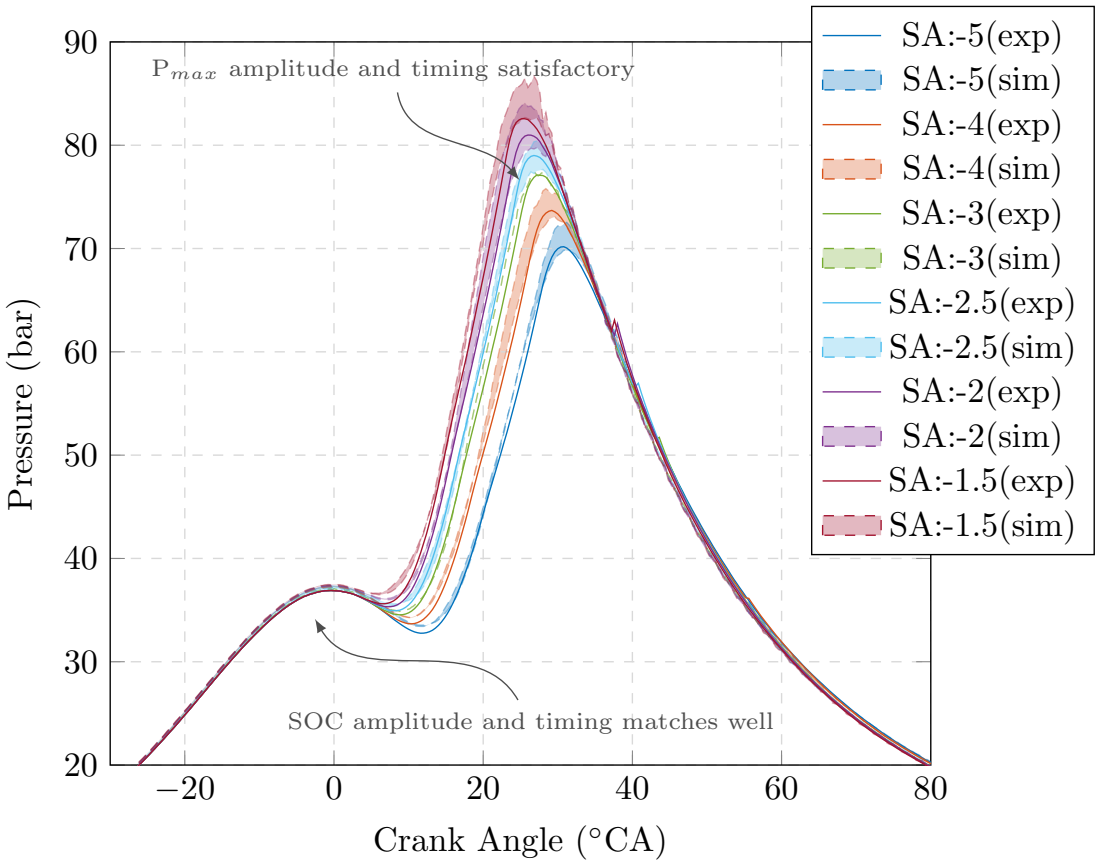

Figure 5-3: Comparison of simulation results for a spark sweep against experimental data. The shaded regions represent the experimental data whilst the solid traces represent the simulation data.

legend)). The comparison with the experimental data across the same spark sweep is shown in Figure 5-3 with the shaded traces representing the experimental data and the solid traces representing the simulation results.

By nature the experimental data exhibits less regular spacing between pressure curves for each ignition angle, but overall the results in Figure 5-3 achieve a satisfactory match for behaviour across a spark sweep.

5.6 Performance of the model in predicting dilution effects

Once the model had been validated for a spark sweep at the 0% EGR condition its response to dilution was tested against experimental results. The initial test focused on

the response to EGR addition at equivalent ignition angles. This limited the available EGR rates to 3, 6, and 9% due to the limit on retardation at higher EGR rates. For these tests the EGR was modelled without any minor species and compared to the experimental results for catalysed EGR.

Figure 5-4 presents the results of an initial test of EGR response, with all four test points taken with an ignition angle of -2 CAD (BTDC). It is immediately apparent that the dilution effects of EGR are not well captured in this plot. The rapidity with which the flame growth occurs, and the magnitude of the peak pressure, suggest that the EGR correlation within the model is not reducing the combustion rates enough to represent those seen experimentally.

Whilst the inlet temperature was reduced by higher EGR rates during the experimental phase, the same was not true for the model since the total charge mass still provided a good fit to the motored portion of the pressure curve. For this reason the initial temperature was kept constant for increasing EGR rates in the model.

5.6.1 Adjustments to the laminar flame speed correlation

The laminar flame speed correlation is the only part of the flame propagation model that includes any dependency on dilution of the in-cylinder mixture. As such it is the most obvious candidate to adjust to improve the dilution response of the model.

To minimise the complexity of this study only the laminar flame speed coefficients relating to dilution response were altered. But it must be noted that reviewing the complete set of laminar flame speed correlations for the gasoline model may be prudent in order to improve its applicability to modern fuels.

The flame speed correlation employed by the SRM software is based upon the laminar flame speed correlations published by Heywood [18], which were originally derived from experiments in a combustion bomb by Rhodes and Keck in 1985 [235]. Their experiments were performed with "multicomponent fuels similar to gasoline", with a CO_2 and N_2

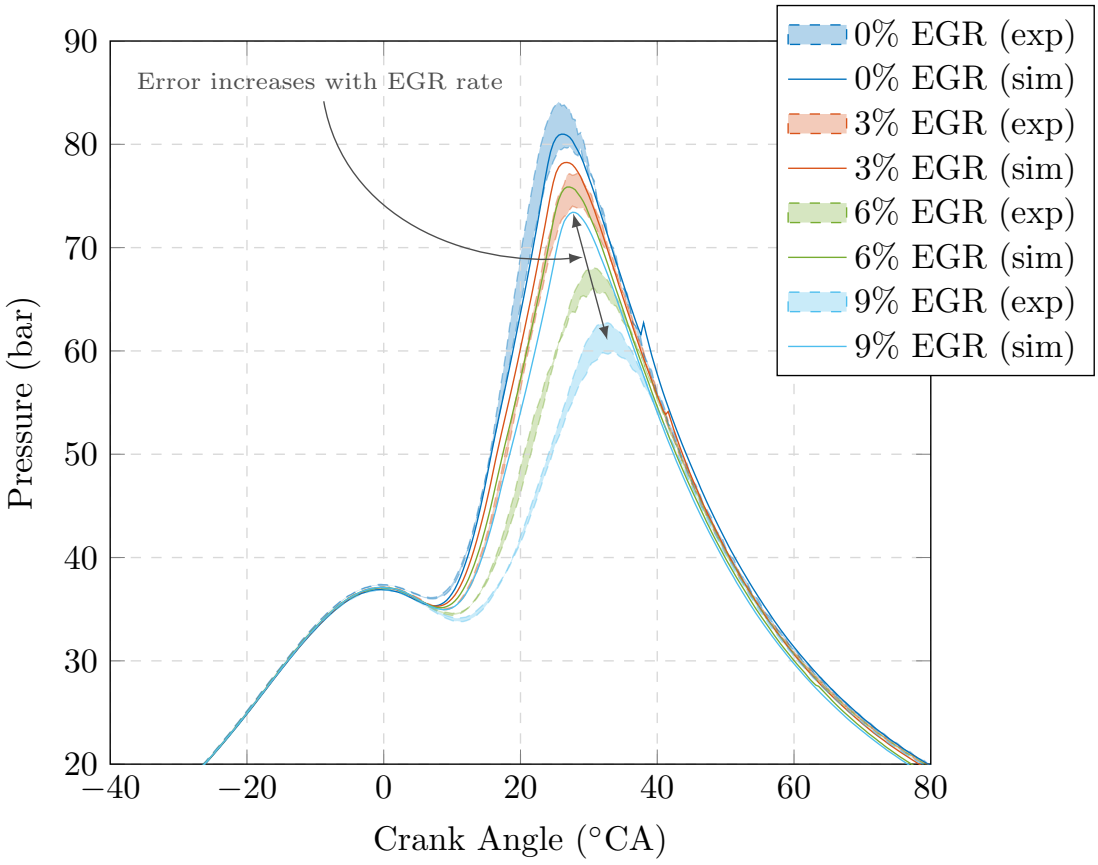

Figure 5-4: Comparison of simulation results for EGR rates of 0,3,6 and 9% against their corresponding experimental results – all with a spark angle of -2 CAD. It is apparent in this plot that the dilution effects of EGR are not well captured.

diluent being used to approximate EGR effects, with the correlation taking the form:

$$S_L(\tilde{x}_b) = S_L(\tilde{x}_b = 0)(1 - EGR_A \tilde{x}_b^{EGR_B}) \tag{5.10}$$

Where $\tilde{x}_b$ is the mass fraction of burned gas (EGR and RGF) and EGR_A and EGR_B are constants with values of 2.06 and 0.77 respectively.

With recent progress in gasoline fuels and in high load gasoline combustion systems the applicability of this correlation for modern engines could be challenged. Both Rockstoh et al [236] and Cracknell et al [237] highlight the advances that faster burning fuels have enabled, the former with a focus on the "design" of synthetic gasoline blends with higher laminar flame speeds and EGR tolerance.

This kind of development of synthetic fuel blends with optimised properties provides a strong argument for the laminar burning correlations in combustion modelling to be likewise updated. Such work has been completed recently by [238–240] who all propose chemistry-based methods to derive the correlations. Duva et al [241] investigated laminar flame speeds of iso-octane with CO_2 dilution to simulate EGR in a constant volume combustion chamber, finding a reduction in S_L of 47-51% for 15% CO_2 dilution. Substituting an EGR rate of 15% into Equation 5.10 provides a reduction of 48% which, although not designed for pure CO_2, gives broadly similar results to those found by Dvua et al [241].

Bellis et al [242] have published updated correlations based on simulation work done in Canterra software with the same semi-detailed mechanism from Andrae et al [171] that is used in this thesis. Their study found that S_L mainly depended on the sensitivity of the fuel, which allowed them to simplify the data fitting – although having said this they do have 5th order terms for most of their coefficients. This means that instead of the 10 coefficients used by Rhodes and Keck's model [235], they use 44 coefficients to model the interdependence between the equivalence ratio, fuel sensitivity, temperature,

and pressure.

The SRM suite software offers the opportunity to adjust the values of the coefficients, but not the number of coefficients, that impact the laminar flame speed. Unfortunately this rules out the possibility of testing the performance of Bellis et al's correlation [242] in this model.

Therefore the coefficients that were identified to calibrate the model's response to EGR addition were the two constants, EGR_A and EGR_B from Equation 5.10.

For the purposes of this test it was required that the ignition angle was common throughout the range of EGR rates used for the test. This restricted the test conditions to a maximum EGR rate of 9%, since at higher EGR rates the spark was not retarded enough to overlap with ignition timings at 0% EGR during the experimental phase.

The model was run with EGR rates of 3, 6, and 9%, using the calibrated parameters from the 0% EGR condition.

The two EGR coefficients were swept through values from 1.5 to 5 and from 0.4 to 1 for EGR_A and EGR_B respectively. Residuals were blended into the oxidiser composition for the purposes of this test, so that the values of the EGR coefficients did not impact the 0% EGR case.

Despite being a fairly crude method, the RMSE was used again as a measure of fit between the simulated pressure traces and corresponding experimental pressure curves. Since only two parameters were being varied this effectively provided a "surface of fit" for each EGR condition, illustrated in Figure 5-5[8].

Each of the surfaces has a "trough" of lowest RMSE values where the RMSE values along each trough (displayed in Figure 5-6) remain fairly constant. Figure 5-6 also demonstrates how the RMSE values increase for higher EGR rates, which suggests that other parameters need to be adjusted to improve the EGR response further. Viewing these

[8]This method is broadly similar to the original calibration method used earlier in this chapter, but in that instance more than 2 parameters were being varied so the "surface of fit" extended into multiple dimensions.

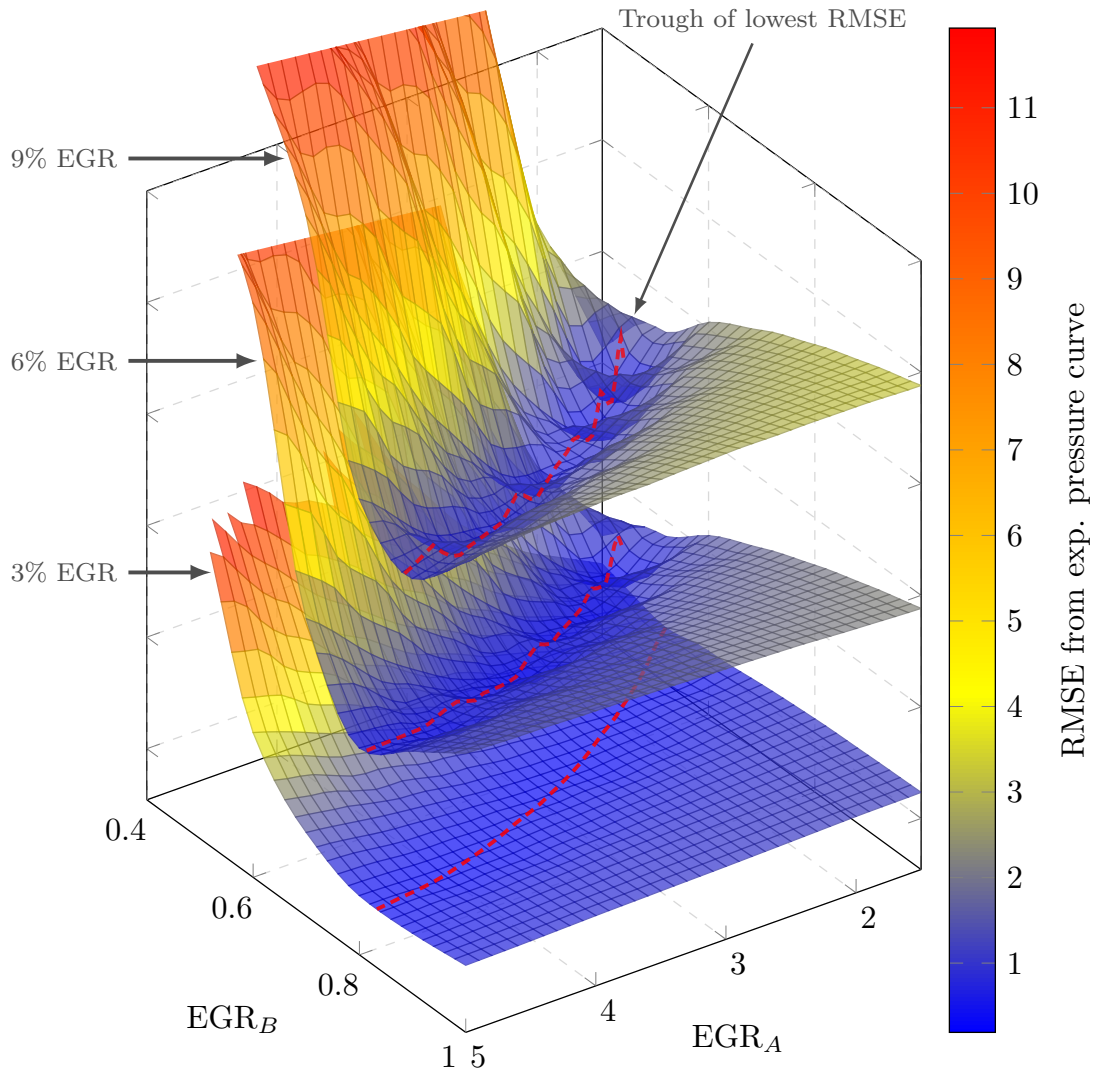

Figure 5-5: Stacked "surface of fit" plots for 3, 6 and 9% EGR. The dashed red lines lie along the troughs of lowest RMSE for each EGR rate.

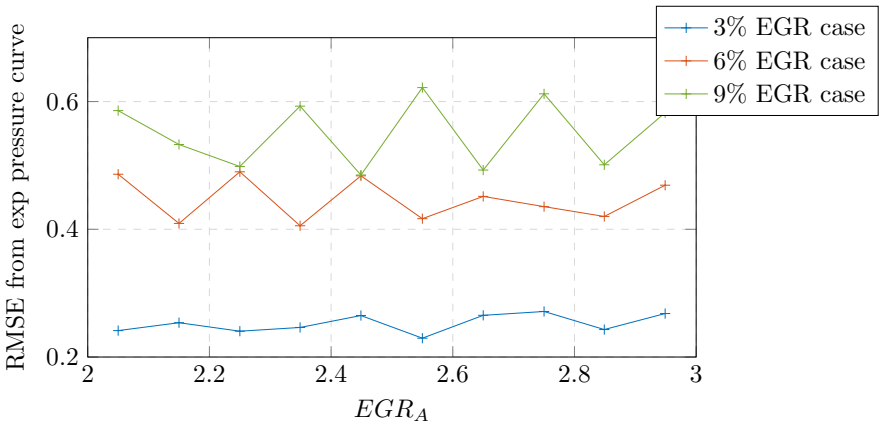

Figure 5-6: The RMSE values along each trough in Figure 5-5 show relatively constant values, which also increase with higher EGR rates.

troughs from above, as illustrated in Figure 5-7, reveals their intersection point.

The resulting EGR response with the adjusted EGR flame speed coefficients is illustrated in Figure 5-8 for the constant ignition angle that was used. Whilst the match improved, the 6 and 9% EGR conditions still show a considerable discrepancy.

Since it was assumed that the EGR coefficients that provide the best fit for this particular model lie in the space illustrated in Figure 5-5, another method was tested in an effort to move the EGR response closer to that seen in the experimental data.

Overlaying the three surfaces and adding their values produces the surface plotted in Figure 5-9. The minimum total RMSE predicted by this model occurs at EGR coefficient values of $EGR_A = 1.9$ and $EGR_B = 0.52$, indicated by the orange arrow in Figure 5-9.

This second method improved the match for the 6% EGR case, but reduced the accuracy for the 9% EGR case. These results demonstrate that a certain level of improvement can be achieved by adjustment of the laminar flame speed model, but with the limitations imposed by the software on the format of the flame speed model a satisfactory match cannot be achieved for this model.

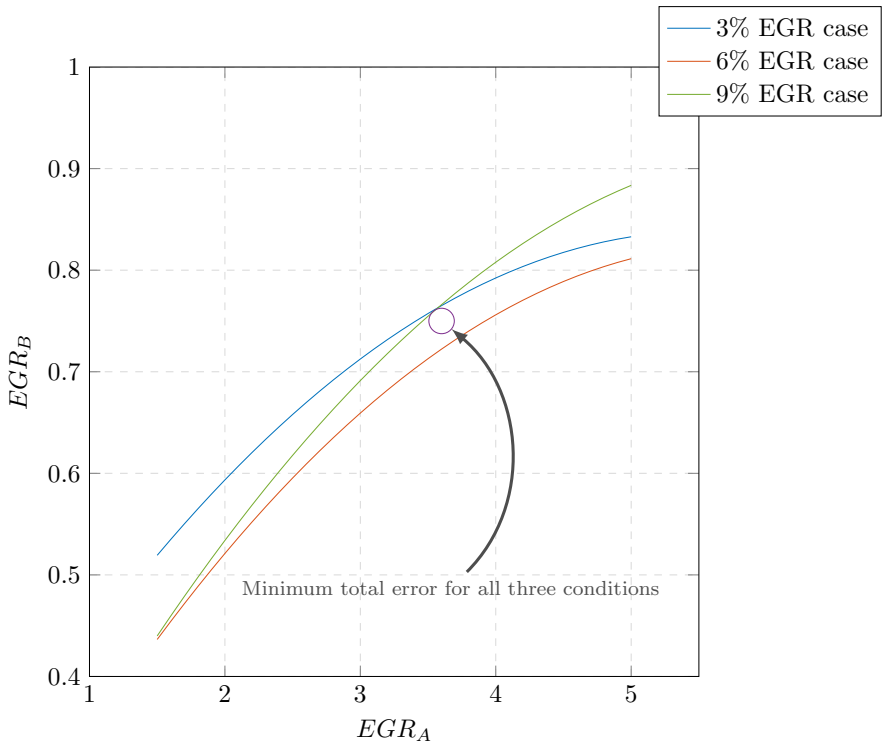

Figure 5-7: The best fit lines along each trough do not have a common intersection point, so the point of lowest error was selected, which corresponds to values of $EGR_A = 3.6$ and $EGR_B = 0.75$. The model was re-run with these values to assess the adjusted response to dilution.

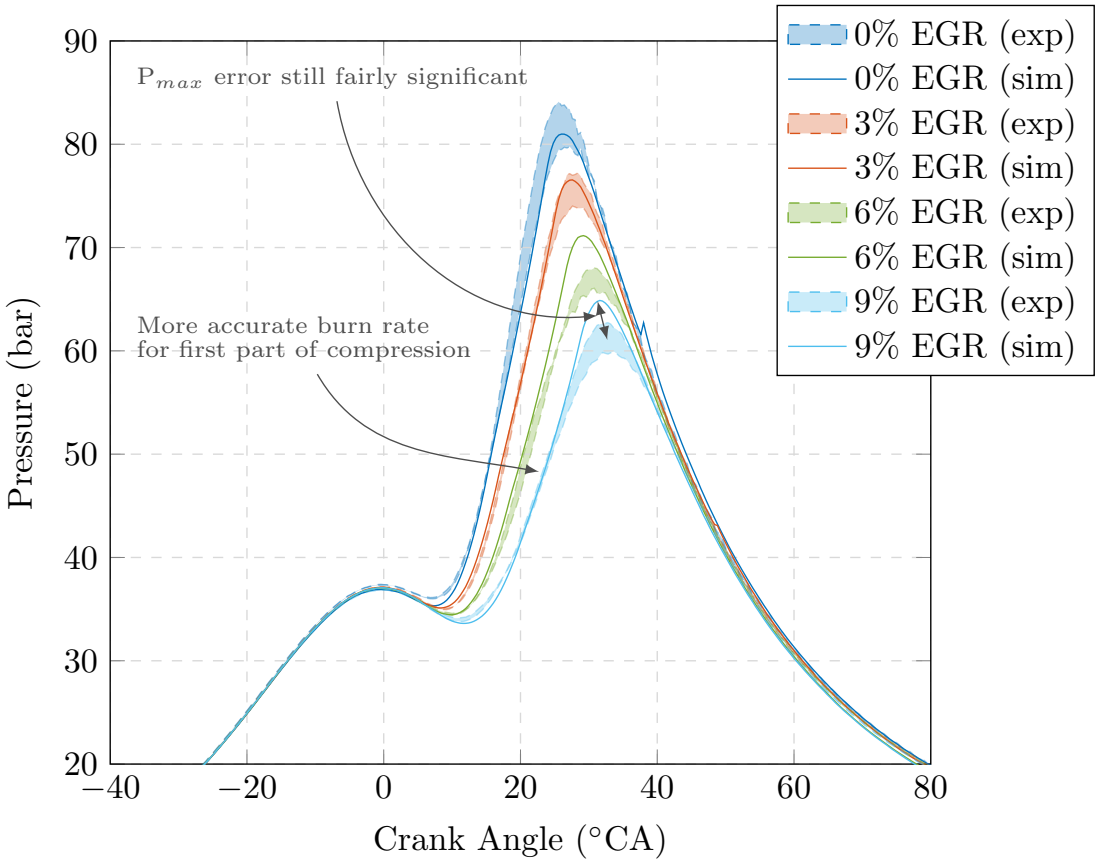

Figure 5-8: Comparison of simulation results for EGR rates of 0,3,6 and 9% with adjusted laminar flame speed coefficients against their corresponding experimental results – all with a spark angle of -2 CAD. Whilst the dilution response has been improved for this iteration, it still requires further improvement.

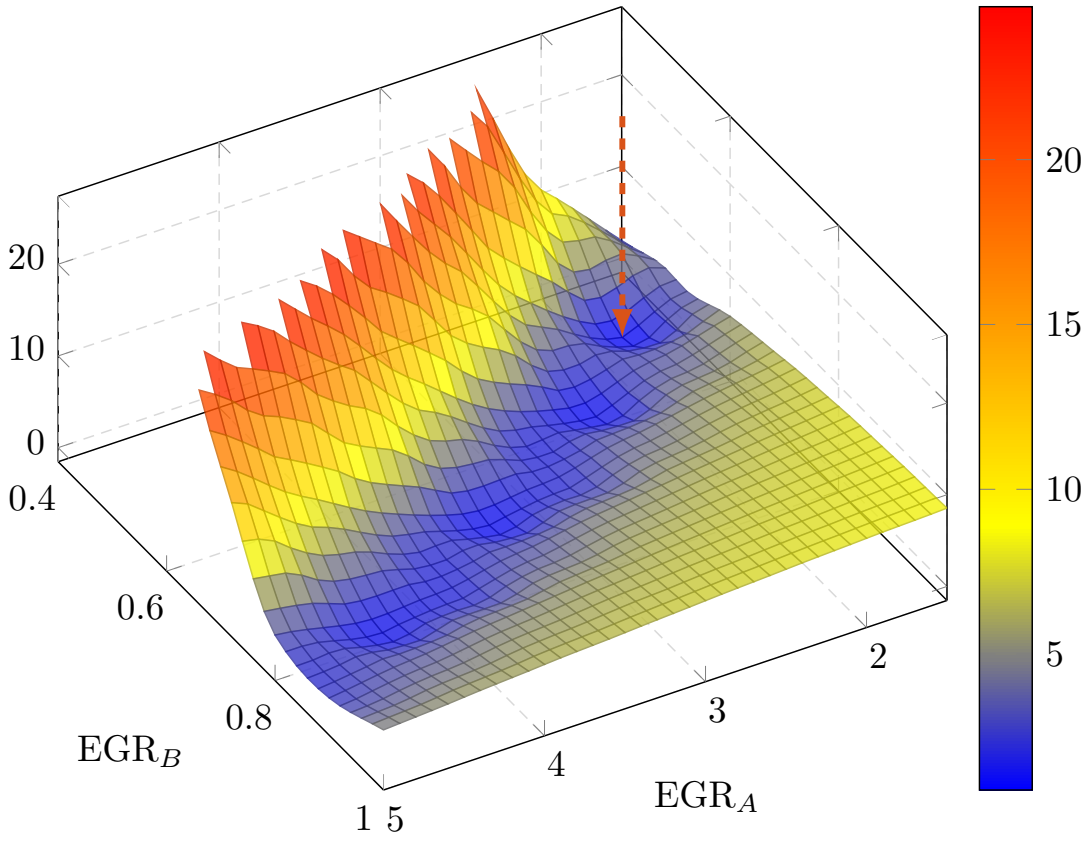

Figure 5-9: The surface produced by adding the RMSE values from all three conditions in Figure 5-5 together. This produces quite a different minimum to that found by the least squares difference method from the trend lines shown in Figure 5-7, although it should be noted that the RMSE values still appear to have a region of minima along the valley of the surface.

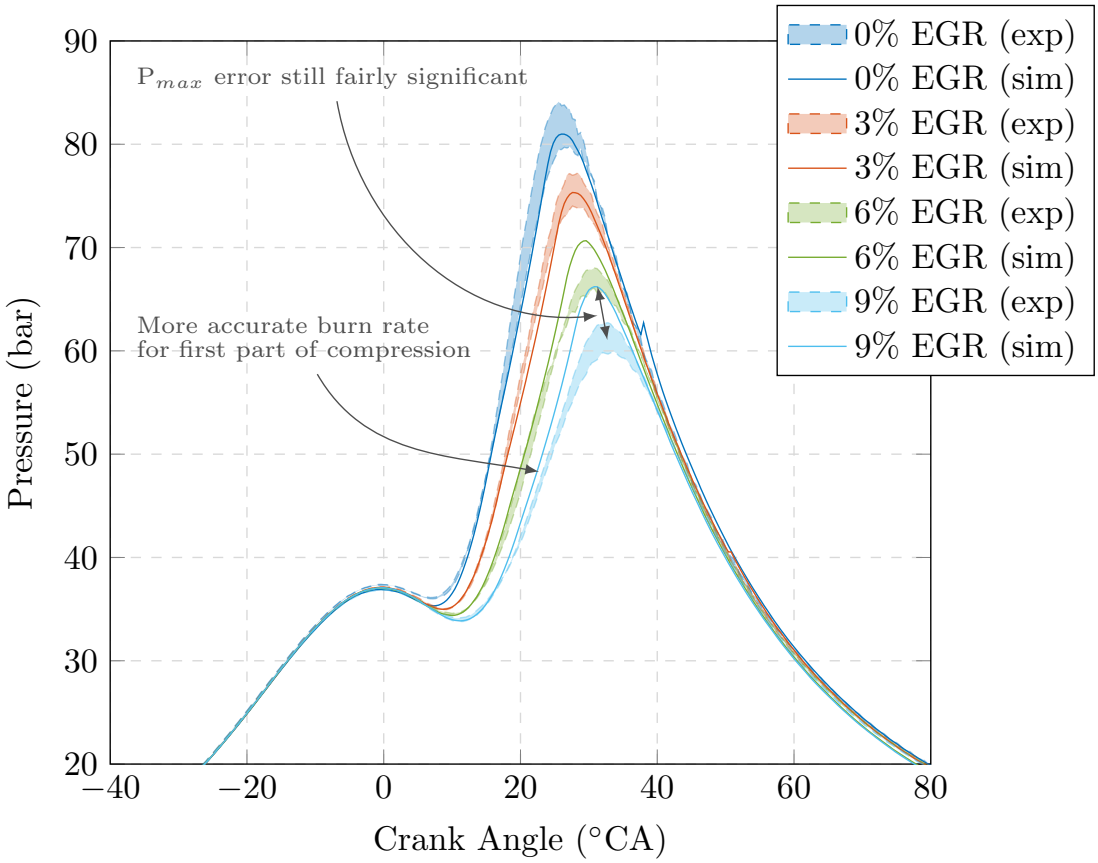

Figure 5-10: Comparison of the simulation results for EGR rates of 0,3,6 and 9% with adjusted laminar flame speed coefficients from the method described in Figure 5-9 – all with a spark angle of -2 CAD. There is very little difference from the response shown in Figure 5-8.

5.6.2 Adjustments to the fractal flame propagation model

Whilst adjustment of the EGR coefficients of the laminar flame speed model has achieved some improvement, it is evident that this adjustment alone is not sufficient to provide a satisfactory response to dilution.

Two of the parameters from those used to calibrate the initial model can affect the pressure curve in the manner required to improve the match for higher EGR rates.

Adjustments to the wall influence factor

The first parameter that was tested is the wall influence factor. This defines the distance from the cylinder wall at which the flame-wall interactions start to influence the flame speed. More details of how it fits within the model are included in Appendix A.2. An increase to this parameter with EGR rate equates to the physical effect of the EGR gases increasing the strength of the flame-wall interaction effect. There is no evidence of this phenomenon in the literature, it was selected for tests here because of the effect that it has on the resulting modelled pressure curve.

At this stage only a linear relationship was investigated to test how well the fit can be improved, but more detailed optimisation processes are recommended for further work in this area. The wall influence factor was increased to the value at which the error at the 9% condition was minimised whilst keeping all other parameters constant. This provided the gradient for its relationship with the EGR rate.

The wall influence factor defines the distance from the wall at which the flame speed will start to be reduced. This has the effect of lowering the peak pressure without impacting significantly on the combustion phasing.

The results of the first test, displayed in Figure 5-11, show the improvement gained by adjustment of the wall influence factor. Whilst peak pressure values are improved, the error in the phasing of the peak pressure increases progressively with the EGR rate.

This test demonstrates the application of a relationship that has no physical basis but was

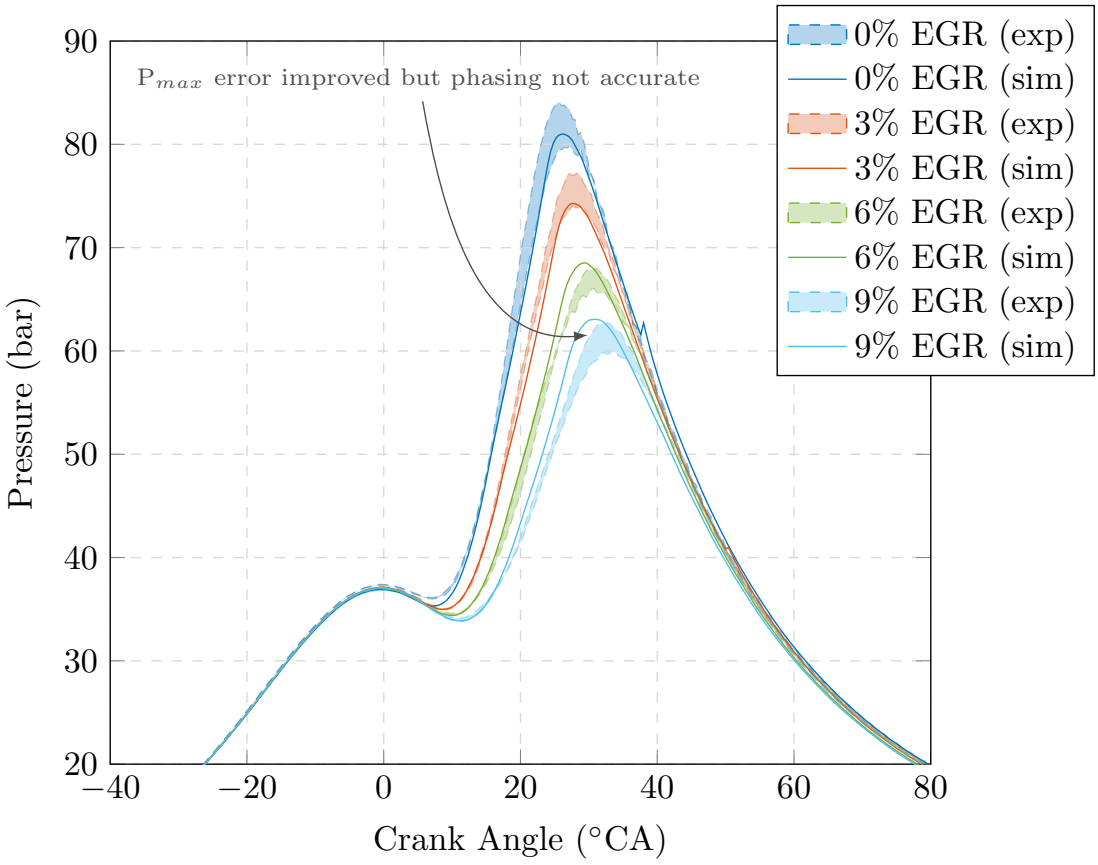

Figure 5-11: Comparison of the simulation results for EGR rates of 0,3,6 and 9% with adjusted laminar flame speed coefficients plus a relationship between EGR rate and wall influence parameter.

selected purely for the numerical effect within the model in moving the response closer to that seen experimentally. Although an improvement is observed in the match between the predicted and experimental results, it does not provide a satisfactory response. This demonstrates an example of how the model may be manipulated, but the wall influence factor is not considered a suitable parameter to achieve the desired effect.

Adjustments to the turbulence dissipation factor

The second parameter that was adjusted to test the improvement that it could offer to the EGR response was the turbulence dissipation constant. This describes the reduction in turbulent energy as the flame propagates through the cylinder, therefore affecting the angle and magnitude of the maximum pressure. Again, only a linear relationship was investigated. An increase to the turbulence dissipation constant with increasing EGR rate effectively increases the damping of the turbulent kinetic energy with higher EGR rates.

Whilst this phenomenon is not documented in the literature, it may be feasible to propose that EGR addition could impact the turbulent kinetic energy.

The turbulence dissipation factor is a term within the k-ϵ turbulence model which defines the rate at which the turbulent kinetic energy dissipates, denoted by ϵ in the turbulence production equation:

$$\frac{dk}{dt} = \frac{dk_{inj}}{dt} + \frac{dk_{den}}{dt} + \frac{dk_{squ}}{dt} + \frac{dk_{prod}}{dt} - \epsilon \tag{5.11}$$

where k_{inj}, k_{den}, k_{squ}, k_{prod} denote the kinetic energy effect of injection, density change, squish, and swirl/tumble respectively.

The viscous dissipation term, ϵ, is given by:

$$\epsilon = \frac{nk^{\frac{3}{2}}}{V_{cyl}^{\frac{1}{3}}} \tag{5.12}$$

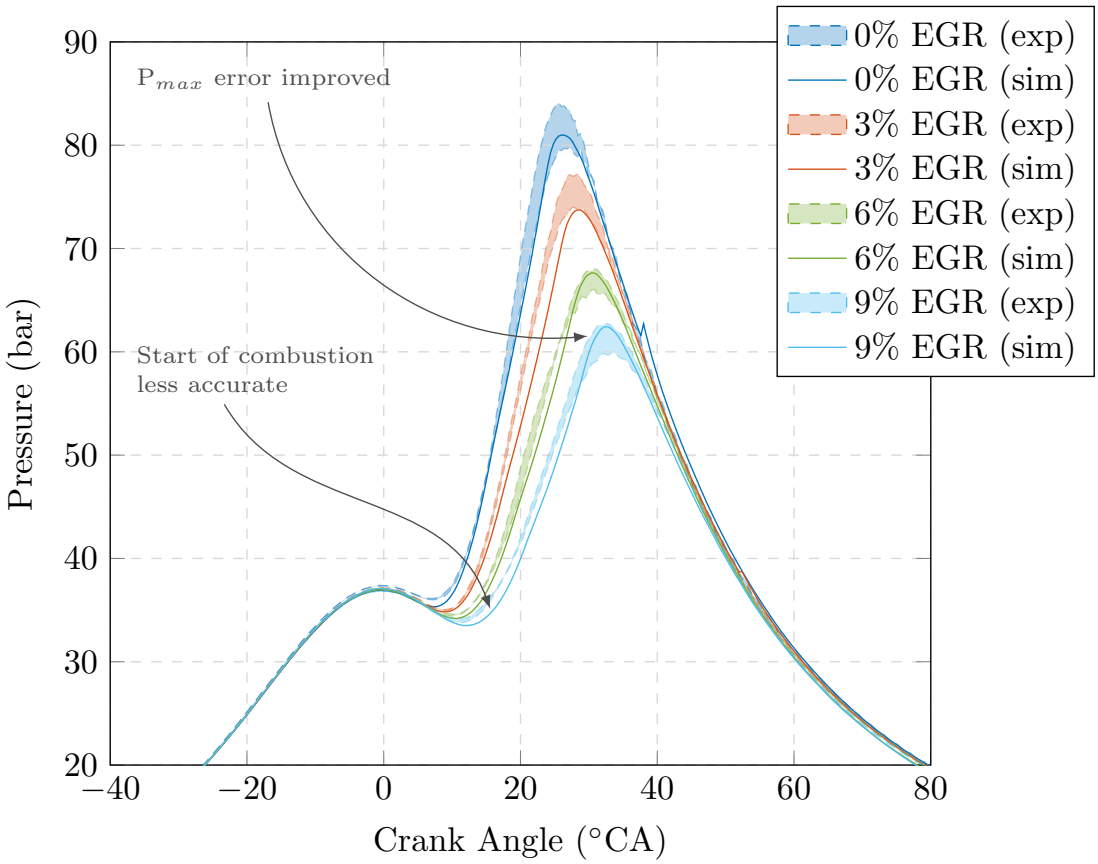

Figure 5-12: Comparison of the simulation results for EGR rates of 0,3,6 and 9% with adjusted laminar flame speed coefficients plus a relationship between EGR rate and turbulent dissipation.

where V_{cyl} is the instantaneous cylinder volume, and n is the turbulence dissipation constant.

The proportional increase to the turbulence dissipation constant improved the phasing of the maximum pressure as well as improving the accuracy of its amplitude (Figure 5-12). The trade-off was slight discrepancy in the pressure development at the start of combustion, which did not develop quite as rapidly as shown in the experimental results.

These results provide encouragement that although the initial model did not replicate dilution effects accurately, some small changes to the sub models can improve this match considerably. For this model it appears that updated correlations for the fractal flame propagation model would improve the capability of the SRM to model the combustion

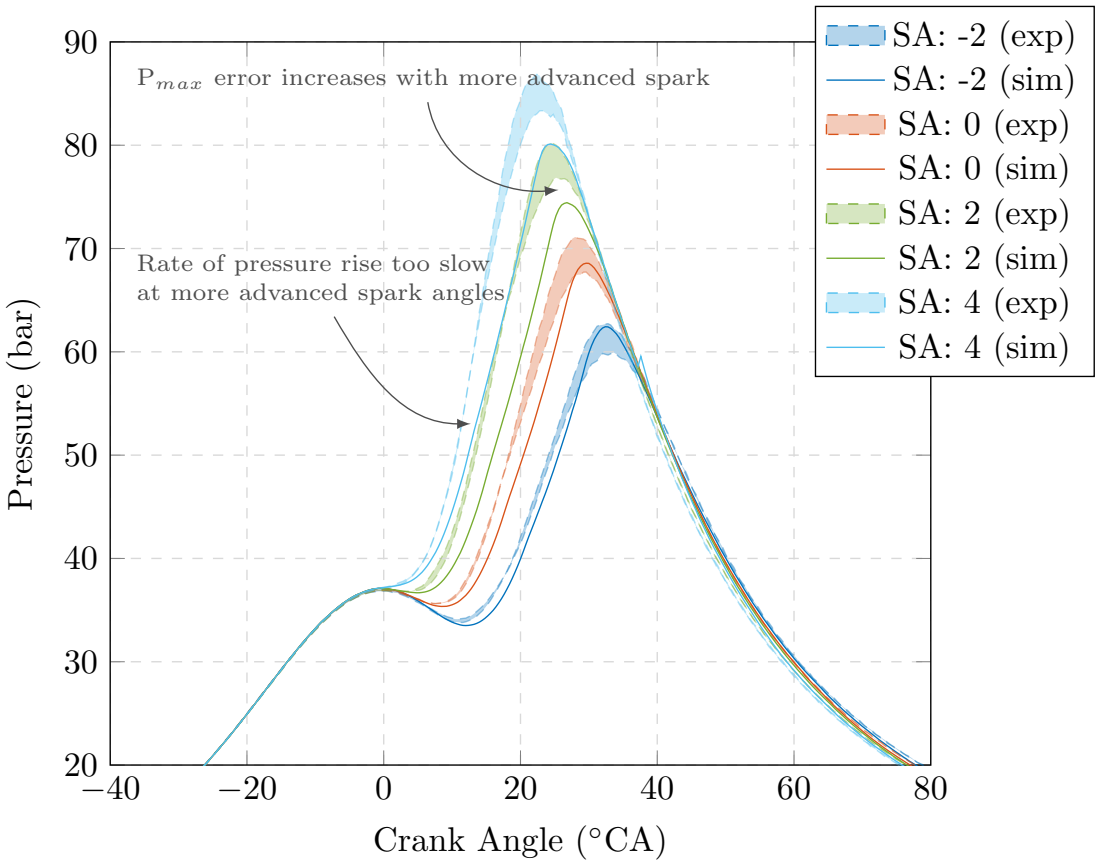

Figure 5-13: Test for a spark sweep at 12% EGR to confirm whether the prediction for different spark angles remains accurate with inclusion of EGR. The accuracy appears to diminish at the extremes of the range tested, but it must be noted that this is a larger range of spark angles than that tested for the 0% EGR case.

effects of charge dilution.

The accuracy of the simulated results at more advanced ignition angles was not sufficient to compare higher EGR rates, which span more advanced ignition windows than those presented for the 0-9% EGR cases, as is evident in Figure 5-13. It is evident that further improvements are required to enable accurate prediction of EGR effects over a wider range with this model.

Improvement of the model to replicate EGR response across a wider range of operating conditions does not fall within the scope of this thesis as it would require a much broader range of experimental data. It is anticipated that any work undertaking this task would benefit from the use of a single cylinder engine to allow much more strictly defined

boundary conditions than can be offered for a multi-cylinder engine.

At this stage the SRM still relies heavily on the calibration of empirical relationships to model combustion. This limits its predictive capability compared to CFD methods, but it can still go some way to bridging the gap between fully empirical and CFD methods. There is potential for further improvements to enhance the predictive capability of the SRM model, especially by integration of CFD methods to define boundary conditions with more confidence, but it will likely always have some dependence on calibration of empirical models. Of these the flame propagation model stands out as requiring further improvement to accurately predict EGR effects.

5.7 Comparison of dilution mixtures by simulation

To take a closer look at the chemical interactions within the model another calibration was performed for the 12% EGR case at KLSA. Calibration to this specific operating point effectively negated the effects of flame speed correlations, since the calibration was effectively reduced to a curve-fitting exercise. Because the emphasis for this particular investigation is on the pre-flame chemistry in the end gas, the model only needs to reproduce the pressure and temperature histories during combustion. This is a similar approach to that adopted by Agbro et al [218].

Whilst the catalysis removed all of the NOx from the EGR gases during the experimental phase (described in Chapter 4), there were still very low trace amounts of CO and HCs left after catalysis, so these were added to the model in equivalent quantities. The HC content was approximated as methane.

The water content of the EGR gases during experimentation was an unknown quantity due to measurement equipment availability and the lack of control over the extent of cooling of the EGR gases as they recirculated to the inlet. Between test periods water was observed to have leaked past the piston rings of the EGR pump engine and settled in the sump to form an emulsion with the oil[9]. The EGR gases that were returned to the inlet contained some water as evidenced by moisture inside the piping that connected the EGR pump to the engine manifold. Some of the water vapour in the EGR gases would also be expected to condense on exposure to the cooler fresh charge when being mixed upstream of the engine manifold.

It can be said with confidence that a significant amount of water contained in the exhaust gases was not present in the EGR gases, but the exact content is not known. Further to this, any water within the EGR gases would most likely have condensed before having reached the cylinder, and so its evaporation would be one of its primary impacts on combustion. The chemical mechanism employed in this work specified all components

[9]This oil had to be changed after every complete day of testing to ensure operation of the pump was not compromised.

in gaseous phase, which neglects the evaporative cooling effect of water and therefore a major aspect in its effect on combustion.

Without having knowledge of the exact water content of the EGR gases, the value estimated from the simplified combustion equation from Stone [214] was used (Equation 4.2). An analysis of the effect of water addition in the model is carried out in Section 5.7.3 of this chapter.

5.7.1 Knock prediction in the model

Autoignition is evident in the model by observation of the heat release and radical concentrations in the end gas. The presence of autoignition does not necessarily indicate knocking combustion, but its onset angle and magnitude can be a useful indicator of the propensity to knock for a given condition.

This is similar to the method described by Pasternak et al [150], which has been adopted here for its simplicity and to allow the unbiased comparison between pre and post-catalyst EGR – since it does not involve the relative subjectivity of applying thresholds that are inherent to knock quantification.

Accurate identification of the angle of knock onset is not a priority in this investigation, since the variance in the experimental data does not provide definitive evidence on the effect of EGR composition on knock onset angle (as reported in Chapter 4).

5.7.2 Modelling pre and post-catalyst EGR effects

The most apparent difference between the experimental pre and post-catalyst results in Chapter 4 was the change in knock propensity between the two EGR modes. The simplest metric by which to assess this is the change in KLSA between the two conditions.

The KLSA values for the 12% EGR condition were 4.5 and 5°CA for the pre and post-catalyst EGR compositions respectively. A spark sweep was performed with both the

pre and post-cat EGR models. These were advanced until autoignition was predicted for each model.

Figures 5-14 and 5-15 show results from these two tests. The heat release plots in Figure 5-14 have an unusual shape relative to that normally seen experimentally, exhibiting a very abrupt drop after a slight plateau at the peak. This appears to be a characteristic of the fractal flame propagation model that is influenced by the pressure equalisation step (step 10 in Figure 5-1). This perhaps highlights an area in which the model could have been improved.

The late spikes in the heat release plots at the top of Figure 5-14 indicate the occurrence of autoignition, albeit much later than was observed in the experimental data. The absolute timing of these AI events is not of paramount importance to this investigation, as a certain amount of tuning can be done by adjustment of the heat transfer and wall influence models to advance the AI propensity.

The AI events are triggered at temperatures exceeding 1000 K, and are accompanied by a very rapid increase in OH radicals (illustrated in Figure 5-15). A logarithmic y axis has been used to enable the low and high temperature OH peaks to be visible.

The role of NO in this process is revealed by its consumption (Figure 5-15), which happens much earlier than the autoignition event but corresponds to the initial heat release in the end gas (Figure 5-14) and an initial peak in OH radical concentration. It is evident that all of the NO in the end gas is predicted to be consumed during the low temperature regime.

The results displayed in Figures 5-14 and 5-15 suggest that low temperature chain initiation reactions would be expected to occur in the end gas for both knocking and non-knocking conditions. These release a certain amount of heat for all cases – for the condition shown this occurs at around 750-800 K, and increases the temperature to around 900-950 K – which moves it closer to the intermediate temperature regime. At this point the non-autoigniting conditions reach chain termination and no further heat

release is observed. The autoigniting cases continue to release heat, until the temperature exceeds around 1000 K, where sudden ignition of the end gas occurs.

If Bozza et al's approximation for the end gas heat release exceeding 1% of the total for the combustion process [243] was to be used only the two most advanced uncatalysed conditions would be classed as knocking cycles. The total heat released for all conditions is close to 1600 J, so a threshold of 16 J discounts any of the catalysed EGR conditions from being classed as knocking by this method.

The model predicts the onset of autoignition at a spark angle of 4.5°CA for pre-catalyst EGR, which compares to 7°CA for post-catalyst EGR. If the difference in autoignition onset angles is assumed to be representative of the difference in knock onset angles, this advance of 2.5°CA is significantly larger than the difference observed experimentally between the two EGR compositions[10].

The fact that this model appears to predict a far larger benefit to KLSA from EGR catalysis than was observed experimentally suggests that the impact of the NO model may be greater than the experimental data would suggest. Conversely, the low temperature initiation reactions for TRFs in the absence of NO may not be well represented in the mechanism. This could be a factor impacted by the simplicity of the PRF model within the kinetic mechanism.

Both the temperature and the radical concentration are important factors in assessing the reactivity of the end gas mixture. The concentration of the most potent radical, OH, is often used as an indicator of the propensity to autoignite.

The plots in Figure 5-15 illustrate the radical evolution in the end gas for Semenov's low temperature hydrocarbon oxidation process [94].

The chain initiation process:

$$RH + O_2 \rightarrow \dot{R} + HO_2$$

[10]The autoignition onset would be expected to occur at more retarded spark angles than KLSA since at its onset the autoignition is not powerful enough to cause knock.

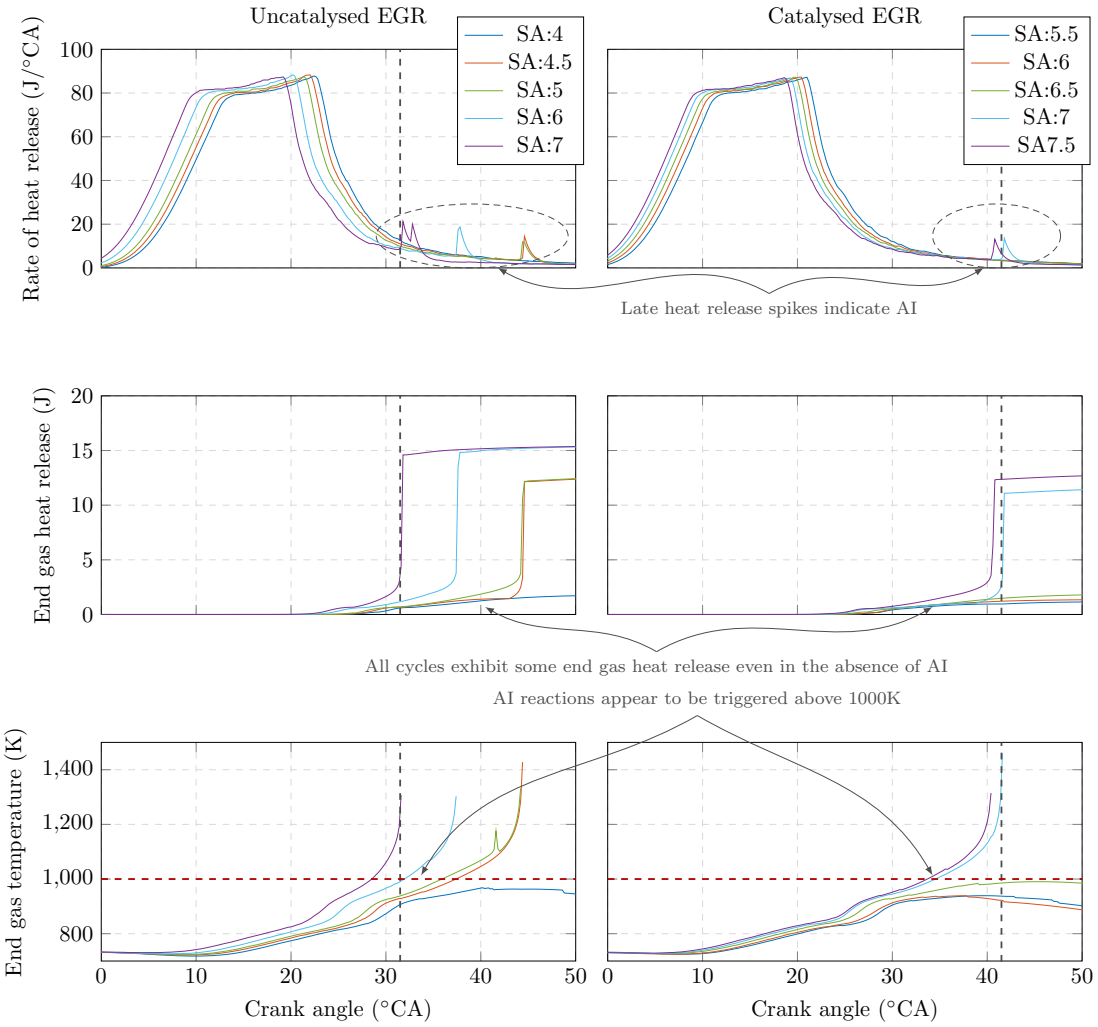

Figure 5-14: Comparison of the heat release and temperature rise in the end gas for uncatalysed vs catalysed EGR. The vertical dashed line provides a reference for the onset of AI at an ignition angle of 7°CA for comparison between the two EGR compositions.

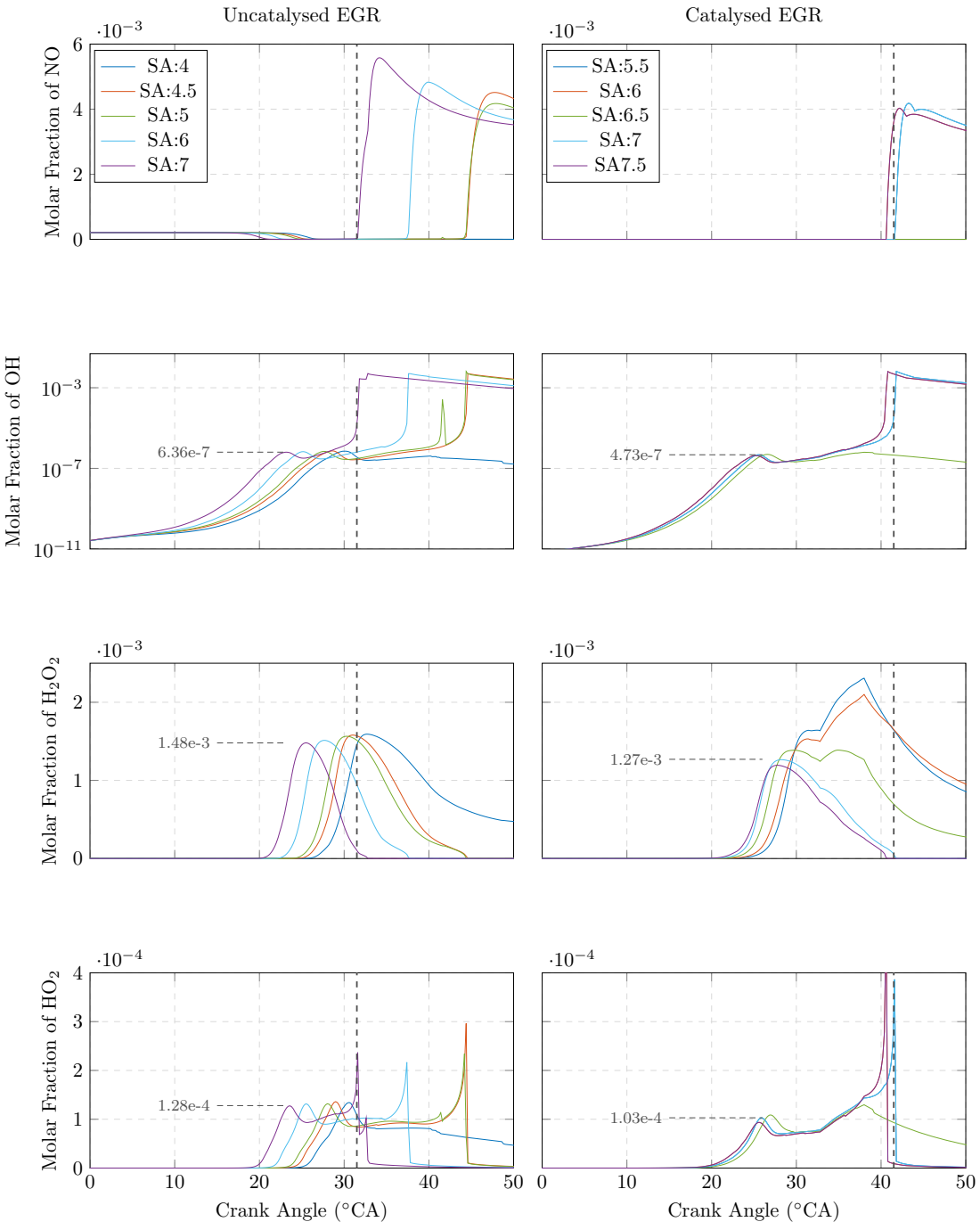

Figure 5-15: Comparison of the species evolution in the end gas for uncatalysed vs catalysed EGR. The uncatalysed EGR cases exhibit higher peak concentrations of OH, H_2O_2, and HO_2 radicals during their low temperature chemistry at equivalent spark angles. The vertical dashed line provides a reference for the onset of AI at an ignition angle of 7°CA for comparison between the two EGR compositions.

which then enables:

$$\dot{R} + O_2 \rightarrow \text{olefin} + HO_2$$

is evident by the increase in the HO_2 concentration at around 20°CA. The fall after the initial peak in HO_2 concentration corresponds to an increase in H_2O_2 radical concentration, which is explained in Semenov's theory by:

$$ROH + HO_2 \rightarrow R\dot{O} + H_2O_2.$$

The OH radical pool is also increased by:

$$\dot{R} + HO_2 \rightarrow R\dot{O} + OH$$

but the plots show no lag between the HO_2 and OH production which suggests alternative paths for OH production are also active.

At the onset of autoignition there is a spike in both the OH and HO_2 radical concentrations which corresponds to the sudden consumption of all remaining H_2O_2 radicals. This occurs at temperatures in excess of 1000 K, and is governed by high temperature chemistry. The plot of the H_2O_2 concentration for catalysed EGR reveals a continued increase in H_2O_2 for cycles that do not exhibit AI events, which is evidence for there being insufficient temperature for the H_2O_2 dissociation reactions to take place.

The autoignition events appear to occur during the transition to the high temperature chemistry regime. Galloni et al [139] state that autoignition will occur when there is sufficient time for the pre-flame chemistry to complete before consumption by the flame front. The results presented here suggest that the temperature of the end gas is a very significant factor in this determination. Whether the completion of the low temperature chemistry is the factor that determines there being sufficient temperature, or whether the temperature determines the completion of the low temperature chemistry is unclear from these results. But there will be a point beyond which the temperature threshold

will not be reached due to expansion as the piston moves down.

Comparison between the pre-catalyst and post-catalyst results in Figures 5-14 and 5-15 reveals more low temperature heat release at earlier crank angles for the uncatalysed EGR conditions with equivalent spark timing. This increases the end gas temperature by a larger amount which moves it closer to the high temperature regime. Annotations to the plots in Figure 5-15 highlight the values of radical concentrations during the low temperature chemistry for the spark angle of 7°CA, which is an autoigniting condition for both models.

The HO_2 radical concentrations appear to be higher for the uncatalysed EGR cases, and the H_2O_2 radical concentrations lower. This suggests that there may be a lower concentration of ROH radicals available to combine with HO_2 to produce H_2O_2, which in turn suggests that the uncatalysed EGR conditions may introduce an alternative path for the chain initiation reactions.

It is likely that the alternative paths to radical production are due to the presence of NO, and the details of this are discussed further in Section 5.7.3.

5.7.3 Modelling the impacts of the minor species in EGR

The 12% EGR model also provided the base upon which to conduct a sensitivity analysis of the EGR minor species in relation to autoignition propensity. The species selected for the investigation were the minor species NO, CO, H_2O and HCs. Unburned hydrocarbons were assumed to be entirely formed of methane, which may not be entirely accurate but was deemed an acceptable assumption for this investigation since no detailed breakdown of the HC emissions was measured during the experimental phase, and CH_4 is a stable intermediate product of hydrocarbon oxidation.

The initial concentrations of NO, CO, H_2O and HCs were calculated in relation to their measured concentrations from the experimental data at this operating condition. The concentrations were swept from 0% to 200% of that found in the real EGR gases, as

Table 5.4: Table of test points for the species sensitivity test

Species	Concentration (in EGR)					
	25%	50%	75%	100%	150%	200%
NO	500ppm	1000ppm	1500ppm	2000ppm	3000ppm	4000ppm
CO	0.1875%	0.375%	0.5625%	0.75%	1.125%	1.5%
H2O	1.9%	3.8%	5.7%	7.6%	11.4%	15.2%
CH4	325ppm	750ppm	1075ppm	1500ppm	2250ppm	3000ppm

detailed in Table 5.4, and their individual impacts were assessed.

All tests were performed with an ignition angle of 6°CA BTDC since it was the most advanced spark angle recorded experimentally that was common to both EGR compositions.

The impact of NO addition

Figure 5-16 illustrates the difference in end gas heat release and OH species evolution caused by addition of NO. At the chosen condition there is no autoignition for the baseline case, but even the addition of 500 ppm of NO in the EGR gases [11] speeds up the low temperature chemistry significantly and triggers autoignition late in the cycle. At concentrations higher than this the pre-flame chemistry is sped up further, but the maximum rate occurs for the 1000 ppm case (equivalent to around 105 ppm of NO at the inlet). This is consistent with experimental results reported in the literature.

The traces in Figure 5-16 show a certain amount of discontinuity due to the sequential autoignition of different particles in the end gas, some of which are then consumed by the flame front before they have released all of their energy in the unburned zone which gives rise to a saw-tooth shape to some of the plots. It is expected that increasing the particle number beyond 100 (such as 1000) would smooth this out significantly by enabling a more continuous distribution of species and temperature, but this would come at the expense of running times. An increase in the number of particles could have a knock-on

[11] Equivalent to 52.5 ppm at the inlet – 25% of the concentration seen for the uncatalysed EGR gas.

effect on the severity and timing of the autoignition onset due to the available energy in any autoigniting particle and how quickly it would trigger ignition in neighbouring particles in relation to the advancing flame front.

Although Chen et al [5] do state that the detailed chemistry of NO and hydrocarbon interactions are not fully understood, they do describe the established principles by which NO is expected to influence the oxidation of paraffinic fuels such as n-heptane and iso-octane. These are illustrated in Figure 5-17 where solid lines represent reaction paths without NO, and the dashed lines represent oxidation paths with NO. The reactions R1, R2, and R3 correspond to:

$$\text{R1: } NO + HO_2 \leftrightarrow NO_2 + OH \tag{5.13}$$

$$\text{R2: } NO + OH + M \leftrightarrow HONO + M \tag{5.14}$$

$$\text{R3: } NO + RO_2 \leftrightarrow NO_2 + RO \tag{5.15}$$

During the low temperature regime Reaction 1 increases reactivity of the mixture by increasing the OH radical pool, Reaction 2 slows oxidation by producing the less reactive HONO molecule. Reaction 3 can have either an accelerating or inhibitory effect depending on whether it converts RO_2 or ROO radicals to RO radicals. At higher temperatures the reverse of Reaction R2 becomes more dominant which then increases the OH radical pool further [118].

Whilst Figure 5-17 describes the NO interactions with paraffinic fuels, the toluene content of the fuel increases the complexity of the interactions. The reactions of benzyl radicals via:

$$benzyl + NO_2 \rightarrow C_6H_5CH_2O + NO$$

converts a stable benzyl radical into the more reactive benzyloxy radical ($C_6H_5CH_2O$) whilst also converting NO_2 back to NO which can produce more OH radicals via Reaction 1 [170].

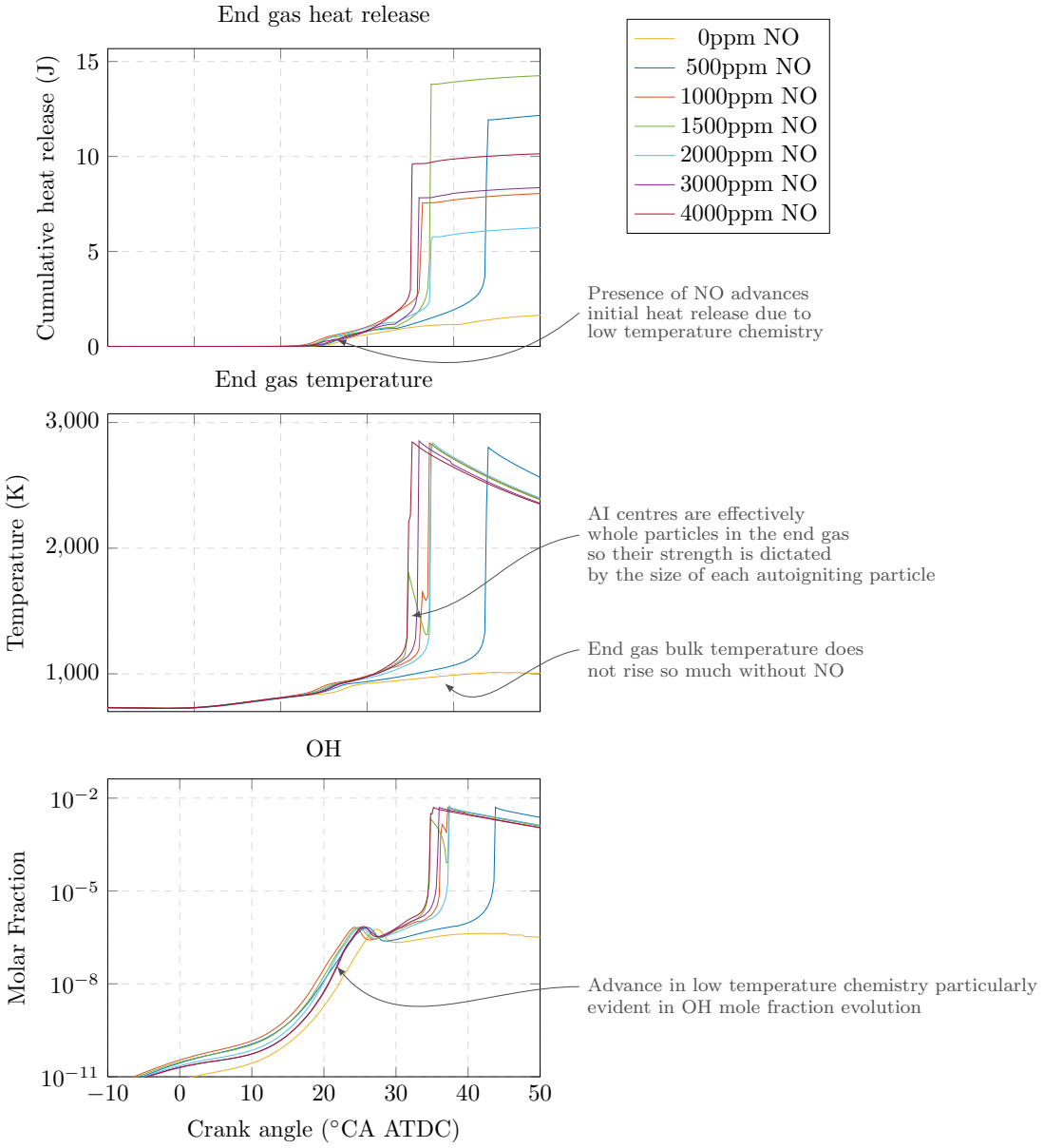

Figure 5-16: Plots representing the end gas heat release and OH radical evolution for a sweep of NO concentrations at 10.5% EGR and spark angle of 6°CA BTDC. There is a noticeable difference between the cases with NO and the baseline case (yellow).

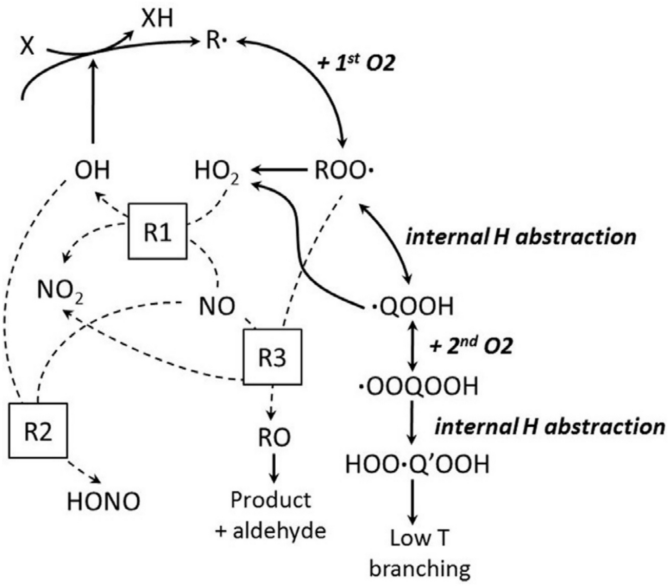

Figure 5-17: Diagram of hydrocarbon oxidation interactions for n-heptane, with solid lines representing reaction paths without NO, and dashed lines representing reaction paths with NO. Reproduced from [5].

The benzyloxy radical can then decompose via:

$$C_6H_5CH_2O \rightarrow C_6H_5 + CH_2O$$

The advance in production of the benzyloxy radical for mixtures containing NO is evident in Figure 5-18, which is followed by production of C_6H_5 and CH_2O, both of which are consumed during the AI events.

Whilst this description of the relevant paths is not exhaustive, it summarises some of the key reactions which contribute to the promoting effect of NO on autoignition. At the conditions tested here the predicted effect of NO is to promote autoignition with a fairly constant impact for concentrations above 105ppm at the inlet (1000ppm in the EGR). The reactivity of the mixture is increased during the low temperature regime via a number of paths which become available via interactions with NO and its products. This increases the pre-flame heat release which increases the propensity for autoignition to occur in regions of the unburned zone that have sufficient temperature to activate the high temperature reaction paths.

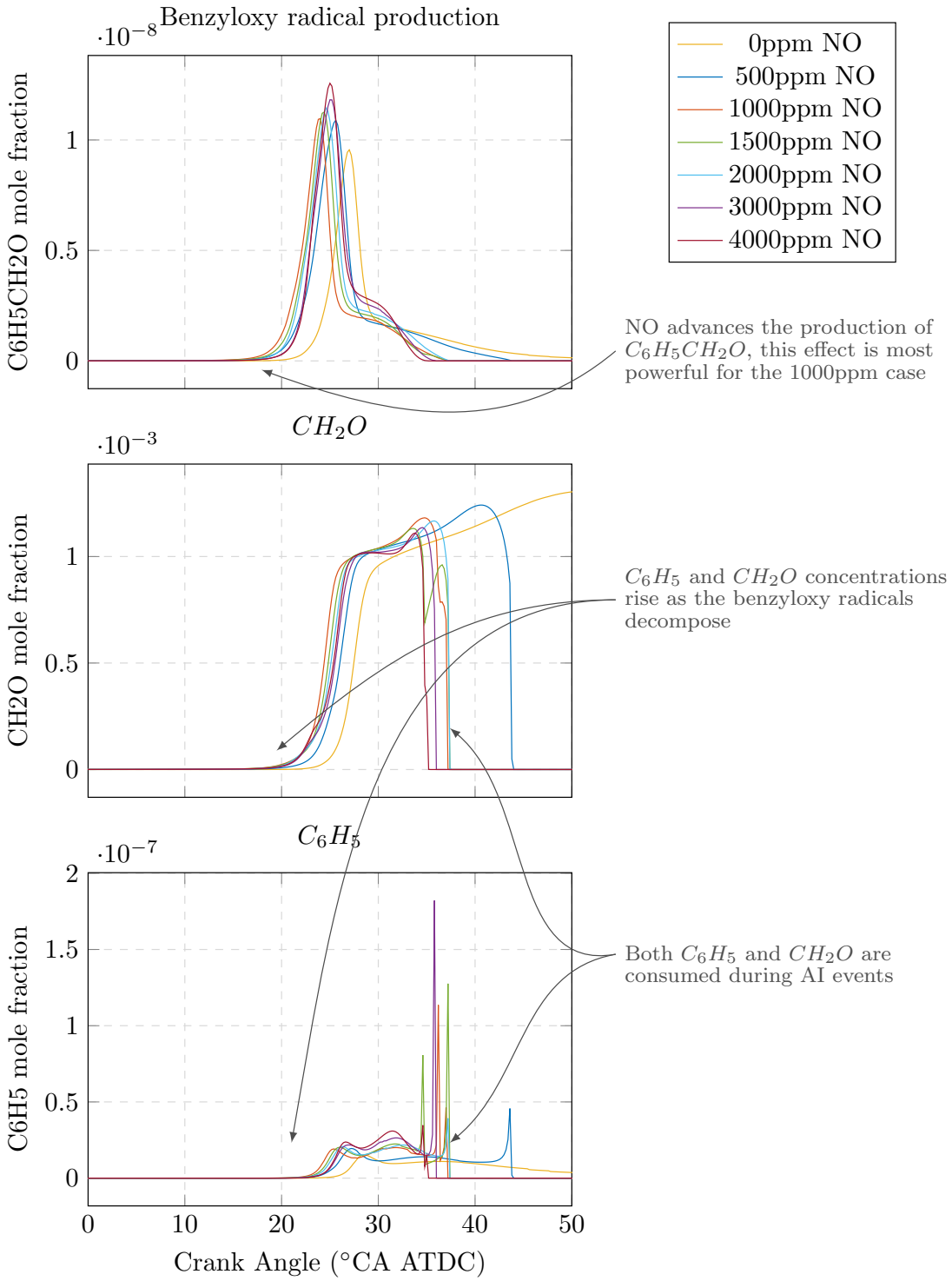

Figure 5-18: End gas mole fractions of $C_6H_5CH_2O$, C_6H_5 and CH_2O during a sweep of NO concentration at 10.5% EGR and with a spark angle of 6°CA BTDC. Increased NO concentrations result in increased production of these compounds, which are then consumed during AI events.

The impact of CO addition

The introduction of CO into the EGR gases is demonstrated in Figure 5-19. It appears to have little effect on the end gas chemistry at the condition tested here. The variation between the traces for different CO concentrations does not appear to follow any trend, and stays within a small enough window that the variability can be assumed to be due to the stochastic nature of the heat transfer and mixing models.

Subramanian et al [244] observed an inhibitory effect of CO on autoignition at low temperatures ≈600K, and a promoting effect at high temperatures of around 1000K, whilst investigating n-heptane combustion. These findings were confirmed by experimentation on HCCI combustion by Anderlohr et al [245], and Topinka et al [72] who investigated this phenomenon in an SI engine.

It appears that for the condition tested here the model does not predict a significant impact for CO, but this also occurs in a region that sits between those previously discussed [72, 244, 245] and is close to the NTC region. Considering this it is not surprising that the CO is not impacting combustion in the model, and this is likely to be representative of real effects. The promoting effect at around 1000K that has been reported in the literature does suggest that CO could increase the intensity of autoignition events once the high temperature reactions begin. This would mean the presence of CO in combination with an autoignition promoter such as NO may further increase the knock propensity of a mixture.

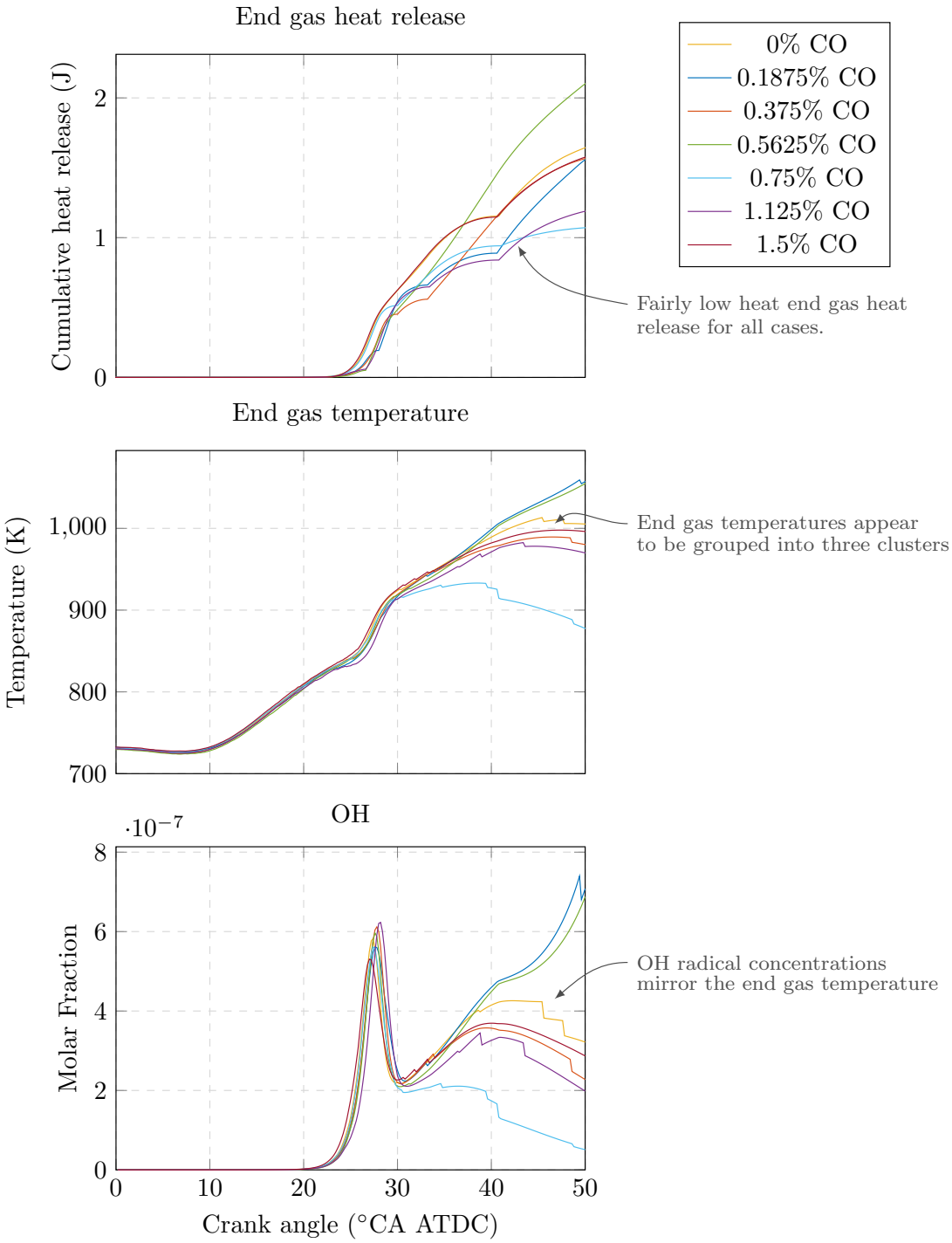

Figure 5-19: Plots representing the end gas heat release and OH species initiation during a sweep of CO concentration for a pre vs post-catalyst EGR at 10.5% EGR and a spark angle of 6°CA BTDC.

The impact of H_2O addition

Previous investigations of H_2O interactions in hydrocarbon oxidation have focused primarily on the evaporative cooling effect that it provides [246]. As has been mentioned previously, species could only be defined in their gaseous phase in this model[12] so any water in the EGR was included as water vapour. In the experimental phase it is expected that the water being recirculated to the inlet would have at least partially condensed both through contact with the pipe walls in transit, and on mixing with the cooler fresh charge. Therefore these simulation results are not fully representative of the global effect of water addition, but instead isolate the predicted chemical effect. This would be present predominantly through the dilution effect of the water molecules in the mixture rather than direct chemical interactions, although Anderlohr et al [247] comment that water may react as a collision partner in H_2O_2 dissociation.

The plots in Figure 5-20 give some indication of an increased dilution effect in the initial heat release (at around 25°CA) between the dry condition and those with water but there does not appear to be a strong trend with the H_2O concentration in any of the plots.

The most noticeable difference between the conditions is apparent later in the cycle (beyond 40°CA) in the temperature and OH mole fraction plots. There appears to be three groupings, the first (highest temperature and OH concentration) just being the dry condition. The second and third groups do not correlate with the heat release and so are more likely to be a product of the stochastic heat transfer and mixing models.

The knock suppressing effect of water is well established in the literature, so the results of this test add support to the theory that this suppressant effect is predominantly due to the evaporative cooling (which is not included in the model) rather than the chemical interactions or collisions.

[12]This is due to the definitions available in the mechanism file

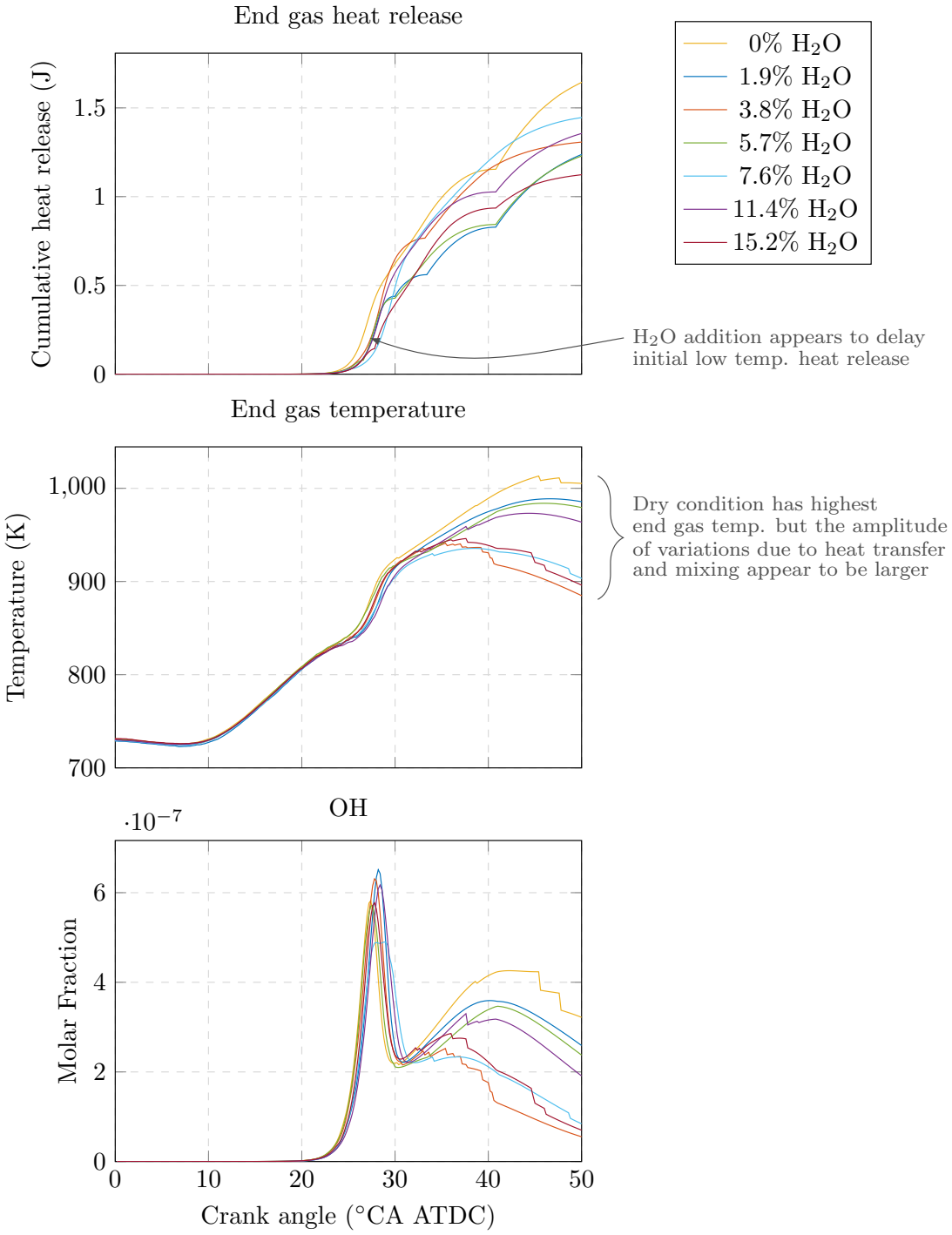

Figure 5-20: Plots representing the end gas heat release and OH species evolution for a sweep of water content at 10.5% EGR with a spark angle of 6°CA BTDC.

The impact of CH_4 addition

Similarly to the H_2O test in the previous section, CH_4 appears to initially have a dilution effect on the end gas mixture, which is demonstrated by the delay in the initial heat release compared to the baseline condition in Figure 5-21 at around 25°CA.

After this the highest CH_4 concentration of 3000 ppm (equivalent to 315ppm of the total charge) produces the largest amount of heat in the end gas, which leads to a very late AI event after 50°CA. This suggests that at much higher concentrations than those seen in EGR the excess CH_4 may enable an increase in the concentration of CH_3 radicals to help promote autoignition. This does, however, occur very late in the cycle so is unlikely to cause knock.

This model predicts that the primary effect of excess hydrocarbons on autoignition is to delay the chain initiation reactions by dilution of the end gas mixture. This suggests that from a perspective of HC content uncatalysed EGR is preferable as it increases the calorific content of the charge without any increase to knock propensity. The assumption of all unburned HCs taking the form of CH_4 is of course a simplification of real conditions, and less stable hydrocarbons that may be present in EGR gases could promote autoignition, especially in combination with NO.

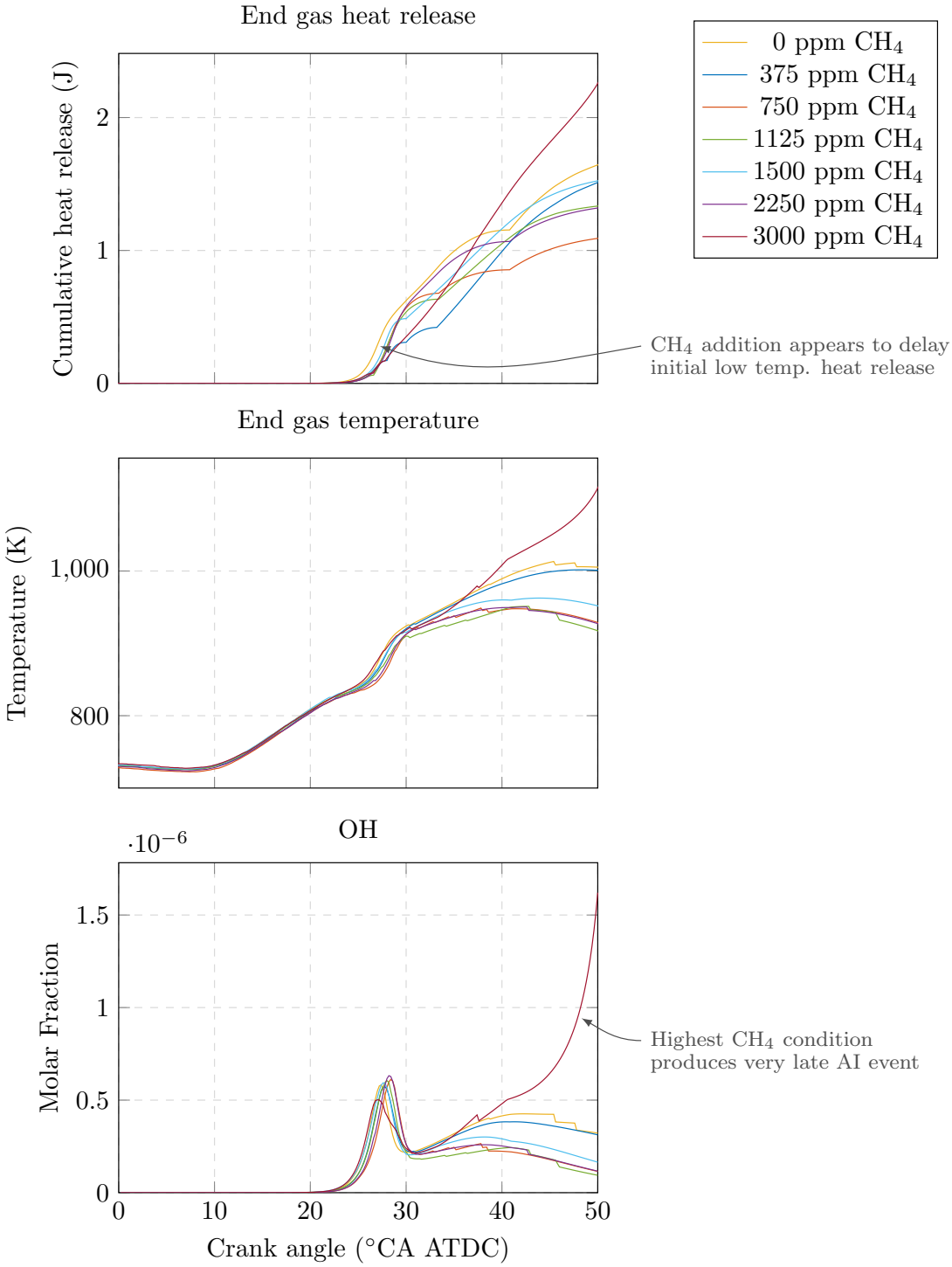

Figure 5-21: Plots representing the end gas heat release and OH species evolution for a sweep of CH_4 content at 10.5% EGR with a spark angle of 6°CA BTDC.

Summary of individual species impacts

Of the minor species present in EGR this model only predicts a significant impact for the NO content. The AI promoting effect is strongest at total charge concentrations of around 100 ppm, and very little inhibiting effect is observed for the concentrations tested (up to 420 ppm).

CO does not have any significant effect on the end gas chemistry in the model, although evidence from the literature suggests that it may promote AI in combination with NO due to its effect at increased temperatures. Both CH_4 and H_2O show a slight dilutive effect during the chain initiation process in the end gas, but the total heat released and radical concentration for both of these tests appears to show that the heat transfer and mixing models are the dominant factors in determining the end gas processes for these species. This does, of course, discount the evaporative cooling effect that is known to have a significant impact for water addition.

5.8 Conclusions and further use of this model

The work in this chapter serves as a preliminary investigation into the simulation methods that could help to implement the experimental findings from earlier in this thesis into modelling processes.

The outcomes of this chapter are:

- Application of a new method to improve calibration speed and effectiveness for the CMCL SRM modelling suite.
- An assessment of new modelling techniques on predicting dilution response in a 1 litre GDI engine and indication of where these models could be improved to enhance their predictive ability.
- An analysis of the chemical interactions that are predicted by a semi-detailed model in comparing the effects of different EGR compositions on combustion and

the effects of the minor species in EGR.

The dilution response of the model was improved by adjustments to both the laminar flame speed correlation and the turbulent mixing model. Whilst these adjustments cannot be validated across a broader operating range for this study, they provide evidence that the model can reproduce experimentally observed phenomena. Having said this the model is still operating in a predominantly empirical form, and further progress is required to move more into the fully predictive realm.

The work in this chapter is by no means an exhaustive application of the modelling techniques for analysing dilution effects. Both the numerical and the chemical aspects can be optimised, and for reliable prediction of dilution effects progress is required on both fronts.

This work has just scratched the surface in an area where there is a huge amount of potential for improvement, and where the knock-on effects to OEMs could be extremely significant in terms of both minimising costs and progressing technology at a faster rate.

Development of lighter, faster models that can accurately predict dilution effects would be very valuable in the assessment of engine architectures to guide development of future powertrain integration. In this case the detailed interactions can be sacrificed to a certain extent where the engine output, knock limits, and emissions are the most important factors. It must be noted that the variability inherent in SI engine combustion should be considered in these models, since a model that represents engine output by reproducing a mean pressure trace will not accurately represent knocking cycles, and vice versa, whilst emissions data would be most accurately represented by distributions encompassing the spread seen in real data.

Future combustion models must be capable of accounting for changes in fuel compositions, especially with the rising profile of synthetic and advanced gasoline fuels. The variation that has been observed in previous studies on NO effects for different fuels

makes this point especially pertinent when considering chemical effects of EGR. This is also very relevant when considering the effects of residual gases.

The implementation of models of this nature still require tuning before being able to accurately represent a combustion system, and this will still require validation by experimental data for the foreseeable future. In this respect they are still fundamentally empirical models but the integration of kinetic models into them provides much more potential for their predictive ability. This could reduce the amount of experimental validation required for a given combustion system.

The integration between this type of model and CFD technology for determining more accurate initial conditions for the combustion model (such as the method employed by Linse et at [151]) could provide the most benefit in terms of reducing the reliance on effectively "curve fitting" to estimate the initial conditions that cannot be measured reliably during the experimental stage. Work by Rota et al [248] demonstrates the effectiveness of integrating CFD methods into the calibration process for PDF combustion models by using 3-D models to capture the effects of geometry and injector design on the in-cylinder air motion. It is anticipated that this is where PDF modelling can offer the most benefit to virtual engine validation and optimisation.

It is envisioned that to improve the predictive capability of the SRM suite for EGR operation an updated laminar flame speed correlation should be implemented which accounts for fuel effects as well as dilution. Adjustments to the flame speed correlation alone are unlikely to achieve a good fit, but other sub models within the fractal flame propagation model will probably require some relationship with the dilution rate to better match the phenomena observed.

The investigation into the chemical predictions made by the model support evidence from the literature on the effects of NO, and predict that it is the most potent of the minor species in EGR. It also predicts that NO does not only accelerate the production of OH radicals during the low temperature chemistry, but that of other radicals which

participate in AI events.

CHAPTER 6

CONCLUSIONS AND FURTHER WORK

This chapter reviews the work described in the previous chapters and summarises the key points arising from it. The wider implications of these results are discussed, followed by recommendations for future work in this area.

6.1 Conclusions

This thesis has focused on the chemical effects of different EGR compositions on GDI combustion, with pre and post catalyst EGR being compared in two experimental campaigns. The experimental results provide some insight into the mechanisms behind the EGR composition effects on combustion, and guided a model calibration process to assess the performance of the relatively new Stochastic Reactor Model in simulating EGR effects in a GDI engine. The modelling process was also used to assess the predicted effects of the minor species in EGR on combustion.

The aims of the thesis are laid out below with their corresponding outcomes.

"To conduct a detailed literature review on the current status of EGR application in GDI engines and how EGR composition integrates into this understanding. This will progress into a review of combustion simulation methods with respect to the effects of inlet charge composition."

The literature on EGR operation has been reviewed and the compositional effects that are reported in the literature have been assessed. This includes the numerous studies involving HCCI combustion where there is a larger body of work relating to NO effects on the autoignitive properties of air-fuel mixtures.

These studies provide some insight into the mixture effects on autoignition in GDI engines, but must be treated with caution since the temperature and pressure histories in HCCI engines are quite different to those seen in the end gas during SI combustion.

The effects of EGR composition that are reported in the literature document the effects of the minor species in isolation and also compare the effects of catalysed EGR against uncatalysed EGR on real engines. These on-engine tests are strongly affected by the effects of EGR architecture and their corresponding impact on turbocharger performance, so do not effectively isolate the impact of EGR catalysis on the combustion system.

The simulation techniques that have been reviewed focus mainly on the fairly novel

method of stochastic modelling, and are discussed in relation to both the evaluation of knocking combustion and the kinetic mechanisms that they employ. Whilst some of these studies do include EGR in their models, their accuracy in emulating the effects of EGR addition and composition has not been focused on.

"To design and execute an experimental campaign capable of delivering combustion data across a range of dilution concentrations to observe the effects on knocking combustion and engine performance."

Two experimental campaigns have been conducted with the first providing lessons on which to base improvements to the processes used for the second, such as more precise control over scavenging and maintenance of catalyst temperature. The results of this first experimental campaign support the theory that NO concentrations can have a significant impact on knock limits.

The second campaign provided more details on the combustion effects. KLSA effects between the two EGR compositions were not as pronounced for this phase of testing as was observed during the first phase, but still provided strong evidence for the increased knock inhibiting effect of post-catalyst EGR.

The magnitude of the KLSA improvement seen for EGR addition was below the levels often reported in the literature – averaging 0.7°CA of advance per 1% EGR where a figure of 1°CA improvement is often reported. This could be due to the characteristics of this particular combustion system or the fuel composition used for the experiment, and highlights the significance of the individual specifics of a combustion system when assessing the impact of EGR.

The data also gives some indication that the knock onset angle can be advanced by the presence of NO, but this effect does not appear strong enough to show a decisive trend. The effect on knock intensity, however, is very strong and the catalysis of the EGR gases greatly reduced the knock intensity at equivalent spark angles.

"To build a model of the combustion system and assess its accuracy in predicting dilution effects against experimental data."

A model was built and calibrated using the Stochastic Reactor Model Suite developed by CMCL Innovations. A calibration process was developed in an effort to ensure an optimum calibration was achieved, and the model was tested against the experimental results from Chapter 4.

The model achieved a good response to changes of spark angle within a ±2°CA range without EGR, but the response to EGR addition was not accurate. Adjustments to the laminar flame speed correlation achieved a better fit for this model but are not proven for other models or conditions outside those that were tested. Similarly, the introduction of an additional dependence on EGR rate improved the performance of the flame propagation model across the range of EGR rates tested.

Both of these adjustments serve as an indication of where improvements can be made to the EGR response of the stochastic reactor model and by no means constitute a global improvement.

"To gather information on the most pertinent mechanisms that are relevant to comparisons in EGR composition."

The experimental comparisons indicated that changes in EGR composition can have a significant impact on combustion and this was further investigated by simulation methods with the stochastic reactor model. A well validated semi-detailed chemical mechanism for NO interactions with TRF fuels was used to assess the impacts of EGR composition as well as the individual effects of each of the most prominent minor species in EGR.

The predicted AI propensity was significantly higher for uncatalysed EGR when compared to catalysed EGR, and NO was observed to be the primary cause for this increased reactivity. The addition of NO not only increased the availability of OH radicals during the low temperature reactions, but also increased production of other reactive species

such as benzyloxy radicals.

6.1.1 Contributions

This thesis has provided an experimental quantification of EGR compositional effects on high load GDI engine combustion independently of turbomachinery effects. Previously work of a similar nature has been affected by turbocharger performance or architecture effects ([3,66]) which don't allow a direct assessment of the effects that EGR catalysis has on combustion. To the author's knowledge no previous study has successfully compared the effects of pre and post-catalyst EGR on a boosted combustion system without turbocharger performance impacting the results. These results, and further testing of this nature, provides an opportunity for improvement to combustion models which require strictly imposed boundary conditions to provide accurate validation.

A pairing method was developed to compare the knocking cycle data for the two EGR compositions. This enabled a comparison of the knock onset angles which accounted for the variability that is inherent to combustion engine data. To the authors knowledge this technique has not been employed previously for this type of comparison, and whilst used here for analysis of knocking combustion, it could be a valuable tool in any field where analysis of stochastic phenomena is required.

A PDF-based modelling method has been tested against this experimental data which has highlighted some areas of improvement that are required to enable a more predictive model. It appears that the software used for this study has not previously been applied to GDI combustion in this way, although some success in emulating EGR effects has been demonstrated by researchers with a competitor software using a PRF fuel and a look-up based approach to flame propagation rates [154]. The potential of this method to account for compositional effects on combustion has been demonstrated, but further improvements are required in order to enable accurate results for one model across a range of operating conditions.

A tool has been developed to improve the efficiency of the iterative model calibration

process, and was used to ensure accurate calibrations of the model. Further development of this method could enable more consistent model calibration standards without so much reliance on user experience, and integration of CFD methods to assist in the calibration of the sub-models relating to geometry and in-cylinder air motion such as that described by Rota et al [248] could be very valuable for this process.

A comparison has been made on the predicted effect of the different EGR compositions on autoignition, which has confirmed findings of previous work [111] whilst also highlighting further areas that require improvement to be applicable to future demands of advanced fuels and combustion systems.

6.2 Further work

This thesis has demonstrated the effect of EGR catalysis on GDI combustion experimentally and assessed the ability of a PDF-based model to reproduce these effects. Improvements can be made, and will be very valuable, in the application of simulation models to characterise EGR effects (both dilution and chemical) on GDI combustion.

The results presented in Chapter 5 indicate that faster simulation methods still cannot operate in a fully predictive manner but still require the calibration of various empirical models which cannot necessarily represent a combustion system across its entire operating range without recalibration.

Improvements to these empirical models could broaden the operating window which they can represent, as demonstrated by the adjustments to the fractal model in this work, but it is unlikely that simulation methods will move entirely away from using empirical relationships without using much heavier and slower CFD methods.

The model calibration process that is used in Chapter 5 has room for improvement, and integration of CFD methods into the calibration process to refine boundary conditions for the model has the potential to reduce errors and improve consistency of model calibrations. An example of this is provided by Rota et al who use CFD modelling to

capture the effects of geometry and injector design on the in-cylinder flow, and successfully emulate the behaviour of a single cylinder gasoline engine with a combination of 0-D, 1-D and 3-D methods [248].

The chemical aspect of combustion modelling is an area that is in constant flux as new mechanisms are developed, yet the detailed interactions for many fuel components with NO are still not fully understood. As the capabilities of computational hardware continue to improve it is likely that more detailed mechanisms will become more feasible for use with quasi-dimensional models. This may become a requirement as the technology in gasoline fuels also continues to develop and mixture effects become more significant in modelling combustion systems. Currently, understanding of the interactions between NO and the aromatic and oxygenate components of gasoline fuels requires improvement to enable the development of efficient and accurate kinetic mechanisms for modern fuels.

Ultimately the integration of the compositional effects of both EGR and fuel will be very valuable in improving simulation methods for powertrain development and optimisation, but the requirement for experimental methods in this process will likely remain.

REFERENCES

[1] Fabio Bozza, Vincenzo De Bellis, and Luigi Teodosio. Potentials of cooled EGR and water injection for knock resistance and fuel consumption improvements of gasoline engines. *Applied Energy*, 169:112–125, 2016.

[2] H. Lu, Z. Hu, J. Deng, Z. Wu, L. Li, F. Yuan, Degang Xie, Shuang Yuan, and Yuan Shen. Study on Fuel Economy Improvement by Low Pressure Water-Cooled EGR System on a Downsized Boosted Gasoline Engine. *SAE Technical Papers*, 2016.

[3] Henrik Hoffmeyer, Emanuela Montefrancesco, Linda Beck, Jürgen Willand, Florian Ziebart, and Fabian Mauss. CARE – CAtalytic Reformated Exhaust Gases in Turbocharged DISI-Engines. *SAE International*, pages 139–148, 2009.

[4] Andy D. B. Yates, André Swarts, and Carl L. Viljoen. Correlating Auto-Ignition Delays And Knock-Limited Spark-Advance Data For Different Types Of Fuel. *SAE International*, 2005.

[5] Zhongyuan Chen, Peng Zhang, Yi Yang, Michael J. Brear, Xin He, and Zhi Wang. Impact of nitric oxide (NO) on n-heptane autoignition in a rapid compression machine. *Combustion and Flame*, 186:94–104, 2017.

[6] CMCL Innovations. *kinetics & SRM Engine Suite User Manual*. 2018.

[7] Mani Sarathy, Nour Atef, Adamu Alfazazi, Jihad Badra, Yu Zhang, Tom Tzanetakis, and Yuanjiang Pei. Reduced Gasoline Surrogate (Toluene/n-Heptane/iso-Octane) Chemical Kinetic Model for Compression Ignition Simulations. *SAE Technical Paper Series*, 1:1–11, 2018.

[8] Liming Cai and Heinz Pitsch. Optimized chemical mechanism for combustion of gasoline surrogate fuels. *Combustion and Flame*, 162(5):1623–1637, 2015.

[9] Cécile Pera and Vincent Knop. Methodology to define gasoline surrogates dedicated to auto-ignition in engines. *Fuel*, 96:59–69, jun 2012.

[10] Xin He, Yunliang Qi, Zhi Wang, Jianxin Wang, Shijin Shuai, and Ling Tao. Visualization of the Mode Shapes of Pressure Oscillation in a Cylindrical Cavity. *Combustion Science and Technology*, 187(10):1610–1619, 2015.

[11] FEV. The future drives electric?, 2017.

[12] Electric car market statistics, 2019.

[13] Terry Alger, Thierry Chauvet, and Zlatina Dimitrova. Synergies between High EGR Operation and GDI Systems. *SAE International*, 2008.

[14] D. Parsons, S. Akehurst, and C. Brace. The potential of catalysed exhaust gas recirculation to improve high-load operation in spark ignition engines. *International Journal of Engine Research*, oct 2014.

[15] H R Ricardo. Paraffin as Fuel. *The Automobile Engineer*, pages 2–5, 1919.

[16] H R Ricardo. Some Possible Lines of Development in Aircraft Engines. *American Sociaety of Naval Engineers*, 33(3):591–606, 1921.

[17] P Eyzat and J C Guibet. A New Look at Nitrogen Oxides Formation in Internal Combustion Engines. *SAE International*, 1968.

[18] John B Heywood. *Internal Combustion Engine Fundamentals*. McGraw-Hill Inc., 1988.

[19] H.K. Newhall. Control of Nitrogen Oxides By Exhaust Recirculation - A Preliminary Theoretical Study. *SAE Technical Paper Series*, pages 1820–1836, 1967.

[20] Bernhard Flaig, Uwe Beyer, and Marc-Oliver Andre. Industry Exhaust Gas Recirculation Exhaust Gas Recirculation. *MTZ Worldwide*, 71(01):22–27, 2010.

[21] Vikram Mittal, Bridget M Revier, and John B Heywood. Phenomena that Determine Knock Onset in Spark-Ignition Engines. *SAE International*, 2007.

[22] G. Konig and C. G. W. Sheppard. End Gas Autoignition and Knock in a Spark Ignition Engine. *SAE Technical Paper Series*, 1, 1990.

[23] Christo Boyadjiev. *Theoretical Chemical Engineering: Modelling and Simulation*. Springer, 2010.

[24] Börje Grandin and Hans-erik Ångström. Replacing Fuel Enrichment in a Turbo Charged SI Engine : Lean Burn or Cooled EGR Reprinted From : Combustion and Emission Formation in SI Engines. *SAE International*, 1999.

[25] Koichi Hatamura, Motoo Hayakawa, Tsuyoshi Goto, and Mitsuo Hitomi. A study of the improvement effect of Miller-cycle on mean effective pressure limit for high-pressure supercharged gasoline engines. *JSAE Review*, 18(2):101–106, 1997.

[26] Tie Li, Yi Gao, Jiasheng Wang, and Ziqian Chen. The Miller cycle effects on improvement of fuel economy in a highly boosted, high compression ratio, direct-injection gasoline engine: EIVC vs. LIVC. *Energy Conversion and Management*, 79:59–65, mar 2014.

[27] Jinxing Zhao. Research and application of over-expansion cycle (Atkinson and Miller) engines â A review. *Applied Energy*, 185:300–319, 2017.

[28] Wolfgang Demmelbauer-Ebner, Kai Persigehl, Michael Gorke, and Eike Werstat. The new 1.5-l four-cyliner TSI engine from Volkswagen. *MTZ Worldwide*, pages 16–22, feb 2017.

[29] Ralf Budack, Rainer Wurms, Gunther Mendl, and Thomas Heiduk. The new Audi 2.0-l I4 TFSI engine. *MTZ Worldwide*, pages 16–23, may 2016.

[30] Arturo Iacobacci, Luca Marchitto, and Gerardo Valentino. Water Injection to Enhance Performance and Emissions of a Turbocharged Gasoline Engine under High Load Condition. *SAE International Journal of Engines*, 10(3):928–937, 2017.

[31] Cinzia Tornatore, Daniela Siano, Luca Marchitto, Arturo Iacobacci, Gerardo Valentino, and Fabio Bozza. Water Injection: a Technology to Improve Performance and Emissions of Downsized Turbocharged Spark Ignited Engines. *SAE International Journal of Engines*, 10(5):2319–2329, 2017.

[32] Alberto Boretti. Water injection in directly injected turbocharged spark ignition engines. *Applied Thermal Engineering*, 52(1):62–68, apr 2013.

[33] F. Hoppe, M. Thewes, H. Baumgarten, and J. Dohmen. Water injection for gasoline engines: Potentials, challenges, and solutions. *International Journal of Engine Research*, 17(1):86–96, 2016.

[34] M. R. Rowe and G. T. Ladd. Water Injection for Aircraft Engines. *SAE International*, 54(1), 1946.

[35] Sipeng Zhu, Bo Hu, Sam Akehurst, Colin Copeland, Andrew Lewis, Hao Yuan, Ian Kennedy, Johan Bernards, and Ciaran Branney. A review of water injection applied on the internal combustion engine. *Energy Conversion and Management*, 184(February):139–158, 2019.

[36] Achint Rohit, Sridev Satpathy, Jeongyong Choi, John Hoard, Gopichandra Surnilla, and Mohannad Hakeem. Literature Survey of Water Injection Benefits on Boosted Spark Ignited Engines. *SAE International*, 2017.

[37] Martin Bohm, Werner Mahrle, Hans-Christian Bartelt, and Stephen Rubbert. Functional integration of water injection into the gasoline engine. *MTZ Worldwide*, pages 36–40, jan 2016.

[38] J Stokes, T H Lake, and R J Osborne. A Gasoline Engine Concept for Improved Fuel Economy - The Lean Boost System. *SAE International*, 2000.

[39] Tim Lake, John Stokes, Richard Murphy, Richard Osborne, and Ford-werke Ag. Turbocharging Concepts for Downsized DI Gasoline Engines. *SAE International*, 2004.

[40] Alasdair Cairns, Hugh Blaxill, and Graham Irlam. Exhaust Gas Recirculation for Improved Part and Full Load Fuel Economy in a Turbocharged Gasoline Engine Reprinted From SI Combustion and Direct Injection SI Engine Technology. *SAE International*, 2006.

[41] Alasdair Cairns and Hugh Blaxill. The Effects of Combined Internal and External Exhaust Gas Recirculation on Gasoline Controlled Auto-Ignition. *SAE International*, 2005.

[42] Alasdair Cairns, Neil Fraser, and Hugh Blaxill. Pre Versus Post Compressor Supply of Cooled EGR for Full Load Fuel Economy in Turbocharged Gasoline Engines. *SAE International*, 2008.

[43] J.W.G. Turner, R.J. Pearson, M.D. Bassett, and J. Oscarsson. Performance and Fuel Economy Enhancement of Pressure Charged SI Engines through Turboexpansion - An Initial Study. *SAE International*, 2003.

[44] J W G Turner, R J Pearson, M D Bassett, and D W Blundell. The Turboexpansion Concept - Initial Dynamometer Results. *SAE International*, 2005.

[45] J W G Turner, G Pitcher, P Burke, C P Garner, G Wigley, P Stansfield, H Nuglisch, N Ladommatos, R Patel, and P Williams. The HOTFIRE Homogeneous GDI and Fully Variable Valve Train Project - An Initial Report Reprinted From : SI Combustion and Direct Injection SI Engine Technology. *SAE International*, 2006.

[46] Bo Hu, Colin Copeland, Pengfei Lu, Sam Akehurst, Chris Brace, J.W.G Turner, Alessandro Romagnoli, and Ricardo Martinez-Botas. A New De-throttling Concept in a Twin-Charged Gasoline Engine System. *SAE International Journal of Engines*, 8(4), 2015.

[47] Schoeffmann Wolfgang, Helfried Sorger, Siegfried Loesch, Wolfgang Unzeitig, Thomas Huettner, and Alois Fuerhapter. The 2-Step VCR Conrod System - Modular System for High Efficiency and Reduced CO2. *SAE Technical Paper*, 2017.

[48] H L Horning. The Cooperative Fuel Research Committee Engine. *Annual meeting paper*, ascertain:436–440, 1931.

[49] Shuji Kojima, Shinichi Kiga, Katsuya Moteki, Eiji Takahashi, and Kazuya Matsuoka. Development of a New 2L Gasoline VC-Turbo Engine with the World's First Variable Compression Ratio Technology. *SAE International*, pages 1–10, 2018.

[50] Vincent Collee, Cyrille Constensou, Frederic Dubois, and Laurent Guilly. Variable compression ratio for future emission standards. *MTZ Worldwide*, pages 52–56, apr 2017.

[51] Denis Pendovski, Markus Jesser, Daniel Henaux, Knut Habermann, and Alexander Tolga Uhlmann. Numerical methods for a holistic design of a VCR conrod. In *FEV second international conference on variable compression ratio*, 2019.

[52] B. de Gooijer, S. Wagenaar, J. Trieschmann, and C. Ebbinghaus. Gomecsys VCR technology - Driveability of a VCR demo car. In *FEV second international conference on variable compression ratio*, 2019.

[53] Dietmar Schulze, David Huber, and Mario Witopil. 2 step variable compression ratio - system development and industrialisation. In *FEV second international conference on variable compression ratio*, 2019.

[54] Oldrich Vitek, Jan Macek, Milos Polasek, Stefan Schmerbeck, and Thomas Kammerdiener. Comparison of Different EGR Solutions. *SAE International*, pages 776–790, 2008.

[55] Sebastien Potteau, Philippe Lutz, Samuel Leroux, Stephanie Moroz, and Eva Tomas. Cooled EGR for a Turbo SI Engine to Reduce Knocking and Fuel Consumption. *SAE International*, 2007.

[56] J W G Turner, R J Pearson, R Curtis, and B Holland. Effects of Cooled EGR Routing on a Second-Generation DISI Turbocharged Engine Employing an Integrated Exhaust Manifold. *SAE International*, 2009.

[57] Enzo Galloni, Gustavo Fontana, and Roberto Palmaccio. Numerical analyses of EGR techniques in a turbocharged spark-ignition engine. *Applied Thermal Engineering*, 39:95–104, jun 2012.

[58] T Hattrell, C G W Sheppard, A A Burluka, J Neumeister, and A Cairns. Burn Rate Implications of Alternative Knock Reduction Strategies for Turbocharged SI Engines. *SAE International*, 2006.

[59] Börje Grandin and Hans-erik Ångström. Knock Suppression in a Turbocharged SI Engine by Using Cooled EGR. *SAE International*, 1998.

[60] G. Fontana and E. Galloni. Experimental analysis of a spark-ignition engine using exhaust gas recycle at WOT operation. *Applied Energy*, 87(7):2187–2193, jul 2010.

[61] Michele Kaiser, Uwe Krueger, Roderick Harris, and Luke Cruff. Doing More with Less - The Fuel Economy Benefits of Cooled EGR on a Direct Injected Spark Ignited Boosted Engine. *SAE International*, 2010.

[62] Guillaume Bourhis, Jonathan Chauvin, Xavier Gautrot, and Loic De Francqueville. LP EGR and IGR Compromise on a GDI Engine at Middle Load. *SAE International*, 2013.

[63] Bjoern Hoepke, Stefan Jannsen, Emmanuel Kasseris, and Wai K. Cheng. EGR Effects on Boosted SI Engine Operation and Knock Integral Correlation. *SAE International*, pages 547–559, apr 2012.

[64] Lurun Zhong, Marc Musial, Ronald Reese, and Greg Black. EGR Systems Evaluation in Turbocharged Engines. *SAE International*, apr 2013.

[65] Y. Chao, H. Lu, Z. Hu, J. Deng, Z. Wu, L. Li, Y. Shen, and S. Yuan. Comparison of Fuel Economy Improvement by High and Low Pressure EGR System on a Downsized Boosted Gasoline Engine. *SAE Technical Papers*, 2017.

[66] David B Roth, Philip Keller, and Michael Becker. Requirements of External EGR Systems for Dual Cam Phaser Turbo GDI Engines. *SAE International*, 2010.

[67] S . S . Ahmed, G . Moréac, T . Zeuch, and F . Mauss. Reduced Mechanism for the Oxidation of the Mixtures of n-Heptane and iso-Octane. *Proceedings of the European Combustion Meeting*, 2005.

[68] Gregory P. Smith, David M. Golden, Michael Frenklach, Nigel W. Moriarty, Boris Eiteneer, Mikhail Goldenberg, C. Thomas Bowman, Ronald K. Hanson, Soonho Song, William C. Gardiner, Vitali V. Lissianski, and Zhiwei Qin. GRI-Mech 3.0.

[69] Andrew Lewis, Sam Akehurst, Jamie Turner, R Patel, and A Popplewell. Observations on the measurement and performance impact of catalyzed vs . non catalyzed EGR on a heavily downsized DISI engine. *SAE International*, 2014.

[70] M. Fischer, P. Kreutziger, Y. Sun, and A. Kotrba. Clean EGR for Gasoline Engines – Innovative Approach to Efficiency Improvement and Emissions Reduction Simultaneously. *SAE Technical Papers*, pages 1–9, 2017.

[71] Qilong Lu, Magdi Khair, Jeongmin Lee, Seongoh Lee, Euisung Lee, and Kwonoh Oh. A Filtration System for High-Pressure Loop EGR. *SAE International*, 2011.

[72] Jennifer A Topinka, Michael D Gerty, John B Heywood, and James C Keck. Knock Behavior of a Lean-Burn , H 2 and CO Enhanced , SI Gasoline Engine Concept. *SAE International*, 2004.

[73] Xiaoguo Tang, Daniel M Kabat, Robert J Natkin, William F Stockhausen, and James Heffel. Ford P2000 Hydrogen Engine Dynamometer Development. *SAE International*, 2002.

[74] Daniel Fennell, Jose M Herreros, Athanasios Tsolakis, Hongming Xu, Kirsty Cockle, and Paul Millington. GDI Engine Performance and Emissions with Reformed Exhaust Gas Recirculation (REGR) Reformate Combustion in Gasoline Engines. *SAE International*, 2013.

[75] Terry Alger and Barrett Mangold. Dedicated EGR : A New Concept in High Efficiency Engines. *SAE International*, 2(1):620–631, 2009.

[76] Christopher Chadwell, Terrence Alger, Jacob Zuehl, and Raphael Gukelberger. A Demonstration of Dedicated EGR on a 2.0 L GDI Engine. *SAE International Journal of Engines*, 7(1):434–447, apr 2014.

[77] Raphael Gukelberger, Jess Gingrich, Terrence Alger, and Steven Almaraz. LPL EGR and D-EGR® Engine Concept Comparison Part 2: High Load Operation. *SAE International Journal of Engines*, 8(2):547–556, apr 2015.

[78] Yan Chang, James P. Szybist, Josh A Pihl, and Daniel William Brookshear. Catalytic EGR-Loop Reforming for High Efficiency in a Stoichiometric SI Engine through TCR and Dilution Limit Extension. 2. Engine Performance. *Energy & Fuels*, 2017.

[79] Kengo Kumano and Shiro Yamaoka. Analysis of Knocking Suppression Effect of Cooled EGR in Turbo-Charged Gasoline Engine. *SAE International*, 2014.

[80] Zhijin Zhang, Haiyan Zhang, Tianyou Wang, and Ming Jia. Effects of tumble combined with EGR (exhaust gas recirculation) on the combustion and emissions in a spark ignition engine at part loads. *Energy*, 65:18–24, 2014.

[81] Zhimin Liu and David Cleary. Fuel Consumption Evaluation of Cooled External EGR for a Downsized Boosted SIDI DICP Engine. *SAE International*, 2014.

[82] Ziga Ivanic, Ferran Ayala, Joshua Goldwitz, and John B Heywood. Effects of Hydrogen Enhancement on Efficiency and NOx Emissions of Lean and EGR-Diluted Mixtures in a SI Engine Reprinted From : SI Combustion and Direct Injection SI Engine Technology. *SAE International*, 2005.

[83] Sang Ki Park, Jungkoo Lee, Kyungcheol Kim, Seongho Park, and Hyung Man Kim. Experimental characterization of cooled EGR in a gasoline direct injection engine for reducing fuel consumption and nitrogen oxide emission. *Heat and Mass Transfer/Waerme- und Stoffuebertragung*, 51(11):1639–1651, 2015.

[84] Loic Francqueville and Jean-Baptiste Michel. On the Effects of EGR on Spark-Ignited Gasoline Combustion at High Load. *SAE International Journal of Engines*, 7(4):1808–1823, 2014.

[85] Konstantinos Siokos, Rohit Koli, Robert Prucka, Jason Schwanke, and Julia Miersch. Assessment of Cooled Low Pressure EGR in a Turbocharged Direct Injection Gasoline Engine. *SAE International Journal of Engines*, 8(4):2015–01–1253, apr 2015.

[86] Ting Liu, Fuyuan Zhang, Yuedong Chao, Zongjie Hu, and Liguang Li. Effect of EGR Temperature on PFI Gasoline Engine Combustion and Emissions. *SAE International*, 2018.

[87] Tao Yin, Tie Li, Longhua Chen, and Bin Zheng. Optimization of Compression Ratio of a Boosted PFI SI Engine with Cooled EGR. *SAE International*, 2014.

[88] Jianye Su, Min Xu, Tie Li, Yi Gao, and Jiasheng Wang. Combined effects of cooled EGR and a higher geometric compression ratio on thermal efficiency improvement of a downsized boosted spark-ignition direct-injection engine. *Energy Conversion and Management*, 78:65–73, feb 2014.

[89] Terrence Alger, Raphael Gukelberger, Jess Gingrich, and Barrett Mangold. The Impact of Cooled EGR on Peak Cylinder Pressure in a Turbocharged, Spark Ignited Engine. *SAE International Journal of Engines*, 8(2):455–463, apr 2015.

[90] Dongxian Song, Ning Jia, Xiangyang Guo, Xingxing Ma, Zhigang Ma, Dingwei Gao, Kejun Li, Haipeng Lai, and Chunhui Zhang. Low Pressure Cooled EGR for Improved Fuel Economy on a Turbocharged PFI Gasoline Engine. *SAE International*, 2014.

[91] Yorick Duchaussoy, Alain Lefebvre, Robert Bonetto, and S A Renault. Dilution Interest on Turbocharged SI Engine Combustion. *SAE International*, 2003.

[92] E. Galloni, G. Fontana, and R. Palmaccio. Effects of exhaust gas recycle in a downsized gasoline engine. *Applied Energy*, 105:99–107, may 2013.

[93] Daisuke Takaki, Hirofumi Tsuchida, Tetsuya Kobara, Mitsuhiro Akagi, Takeshi Tsuyuki, and Morihiro Nagamine. Study of an EGR System for Downsizing Turbocharged Gasoline Engine to Improve Fuel Economy. *SAE International*, 2014.

[94] Nikolai Semenov and J.E.S. Bradley. *Some problems of chemical kinetics and reactivity*. Pergamon Press, 1958.

[95] James A. Miller, Michael J. Pilling, and Jürgen Troe. Unravelling combustion mechanisms through a quantitative understanding of elementary reactions. *Proceedings of the Combustion Institute*, 30(1):43–88, 2005.

[96] A. F. Khan. *Chemical kinetics modelling of combustion in SI engines*. PhD thesis, University of Leeds, 2014.

[97] J. Warnatz, U. Maas, and R. W. Dibble. *Combustion: Physical and Chemical Fundamentals, Modelling and Simulation, Experiments, Pollutant Formation*. Springer, 4th edition, 2006.

[98] Charles K. Westbrook. Chemical kinetics of hydrocarbon ignition in practical combustion systems. In *Proceedings of the Combustion Institute*, volume 28, pages 1563–1577, jan 2000.

[99] A Frassoldati, T Faravelli, and E Ranzi. Kinetic modeling of the interactions between NO and hydrocarbons at high temperature. *Combustion and Flame*, 135:97–112, 2003.

[100] Peter Glarborg, M U Alzueta, Kim Dam-Johansen, and J A Miller. Kinetic Modeling of Hydrocarbon/Nitric Oxide Interactions in a Flow Reactor. *Combustion and Flame*, 115(1-2):1–27, 1998.

[101] Philippe Dagaut, Franck Lecomte, Sébastien Chevailler, and Michel Cathonnet. The reduction of NO by ethylene in a jet-stirred reactor at 1 atm: Experimental and kinetic modelling. *Combustion and Flame*, 119(4):494–504, 1999.

[102] Toshiji Amano and Frederick L Dryer. Effect of Dimethyl Ether, NOx and Ethane on CH4 Oxidation: High Pressure, Intermediate-Temperature Experiments and Modelling. *Twenty-seventh International Symposium on Combustion*, pages 397–404, 1998.

[103] P Dagaut and a Nicolle. Experimental study and detailed kinetic modeling of the effect of exhaust gas on fuel combustion: mutual sensitization of the oxidation of nitric oxide and methane over extended temperature and pressure ranges. *Combustion and Flame*, 140(3):161–171, feb 2005.

[104] P. A. Glaude, N. Marinov, Y. Koshiishi, N. Matsunaga, and M. Hori. Kinetic modeling of the mutual oxidation of NO and larger alkanes at low temperature. *Energy and Fuels*, 19(5):1839–1849, 2005.

[105] Morio Hori, Naoki Matsunaga, Nick Marinov, William Pitz, and Charles Westbrook. An experimental and kinetic calculation of the promotion effect of hydrocarbons on the NO-NO2 conversion in a flow reactor. *27th Symposium on Combustion*, pages 389–396, 1998.

[106] Philippe Dagaut, Jocelyn Luche, and Michel Cathonnet. Reduction of NO by n -Butane in a JSR: Experiments and Kinetic Modeling. *Energy & Fuels*, 14(3):712–719, 2001.

[107] A A Burluka, K Liu, C G W Sheppard, A J Smallbone, and R Woolley. The Influence of Simulated Residual and NO Concentrations on Knock Onset for PRFs

and Gasolines Reprinted From : SI Engine Experiment and Modeling. *SAE International*, 2004.

[108] S K Prabhu, H Li, D L Miller, and N P Cernansky. The Effect of Nitric Oxide on Autoignition of a Primary Reference Fuel Blend in a Motored Engine. *SAE International*, 1993.

[109] Per Risberg, David Johansson, Johan Andrae, Gautam Kalghatgi, Pehr Bjornbom, and Hans-Erik Angstrom. The Influence of NO on the Combustion Phasing in an HCCI Engine. *SAE International*, 2006.

[110] Chitralkumar V Naik, Karthik Puduppakkam, and Ellen Meeks. Modeling the Detailed Chemical Kinetics of NOx Sensitisation for the Oxidation of a Model fuel for Gasoline. *SAE International*, pages 556–566, 2010.

[111] O Stenlaas, A Gogan, R Egnell, and B Sunden. The Influence of Nitric Oxide on the Occurrence of Autoignition in the End Gas of Spark Ignition Engines. *SAE International*, 2002.

[112] Y Kawabata, T Sakonji, and T Amano. The Effect of NOx on Knock in Spark-Ignition Engines. *SAE International*, 1999.

[113] O Stenlaas, P Einewall, R Egnell, and B Johansson. Measurement of Knock and Ion Current in a Spark Ignition Engine with and without NO Addition to the Intake Air Reprinted From : SI Combustion. *SAE International*, 2003.

[114] A Dubreuil, F Foucher, and C Mounaim-Rousselle. Effect of EGR Chemical Components and Intake Temperature on HCCI Combustion Development. *SAE International*, pages 776–790, 2006.

[115] P J Roberts and C G W Sheppard. The Influence of Residual Gas NO content on Knock Onset of Iso-octane , PRF , TRF and ULG Mixtures in SI Engines. *SAE International*, pages 1–22, 2013.

[116] G. Moréac, P Dagaut, J.F. Roesler, and M. Cathonnet. Nitric oxide interactions with hydrocarbon oxidation in a jet-stirred reactor at 10 atm. *Combustion and Flame*, 145(3):512–520, may 2006.

[117] Francesco Contino, Fabrice Foucher, Philippe Dagaut, Tommaso Lucchini, Gianluca D'Errico, and Christine Mounaïm-Rousselle. Experimental and numerical analysis of nitric oxide effect on the ignition of iso-octane in a single cylinder HCCI engine. *Combustion and Flame*, 160(8):1476–1483, aug 2013.

[118] Zhongyuan Chen, Hao Yuan, Tien Mun Foong, Yi Yang, and Michael Brear. The impact of nitric oxide on knock in the octane rating engine. *Fuel*, 235:495–503, 2019.

[119] T Faravelli, A Frassoldati, and E Ranzi. Kinetic modeling of the interactions between NO and hydrocarbons in the oxidation of hydrocarbons at low temperatures. *Combustion and Flame*, 132:188–207, 2003.

[120] S. Verhelst and C. G W Sheppard. Multi-zone thermodynamic modelling of spark-ignition engine combustion - An overview. *Energy Conversion and Management*, 50(5):1326–1335, 2009.

[121] Cinzia Tornatore, Fabio Bozza, Vincenzo De Bellis, Luigi Teodosio, Gerardo Valentino, and Luca Marchitto. Experimental and numerical study on the influence of cooled EGR on knock tendency, performance and emissions of a downsized spark-ignition engine. *Energy*, 172:968–976, 2019.

[122] Jing Yang Tan, Fabrizio Bonatesta, Hoon Kiat Ng, and Suyin Gan. Developments in computational fluid dynamics modelling of gasoline direct injection engine combustion and soot emission with chemical kinetic modelling. *Applied Thermal Engineering*, 107:936–959, 2016.

[123] M. C. Drake and D. C. Haworth. Advanced gasoline engine development using optical diagnostics and numerical modeling. *Proceedings of the Combustion Institute*, 31 I(1):99–124, 2007.

[124] Stefano Fontanesi, Stefano Paltrinieri, Alessandro D'Adamo, Giuseppe Cantore, and Christopher Rutland. Knock Tendency Prediction in a High Performance Engine Using LES and Tabulated Chemistry. *SAE International Journal of Fuels and Lubricants*, 6(1):98–118, apr 2013.

[125] Stefano Fontanesi, Giuseppe Cicalese, Alessandro D'Adamo, and Giuseppe Cantore. A Methodology to Improve Knock Tendency Prediction in High Performance Engines. *Energy Procedia*, 45:769–778, 2014.

[126] S. Fontanesi, a. D'Adamo, and C. J. Rutland. Large-Eddy simulation analysis of spark configuration effect on cycle-to-cycle variability of combustion and knock. *International Journal of Engine Research*, 16(3):403–418, jan 2015.

[127] M. P. Halstead, L. J. Kirsch, A. Prothero, and C. P. Quinn. A Mathematical Model for Hydrocarbon Autoignition at High Pressures. *Proceedings of the Royal Society A: Mathematical, Physical and Engineering Sciences*, 346(45-60):515–538, 1975.

[128] Tien Mun Foong. *On the Autoignition of Ethanol / Gasoline Blends in Spark-Ignition Engines*. PhD thesis, University of Melbourne, 2013.

[129] J. C. Livengood and P. C. Wu. Correlation of autoignition phenomena in internal combustion engines and rapid compression machines. *Symposium (International) on Combustion*, 5(1):347–356, 1955.

[130] Longhua Chen, Tie Li, Tao Yin, and Bin Zheng. A predictive model for knock onset in spark-ignition engines with cooled EGR. *Energy Conversion and Management*, 87:946–955, nov 2014.

[131] Alexander Fandakov, Michael Grill, Michael Bargende, and Andre Casal Kulzer. Two-Stage Ignition Occurrence in the End Gas and Modeling Its Influence on Engine Knock. *SAE International Journal of Engines*, 10(4):2109–2128, 2017.

[132] R Worret, S Bernhardt, F Schwarz, and U Spicher. Application of Different Cylinder Pressure Based Knock Detection Methods in Spark Ignition Engines. *SAE Technical Paper*, 2002.

[133] Alexander Fandakov, Grill Michael, Michael Bargende, and Andre Casal Kulzer. A Two-Stage Knock Model for the Development of Future SI Engine Concepts. *SAE Technical Paper*, 2018.

[134] D. Bradley, C. Morley, X. J. Gu, and D. R. Emerson. Amplified Pressure Waves During Autoignition: Relevance to CAI Engines. *SAE Technical Paper Series*, 2002.

[135] F Bozza, D Siano, and E Torella. Cycle-by-Cycle Analysis, Knock Modeling and Spark-Advance Setting of a Downsized Spark-Ignition Turbocharged Engine. *SAE Int. J. Engines*, 2(2):381–389, 2009.

[136] Xudong Zhen, Yang Wang, and Yongsheng Zhu. Study of knock in a high compression ratio SI methanol engine using les with detailed chemical kinetics. *Energy Conversion and Management*, 75:523–531, 2013.

[137] Gequn Shu, Jiaying Pan, and Haiqiao Wei. Analysis of onset and severity of knock in SI engine based on in-cylinder pressure oscillations. *Applied Thermal Engineering*, 51(1-2):1297–1306, 2013.

[138] Gequn Shu, Jiaying Pan, Haiqiao Wei, and Ning Shi. Simulation research on the effect of cooled EGR, supercharging and compression ratio on downsized SI engine knock. *Chinese Journal of Mechanical Engineering*, 26(2):341–350, 2013.

[139] E. Galloni, G. Fontana, and S. Staccone. Numerical and experimental characterization of knock occurrence in a turbo-charged spark-ignition engine. *Energy Conversion and Management*, 85:417–424, sep 2014.

[140] Markus Kraft, Peter Maigaard, Fabian Mauss, Magnus Christensen, and Bengt Johansson. Investigation of combustion emissions in a homogeneous charge compression injection engine: Measurements and a new computational model. *Proceedings of the Combustion Institute*, 28(1):1195–1201, 2000.

[141] P. Maigaard, F. Mauss, and M. Kraft. Homogeneous Charge Compression Ignition Engine: A Simulation Study on the Effects of Inhomogeneities. *Journal of Engineering for Gas Turbines and Power*, 125(2):466, 2003.

[142] Amit Bhave, Michael Balthasar, Markus Kraft, and Fabian Mauss. Numerical Analysis of a Natural Gas Fuelled HCCI Engine with Exhaust Gas Recirculation Using a Stochastic Reactor Model. *Cambridge Centre for Computational Chemical Engineering*, 5(1):93–104, 2003.

[143] Sebastian Mosbach, Amit Bhave, Robert W. Dibble, J. Hunter Mack, Fabian Mauss, and Markus Kraft. Simulating a Homogeneous Charge Compression Ignition Engine Fuelled with a DEE/EtOH Blend. *SAE Technical Paper Series*, 2006.

[144] Amit Bhave, Markus Kraft, Luca Montorsi, and Fabian Mauss. Modelling a Dual-Fuelled Multi-Cylinder HCCI Engine Using a PDF Based Engine Cycle Simulator. *SAE Technical Paper Series*, 2004.

[145] Amit Bhave, Markus Kraft, Fabian Mauss, Hua Zhao, Markus Kraft, Amit Bhave, and Aaron Oakley. Evaluating the EGR-AFR Operating Range of a HCCI Engine. *SAE Technical Paper Series*, 2005.

[146] A Gogan, B Sunden, H Lehtiniemi, and F Mauss. Stochastic Model for the Investigation of the Influence of Turbulent Mixing on Engine Knock Reprinted From : SI Engine Experiment and Modeling. *SAE Transactions Journal of Engines*, 2004.

[147] Martin Tunér, Michal Pasternak, Fabian Mauss, and Henry Bensler. A PDF-Based Model for Full Cycle Simulation of. *SAE Technical Paper*, 2008.

[148] Martin Tunér. *Stochastic Reactor Models for Engine Simulations*. PhD thesis, Lund University, 2008.

[149] Simon Bjerkborn, Karin Frojd, Cathleen Perlman, and Fabian Mauss. A Monte Carlo Based Turbulent Flame Propagation Model for Predictive SI In-Cylinder Engine Simulations Employing Detailed Chemistry for Accurate Knock Prediction. *SAE International Journal of Engines*, 5(4):1637–1647, 2012.

[150] Michal Pasternak, Fabian Mauss, Marc Sens, Michael Riess, Andreas Benz, and Karl Georg Stapf. Gasoline engine simulations using zero-dimensional spark ignition stochastic reactor model and three-dimensional computational fluid dynamics engine model. *International Journal of Engine Research*, 17(1):76–85, 2016.

[151] Dirk Linse, Andreas Kleemann, and Christian Hasse. Probability density function approach coupled with detailed chemical kinetics for the prediction of knock in turbocharged direct injection spark ignition engines. *Combustion and Flame*, 161(4):997–1014, 2014.

[152] Jiawei Lai, Andreas Manz, David Ooi, Sebastian Mosbach, Jennifer Anna Noble, Kok Foong Lee, Jan Niklas Geiler, Dumitru Duca, Amit Bhave, Nick Eaves, and Cristian Focsa. Model Guided Application for Investigating Particle Number (PN) Emissions in GDI Spark Ignition Engines. *SAE Technical Paper Series*, 1, 2019.

[153] Corinna Netzer, Lars Seidel, Michal Pasternak, Christian Klauer, Cathleen Perlman, Frederic Ravet, Fabian Mauss, Michal Pasternak, Frederic Ravet, Fabian Mauss, Lars Seidel, and Cathleen Perlman. Engine Knock Prediction and Evaluation Based on Detonation Theory Using a Quasi-Dimensional Stochastic Reactor Model. *SAE Technical Papers*, 2017.

[154] Michal Pasternak, Fabian Mauss, Marc Sens, Michael Rieß, Andreas Benz, and Fabio Xavier. 0D/3D Simulations of Combustion in Gasoline Engines Operated with Multiple Spark Plug Technology. *SAE Technical Paper Series*, 1, 2015.

[155] Vincent Talon, Maria Rivas, Emmanuel Witrant, Christian Caillol, Pascal Higelin, and Olivier Sename. Validation and Application of a New 0D Flame/Wall Interaction Sub Model for SI Engines. *SAE International Journal of Engines*, 5(3):718–733, 2011.

[156] Syed Sayeed Ahmed, Fabian Mauß, Gladys Moréac, and Thomas Zeuch. A comprehensive and compact n-heptane oxidation model derived using chemical lumping. *Physical Chemistry Chemical Physics*, 9(9):1107–1126, 2007.

[157] H J Curran, P Gaffuri, W J Pitz, and C K Westbrook. A Comprehensive Modeling Study of iso-Octane Oxidation. *Combustion and Flame*, 129:253–280, 2002.

[158] Thomas Lauer, Michael Heiss, Nikola Bobicic, Werner Holly, and Stefan Pritze. A Comprehensive Simulation Approach to Irregular Combustion. *SAE International*, 2014.

[159] S. Mani Sarathy, Goutham Kukkadapu, Marco Mehl, Weijing Wang, Tamour Javed, Sungwoo Park, Matthew A. Oehlschlaeger, Aamir Farooq, William J. Pitz, and Chih Jen Sung. Ignition of alkane-rich FACE gasoline fuels and their surrogate mixtures. *Proceedings of the Combustion Institute*, 35(1):249–257, 2015.

[160] S. Mani Sarathy, Goutham Kukkadapu, Marco Mehl, Tamour Javed, Ahfaz Ahmed, Nimal Naser, Aniket Tekawade, Graham Kosiba, Mohammed AlAbbad, Eshan Singh, Sungwoo Park, Mariam Al Rashidi, Suk Ho Chung, William L. Roberts, Matthew a. Oehlschlaeger, Chih-Jen Sung, and Aamir Farooq. Compositional effects on the ignition of FACE gasolines. *Combustion and Flame*, 169:171–193, 2016.

[161] Bingjie Chen, Casimir Togbé, Zhandong Wang, Philippe Dagaut, and S. Mani Sarathy. Jet-stirred reactor oxidation of alkane-rich FACE gasoline fuels. *Proceedings of the Combustion Institute*, 36(1):517–524, 2017.

[162] Hatem Selim, Samah Y. Mohamed, Alaa E. Dawood, and S. Mani Sarathy. Understanding premixed flame chemistry of gasoline fuels by comparing quantities of interest. *Proceedings of the Combustion Institute*, 36(1):1203–1211, 2017.

[163] S. Mani Sarathy, Aamir Farooq, and Gautam T. Kalghatgi. Recent progress in gasoline surrogate fuels. *Progress in Energy and Combustion Science*, 65:67–108, 2018.

[164] Tianfeng Lu and Chung K. Law. Toward accommodating realistic fuel chemistry in large-scale computations. *Progress in Energy and Combustion Science*, 35(2):192–215, 2009.

[165] Chitralkumar V. Naik, Karthik Puduppakkam, Cheng Wang, Jeyapandian Kottalam, Long Liang, Devin Hodgson, and Ellen Meeks. Applying Detailed Kinetics to Realistic Engine Simulation: the Surrogate Blend Optimizer and Mechanism Reduction Strategies. *SAE International Journal of Engines*, 3(1):241–259, 2010.

[166] Kyle E. Niemeyer, Chih Jen Sung, and Mandhapati P. Raju. Skeletal mechanism generation for surrogate fuels using directed relation graph with error propagation and sensitivity analysis. *Combustion and Flame*, 157(9):1760–1770, 2010.

[167] A. Stagni, A. Frassoldati, A. Cuoci, T. Faravelli, and E. Ranzi. Skeletal mechanism reduction through species-targeted sensitivity analysis. *Combustion and Flame*, 163:382–393, 2016.

[168] Haoran Hu and James Keck. Autoignition of Adiabatically Compressed Combustible Gas Mixtures. *SAE Technical Paper Series*, 1, 1987.

[169] H.J. Curran, P. Gaffuri, W.J. Pitz, and C.K. Westbrook. A Comprehensive Modeling Study of n-Heptane Oxidation. *Combustion and Flame*, 114(1-2):149–177, jul 1998.

[170] J. M. Anderlohr, R. Bounaceur, a. Pires Da Cruz, and F. Battin-Leclerc. Modeling of autoignition and NO sensitization for the oxidation of IC engine surrogate fuels. *Combustion and Flame*, 156(2):505–521, 2009.

[171] J. C.G. Andrae. Kinetic modeling of the influence of NO on the combustion phasing of gasoline surrogate fuels in an HCCI engine. *Energy and Fuels*, 27(11):7098–7107, 2013.

[172] Zhaolei Zheng and Zhumei Lv. A new skeletal chemical kinetic model of gasoline surrogate fuel with nitric oxide in HCCI combustion. *Applied Energy*, 147:59–66, jun 2015.

[173] Hatim Machrafi. Experimental validation of a kinetic multi-component mechanism in a wide HCCI engine operating range for mixtures of n-heptane, iso-octane and toluene: Influence of EGR parameters. *Energy Conversion and Management*, 49(11):2956–2965, nov 2008.

[174] Hatim Machrafi, Simeon Cavadias, and Jacques Amouroux. The development and experimental validation of a reduced ternary kinetic mechanism for the autoignition at HCCI conditions, proposing a global reaction path for ternary gasoline surrogates. *Fuel Processing Technology*, 90(2):247–263, 2009.

[175] Hatim Machrafi, Simeon Cavadias, and Philippe Guibert. An experimental and numerical investigation on the influence of external gas recirculation on the HCCI autoignition process in an engine: Thermal, diluting, and chemical effects. *Combustion and Flame*, 155(3):476–489, 2008.

[176] Yongrae Kim, Kyoungdoug Min, Min Soo Kim, Suk Ho Chung, and Choongsik Bae. Development of a Reduced Chemical Kinetic Mechanism and Ignition Delay Measurement in a Rapid Compression Machine for CAI Combustion. *SAE Technical Paper Series*, 1, 2007.

[177] Kyeonghyeon Lee, Yongrae Kim, and Kyoungdoug Min. Development of a reduced chemical kinetic mechanism for a gasoline surrogate for gasoline HCCI combustion. *Combustion Theory and Modelling*, 15(1):107–124, 2011.

[178] Abhijeet Raj, Iran David Charry Prada, Amer Ahmad Amer, and Suk Ho Chung. A reaction mechanism for gasoline surrogate fuels for large polycyclic aromatic hydrocarbons. *Combustion and Flame*, 159(2):500–515, 2012.

[179] Yao Dong Liu, Ming Jia, Mao Zhao Xie, and Bin Pang. Development of a new skeletal chemical kinetic model of toluene reference fuel with application to gasoline surrogate fuels for computational fluid dynamics engine simulation. *Energy and Fuels*, 27(8):4899–4909, 2013.

[180] Marco Mehl, William J. Pitz, Charles K. Westbrook, and Henry J. Curran. Kinetic modeling of gasoline surrogate components and mixtures under engine conditions. *Proceedings of the Combustion Institute*, 33(1):193–200, 2011.

[181] J.C.G. Andrae and R.a. Head. HCCI experiments with gasoline surrogate fuels modeled by a semidetailed chemical kinetic model. *Combustion and Flame*, 156(4):842–851, apr 2009.

[182] J. C.G. Andrae. Comprehensive chemical kinetic modeling of toluene reference fuels oxidation. *Fuel*, 107:740–748, 2013.

[183] Hu Wang, Mingfa Yao, Zongyu Yue, Ming Jia, and Rolf D. Reitz. A reduced toluene reference fuel chemical kinetic mechanism for combustion and polycyclic-aromatic hydrocarbon predictions. *Combustion and Flame*, 162(6):2390–2404, mar 2015.

[184] Yan Zhao An, Yi Qiang Pei, Jing Qin, Hua Zhao, and Xiang Li. Kinetic modeling of polycyclic aromatic hydrocarbons formation process for gasoline surrogate fuels. *Energy Conversion and Management*, 100:249–261, 2015.

[185] Yan zhao An, Yi qiang Pei, Jing Qin, Hua Zhao, Sheng ping Teng, Bing Li, and Xiang Li. Development of a PAH (polycyclic aromatic hydrocarbon) formation model for gasoline surrogates and its application for GDI (gasoline direct injection) engine CFD (computational fluid dynamics) simulation. *Energy*, 94:367–379, 2016.

[186] Chitralkumar V. Naik, Karthik V. Puduppakkam, Abhijit Modak, Ellen Meeks, Yang L. Wang, Qiyao Feng, and Theodore T. Tsotsis. Detailed chemical kinetic mechanism for surrogates of alternative jet fuels. *Combustion and Flame*, 158(3):434–445, 2011.

[187] Song-Charng Kong, Yong Sun, and Rolf D. Rietz. Modeling Diesel Spray Flame Liftoff, Sooting Tendency, and NOx Emissions Using Detailed Chemistry With Phenomenological Soot Model. *Journal of Engineering for Gas Turbines and Power*, 129(1):245, 2007.

[188] N. Lamoureux, P. Desgroux, A. El Bakali, and J. F. Pauwels. Experimental and numerical study of the role of NCN in prompt-NO formation in low-pressure CH4-O2-N2 and C2H2-O2-N2 flames. *Combustion and Flame*, 157(10):1929–1941, 2010.

[189] Jonathan Etheridge, Sebastian Mosbach, Markus Kraft, Hao Wu, and Nick Collings. Modelling cycle to cycle variations in an SI engine with detailed chemical kinetics. *Combustion and Flame*, 158(1):179–188, 2011.

[190] Andy D. B. Yates, André Swarts, and Carl L. Viljoen. An Investigation Of Anomalies Identified Within The ASTM Research And Motor Octane Scales. *SAE Technical Paper Series*, 1, 2003.

[191] A Swarts, A Yates, C Viljoen, and R Coetzer. A further study of inconsistencies between auto-ignition and knock intensity in the CFR octane rating engine. *SAE Technical Paper*, 2005.

[192] M Mehl, J Y Chen, W J Pitz, S M Sarathy, and C K Westbrook. An Approach for Formulating Surrogates for Gasoline with Application toward a Reduced Surrogate Mechanism for CFD Engine Modeling. *Energy and Fuels*, pages 5215–5223, 2011.

[193] Neal Morgan, Andrew Smallbone, Amit Bhave, Markus Kraft, Roger Cracknell, and Gautam Kalghatgi. Mapping surrogate gasoline compositions into RON/MON space. *Combustion and Flame*, 157(6):1122–1131, jun 2010.

[194] Hao Yuan, Yi Yang, Michael J. Brear, Tien Mun Foong, and James E. Anderson. Optimal octane number correlations for mixtures of toluene reference fuels (TRFs) and ethanol. *Fuel*, 188:408–417, 2017.

[195] Tien Mun Foong, Kai J. Morganti, Michael J. Brear, Gabriel da Silva, Yi Yang, and Frederick L. Dryer. The octane numbers of ethanol blended with gasoline and its surrogates. *Fuel*, 115:727–739, jan 2014.

[196] Jihad A. Badra, Nehal Bokhumseen, Najood Mulla, S. Mani Sarathy, Aamir Farooq, Gautam Kalghatgi, and Patrick Gaillard. A methodology to relate octane numbers of binary and ternary n-heptane, iso-octane and toluene mixtures with simulated ignition delay times. *Fuel*, 160:458–469, 2015.

[197] Andrew J Smallbone, Neal Morgan, Markus Kraft, Roger F Cracknell, Gautam Kalghatgi, A Bhave, Markus Kraft, Roger F Cracknell, and Gautam Kalghatgi. Simulating combustion of practical fuels and blends for modern engine applications using detailed chemical kinetics. *SAE Technical Papers*, pages 1–23, 2010.

[198] C. K. Westbrook, M. Sjöberg, and N. P. Cernansky. A new chemical kinetic method of determining RON and MON values for single component and multicomponent mixtures of engine fuels. *Combustion and Flame*, 195:50–62, 2018.

[199] Karthik V. Puduppakkam, Long Liang, Chitralkumar V. Naik, Ellen Meeks, and Bruce G. Bunting. Combustion and Emissions Modeling of a Gasoline HCCI Engine Using Model Fuels. *SAE Technical Paper Series*, 1, 2010.

[200] Xingyuan Su, Youngchul Ra, and Rolf D. Reitz. A Surrogate Fuel Formulation Approach for Real Transportation Fuels with Application to Multi-Dimensional Engine Simulations. *SAE International Journal of Fuels and Lubricants*, 7(1):236–249, 2014.

[201] J.W.G. Turner, A. Popplewell, R. Patel, T.R. Johnson, N.J. Darnton, S. Richardson, S.W. Bredda, R.J. Tudor, C.I. Bithell, R. Jackson, S.M. Remmert, R.F. Cracknell, J.X. Fernandes, A.G.J. Lewis, S. Akehurst, C.J. Brace, C. Copeland, R. Martinez-Botas, A. Romagnoli, and A.a. Burluka. Ultra Boost for Economy: Extending the Limits of Extreme Engine Downsizing. *SAE International*, 7(1):387–417, apr 2014.

[202] R.M. Siewert, R.B. Krieger, M.S. Huebler, P.C. Baruah, B. Khalighi, and M. Wesslau. Modifying an intake manifold to improve cylinder-to-cylinder EGR distribution in a di diesel engine using combined CFD and engine experiments. *SAE Technical Papers*, 2001.

[203] Alexander Sakowitz, Simon Reifarth, Mihai Mihaescu, and Laszlo Fuchs. Modeling of EGR Mixing in an engine intake manifold using LES. *International Conference on LES for Internal Combustion Engine Flows, Paris, 28-29 november 2012*, 69(1):1–9, 2012.

[204] S Reifarth, E Kristensson, J Borggren, A Sakowitz, and H.-E Angstrom. Analysis of EGR/Air Mixing by 1-D Simulation, 3-D Simulation and Experiments. *SAE Technical Paper*, 2014.

[205] J. N. Kim, H. Y. Kim, S. S. Yoon, J. H. Sohn, and C. R. Kim. Numerical studies on the mixing characteristics of exhaust gas recirculation gases with air, and their dependence on system geometries in four-cylinder engine applications. *Proceedings of the Institution of Mechanical Engineers, Part D: Journal of Automobile Engineering*, 223(4):585–597, 2009.

[206] Pavlos Dimitriou, Richard Burke, Colin Copeland, and Sam Akehurst. Study on the Effects of EGR Supply Configuration on Cylinder-to- Cylinder Dispersion and Engine Performance Using 1D-3D Co- Simulation. *SAE International*, 2015.

[207] Karl Giles. *Predicting abnormal combustion in highly boosted spark ignition engines*. PhD thesis, University of Bath, 2018.

[208] C S Draper. Pressure waves accompanying detonation in the internal combustion engine. *Journal of Aeronautical Sciences*, 5(6):219–226, 1938.

[209] S. M. Remmert, S. B. Campbell, R. F. Cracknell, A. Scheutze, A. G. J. Lewis, Karl Giles, Sam Akehurst, J W G Turner, R. Patel, and A. Popplewell. Octane Appetite: The Relevance of a Lower Limit to the MON Specification in a Downsized, Highly Boosted DISI Engine. *SAE International*, 2014.

[210] Gordon J Bartley. Identifying Limiters to Low Temperature Catalyst Activity. *SAE Technical Paper*, page 11, 2015.

[211] Joseph R. Theis, Andrew Getsoian, and Christine Lambert. The Development of Low Temperature Three-Way Catalysts for High Efficiency Gasoline Engines of the Future. *SAE International Journal of Fuels and Lubricants*, 10(2), 2017.

[212] J. A. Eng, W. R. Leppard, P. M. Najt, and F. L. Dryer. The Interaction Between Nitric Oxide and Hydrocarbon Oxidation Chemistry in a Spark Ignition Engine. *SAE International*, 1997.

[213] Chris Carey, Matthew Mcallister, Malcolm Sandford, Steve Richardson, Steven Pierson, Nick Darnton, Scott Bredda, Sam Akehurst, Chris Brace, James Turner, Richard Pearson, Nick Luard, Ricardo Martinez-botas, Colin Copeland, Mike Lewis, and Jason Fernandes. Extreme engine downsizing. Technical report, Jaguar Land Rover, UK, 2011.

[214] Richard Stone. *Introduction to Internal Combustion Engines*. Palgrave Macmillan, third edition, 1999.

[215] Hugh W Coleman and W Glenn Steele. *Experimentation, validation, and uncertainty analysis for engineers*. Wiley, 3rd edition, 2009.

[216] Arsham J. Shahlari and Jaal B. Ghandhi. A Comparison of Engine Knock Metrics. *SAE International*, 2012.

[217] Derek A Splitter and James P Szybist. Experimental Investigation of Spark-Ignited Combustion with High- Octane Biofuels and EGR. 1. Engine Load Range and Downsize Downspeed Opportunity. *Energy and Fuels*, 28:1418–1431, 2014.

[218] E. Agbro, A. S. Tomlin, W. Zhang, A. Burluka, F. Mauss, M. Pasternak, A. Alfazazi, and S. M. Sarathy. Chemical Kinetic Modeling Study on the Influence of n-Butanol Blending on the Combustion, Autoignition, and Knock Properties of Gasoline and Its Surrogate in a Spark-Ignition Engine. *Energy and Fuels*, 32(10):10065–10077, 2018.

[219] Andrew Smallbone, Amit Bhave, Aaron Coble, Sebastian Mosbach, Markus Kraft, Neal Morgan, and Gautam Kalghatgi. Simulating PM Emissions and Combustion Stability in Gasoline / Diesel Fuelled Engines. *SAE International*, 2011.

[220] A.R.a Coble, A.a Smallbone, A.a Bhave, S.b Mosbach, M.b Kraft, P.c Niven, and S.d Amphlett. Implementing detailed chemistry and in-cylinder stratification into 0/1-D IC engine cycle simulation tools. *SAE Technical Papers*, 2011.

[221] Sebastian Mosbach, Amit Bhave, Jonathan Etheridge, Andrew Smallbone, Markus Kraft, and Aaron Coble. Optimisation of Injection Strategy, Combustion Characteristics and Emissions for IC Engines Using Advanced Simulation Technologies. *SAE Technical Paper Series*, 1, 2011.

[222] Haiyun Su, Alexander Vikhansky, Sebastian Mosbach, Markus Kraft, Amit Bhave, Kyoung Oh Kim, Tatsuo Kobayashi, and Fabian Mauss. A computational study of an HCCI engine with direct injection during gas exchange. *Combustion and Flame*, 147(1-2):133–149, 2006.

[223] Shigeyuki Tanaka, Ferran Ayala, and James C. Keck. A reduced chemical kinetic model for HCCI combustion of primary reference fuels in a rapid compression machine. *Combustion and Flame*, 133(4):467–481, 2003.

[224] N. Peters, G. Paczko, R. Seiser, and K. Seshadri. Temperature cross-over and non-thermal runaway at two-stage ignition of n-heptane. *Combustion and Flame*, 128(1-2):38–59, jan 2002.

[225] Maria U Alzueta, Peter Glarborg, and Kim Dam-Johansen. Experimental and kinetic modeling study of the oxidation of benzene. *Int. J. Chem. Kinet.*, 32(8):498–522, 2000.

[226] Xian Zhong and Joseph W. Bozzelli. Thermochemical and kinetic analysis on the addition reactions of H, O, OH, and HO2with 1,3 cyclopentadiene. *International Journal of Chemical Kinetics*, 29(12):893–913, 1997.

[227] Xian Zhong and Joseph W. Bozzelli. Thermochemical and Kinetic Analysis of the H, OH, HO 2 , O, and O 2 Association Reactions with Cyclopentadienyl Radical. *The Journal of Physical Chemistry A*, 102(20):3537–3555, 1998.

[228] James A. Miller and Carl F. Melius. Kinetic and thermodynamic issues in the formation of aromatic compounds in flames of aliphatic fuels. *Combustion and Flame*, 91(1):21–39, 1992.

[229] Jean-Francois Pauwels, Joanne V Volponi, and James A Miller. The Oxidation of Allene in a Low-Pressure H2 / O2 / Ar-C3 H4 Flame. *Combustion Science and Technology*, 110-111(1):249–276, 1995.

[230] N M Marinov, W J Pitz, C K Westbrook, M J Castaldi, and S M Senkan. Modeling of Aromatic and Polycyclic Aromatic Hydrocarbon Formation in Premixed Methane and Ethane Flames. *Combustion Science and Technology*, 116-117(1-6):211–287, aug 1996.

[231] J. C.G. Andrae, T. Brinck, and G. T. Kalghatgi. HCCI experiments with toluene reference fuels modeled by a semidetailed chemical kinetic model. *Combustion and Flame*, 155(4):696–712, 2008.

[232] P. Dirrenberger, P. A. Glaude, R. Bounaceur, H. Le Gall, A. Pires Da Cruz, A. A. Konnov, and F. Battin-Leclerc. Laminar burning velocity of gasolines with addition of ethanol. *Fuel*, 115:162–169, 2014.

[233] Tien Mun Foong, Michael J. Brear, Kai J. Morganti, Gabriel Da Silva, Yi Yang, and Frederick L. Dryer. Modeling End-Gas Autoignition of Ethanol/Gasoline Surrogate Blends in the Cooperative Fuel Research Engine. *Energy and Fuels*, 31(3):2378–2389, 2017.

[234] J Baronick, B Heller, G Lach, and H Luf. Modal Measurement of Raw Exhaust Volume and Mass Emissions by SESAM. *SAE International*, 1998.

[235] David B Rhodes and James C Keck. Laminar Burning Speed Measurements of Indolene-air-Diluent Mixtures at High Pressures and Temperatures. *SAE Technical Paper*, 1985.

[236] Toby Rockstroh, Victor Burger, Andy Yates, and Dylan Smit. Laminar Flame Speed Characterization of Synthetic Gasoline Components. *SAE Technical Paper*, 2014.

[237] Roger Cracknell, Sarah Remmert, and Arjun Prakash. Evaluating fuel laminar burning velocity as a parameter in performance of spark ignition engines. In *FISITA World Automotive Congress Proceedings*, pages 5–7, 2014.

[238] Giulio Cazzoli, Claudio Forte, Gian Marco Bianchi, Stefania Falfari, and Sergio Negro. A Chemical-Kinetic Approach to the Definition of the Laminar Flame Speed for the Simulation of the Combustion of Spark-Ignition Engines. *SAE Technical Paper Series*, 1, 2017.

[239] Alessandro D'Adamo, Marco Del Pecchia, Sebastiano Breda, Fabio Berni, Stefano Fontanesi, and Jens Prager. Chemistry-Based Laminar Flame Speed Correlations for a Wide Range of Engine Conditions for Iso-Octane, n-Heptane, Toluene and Gasoline Surrogate Fuels. *SAE Technical Paper Series*, 1, 2017.

[240] Marco Del Pecchia, Sebastiano Breda, Alessandro D'Adamo, Stefano Fontanesi, Adrian Irimescu, and Simona Merola. Development of Chemistry-Based Laminar Flame Speed Correlation for Part-Load SI Conditions and Validation in a GDI Research Engine. *SAE International Journal of Engines*, 11(6):715–741, 2018.

[241] Berk Can Duva, Lauren Chance, and Elisa Toulson. Laminar Flame Speeds of Premixed Iso-Octane/Air Flames at High Temperatures with CO 2 Dilution. *SAE International*, pages 1–10, 2019.

[242] Vincenzo De Bellis, Enrica Malfi, Luigi Teodosio, Pietro Giannattasio, and Fabio Di Lenarda. A Novel Laminar Flame Speed Correlation for the Refinement of the Flame Front Description in a Phenomenological Combustion Model for Spark-Ignition Engines. *SAE International Journal of Engines*, 2018.

[243] F. Bozza, A. Gimelli, S. S. Merola, and B.M. Vaglieco. Validation of a Fractal Combustion Model through Flame Imaging. *SAE Technical Paper Series*, 2005.

[244] G. Subramanian, A. Pires Da Cruz, R. Bounaceur, and L. Vervisch. Chemical impact of CO and H2 addition on the autoignition delay of homogeneous n-heptane/air mixtures. *Combustion Science and Technology*, 179(9):1937–1962, 2007.

[245] J. M. Anderlohr, a. Piperel, a. Pires Da Cruz, R. Bounaceur, F. Battin-Leclerc, P. Dagaut, and X. Montagne. Influence of EGR compounds on the oxidation of an HCCI-diesel surrogate. *Proceedings of the Combustion Institute*, 32 II(2):2851–2859, 2009.

[246] Magnus Sjöberg, John E Dec, and Wontae Hwang. Thermodynamic and Chemical Effects of EGR and Its Constituents on HCCI Autoignition. *SAE International*, pages 776–790, 2007.

[247] Jorg M Anderlohr, Antonio Pires da Cruz, Roda Bounaceur, and Frederique Battin-Leclerc. Thermal and Kinetic Impact of CO, CO2, and H2O on the Post-oxidation of IC-Engine Exhaust Gases. *Combustion Science and Technology*, 182(1):39–59, 2010.

[248] Christian Rota, Kenan Mustafa, Nicholas Winder, Richard Osborne, Robert Morgan, David Mason, and Morgan Heikal. Implementation of a 0-D/1-D/3-D Process for the Heat Release Prediction of a Gasoline Engine in the Early Development Stage. *SAE Technical Paper Series*, 1:1–14, 2019.

[249] G Damköhler. Elektrochem, translation. Technical report, NACA Tech. Memo 1112, 1940.

[250] Domenic A. Santavicca, Deryuh Liou, and Gary L. North. A Fractal Model of Turbulent Flame Kernel Growth. *SAE Technical Paper Series*, 1990.

[251] Santosh Trimbake. Combustion Characterizations of Ethanol / Gasoline Blended Fuel in {SI} Engine Using Fractal Combustion Model. *SAE Technical Paper*, 2017.

[252] Gerhard Regner, Ho Teng, Peter Van Wieren, Jae In Park, Soo Youl Park, and Dae Joon Yeom. Performance Analysis and Valve Event Optimization for SI Engines Using Fractal Combustion Model. *SAE Technical Paper Series*, pages 776–790, 2006.

APPENDIX A

APPENDICES TO CHAPTER 5

A.1 The stochastic reactor model

The following sections describe the form of the different sub-models that make up the PDF transport equation in Section 5.2.

A.1.1 Chemical kinetics

The changes in composition and temperature due to chemical reactions are represented by the first term in Equation 5.3. The function G(ψ) is described by equations A.1.1 and A.1.1:

$$G_i(\psi) = \frac{M_i \dot{\omega}_i}{\rho}, i = 1, ..., N_S, \tag{A.1}$$

$$G_{N_S+1}(\psi) = -\frac{1}{c_v \rho} \sum_{j=1}^{N_S} e_j M_j \dot{\omega_j} - \frac{p}{c_v m} \frac{dV}{dt} \tag{A.2}$$

where M_i is the molecular mass, $\dot{\omega}_i$ is the production rate, e_i is the specific internal energy of species i; c_v is the specific heat capacity, m is the total mass, and V is the cylinder volume.

The reactions are modelled by a two-zone combustion model which is elaborated upon in Section A.2.

A.1.2 Turbulent mixing

The turbulent mixing model is a key component to the prediction of composition in the cylinder. Higher rates of turbulent mixing reduce the stratification of the mixture, resulting in a more homogeneous distribution. The mixing models are parameterised by a scalar mixing rate, which is defined in terms of τ_m, the mixing time, which is given by:

$$\frac{1}{\tau_m} = \frac{C_\phi}{2\tau} \tag{A.3}$$

where τ is a turbulence time-scale and C_ϕ is a mechanical-to-scalar time-scale ratio which remains constant during combustion events.

This model used a detailed $k - \epsilon$ turbulence time-scale model to define tau, which is calculated by the ratio of the turbulent kinetic energy, k, and the turbulence dissipation term, ϵ:

$$\tau = \frac{k}{\epsilon} \tag{A.4}$$

The value of k is time-dependent, approximated by solving the following quasi-dimensional

ODE to account for the various factors impacting the turbulence:

$$\frac{dk}{dt} = \underbrace{\frac{dk_{inj}}{dt}}_{\substack{\text{injection}\\ \text{effect}}} + \underbrace{\frac{dk_{den}}{dt}}_{\substack{\text{change in}\\ \text{density effect}}} + \underbrace{\frac{dk_{squ}}{dt}}_{\substack{\text{squish}\\ \text{effect}}} + \underbrace{\frac{dk_{prod}}{dt}}_{\substack{\text{swirl and}\\ \text{tumble effect}}} - \epsilon \tag{A.5}$$

The viscous dissipation term, ϵ, is given by:

$$\epsilon = \frac{C_{diss} k^{\frac{3}{2}}}{V_{cyl}^{\frac{1}{3}}} \tag{A.6}$$

where V_{cyl} is the instantaneous cylinder volume and C_{diss} is the turbulence dissipation constant that has been used in Section 5.6.2 of Chapter 5 to refine the flame propagation model.

A.1.3 Piston movement

The main effect of the piston movement is to change the instantaneous volume, $V(t)$, of the cylinder. This is calculated in terms of crank angle ,θ, by the geometry of the cylinder – specifically, the bore, b, the conrod length, l, the crank radius, r, and the clearance volume, V_c:

$$V(t) = V_c + \frac{\pi}{4} b^2 (l + a - a\cos\theta - \sqrt{l^2 - a^2 \cos^2\theta} \tag{A.7}$$

where $a = l/r$.

In addition to the instantaneous volume, the piston movement also impacts the turbulence of the charge, and this is factored into the swirl and tumble models within the detailed $k - \epsilon$ turbulence model.

A.1.4 Convective heat transfer

Heat transfer between the charge and the cylinder walls can effectively create a lower temperature boundary surrounding a hotter core. This temperature stratification can

significantly affect the combustion phasing and duration [6]. The SRM model uses a finite difference scheme to model the convective heat transfer:

$$\frac{1}{h}[U(\psi_{N_S+1}+h)\mathcal{F}(\psi_1,...,\psi_{N_S},\psi_{N_S+1}+h;t)-U(\psi_{N_S+1})\mathcal{F}(\psi;t)] \tag{A.8}$$

where h determines the amplitude of the temperature fluctuation.

To produce inhomogeneities in the temperature distribution a stochastic jump process is used to calculate the value for h, which takes the form:

$$h^{(i)}=\left|\frac{T^{(i)}-T_w}{C_h}\right| \tag{A.9}$$

where C_h is a constant that defines the magnitude of the fluctuation over and exponentially distributed time-step, $\hat{\tau}$.

The heat transfer between the cylinder charge and the walls is modelled by $U(T)$:

$$U(T)=\frac{C_{HT}h_gA}{c_vm}(T-T_w) \tag{A.10}$$

where h_g is the heat transfer coefficient, C_{HT} is a constant heat transfer multiplier, and A is the available heat transfer area, which is dependent upon cylinder geometry and piston position.

h_g is defined by the Woshni heat transfer correlation:

$$h_q=3.26B^{-}0.2p^{0}.8T^{-}0.53w^{0}.8 \tag{A.11}$$

where B, p, and T are cylinder bore, pressure, and temperature; w is the local gas velocity defined by a combination of the mean piston speed and the contribution of combustion on the the cylinder pressure.

A.1.5 Fuel injection

The stochastic reactor model has the capability to model injection events, either with a physical model or a PDF-based model. Since the aims of this study were to assess the modelling of dilution effects, the injection models were not used, as they added an increased level of complexity to the model in an area that is not strictly relevant to the experimental aims.

A.2 Two-zone model

The stochastic model uses a two-zone spark ignition model, as illustrated in Figure A-1, in which the burned zone and unburned zone contain N_b and N_u number of particles respectively. Mixing occurs within each zone but not between zones.

The flame propagation model – step 7 in Figure 5-1 – begins at CAD_{spark} at which point the burned zone is defined by an initial flame radius. From this point the model simulates the burn process by moving mass from one unburned particle at a time into the burned zone.

Recent updates to the SRM Suite software have included the integration of a fractal flame propagation model as an alternative to the field entrainment model. Verhelst et al comment that these original entrainment equations were never a phenomenological model of the flame development but rather a mathematical correlation to the observed MFB profile.

The fractal flame propagation model represents the flame wrinkling effects during turbulent combustion for quasi-dimensional models. The model relates laminar flame speeds to turbulent flame speeds according to the increase in the flame surface due to flame wrinkling – along the lines of relationships first introduced by Damkolher in 1940 [249]:

$$\frac{dm_b}{dt} = \rho_u \left(\frac{A_T}{A_L}\right) A_L S_L = \rho_u A_L S_T \tag{A.12}$$

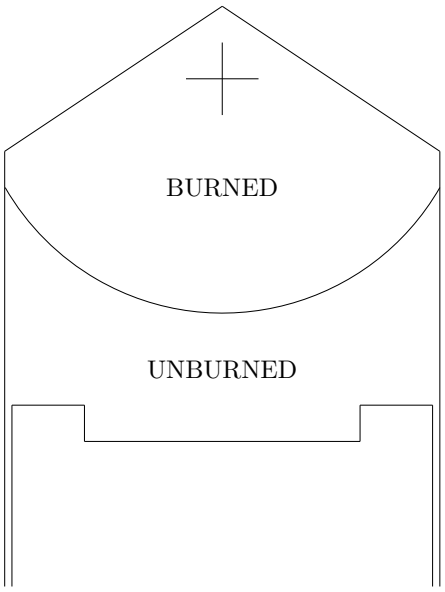

Figure A-1: Schematic of the zones that the two zone model is divided into. The burned zone propagates in a spherical shape, which becomes truncated by the cylinder walls and roof. Recreated from [6].

ρ_u = *density of unburned mixture*

A_T = *turbulent flame surface area*

A_L = *laminar flame surface area*

S_L = *laminar flame speed*

S_T = *turbulent flame speed*

Bozza et al [243] derive the terms which then build on this relationship to describe the fractal model in the form:

$$\frac{dm_b}{dt} = \rho_u \left(\frac{L_{max}}{L_{min}}\right)^{D_3-2} A_L S_L \tag{A.13}$$

where L_{max} and L_{min} are the maximum and minimum turbulent length scales[1] and D_3 is the fractal dimension which is given by:

$$D_3 = \frac{2.35\acute{u} + 2.05 S_L}{\acute{u} + S_L} \tag{A.14}$$

[1] L_{max} is proportional to the flame radius, and L_{min} is proportional to the instantaneous clearance height of the cylinder and the turbulent Reynolds number.

where ú is the turbulence intensity [2], given by:

$$\acute{u} = \sqrt{\frac{2k}{3}} \tag{A.15}$$

Where k is the turbulent energy.

Bozza et al [243] went on to validate their fractal combustion model against flame imaging data, which supported its use over the alternative entrainment mechanism which has not been experimentally observed in real premixed flames [251].

The fractal flame propagation model is becoming increasingly common in quasi-dimensional combustion modelling, both Regner et al [252] and Trimbake et al [251] describe it as "one of the dominant quasi-dimensional models" due to its simplicity and ability to account for combustion chamber shape, flow characteristics, and residual gas content.

The SRM Suite uses a modified fractal model to account for wall-flame distances with the form [6]:

$$S_T = f_g f_w S_L \left(\frac{L_{max}}{L_{min}} \right)^{D_3 - 2} \tag{A.16}$$

where f_g and f_w describe the flame kernel growth and wall influence factors respectively.

The burn rate is defined by this fractal flame propagation model, in which the increase in flame radius is calculated by multiplying the total flame speed, S_T, with the time step:

$$R_{f;n} = R_{f;n-1} + S_T \Delta t \tag{A.17}$$

[2] The turbulence intensity relates the instantaneous turbulent energy at the flame front, described by Santavicca et al [250] as the square root of the area under the turbulence energy spectrum over the range of frequency components greater than the reciprocal lifetime. This increases as the flame propagates.

The total flame speed is defined by:

$$S_T = f_g f_w S_L \left(\frac{L_{max}}{L_{min}}\right)^{D_3-2} \tag{A.18}$$

S_L is the laminar flame speed, calculated using standard laminar flame speed correlations published by Heywood [18] [3]

f_g is the flame kernel growth factor, calculated as a function of crank angle and the characteristic time constant, τ, which is a user defined input to the model:

$$f_g = 1 - exp\left(-\frac{CAD - CAD_{spark}}{\tau}\right) \tag{A.19}$$

f_w is the flame wall interaction factor, which accounts for the damping effect of the wall on the flame speed when in close proximity. It is defined by two inputs to the model, the wall quenching zone and the wall influence zone, which are illustrated in Figure A-2. Here green trace represents the amplitude of f_w, which is at unity in the fully turbulent region, reduced in the influence zone by the wall interactions with the flow around the flame, and quenched to zero on the boundary of the quenching zone where heat lost to the wall leads to localised quenching.

Since the model does not use spatial coordinates to represent the flame front, a mean flame to wall distance, d_{rms} is used to account for the cylinder geometry, which is illustrated in Figure A-3[4].

L_{min} and L_{max} are the minimum and maximum flame wrinkling scales, calculated as a function of the turbulent Reynolds number (Equation A.20) and flame radius (Equation A.21) respectively.

[3] This correlation takes the form: $S_L = S_{L0} \frac{T_u}{T_0}^{\alpha} \frac{p}{p_0}^{\beta}$ where $S_{L0} = 0.305 - 0.549(\phi - 1.21)^2$, $\alpha = 2.4 - 0.271(\phi^{3.51})$ and $\beta = -0.357 + 0.14(\phi^{2.77})$.

[4] The calculation of F_w should probably be added to the appendices...

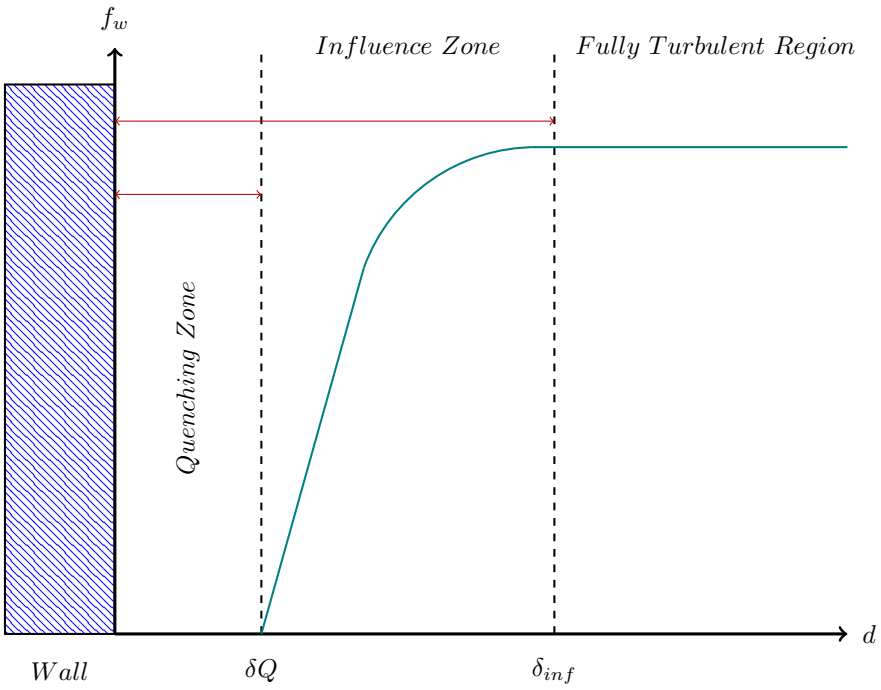

Figure A-2: Schematic of the flame-wall interaction parameters, showing how f_w changes as the flame approaches the wall. Recreated from [6].

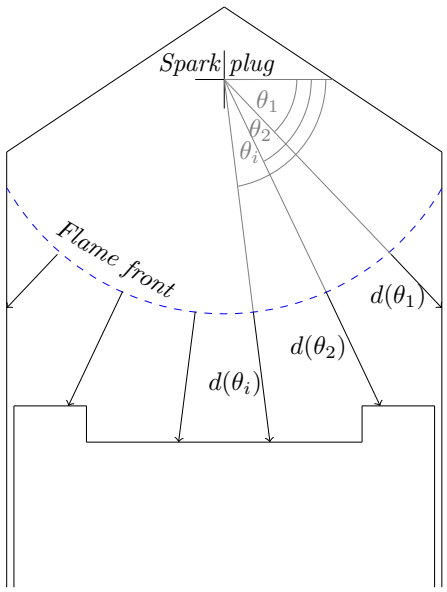

Figure A-3: Schematic of how the flame to wall distance is represented. The geomtry of the cylinder is accounted for by the mean flame to wall distance, d_{rms}. Recreated from [6].

$$L_{min} = \frac{L_{integral}}{Re_t^{3/4}} \tag{A.20}$$

$$L_{max} = C_{scale} R_f \tag{A.21}$$

D_3 is the fractal dimension as defined by Bozza et al [243] in Equation A.14.

For the calibration process described in Section 5.4 of Chapter 5 the flame propagation parameters that were used to calibrate the model were:

- The pressure equilibration constant.
- The wall influence constant, as described in Figure A-2.
- The characteristic time constant, τ in Equation A.19.
- The flame scale constant, C_{scale} in Equation A.21.
- The turbulence dissipation constant, C_{diss} in Equation A.6.

A.3 Demonstration of the calibration tool in use

Screen shots of the calibration tool in use are depicted in Figures A-4, A-5, and A-6 to provide an example of its operation.

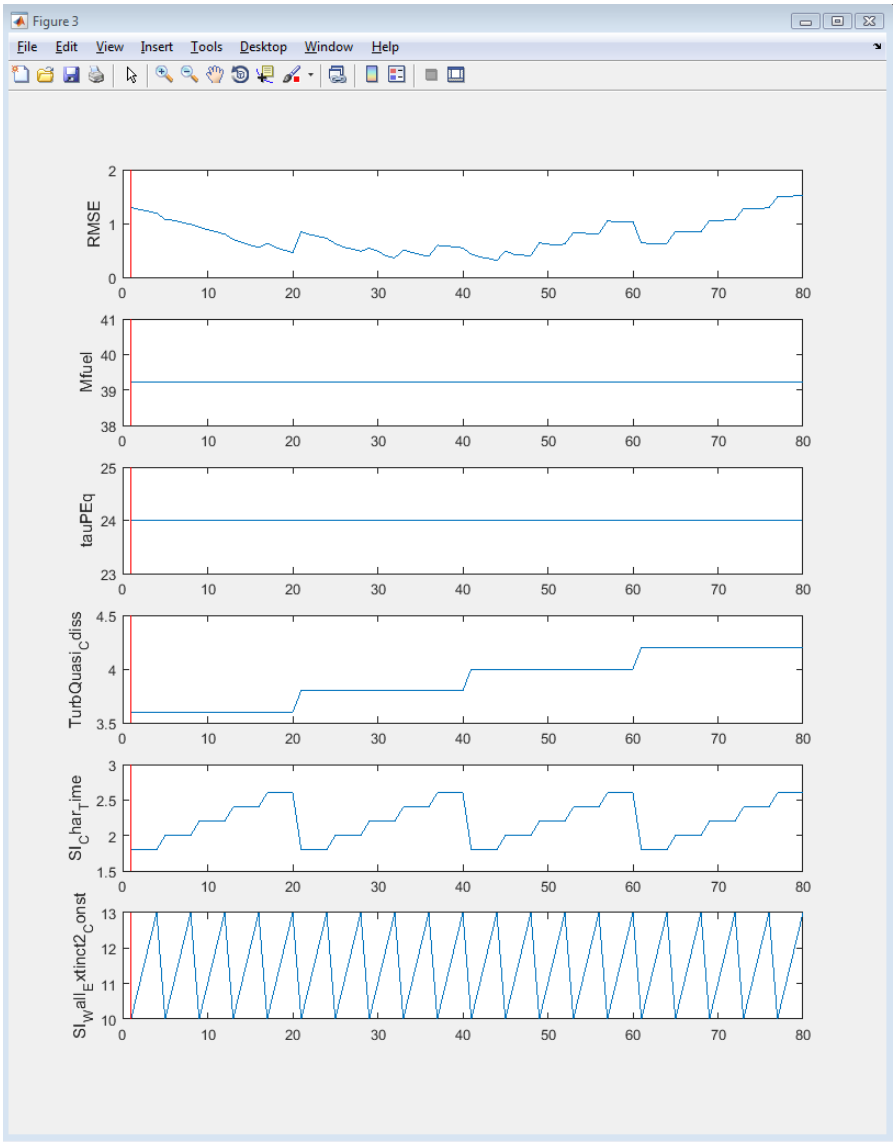

Figure A-4: Plots depicting the values of all variables for each case during a calibration run in the SRM software. The RMSE for each case is displayed in the top plot and the mass of fuel in the plot below this. For this run the pressure equilibration constant (tauPeq) was not varied.

```
Command Window
  >> SRM_CalibTool_V4
  Number of parameters = 4
      'Parameters detected:'    'tauPEq'    'TurbQuasi-Cdiss'    'SI_Char_Time'    'SI_Wall_Extinct2_C...'

      'Parameters:'    'tauPEq'    'TurbQuasi_Cdiss'    'SI_Char_Time'    'SI_Wall_Extinct2_...'    'RMSE'
      'case 44'        '024.00'    '004.00'             '001.80'          '013.00'                  '0.311'
      'case 43'        '024.00'    '004.00'             '001.80'          '012.00'                  '0.348'
      'case 32'        '024.00'    '003.80'             '002.20'          '013.00'                  '0.360'
      'case 42'        '024.00'    '004.00'             '001.80'          '011.00'                  '0.374'
      'case 36'        '024.00'    '003.80'             '002.40'          '013.00'                  '0.386'

  fx >>
```

Figure A-5: Information displayed in the command window by the calibration tool after processing the simulation data with the corresponding experimental data.

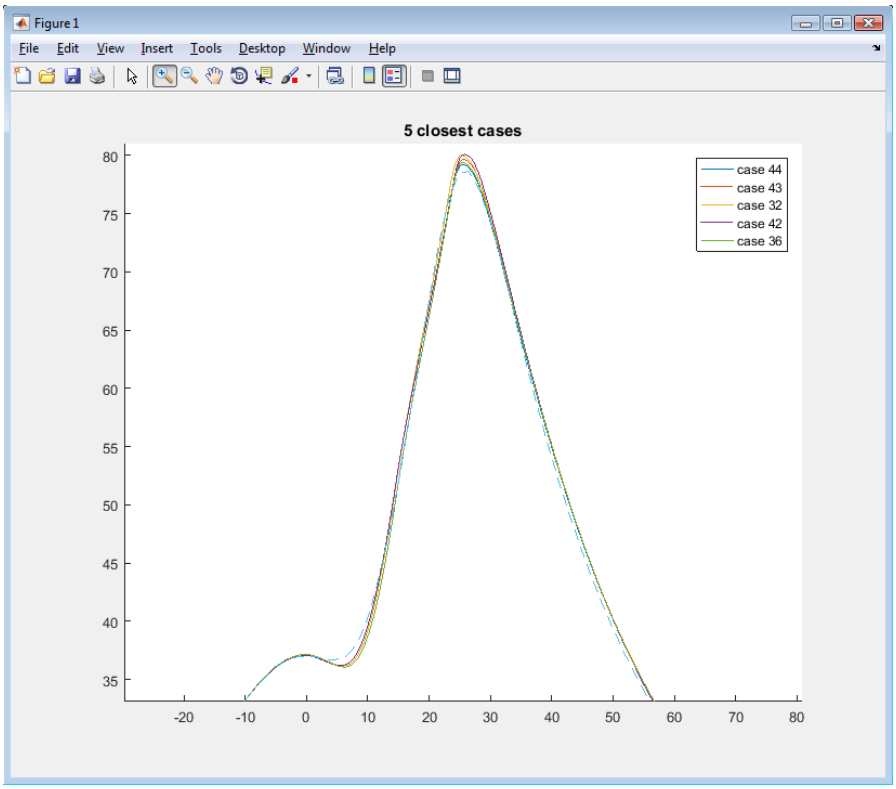

Figure A-6: Pressure traces for the five closest cases according to RMSE values, corresponding to the data displayed in Figures A-4 and A-5.

A.4 Example of unrealistic response of an NO submodel

The following summarises an initial test with a mechanism that was not previously validated for initial NO concentrations, and highlights the care that must be taken in selecting an appropriate mechanism.

The mechanism of Sarathy et al [163] was initially considered due to the rigorous validation evident in its publication and its relatively recent development. However this mechanism did not include any NO interactions, despite mention of NOx emission prediction in its publication. The mechanism of Cai et al [8] was also considered to be well validated, although slightly too large for its application in this study, so the NO submodel from Cai et al's mechanism was blended into the reduced TRF mechanism from Sarathy et al.

During initial runs of the model it became immediately apparent that the heat release behaviour of the model was not realistic with the presence of NO at the inlet. A com-

parison between two conditions is illustrated in Figure A-7 where both blue and orange traces represent a 9% EGR condition, with NO present in the EGR for the blue trace, and without NO present in the EGR for the orange trace. The dashed orange trace is included to provide an example of how a normal combustion event would be expected to appear.

The heat release spike displayed by the blue trace raises the temperature (bottom right plot) which raises the cylinder pressure near TDC as seen in the top left plot. This is caused by the sudden consumption of the available NO before the spark, which is converted to NO_2 whilst breaking down some of the fuel molecules to create a large concentration of HO_2 molecules – which are promptly consumed in the breakdown of more fuel molecules. Interestingly in this case there is only a slight effect on OH radical concentrations, and no OH production pre-ignition. The cause for this phenomenon can be attributed to the activation energy and reaction rate for the NO interaction with the HC molecules being too sensitive for these conditions. Further examination of the source for the NO model that was included reveal that it was initially developed for prediction of NOx emissions by Lamoureux et al [188] and was only validated for conditions where NO was not present before ignition.

Whilst this comparison does not provide any insight into real chemical interactions, it does illustrate the dangers in relying too heavily on mechanisms that are being applied outside of their validation conditions. Care was taken during the following mechanism selection process to ensure that the NO submodels were validated for modelling NO sensitisation of HC molecules.

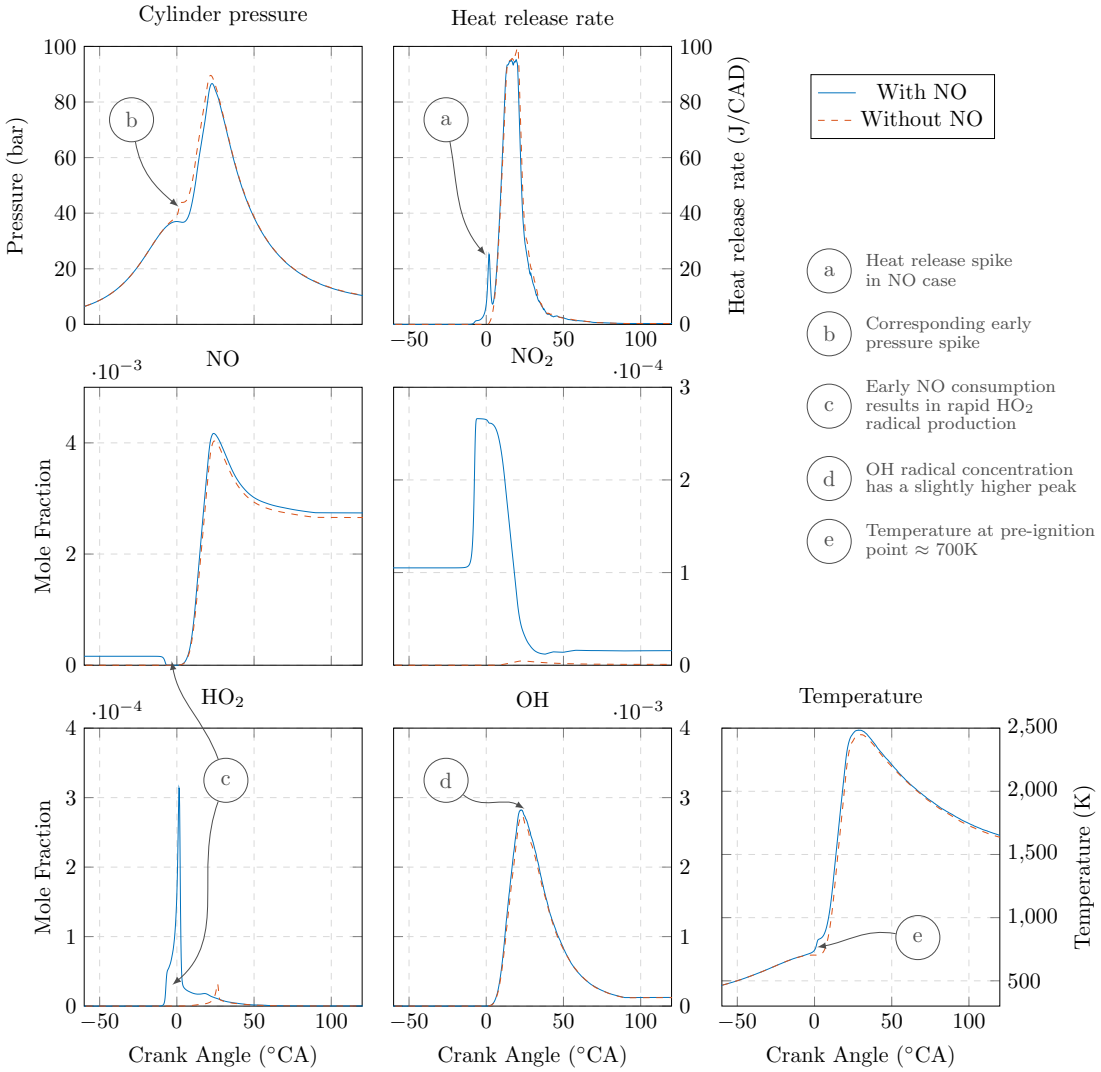

Figure A-7: Illustration of the erroneous early ignition displayed by the model when using the reduced mechanism from [7] blended with the NO sub model from [8]. This phenomenon was only revealed by the addition of NO to the EGR composition, the case displayed in these plots is the 9% EGR case – the blue trace denotes EGR including NO, and the dashed orange trace denotes EGR without NO.